Analysis of aortic-valve blood flow using computational fluid dynamics

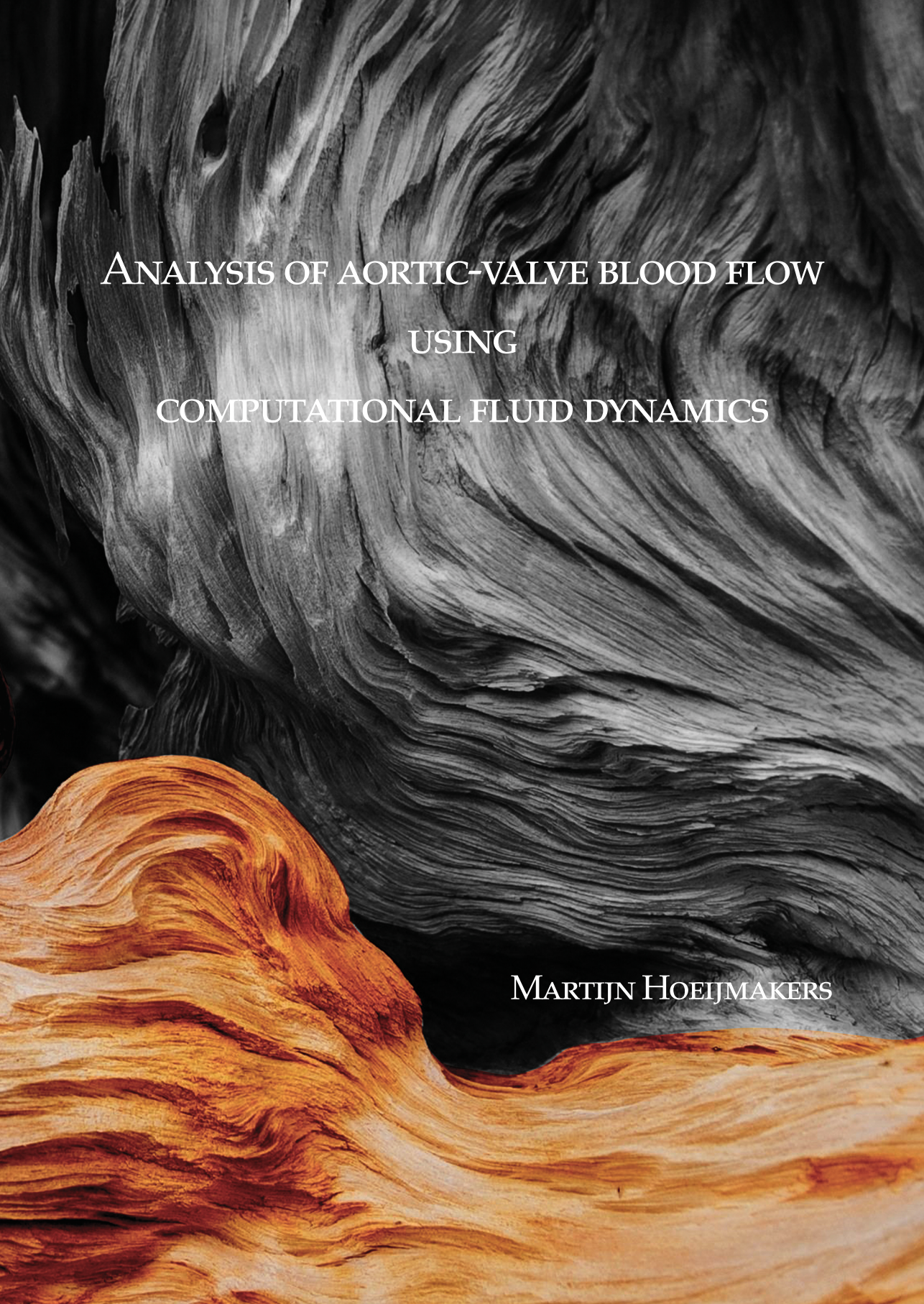

Analysis of aortic-valve blood flow using computational fluid dynamics

Martijn Hoeijmakers

Analysis of aortic-valve blood flow using computational fluid dynamics

A catalogue record is available from the Eindhoven University of Technology Library
ISBN 978-90-386-5188-0

Typeset using LaTeX
Layout: M.J.M.M. Hoeijmakers
Cover: M.J.M.M. Hoeijmakers
Print: Ridderprint | www.ridderprint.nl

The research presented in this thesis was performed at the Eindhoven University of Technology.

This thesis was financially supported by Ansys Inc, Villeurbanne, France

ANALYSIS OF AORTIC-VALVE BLOOD FLOW USING COMPUTATIONAL FLUID DYNAMICS

PROEFSCHRIFT

ter verkrijging van de graad van doctor aan de Technische Universiteit Eindhoven, op gezag van de rector magnificus prof. dr. ir. F.P.T. Baaijens, voor een commissie aangewezen door het College voor Promoties, in het openbaar te verdedigen op vrijdag 8 januari 2021 om 13.30 uur

door

MARTINUS JAN MATHIJS MARTIJN HOEIJMAKERS

geboren te Venray

Dit proefschrift is goedgekeurd door de promotoren en de samenstelling van de promotiecommisie is als volgt:

Voorzitter:	prof. dr. M. Merkx
Promotor:	prof. dr. ir. F.N. van de Vosse
Copromotor:	dr. ir. M.C.M. Rutten
Leden:	prof. dr. ir. P.D. Anderson
	prof. dr. ir. T. Ebbers (Linköping University)
	prof. dr. J. Pluim
	prof. dr. F. Toschi
Adviseurs:	dr. M. Rochette (Ansys Inc.)
	dr. P.A.L. Tonino, MD (Catharina Hospital Eindhoven)

Het onderzoek dat in dit proefschrift wordt beschreven is uitgevoerd in overeenstemming met de TU/e Gedragscode Wetenschapsbeoefening.

CONTENTS

CHAPTER 1 GENERAL INTRODUCTION **1**
1.1 AORTIC VALVE ANATOMY AND FUNCTION 3
1.2 CLINICAL DIAGNOSIS OF AORTIC VALVE STENOSIS 4
1.3 IMAGE-BASED COMPUTATIONAL MODELS 6
1.4 TURBULENCE MODELS 7
1.5 META-MODELS 8
1.6 STATISTICAL SHAPE MODELING 9
1.7 VERIFICATION & VALIDATION OF CFD MODELS 10
1.8 THESIS AIM AND OUTLINE 10

CHAPTER 2 ESTIMATION OF VALVULAR RESISTANCE OF SEGMENTED AORTIC VALVES USING COMPUTATIONAL FLUID DYNAMICS **17**
2.1 INTRODUCTION 19
2.2 MATERIALS AND METHODS 20
2.3 RESULTS 27
2.4 DISCUSSION 30
2.5 CONCLUSION 34

CHAPTER 3 COMBINING STATISTICAL SHAPE MODELING, CFD, AND META-MODELING TO APPROXIMATE THE PATIENT-SPECIFIC PRESSURE-DROP ACROSS THE AORTIC VALVE IN REAL-TIME **39**
3.1 INTRODUCTION 41
3.2 MATERIALS AND METHODS 43
3.3 RESULTS 53
3.4 DISCUSSION 58

CHAPTER 4 SENSITIVITY ANALYSIS AND UNCERTAINTY QUANTIFICATION FOR TRANSVALVULAR PRESSURE-DROP COMPUTATIONS **73**
4.1 INTRODUCTION 75
4.2 MATERIALS AND METHODS 77
4.3 RESULTS 88
4.4 DISCUSSION 90

CHAPTER 5 SCALE-RESOLVING SIMULATIONS OF STEADY AND PULSATILE FLOW THROUGH HEALTHY AND STENOTIC HEART VALVES **101**
5.1 INTRODUCTION 103
5.2 METHODS 104
5.3 RESULTS 112
5.4 DISCUSSION 122

CHAPTER 6 EXPERIMENTAL VALIDATION OF THE SIMULATED TRANSVALVULAR PRESSURE-DROP IN STEADY AND PULSATILE FLOW CONDITIONS **133**
6.1 INTRODUCTION 135
6.2 METHODS 137
6.3 RESULTS 141
6.4 DISCUSSION 146

CHAPTER 7 GENERAL DISCUSSION **153**
7.1 OVERVIEW OF MAIN FINDINGS 155
7.2 IMAGE-BASED COMPUTATIONAL MODELS 156
7.3 IN PURSUIT OF FAST AND ACCURATE PATIENT-SPECIFIC MODELS: IS META-MODELING THE SOLUTION? 157
7.4 VALIDATION OF NUMERICAL MODELS 158
7.5 LIMITATIONS & RECOMMENDATIONS FOR FUTURE WORK 160
7.6 FUTURE OUTLOOK ON COMPUTATIONAL MODELING IN CARDIOLOGY 160
7.7 CONCLUDING REMARKS 161

SUMMARY **165**

SAMENVATTING **169**

CURRICULUM VITAE **173**

LIST OF PUBLICATIONS **175**

Chapter 1

General introduction: CFD models for aortic valve analysis

1.1 AORTIC VALVE ANATOMY AND FUNCTION

THE heart is the central organ in the cardiovascular system. The heart functions as a pulsating pump, contracting about 60 times per minute to consistently provide all organs with sufficient oxygenated blood. The heart contains four heart valves: the tricuspid valve, the pulmonary valve, the mitral valve, and the aortic valve (Figure 1.1). Within the right side of the heart, the tricuspid valve ensures unidirectional blood flow from the right atrium into the right ventricle. Consequently, the pulmonary valve ensures that blood flows from the right ventricle into the pulmonary circulation. Similarly, within the left part of the heart, the mitral valve ensures unidirectional flow from the left atrium into the left ventricle. Finally, the aortic valve ensures that blood flows from the left ventricle into the systemic circulation. Proper opening and closing of each of these valves ensures unidirectional blood flow and that the heart remains an efficient pump. Healthy heart valves are flexible and open and close completely, resulting in minimal obstruction of blood flow. Hence, healthy heart valves exert no additional load on the heart muscle.

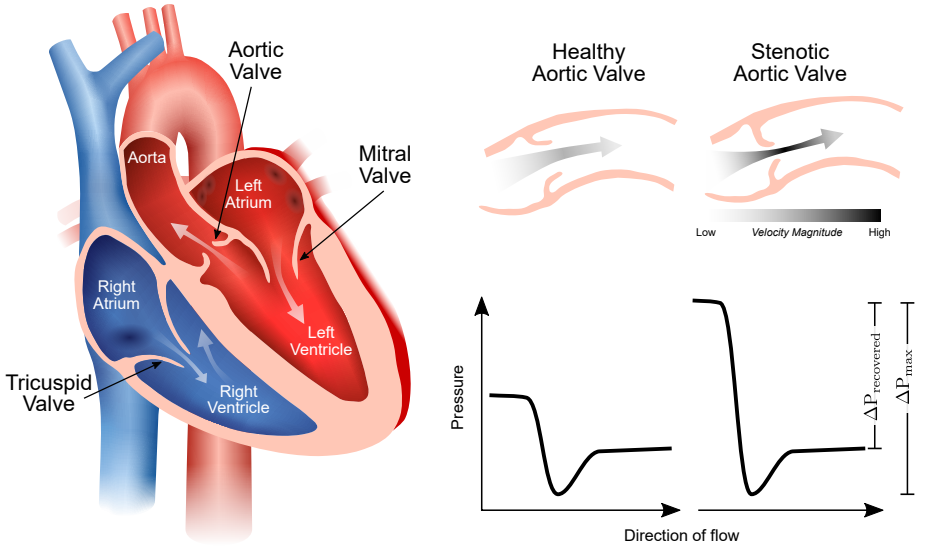

Figure 1.1 Schematic representation of the left and right heart and its heart valves. Pressure is almost completely recovered in healthy aortic valves. Diseased, stenotic heart valves are characterized by a narrow opening, high blood velocity, and large (irreversible) pressure-drop. Note that the pulmonary valve is out of plane, but would be situated between the tricuspid and aortic valves.

It is estimated that 2.5% of the population suffers from some form of heart valve disease (Nkomo et al. 2006). Prevalence increases with age, and studies indicate that heart valve disease is present in about 13% of the population older than 75 years (Nkomo et al. 2006). Various forms of valvular disease exist; but studies suggest that aortic valve stenosis —

the narrowing of the aortic valve opening in systole — is most common and occurs in 43% of patients with a valvular disease (Iung et al. 2003). Aortic valve stenosis is characterized by anatomical alterations of the aortic valve apparatus by the formation of calcifications in, on, and around the valve tissue. This leads to stiffening and reduced flexibility of the leaflets (Leopold 2012). This results in a dysfunctional valve: in systole the valve does not open completely anymore, obstructing blood flow. As a consequence, a large pressure difference is required to maintain blood flow (Figure 1.1), and increases the load on the heart muscle. The increased load on the heart muscle provokes a hypertrophic response that may eventually lead to heart failure. Aortic valve stenosis generally has a long asymptomatic latent period, but once severe symptoms develop, untreated patients have a poor prognosis (Ross and Braunwald 1968).

1.2 CLINICAL DIAGNOSIS OF AORTIC VALVE STENOSIS

The drop in pressure between the left ventricle and the ascending aorta is a key indicator for the severity of aortic valve stenosis (Saikrishnan et al. 2014; Nishimura et al. 2014; Vahanian et al. 2006). In the past, assessment of the pressure-drop was routinely done by cardiac catheterization, an invasive technique that introduces a pressure-wire into the left ventricle and ascending aorta (Nishimura and Carabello 2012). Later, Doppler echocardiography allowed for non-invasive assessment of the pressure-drop (Nishimura and Tajik 1994). This is currently the methodology of choice to determine aortic stenosis severity in clinical practice (Saikrishnan et al. 2014; Nishimura et al. 2014; Falk et al. 2017). Doppler echocardiography is capable of measuring the transvalvular jet velocity through the stenotic heart valve. Consequently, the transvalvular pressure-drop can be estimated from the transvalvular jet velocity (Chambers 2016; Baumgartner et al. 2009; Baumgartner et al. 2016). The transvalvular pressure-drop (in mmHg) is computed based on the principles of the Bernoulli equation, and clinically simplified to $4v^2$, with v the jet velocity in $\mathrm{m{\cdot}s^{-1}}$ (Hatle et al. 1980). This method assumes that when blood is accelerated into the narrowed valve opening, pressure is irreversibly converted to kinetic energy. However, downstream of the valve, flow is decelerated, and pressure may be partially recovered (Figure 1.1). Energy is lost through vortex formation, viscous losses, and losses from turbulence. Pressure recovery can cause significant differences between the Doppler derived transvalvular pressure-drop and the pressure-drop measured by catheterization. In fact, it was shown that the Doppler derived pressure-drops can substantially overestimate stenosis severity for mild to moderately stenotic aortic valves (Niederberger et al. 1996; Voelker et al. 1992; Bahlmann et al. 2010; Laskey and Kussmaul 1994) and valve prostheses (Bach et al. 2012; Vandervoort et al. 1995). Besides the transvalvular pressure-drop, Doppler echocardiography may also be used to estimate the

aortic valve opening area by means of the continuity equation (Chambers 2016). That is:

$$A_{\text{AV}} = \frac{v_{\text{LVOT}} \cdot A_{\text{LVOT}}}{v_{\text{AV}}} \tag{1.1}$$

In Equation 1.1 v_{LVOT} is the left ventricular outflow tract velocity; v_{AV} the velocity at the vena contracta; and A_{AV} the the cross-sectional area of the left ventricular outflow tract. These additional parameters can be obtained by Doppler ultrasound, and be used to obtain the effective orifice area of the valve (A_{AV}). A_{AV} is an estimate of the (effective) cross-sectional area at the vena-contracta, which is slightly smaller than the anatomic orifice area. The ratio between both areas is generally referred to as the contraction coefficient, and may be as low as 0.63 for severely stenotic cases (Migliore et al. 2017).

Clinical classification of aortic valve stenosis is for a large part based on measured values of the transvalvular jet velocity, transvalvular pressure-drop, and aortic valve area (Table 1.1). Severe aortic valve stenosis is classified as: a jet velocity >4.0 m·s^{-1}, a mean transvalvular pressure-drop >40 mmHg and a valve orifice area <100 mm^2. Moderate aortic valve stenosis is classified as: a jet velocity 3.0 – 4.0 m·s^{-1}, a mean transvalvular pressure-drop 20 – 40 mmHg, and a valve area of 100 – 150 mm^2. Mild aortic valve stenosis: a jet velocity 2.6 – 2.9 m·s^{-1}, mean transvalvular pressure-drop of <20 mmHg, and a valve area of >150 mm^2. However, discordant grading based on these metrics is common, with some studies estimating that this occurs in 26-30% of aortic valve stenosis patients with a normal ejection fraction (Berthelot-Richer et al. 2016). This demonstrates that complementary metrics for determining aortic valve disease severity are desirable.

Table 1.1 Grading of aortic valve stenosis severity

	Mild	Moderate	Severe
Transvalvular v_{max} [m·s^{-1}]	2.6 – 2.9	3.0 – 4.0	>4.0
Transvalvular ΔP peak systole [mmHg]	<40	40 – 65	>65
Transvalvular ΔP mean [mmHg]	<20	20 – 40	>40
Effective orifice area [mm^2]	>150	100 – 150	<100

Grading adopted from Chambers (2016)

Comprehensive patient-specific models of the heart and aortic valve have the potential to yield these complementary diagnostic metrics for aortic valve stenosis. For example, by detailed *in-silico* modeling of blood flow around, and through the aortic valve. The

focus of this thesis is to develop such patient-specific computational models. Moreover, model simplifications were systematically investigated, with the ultimate goal of making computational models of blood flow feasible for day-to-day clinical practice.

1.3 IMAGE-BASED COMPUTATIONAL MODELS

Echocardiography is inexpensive, readily available and easy to perform. When echocardiography results are inconclusive, Computed Tomography (CT) or cardiac Magnetic Resonance Imaging (MRI) can be used to derive complementary diagnostic indicators, e.g, the aortic diameter or amount of calcification (Chun et al. 2008; Clavel et al. 2013). Furthermore, both CT and MRI enable detailed three-dimensional segmentations of the full-heart anatomy. Segmentation methods have improved considerably over the past years (Ecabert et al. 2008; Ecabert et al. 2011; Grbic et al. 2012; Ionasec et al. 2010), and have resulted in a tremendous increase in the use of complex three-dimensional patient-specific simulations (Neal and Kerckhoffs 2009). Image-based patient-specific computational models are now widely adopted throughout the cardiovascular research community. For instance, patient-specific computational fluid dynamics (CFD) models are used to assess hemodynamic quantities such as stress, wall shear stress, or pressure drops (Min et al. 2015; Kimura et al. 2017; Morris et al. 2013; Traeger et al. 2015; Cibis et al. 2014; Lantz et al. 2016). These quantities are difficult, or sometimes impossible to assess with imaging techniques alone. Patient-specific CFD models are already applied in order to non-invasively detect coronary artery disease in the clinic (Min et al. 2015; Morris et al. 2013). However, in the field of heart-valve disease, CFD is not yet accepted for clinical diagnostics. Instead, three-dimensional CFD simulations are primarily used to understand the fundamental principles of valve dynamics (Nobili et al. 2008), left ventricular hemodynamics (Doost et al. 2016), or for valve design (Xu et al. 2018). Nevertheless, work by Kelm et al. (2017) and Luraghi et al. (2019) demonstrate that image-based CFD has clinical potential, e.g., for CFD-based virtual treatment. However, patient-specific computational modeling of aortic valve behavior has not yet matured to the point that clinical implementation is viable.

The thin and flexible nature of the aortic valve makes imaging, segmentation, and modeling the patient-specific aortic valve extremely difficult. For instance, the aortic valve is between 0.35 and 3.5 mm thick (Sahasakul et al. 1988). Voxel size of a typical cardiac CT image is $0.5\times0.5\times0.5$ mm (Ghekiere et al. 2017), and thus of the same order as valve thickness. Additionally, temporal resolution of CT is limited by gantry speed, and is around 100 ms (Flohr et al. 2009), and may therefore not be adequate to properly capture the rapid opening ($<$50 ms), and closing ($<$ 60ms) of the aortic valve in systole

(Leyh et al. 1999). However, the valve stays open sufficiently long (around 250 ms) to capture its open state with Electrocardiography-gated CT. Poor image quality and temporal resolution make it challenging to segment the aortic valve. Nevertheless, by making use of the intrinsic shape of the valve, model-based segmentation methods are able to (semi-)automatically generate high quality valve models that are suitable for computational fluid dynamics (Weese et al. 2017; Grbic et al. 2012; Ionasec et al. 2010).

Extracting the valvular shape from imaging seems feasible. However, consequent modeling of valvular dynamics is demanding from a computational point of view. Structural behavior of the aortic valve is strongly coupled to fluid flow, and ideally needs to be treated as such in numerical schemes. Large deformation of the leaflets make the traditional Arbitrary-Euler-Lagrange approach less robust and efficient, e.g., due to mesh distortion and frequent remeshing. Hence, efficient numerical schemes were proposed, such as the immersed-boundary (Gilmanov et al. 2019) and fictitious domain (De Hart et al. 2003) method. Generally, such methods are more efficient, but at the expense of solution accuracy at the solid-fluid interface. Despite such improvements in efficiency, fluid-structure interaction simulations generally require days or weeks to complete for 3-dimensional (3D) geometries, making their use intractable for day-to-day clinical practice. Additionally, valvular dynamics strongly depend on material properties, and are difficult or impossible to reliably obtain from imaging data. Instead, valvular dynamics are often neglected by fixing the aortic valve in its most open position (Weese et al. 2017; Traeger et al. 2015; Bruening et al. 2018; Dwyer et al. 2009), or by deriving patient-specific velocity profiles from phase-contrast MRI (Vergara et al. 2011; Youssefi et al. 2017; Wendell et al. 2013). Neglecting valvular dynamics makes computational models much more efficient, and it was shown that a two-state (open/closed) representation of the aortic valve yielded similar results as a full fluid-structure interaction (fictitious domain) simulation of the aortic valve (Astorino et al. 2012). Omitting the strong fluid-structure coupling substantially reduces numerical complexity. However, computational requirements can still be considerable, but would then mainly be determined by the type of fluid (e.g., constant viscosity and density) and the type of flow: steady or unsteady flow; laminar, transitional or turbulent flow.

1.4 TURBULENCE MODELS

Early in-vivo (Stein and Sabbah 1976; Walburn et al. 1983; Nygaard et al. 1994; Ha et al. 2018; Yamaguchi et al. 1983) and in-vitro (Bluestein and Einav 1995; Yoganathan et al. 1979; Clark 1976) studies have demonstrated that significant random fluctuations in blood velocity — associated with turbulence — can be expected downstream of healthy and

diseased heart valves. Furthermore, it was demonstrated that patients with stenotic heart valves may exhibit higher levels of turbulence compared to healthy individuals. Previous studies have associated high levels of turbulence to hemolysis (Sallam and Hwang 1984; Kameneva et al. 2004) and thrombus formation (Stein and Sabbah 1974; Dangas et al. 2016), suggesting that prediction of turbulence production through modeling is beneficial.

Flow downstream of a (stenotic) heart valve is pulsatile in nature, and is characterized by intermittent (low Reynolds) turbulence (Bluestein and Einav 1995). That is, turbulent structures are generated in systole, but quickly decay in diastole due to viscosity and the lack of flow (energy source). Turbulent flows are characterized by a wide range of spatial and temporal scales in the velocity field, which makes Direct Numerical Simulation (DNS) particularly demanding from a computational point of view. Due to the extensive computational cost of DNS, two modeling strategies are popular: 1) just the largest scales are resolved, e.g., by Large Eddy Simulation (LES), or 2) the time-averaged (turbulent) flow field is solved by making use of the Reynolds Averaged Navier-Stokes (RANS) equations. The LES approach resolves the largest structures in the flow by making use of the filtered Navier-Stokes equations. The main idea is that the largest scales contain most of the energy, and modeling the contribution of the smallest (isotropic) scales is easier. The smallest scales are related to the larger scales through sub-grid models (Lilly 1992), and do not need to be resolved directly, greatly reducing the required computational resources with respect to DNS. In contrast, the RANS approach assumes that the flow can be decomposed into a mean part and a fluctuating part. Through closure models, and a "turbulent viscosity", only the mean turbulent flow is then characterized. Popular models include the $k-\epsilon$ (Launder and Spalding 1974) and Shear-Stress Transport $k-\omega$ models (Menter 1994). RANS models are computationally efficient, but may not always be appropriate for the transitional and intermittent nature of turbulence encountered in cardiovascular flows (Yoganathan et al. 2005). Hence, the applicability of RANS models should be carefully scrutinized, and preferably be compared to a computationally more demanding scale-resolving method, such as DNS or LES. The scale-resolving simulations should give an indication whether the assumptions made under RANS are reasonable for a particular cardiovascular flow configuration.

1.5 META-MODELS

Sections 1.3 and 1.4 provide some suggestions for reducing the computational cost of image-based computational models. However, time-till-outcome for a 3D CFD model can still be considerable. A viable alternative could be to train meta-models (also known as surrogate models) with simulation data. Once a meta-model is trained with suffi-

cient simulation data it can function as an effective surrogate. For instance, Kriging meta-models have been used successfully in optimizing stents, stenoses, bifurcations, or anastomoses (Marsden et al. 2008; Pant et al. 2011; Li et al. 2017). Furthermore, neural network-based meta-models have been trained with simulation data in order to obtain real-time stress distributions on the aortic wall (Liang et al. 2018), aortic flow patterns (Liang et al. 2020), and left ventricular mechanical behavior (Dabiri et al. 2019). However, small uncertainties in shape, e.g., due to segmentation errors, may lead to substantial uncertainty in the result of such hemodynamic simulations (Sen et al. 2014; Sankaran et al. 2015; Sankaran et al. 2016; Sturdy et al. 2019; Venugopal et al. 2018). This uncertainty in simulation results can be quantified by sensitivity analysis and uncertainty quantification, and can help to strengthen confidence in the computational model or for model improvement. The efficient nature of meta-models make them suitable for sensitivity analysis and uncertainty quantification (Quicken et al. 2016), which will — with the shift towards patient-specific models — become increasingly important (Eck et al. 2015).

1.6 STATISTICAL SHAPE MODELING

For the meta-model approach to be clinically applicable, it is key to account for geometrical variation of shape within the population. A popular method to capture shape variation is by a statistical shape model (SSM), which is often obtained through Principal Component Analysis (PCA) (Heimann and Meinzer 2009). PCA decomposes a multivariate data set into a mean and covariance matrix. The sorted eigenvectors (shape modes) and eigenvalues (shape mode coefficients) of the covariance matrix then describe the main directions of shape variance and its relative importance in the population. Applications of SSM's are numerous and some examples include: organ segmentation (Yates and Untaroiu 2018; Spinczyk and Krasoń 2018; Woo et al. 2016), extracting morphological bio-markers of (diseased) organs (Suinesiaputra et al. 2018; Uetani et al. 2014; Bruse et al. 2016), or for relating injuries to morphological changes (Nelson et al. 2017).

In combination with simulation tools such as CFD, the shape modes and corresponding shape mode coefficients can be used to: relate variations in ventricular shape to variations in ventricular blood flow (Khalafvand et al. 2018); correlating aortic aneurysm shape to CFD-derived biomechanical descriptors (Cosentino et al. 2020); or to relate aortic shape variation to numerically computed stress distributions (Liang et al. 2018). The study by Liang et al. (2018) demonstrates that a fast and accurate meta-model can be trained that relates shape coefficients to the expected outcome of the simulation. Well-trained meta-models can produce near real-time results with clinically acceptable accuracy, and may be the right strategy to accelerate acceptance of compute-intensive computational

models in day-to-day clinical practice.

1.7 VERIFICATION & VALIDATION OF CFD MODELS

Previous sections have shown that the use of CFD in the field of cardiovascular research is widely accepted. Nevertheless, CFD remains an intricate tool and models need to be extensively verified and validated. Verification and validation are the primary methods to build and quantify confidence in computational simulations (Oberkampf and Trucano 2002; V&V40 2018). Verification is aimed at the assessment of the accuracy of a computational model with respect to known (analytic) solutions and mainly a mathematical issue. Validation is the assessment of the accuracy of a computational model by comparison to experimental data and is mainly a physics issue (Oberkampf and Trucano 2002). Verification and validation is crucial for establishing model credibility. For instance, results may strongly depend on discretization schemes and model simplifications, which are often a necessity to keep computational cost reasonable. Some typical simplifications for modeling aortic valve blood flow include: 1) neglecting valvular dynamics (section 1.3); 2) assuming fully developed turbulence (section 1.4); 3) neglecting flow pulsatility; and 4) neglecting non-Newtonian behavior. Hence, modeling work should ideally be closely integrated with and guided by *in-vitro* and *in-vivo* experimental data.

1.8 THESIS AIM AND OUTLINE

Patient-specific CFD modeling of blood flow over the aortic valve has the potential to provide complementary diagnostic metrics for aortic valve stenosis. Therefore, the aim of this thesis was two-fold. First, to develop a simulation framework that allows patient-specific simulation of flow through the aortic valve. Second, we aim to drastically reduce computational cost by investigating under what conditions model simplifications hold.

In **Chapter 2** imaging data of the aortic valve and contracting left ventricle is used in combination with a CFD model. Simplifications of the computational framework are systematically analyzed and presented. Additionally, from the CFD data, a valve resistance index is proposed that should more accurately reflect the significance of aortic valve stenosis.

Chapter 3 attempts to relate variations in valvular shape to variations in the CFD-computed pressure-drop. For this we make use of a combination of statistical shape modeling, CFD, and meta-modeling. It is demonstrated, that with this combination, the

computational cost of time-consuming CFD-simulations can be reduced to near real-time.

Chapter 4 uses the meta-model that is presented in **Chapter 3** for sensitivity analysis and uncertainty quantification. Geometrical uncertainty is introduced through the statistical shape model, and is related to uncertainties in the patient-specific transvalvular pressure-drop vs. flow relationship.

In **Chapter 5**, high-fidelity scale-resolving CFD simulations are used to analyze the turbulent flow downstream of a healthy and stenotic heart valve. Similarities and differences between steady and pulsatile flow conditions are presented.

In **Chapter 6**, results of an experimental validation study are presented. 3D printing was used to create physical aortic valve models that were similar to the virtual models used in **Chapters 2 – 5**. The transvalvular pressure-drop of these physical models was experimentally determined in a flow-circuit. Measured pressure-drops were then compared to the numerically computed pressure-drop.

Finally, **Chapter 7** puts the findings of **Chapters 2 – 6** into academic and clinical perspective by addressing relevant literature.

BIBLIOGRAPHY

Astorino, M. et al. (2012). "A robust and efficient valve model based on resistive immersed surfaces". In: *International Journal for Numerical Methods in Biomedical Engineering* 28.9, pp. 937–959.

Bach, D. S. et al. (2012). "In vitro assessment of prosthesis type and pressure recovery characteristics: doppler echocardiography overestimation of bileaflet mechanical and bioprosthetic aortic valve gradients". In: *The Journal of Thoracic and Cardiovascular Surgery* 144.2, pp. 453–458.

Bahlmann, E. et al. (2010). "Impact of pressure recovery on echocardiographic assessment of asymptomatic aortic stenosis: a SEAS substudy". In: *JACC: Cardiovascular Imaging* 3.6, pp. 555–562.

Baumgartner, H. et al. (2009). "Echocardiographic assessment of valve stenosis: EAE/ASE recommendations for clinical practice". In: *European Journal of Echocardiography* 10.1, pp. 1–25.

Baumgartner, H. et al. (2016). "Recommendations on the echocardiographic assessment of aortic valve stenosis: a focused update from the european association of cardiovascular imaging and the american society of echocardiography". In: *European Heart Journal - Cardiovascular Imaging* 18.3, pp. 254–275.

Berthelot-Richer, M. et al. (2016). "Discordant grading of aortic stenosis severity". In: *JACC: Cardiovascular Imaging* 9.7, pp. 797–805.

Bluestein, D. and S. Einav (1995). "The effect of varying degrees of stenosis on the characteristics of turbulent pulsatile flow through heart valves". In: *Journal of Biomechanics* 28.8, pp. 915–924.

Bruening, J. et al. (2018). "Impact of patient-specific LVOT inflow profiles on aortic valve prosthesis and ascending aorta hemodynamics". In: *Journal of Computational Science* 24, pp. 91–100.

Bruse, J. L. et al. (2016). "A statistical shape modelling framework to extract 3d shape biomarkers from medical imaging data: assessing arch morphology of repaired coarctation of the aorta". In: *BMC Medical Imaging* 16.1.

Chambers, J. B. (2016). "The assessment of aortic stenosis: echocardiography and beyond." In: *British journal of hospital medicine* 77 (3), pp. 141–146.

Chun, E. J. et al. (2008). "Aortic stenosis: evaluation with multidetector CT angiography and MR imaging". In: *Korean Journal of Radiology* 9.5, p. 439.

Cibis, M. et al. (2014). "Wall shear stress calculations based on 3d cine phase contrast MRI and computational fluid dynamics: a comparison study in healthy carotid arteries". In: *NMR in Biomedicine* 27.7, pp. 826–834.

Clark, C. (1976). "Turbulent velocity measurements in a model of aortic stenosis". In: *Journal of Biomechanics* 9.11, pp. 677–687.

Clavel, M.-A. et al. (2013). "The complex nature of discordant severe calcified aortic valve disease grading". In: *Journal of the American College of Cardiology* 62.24, pp. 2329–2338.

Cosentino, F. et al. (2020). "Statistical shape analysis of ascending thoracic aortic aneurysm: correlation between shape and biomechanical descriptors". In: *Journal of Personalized Medicine* 10.2, p. 28.

Dabiri, Y. et al. (2019). "Prediction of left ventricular mechanics using machine learning". In: *Frontiers in Physics* 7.

Dangas, G. D. et al. (2016). "Prosthetic heart valve thrombosis". In: *Journal of the American College of Cardiology* 68.24, pp. 2670–2689.

De Hart, J. et al. (2003). "A three-dimensional computational analysis of fluid-structure interaction in the aortic valve". In: *Journal of biomechanics* 36 (1), pp. 103–112.

Doost, S. N. et al. (2016). "Heart blood flow simulation: a perspective review". In: *BioMedical Engineering OnLine*

15.1.

Dwyer, H. A. et al. (2009). "Computational fluid dynamics simulation of transcatheter aortic valve degeneration". In: *Interactive CardioVascular and Thoracic Surgery* 9.2, pp. 301–308.

Ecabert, O. et al. (2008). "Automatic model-based segmentation of the heart in CT images". In: *IEEE Transactions on Medical Imaging* 27.9, pp. 1189–1201.

Ecabert, O. et al. (2011). "Segmentation of the heart and great vessels in CT images using a model-based adaptation framework". In: *Medical Image Analysis* 15.6, pp. 863–876.

Eck, V. G. et al. (2015). "A guide to uncertainty quantification and sensitivity analysis for cardiovascular applications". In: *International Journal for Numerical Methods in Biomedical Engineering* 32.8, e02755.

Falk, V. et al. (2017). "2017 ESC/EACTS guidelines for the management of valvular heart disease". In: *European Journal of Cardio-Thoracic Surgery* 52.4, pp. 616–664.

Flohr, T. G., R. Raupach, and H. Bruder (2009). "Cardiac ct: how much can temporal resolution, spatial resolution, and volume coverage be improved?" In: *Journal of Cardiovascular Computed Tomography* 3.3, pp. 143–152.

Ghekiere, O. et al. (2017). "Image quality in coronary CT angiography: challenges and technical solutions". In: *The British Journal of Radiology* 90.1072, p. 20160567.

Gilmanov, A. et al. (2019). "Image-guided fluid-structure interaction simulation of transvalvular hemodynamics: quantifying the effects of varying aortic valve leaflet thickness". In: *Fluids* 4.3, p. 119.

Grbic, S. et al. (2012). "Complete valvular heart apparatus model from 4d cardiac CT". in: *Medical Image Analysis* 16.5, pp. 1003–1014.

Ha, H. et al. (2018). "Age-related vascular changes affect turbulence in aortic blood flow". In: *Frontiers in Physiology* 9.

Hatle, L., B. A. Angelsen, and A. Tromsdal (1980). "Non-invasive assessment of aortic stenosis by doppler ultrasound." In: *Heart* 43.3, pp. 284–292.

Heimann, T. and H.-P. Meinzer (2009). "Statistical shape models for 3d medical image segmentation: a review". In: *Medical Image Analysis* 13.4, pp. 543–563.

Ionasec, R. I. et al. (2010). "Patient-specific modeling and quantification of the aortic and mitral valves from 4-d cardiac CT and TEE". in: *IEEE Transactions on Medical Imaging* 29.9, pp. 1636–1651.

Iung, B. et al. (2003). "A prospective survey of patients with valvular heart disease in Europe: The Euro Heart Survey on Valvular Heart Disease". In: *European Heart Journal* 24.13, pp. 1231–1243.

Kameneva, M. V. et al. (2004). "Effects of turbulent stresses upon mechanical hemolysis: experimental and computational analysis". In: *ASAIO Journal* 50.5, pp. 418–423.

Kelm, M. et al. (2017). "Model-based therapy planning allows prediction of haemodynamic outcome after aortic valve replacement". In: *Scientific Reports* 7.1.

Khalafvand, S. S. et al. (2018). "Assessment of human left ventricle flow using statistical shape modelling and computational fluid dynamics". In: *Journal of Biomechanics*.

Kimura, N. et al. (2017). "Patient-specific assessment of hemodynamics by computational fluid dynamics in patients with bicuspid aortopathy". In: *The Journal of Thoracic and Cardiovascular Surgery* 153.4, S52–S62.e3.

Lantz, J. et al. (2016). "Patient-specific simulation of cardiac blood flow from high-resolution computed tomography". In: *Journal of Biomechanical Engineering* 138.12, p. 121004.

Laskey, W. K. and W. G. Kussmaul (1994). "Pressure recovery in aortic valve stenosis". In: *Circulation* 89.1,

pp. 116–121.

Launder, B. E. and D. B. Spalding (1974). "The numerical computation of turbulent flows". In: *Computer Methods in Applied Mechanics and Engineering* 3.2, pp. 269–289.

Leopold, J. A. (2012). "Cellular mechanisms of aortic valve calcification". In: *Circulation: Cardiovascular Interventions* 5.4, pp. 605–614.

Leyh, R. G. et al. (1999). "Opening and closing characteristics of the aortic valve after different types of valve-preserving surgery." In: *Circulation* 100 (21), pp. 2153–2160.

Li, H. et al. (2017). "Design optimization of stent and its dilatation balloon using kriging surrogate model". In: *BioMedical Engineering OnLine* 16.1.

Liang, L., W. Mao, and W. Sun (2020). "A feasibility study of deep learning for predicting hemodynamics of human thoracic aorta". In: *Journal of Biomechanics* 99, p. 109544.

Liang, L. et al. (2018). "A deep learning approach to estimate stress distribution: a fast and accurate surrogate of finite-element analysis". In: *Journal of The Royal Society Interface* 15.138, p. 20170844.

Lilly, D. K. (1992). "A proposed modification of the germano subgrid-scale closure method". In: *Physics of Fluids A: Fluid Dynamics* 4.3, pp. 633–635.

Luraghi, G. et al. (2019). "On the modeling of patient-specific transcatheter aortic valve replacement: a fluid-structure interaction approach". In: *Cardiovascular Engineering and Technology* 10.3, pp. 437–455.

Marsden, A. L., J. A. Feinstein, and C. A. Taylor (2008). "A computational framework for derivative-free optimization of cardiovascular geometries". In: *Computer Methods in Applied Mechanics and Engineering* 197.21-24, pp. 1890–1905.

Menter, F. R. (1994). "Two-equation eddy-viscosity turbulence models for engineering applications". In: *AIAA Journal* 32.8, pp. 1598–1605.

Migliore, R. A. et al. (2017). "Estimation of contraction coefficient of gorlin equation for assessment of aortic valve area in aortic stenosis". In: *World Journal of Cardiovascular Diseases* 07.04, pp. 119–130.

Min, J. K. et al. (2015). "Noninvasive fractional flow reserve derived from coronary CT angiography". In: *JACC: Cardiovascular Imaging* 8.10, pp. 1209–1222.

Morris, P. D. et al. (2013). "Virtual fractional flow reserve from coronary angiography: modeling the significance of coronary lesions". In: *JACC: Cardiovascular Interventions* 6.2, pp. 149–157.

Neal, M. L. and R. Kerckhoffs (2009). "Current progress in patient-specific modeling". In: *Briefings in Bioinformatics* 11.1, pp. 111–126.

Nelson, A. E. et al. (2017). "Cross-sectional associations between variations in ankle shape by statistical shape modeling, injury history, and race: the johnston county osteoarthritis project". In: *Journal of Foot and Ankle Research* 10.1.

Niederberger, J. et al. (1996). "Importance of pressure recovery for the assessment of aortic stenosis by doppler ultrasound. role of aortic size, aortic valve area, and direction of the stenotic jet in vitro." In: *Circulation* 94 (8), pp. 1934–1940.

Nishimura, R. A. and B. A. Carabello (2012). "Hemodynamics in the cardiac catheterization laboratory of the 21st century". In: *Circulation* 125.17, pp. 2138–2150.

Nishimura, R. A. and A. J. Tajik (1994). "Quantitative hemodynamics by doppler echocardiography: a noninvasive alternative to cardiac catheterization". In: *Progress in Cardiovascular Diseases* 36.4, pp. 309–342.

Nishimura, R. A. et al. (2014). "2014 AHA/ACC guideline for the management of patients with valvular heart

disease". In: *Journal of the American College of Cardiology* 63.22, e57–e185.

Nkomo, V. T. et al. (2006). "Burden of valvular heart diseases: a population-based study." In: *Lancet* 368 (9540), pp. 1005–1011.

Nobili, M. et al. (2008). "Numerical simulation of the dynamics of a bileaflet prosthetic heart valve using a fluid–structure interaction approach". In: *Journal of Biomechanics* 41.11, pp. 2539–2550.

Nygaard, H. et al. (1994). "Turbulent stresses downstream of three mechanical aortic valve prostheses in human beings." In: *The Journal of thoracic and cardiovascular surgery* 107 (2), pp. 438–446.

Oberkampf, W. L. and T. G. Trucano (2002). "Verification and validation in computational fluid dynamics". In: *Progress in Aerospace Sciences* 38.3, pp. 209–272.

Pant, S. et al. (2011). "Multiobjective design optimisation of coronary stents". In: *Biomaterials* 32.31, pp. 7755–7773.

Quicken, S. et al. (2016). "Application of an adaptive polynomial chaos expansion on computationally expensive three-dimensional cardiovascular models for uncertainty quantification and sensitivity analysis". In: *Journal of Biomechanical Engineering* 138.12, p. 121010.

Ross, J. and E. Braunwald (1968). "Aortic stenosis". In: *Circulation* 38.1s5.

Sahasakul, Y. et al. (1988). "Age-related changes in aortic and mitral valve thickness: implications for two-dimensional echocardiography based on an autopsy study of 200 normal human hearts". In: *The American Journal of Cardiology* 62.7, pp. 424–430.

Saikrishnan, N. et al. (2014). "Accurate assessment of aortic stenosis". In: *Circulation* 129.2, pp. 244–253.

Sallam, A. M. and N. H. C. Hwang (1984). "Human red blood cell hemolysis in a turbulent shear flow: contribution of reynolds shear stresses". In: *Biorheology* 21.6, pp. 783–797.

Sankaran, S., L. Grady, and C. A. Taylor (2015). "Fast Computation of Hemodynamic Sensitivity to Lumen Segmentation Uncertainty". In: *IEEE Transactions on Medical Imaging* 34.12, pp. 2562–2571.

Sankaran, S. et al. (2016). "Uncertainty quantification in coronary blood flow simulations: impact of geometry, boundary conditions and blood viscosity". In: *Journal of Biomechanics* 49.12, pp. 2540–2547.

Sen, Y. et al. (2014). "Image segmentation methods for intracranial aneurysm haemodynamic research". In: *Journal of Biomechanics* 47.5, pp. 1014–1019.

Spinczyk, D. and A. Krasoń (2018). "Automatic liver segmentation in computed tomography using general-purpose shape modeling methods". In: *BioMedical Engineering OnLine* 17.1.

Stein, P. D. and H. N. Sabbah (1976). "Turbulent blood flow in the ascending aorta of humans with normal and diseased aortic valves". In: *Circulation Research* 39.1, pp. 58–65.

Stein, P. D. and H. N. Sabbah (1974). "Measured turbulence and its effect on thrombus formation". In: *Circulation Research* 35.4, pp. 608–614.

Sturdy, J. et al. (2019). "Uncertainty quantification of computational coronary stenosis assessment and model based mitigation of image resolution limitations". In: *Journal of Computational Science* 31, pp. 137–150.

Suinesiaputra, A. et al. (2018). "Statistical shape modeling of the left ventricle: myocardial infarct classification challenge". In: *Journal of Biomedical and Health Informatics* 22.2, pp. 503–515.

Traeger, B. et al. (2015). "Methodological inaccuracies in clinical aortic valve severity assessment: insights from computational fluid dynamic modeling of CT-derived aortic valve anatomy". In: *Theoretical and Computational Fluid Dynamics* 30.1-2, pp. 107–128.

Uetani, M. et al. (2014). "Statistical shape model of the liver and its application to computer-aided diagnosis of liver cirrhosis". In: *Electrical Engineering in Japan* 190.4, pp. 37–45.

V&V40 (2018). *V&v 40 verification and validation in computational modeling of medical devices*. Standard. New York, USA: ASME.

Vahanian, A. et al. (2006). "Guidelines on the management of valvular heart disease: the task force on the management of valvular heart disease of the european society of cardiology". In: *European Heart Journal* 28.2, pp. 230–268.

Vandervoort, P. M. et al. (1995). "Pressure recovery in bileaflet heart valve prostheses : localized high velocities and gradients in central and side orifices with implications for doppler-catheter gradient relation in aortic and mitral position". In: *Circulation* 92.12, pp. 3464–3472.

Venugopal, P. et al. (2018). "Sensitivity of FFR-CT to manual segmentation". In: *Medical Imaging 2018: Biomedical Applications in Molecular, Structural, and Functional Imaging*. Ed. by B. Gimi and A. Krol. SPIE.

Vergara, C. et al. (2011). "Influence of bicuspid valve geometry on ascending aortic fluid dynamics: a parametric study". In: *Artificial Organs* 36.4, pp. 368–378.

Voelker, W. et al. (1992). "Pressure recovery in aortic stenosis: an in vitro study in a pulsatile flow model". In: *Journal of the American College of Cardiology* 20.7, pp. 1585–1593.

Walburn, F. J., H. N. Sabbah, and P. D. Stein (1983). "An experimental evaluation of the use of an ensemble average for the calculation of turbulence in pulsatile flow". In: *Annals of Biomedical Engineering* 11.5, pp. 385–399.

Weese, J. et al. (2017). "CFD- and bernoulli-based pressure drop estimates: a comparison using patient anatomies from heart and aortic valve segmentation of CT images". In: *Medical Physics* 44.6, pp. 2281–2292.

Wendell, D. C. et al. (2013). "Including aortic valve morphology in computational fluid dynamics simulations: initial findings and application to aortic coarctation". In: *Medical Engineering & Physics* 35.6, pp. 723–735.

Woo, J. et al. (2016). "A spatio-temporal atlas and statistical model of the tongue during speech from cine-MRI". in: *Computer Methods in Biomechanics and Biomedical Engineering: Imaging & Visualization* 6.5, pp. 520–531.

Xu, F. et al. (2018). "A framework for designing patient-specific bioprosthetic heart valves using immersogeometric fluid-structure interaction analysis". In: *International Journal for Numerical Methods in Biomedical Engineering* 34.4, e2938.

Yamaguchi, T. et al. (1983). "Measurement of turbulence intensity in the center of the canine ascending aorta with a hot-film anemometer". In: *Journal of Biomechanical Engineering* 105.2, pp. 177–187.

Yates, K. M. and C. D. Untaroiu (2018). "Finite element modeling of the human kidney for probabilistic occupant models: statistical shape analysis and mesh morphing". In: *Journal of Biomechanics* 74, pp. 50–56.

Yoganathan, A. P., K. B. Chandran, and F. Sotiropoulos (2005). "Flow in prosthetic heart valves: state-of-the-art and future directions". In: *Annals of Biomedical Engineering* 33.12, pp. 1689–1694.

Yoganathan, A. P., W. H. Corcoran, and E. C. Harrison (1979). "In vitro velocity measurements in the vicinity of aortic prostheses". In: *Journal of Biomechanics* 12.2, pp. 135–152.

Youssefi, P. et al. (2017). "Patient-specific computational fluid dynamics—assessment of aortic hemodynamics in a spectrum of aortic valve pathologies". In: *The Journal of Thoracic and Cardiovascular Surgery* 153.1, 8–20.e3.

Chapter 2

Estimation of valvular resistance of segmented aortic valves using computational fluid dynamics

This chapter is based on: **M.J.M.M. Hoeijmakers**, D.A. Silva Soto, I. Waechter-Stehle, M. Kastelnik, J. Weese, D.R. Hose, F.N. van de Vosse. Estimation of valvular resistance of segmented aortic valves using computational fluid dynamics. *Journal of Biomechanics*, 2019

ABSTRACT

Aortic valve stenosis is associated with an elevated left ventricular pressure and transaortic pressure drop. Clinicians routinely use Doppler ultrasound to quantify aortic valve stenosis severity by estimating this pressure drop from blood velocity. However, this method approximates the peak pressure drop, and is unable to quantify the partial pressure recovery distal to the valve. As pressure drops are flow dependent, it remains difficult to assess the true significance of a stenosis for low-flow low-gradient patients. Recent advances in segmentation techniques enable patient-specific Computational Fluid Dynamics (CFD) simulations of flow through the aortic valve. In this work a simulation framework is presented and used to analyze data of 18 patients. The ventricle and valve were reconstructed from 4D Computed Tomography imaging data. Ventricular motion was extracted from the medical images and used to model ventricular contraction and corresponding blood flow through the valve. Simplifications of the framework are assessed by introducing two simplified CFD models: a truncated time-dependent and a steady-state model. Model simplifications were justified for cases where the simulated pressure drop was above 10 mmHg. Furthermore, we proposed a valve resistance index to quantify stenosis severity from simulation results. This index was compared to established metrics for clinical decision making, i.e., blood velocity and valve area. It was found that velocity measurements alone do not adequately reflect stenosis severity. This work demonstrated that combining 4D imaging data and CFD has the potential to provide a physiologically relevant diagnostic metric to quantify aortic valve stenosis severity.

2.1 INTRODUCTION

AORTIC valve stenosis (AS) is the narrowing of the aortic valve and disturbs blood flow into the systemic circulation. Once developed, AS consistently increases with age, and it is estimated that 2.8–3.9% of the population older than 70 years of age suffer from some form of AS (Eveborn et al. 2012; Nkomo et al. 2006). AS is often caused by calcification of the Aortic Valve (AV) leaflets, resulting in a stiffer valve that impedes the opening and closing function of the valve. Hence, in systole, the valve may not open completely, and a large pressure difference is required to maintain flow. If left untreated, AS may eventually lead to heart failure.

AS disturbs flow from the ventricle into the aorta, and a large effective pressure difference is required to maintain cardiac output. The drop in pressure is an indicator for the severity of AS. However, non-invasive diagnostic quantitative evaluation of the pressure drop is challenging. Hence, in current clinical practice other indirect metrics are used. At present, the main criteria to judge AS severity are: the mean transaortic pressure drop; maximum velocity of the jet (v_{max}), and the Aortic Valve Area (AVA) by continuity equation (Chambers 2016; Nishimura et al. 2014; Baumgartner et al. 2016). All these metrics are routinely obtained by echocardiography. However, v_{max} and the mean pressure drop are both flow-dependent, and may conflict with AVA measurements for approximately 20–30% of patients with severe AS (Eleid et al. 2013). For this patient group it remains difficult to assess whether AS is significantly present (Vogelgesang et al. 2017).

Echocardiography is inexpensive, readily available and easy to perform, and an established method to derive metrics indicative of stenosis severity. When echocardiography results are inconclusive, Computed Tomography (CT) or cardiac Magnetic Resonance Imaging (MRI) can be used to derive additional indicators, e.g the aortic diameter or amount of calcification (Chun et al. 2008). Furthermore, CT and cardiac MRI enable detailed three-dimensional reconstructions of the full-heart anatomy. Moreover, segmentation methods from cardiac CT and MRI images have improved considerably over the past years (Ecabert et al. 2008; Ecabert et al. 2011; Grbic et al. 2012; Ionasec et al. 2010). Furthermore, recent developments see high-quality valve models incorporated into existing segmentation frameworks (Weese et al. 2017). These detailed 3D models of the AV can be used in combination with 3D Computational Fluid Dynamics (CFD) to evaluate the hemodynamic performance of the patient-specific valve (Weese et al. 2017). However, in order to quantify the load on the ventricle, extending the CFD model to include the (contracting) Left Ventricle (LV) may yield information on the true significance of the stenotic valve.

In systole, a healthy valve opens completely, and imposes little to no resistance to blood flow. However, flow through the diseased valve is similar to flow through an orifice. Blood is accelerated into the orifice, and pressure is converted to kinetic energy. When blood enters the Ascending Aorta (AA), it is decelerated, and pressure is partly recovered. (Figure 2.1). Pressure is not completely recovered due to viscous losses, including those from turbulence. This results in an effective pressure drop between the LV and AA. To quantify the relative contribution of the valve to the effective pressure drop, a valve resistance index is proposed:

$$I_{VR} = \frac{\Delta P_V}{\Delta P_E} \tag{2.1}$$

This index quantifies the pressure loss due to the presence of the valve (ΔP_V) with respect to the total effective pressure loss between the LV and AA (ΔP_E). For healthy valves, pressure is expected to recover approximately to the same pressure level as in the Left Ventricular Outflow Tract (LVOT). When the cross-sectional area of the AA exceeds that of the LVOT, blood velocity (and kinetic energy) in the AA decrease. Consequently, (static) pressure may recover beyond LVOT pressure. However, for diseased valves, it is expected that only a (small) part of pressure is recovered, and excessive viscous and turbulent losses dominate.

The main aim of this work is to evaluate the valve resistance index proposed in Equation 2.1 with clinically accepted measures, such as, v_{max} and the AVA. Additionally, the CFD model with the contracting left ventricle is used to evaluate the accuracy of simplified valve-only CFD models and Bernoulli approximations. For this purpose, the workflow described by Weese et al. (2017) is extended to include both the AV and contracting ventricle.

2.2 MATERIALS AND METHODS

2.2.1 AORTIC VALVE ANATOMIES

Cardiac CT segmentation data was obtained from an anonymized dataset used in a previous study (Weese et al. 2017). Original images were acquired using electrocardiogram-gated CT angiography with 10% intervals of the electrocardiographic R-R interval. CT images had an in-plane resolution of 0.31–0.68 mm and slice thickness of 0.34–0.70 mm.

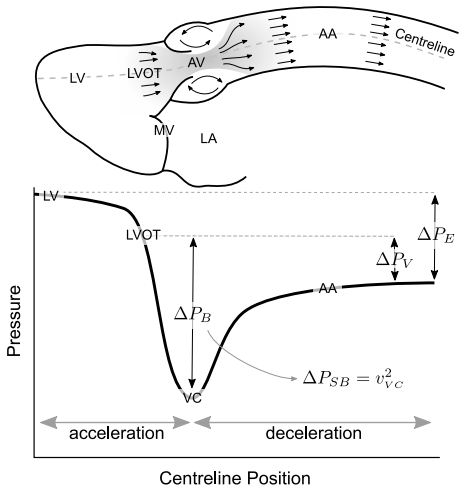

Figure 2.1 Top: schematic of the Left Ventricle (LV), Left Ventricular Outflow Tract (LVOT), Aortic Valve (AV), Vena Contracta (VC) and Ascending Aorta (AA). Bottom: typical pressure along the centreline. ΔP_V: net pressure drop across the AV. ΔP_E: effective pressure drop between the LV and AA. ΔP_B: Bernoulli estimate, i.e., the maximum pressure drop across the valve, ΔP_{SB}: simplified Bernoulli estimate from VC velocity. Mitral Valve (MV) and Left Atrium (LA) are added for anatomical reference.

Segmented anatomical structures include the LV, LVOT and AV. Figure 2.2b shows a typical segmented anatomy at different phases of the cardiac cycle.

Surface models of the LV and AV throughout systole were generated for each patient with a Shape Constrained Deformable Model (SCDM). The authors would like to refer to Ecabert et al. (2008), Ecabert et al. (2011), or Weese et al. (2017) for a detailed description of the SCDM. The surface model at mid-systole was selected, and developed into the CFD model. This model had the valve in the most open position, typically at 20% or 30% of the electrocardiographic R-R interval. The surface model consisted of 3094 vertices and 6169 triangles with an average edge length of 2.6 mm (Figure 2.2b). The geometric AVA was estimated from the structured surface model by a projection method (Weese et al. 2017). All segmentation surface models throughout the cardiac cycle were then converted into binary masks, covering the LV and LVOT, to facilitate registration.

2.2.2 IMAGE REGISTRATION

Each consecutive binarized image pair was registered using The Sheffield Image Registration Toolkit (Barber and Hose 2005). The resulting 3D discrete mapping fields morphed one image onto the next. The Sheffield Image Registration Toolkit produced smooth,

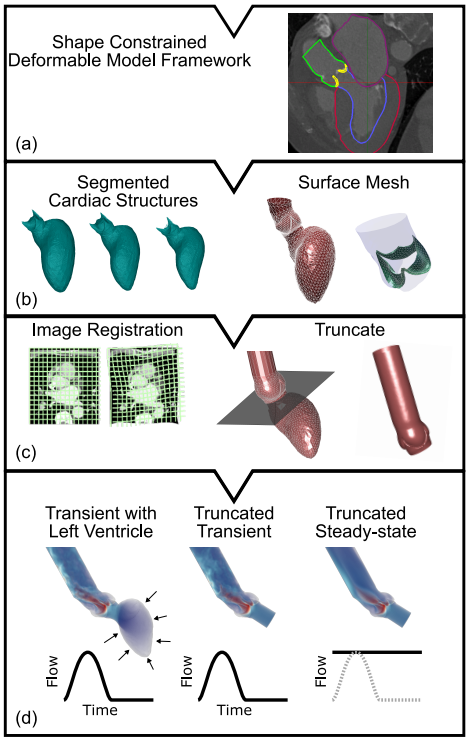

Figure 2.2 Illustration of the workflow from (a) the Shape Constrained Deformable Model framework (Ecabert et al. 2011; Weese et al. 2017); (b) Segmented aortic valve and left ventricle and corresponding surface model; (c) image registration and mesh truncation; (d) 4D CFD Model of the AV and contracting ventricle, 3D truncated transient model, and 3D truncated steady-state model.

non-linear registration maps with sub-pixel accuracy. To compute the 3D mappings between the images, the Sheffield Image Registration Toolkit uses an intensity-based linear least-squares algorithm, iteratively applied to handle large displacements. The 3D registration map was spatially interpolated to the vertices of the surface model at mid-systole. This yielded a set of surface models in the R-R interval with the same topology as the surface model at mid-systole. Registration was done on the binarized images, hence no information on the motion of the AV and AA was available. For this reason, and for CFD stability the mean rigid motion of the model was removed from the overall model motion. Velocity vectors $\vec{v}$ for each vertex n of the surface model were a function of time and computed from the consecutive iso-topological surface models by:

$$\vec{v}_n(t) = \frac{\vec{x}_n(t + \Delta t) - \vec{x}_n(t)}{\Delta t} \tag{2.2}$$

With $\vec{x}$ the position of vertex n at time t in the cardiac cycle. Vertex positions were sparse in time, and were interpolated using cubic splines.

2.2.3 MESH GENERATION

Volumetric meshing was performed with ANSYS Fluent Meshing R17.2 (ANSYS Inc, Canonsburg, Pennsylvania, United States). Structured surface models were truncated at the LVOT by a manually defined plane two to five mm proximal to the valve annulus and orthogonal to the valve axis (Figure 2.2c). The outflow boundary was extended by 3.5 times the diameter of the AA. The inflow boundaries of the truncated models were extended by 1.5 times the LVOT diameter. The volume was filled with tetrahedra in the core, and ten layers of pentahedra elements inflated from the wall. Element sizes were chosen based on a mesh sensitivity study, and ranged between 0.5–2.5 mm. Maximum element edge length in the LV was constrained to 2.5 mm. Edge lengths in the proximity of the AV were constrained to 0.5 mm to capture valve features.

2.2.4 COMPUTATIONAL METHODS

Fluid flow is governed by the Navier-Stokes equations. For moving grids, the integral form of the continuity equation for a control volume Ω with surface Γ can be written as.

$$\frac{\partial}{\partial t}\int_{\Omega} \rho dV + \int_{\Gamma} \rho(\vec{v} - \vec{v}_g) \cdot \vec{n} dA = 0 \tag{2.3}$$

With ρ the density of blood, $\vec{v}$ the velocity vector, $\vec{v}_g$ the velocity of the (boundary) grid, and $\vec{n}$ the normal vector to the surface Γ. Similarly, the momentum equation can be written as:

$$\frac{\partial}{\partial t}\int_{\Omega} (\rho\vec{v}) dV + \int_{\Gamma} \rho\vec{v}(\vec{v} - \vec{v}_g) \cdot \vec{n} dA = -\int_{\Gamma} p\mathbf{I} \cdot \vec{n} dA + \int_{\Gamma} \boldsymbol{\tau} \cdot \vec{n} dA \tag{2.4}$$

Where p is the pressure, $\mathbf{I}$ the identity tensor, and $\boldsymbol{\tau}$ the viscous stress tensor. A diffusion based smoothing method was applied for grid motion.

$$\nabla \cdot (\gamma \nabla \vec{v}_g) = 0 \tag{2.5}$$

$$\gamma = \frac{1}{d^{\alpha}} \tag{2.6}$$

With $\vec{v}_g$ the grid velocity, γ the diffusion coefficient and d the normalized distance to the boundary. For all simulations $\alpha = 1$ and resulted in skewed grid motion towards the interior, i.e., elements in the interior deformed more. The boundary conditions (Figure 2.3) for the diffusion equation were:

$$\begin{aligned} \Gamma_{AA}, \Gamma_{Sinus}, \Gamma_{AV} &: \vec{v}_g = 0 \\ \Gamma_{LVOT} &: \vec{v}_g = f(s)\vec{v}_n(t) \\ \Gamma_{LV} &: \vec{v}_g = \vec{v}_n(t) \end{aligned}$$

$f(s)$ is a ramp function that linearly scaled boundary velocity to zero in the LVOT as a function of the position s in the LVOT, i.e., $f(s) = 1$ at the side of the LV, and $f(s) = 0$ towards the valve.

Blood was modeled as an in-compressible fluid with a density of 1050 kg·m^{-3} and dynamic viscosity of 0.004 Pa· s. No-slip boundary conditions were assumed at the walls, and at boundary Γ_{out} pressure is set to zero. The governing equations were solved with ANSYS Fluent R17.2 (ANSYS Inc, Canonsburg, Pennsylvania, United States). Simulations were executed on the ACC Cyfronet AGH Prometheus Supercomputer (Academic Computer Centre Cyfronet, AGH University of Science and Technology, Kraków, Poland). Each simulation was assigned one compute node with 24 CPU's.

2.2.4.1 TRANSIENT MODELS

For the transient models a (bounded) central difference scheme was used for the advection and diffusion terms. The transient term was integrated with a second order backward difference approximation. Convergence criteria at each time-step were set at 0.05 for locally scaled residuals of x-, y-, z-velocity, and continuity. Sub-grid turbulent dissipation

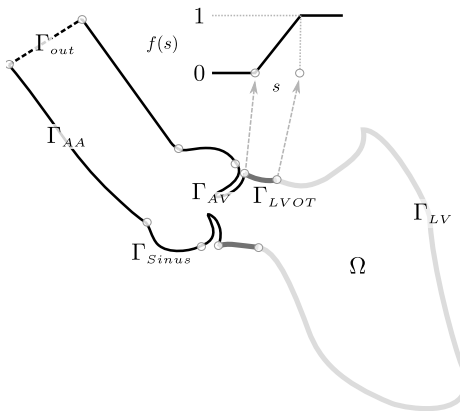

Figure 2.3 Boundary and domain definitions. Boundaries Γ_{LV} (light gray line) and Γ_{LVOT} (dark gray line) are deforming. Γ_{AV}, Γ_{Sinus}, Γ_{AA} (black lines) and Γ_{out} (dashed line) are static boundaries, i.e., $\vec{v}_g$ is zero. Boundary motion is scaled to zero in the LVOT by a ramp function $f(s)$, with s the position in the LVOT

was modeled with Large Eddy Simulation and the Wall Adapting Local Eddy-Viscosity model (Nicoud and Ducros 1999). Time steps were defined as 1/10000th of the cardiac cycle. Vertex velocities were spatially interpolated from the structured surface model onto the re-meshed surface of the computational domain by an inverse distance-weighted interpolation using eight nearest neighbors of the structured model. Stroke volume was pre-computed with a discrete form of Gauss's theorem (Hughes et al. 1996) for the structured and re-meshed surfaces. Vertex velocities of the refined computational mesh were scaled to match the stroke volume of the structured surface model. The time-dependent grid velocity was applied to the boundary of the LV and LVOT. For the truncated model, the pre-computed flow waveform was used as a time-dependent plug-flow boundary condition. To test whether diastolic filling of the ventricle had to be simulated, five cardiac cycles were simulated for case 11. Results in Table 2.1 demonstrate that diastolic filling had a negligible ($< 1\%$) effect on the observed peak-systolic pressure drop and valve resistance index. Hence, diastolic filling was neglected, and only a single systolic cycle was simulated to restrict the computational burden.

2.2.4.2 STEADY-STATE MODEL

Peak flow-rate was obtained from the pre-computed flow waveform, and prescribed as a boundary condition for the truncated steady-state model. Turbulence was modeled with the Shear Stress Transport $k - \omega$ model (Menter 1994).

Table 2.1 Pressure drop results over multiple cardiac cycles for case 11

	Cycle 1	**Cycle 2**	**Cycle 3**	**Cycle**	**Cycle 5**
P_{LV} [mmHg]	6.86	6.90	6.89	6.88	6.94
P_{LVOT} [mmHg]	3.42	3.44	3.43	3.43	3.49
I_{VR} [-]	0.499	0.499	0.498	0.498	0.503

Note: simulations performed with a time-step of $1 \cdot 10^{-3}$s to limit simulation times.

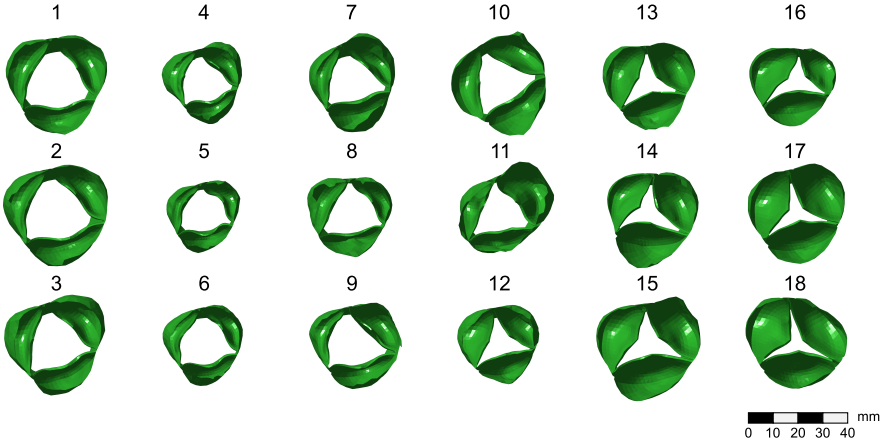

Figure 2.4 Axial view of the segmented AV for all cases. Cases 1–9 have a $I_{VR} < 0.25$, cases 10 and 11 $0.25 < I_{VR} < 0.75$, and cases 12–18 a $I_{VR} > 0.75$. Case numbering corresponds to Table 2.2.

2.2.5 POST-PROCESSING

A centreline with equally spaced points (0.1mm intervals) was defined for each surface model with the Vascular Modelling Toolkit (Antiga et al. 2008). Pressure was evaluated on the centreline, and the effective (ΔP_E) and valve (ΔP_V) pressure-drops were computed. These pressure drops were used to compute the valve resistance index I_{VR} (Equation 2.1). Furthermore, Bernoulli estimates ($\Delta P_B = P_{LVOT} - P_{VC}$) and simplified Bernoulli estimates ($\Delta P_{SB} = 4v_{VC}^2$) were computed from the simulation results. Note that v_{VC} is the velocity at the vena contracta, and corresponds to v_{max}. The point on the centreline closest to the truncation plane was used to evaluate P_{LVOT}. The vena contracta was identified by inspecting the centreline, i.e., where pressure was lowest.

2.3 RESULTS

The workflow described in Figure 2.2 was used on retrospective CT datasets of 18 patients with non-calcified and (partially) severely calcified tricuspid AV's (Figure 2.4). Projected AVA ranged between 0.9 and 4.3 cm^2 (Table 2.2). Image derived maximum flow rate at peak systole ranged between 178 and 635 ml/s, and simulated velocities in the vena contracta range between 0.88 and 5.36 m/s. The effective pressure drop ΔP_E^{CLV} ranges between 2.5 and 102.5 mmHg. Net pressure drops across the aortic valve range between: -2.3 mmHg and 91.5 mmHg for the full model; -1.4 mmHg and 89.5 mmHg for the truncated transient model; 0.4 mmHg and 89.8 mmHg for the steady-state model. ΔP_B^{CLV} and ΔP_{SB}^{CLV} range between 1.0–103.2 mmHg and 3.1–115.1 mmHg. The valve resistance index lies between -0.40 and 0.96. The local pressure gradient in the LVOT was between -0.77 and -0.07 mmHg/mm.

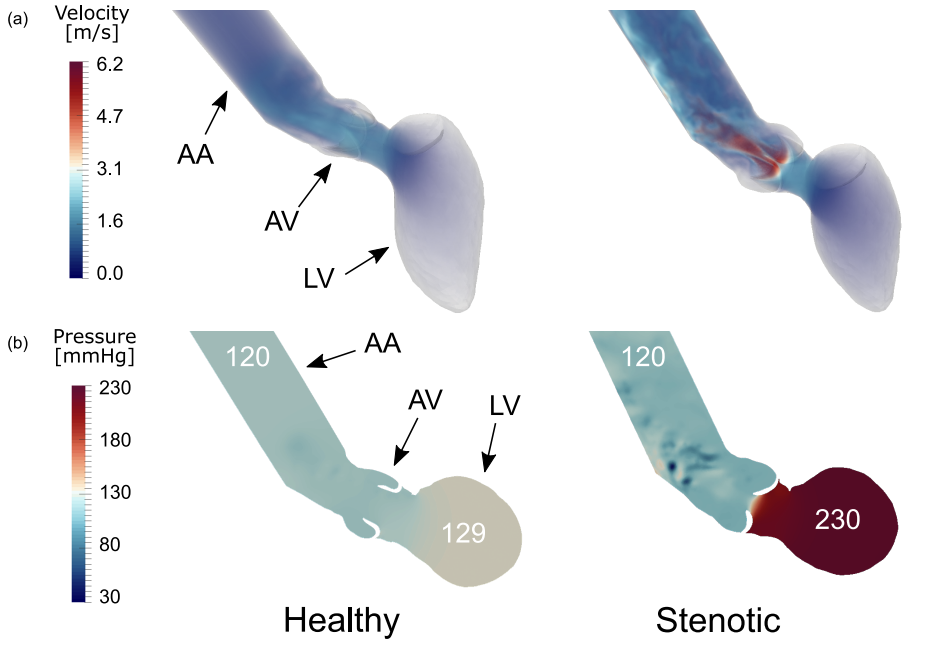

Figure 2.5 Volume renders of velocity (a) and contour plots of pressure (b) at peak systole for a healthy valve (left: case 8) and a stenotic valve (right: case 17).

Figure 2.5 illustrates the CFD results of a healthy (case 8) and a stenotic valve (case 17). The healthy case exhibits a lower jet velocity through the AV than the stenotic case. For the stenotic valve a distinct jet is formed, and turbulent structures develop. The jet is wider and not as pronounced for the healthy valve. Pressure contours demonstrate that

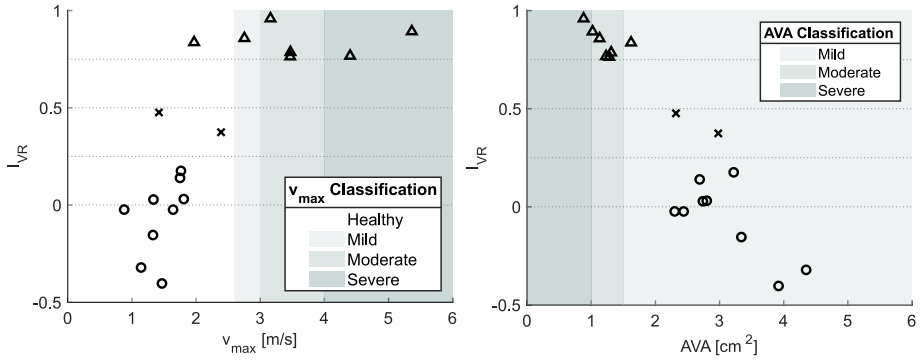

Figure 2.6 Left: CFD derived v_{max} vs. valve resistance index. Severity classifications are based on guidelines (Nishimura et al. 2014). Healthy: $v_{max} < 2.6$ m/s. Mild: 2.6 m/s $< v_{max} < 2.9$ m/s, moderate: 3.0 m/s $< v_{max} < 4.0$ m/s, severe: $v_{max} > 4.0$ m/s. Right: Geometric AVA vs. valve resistance index. Healthy/Mild: AVA > 1.5 cm^2, moderate: 1.0 cm^2 $<$ AVA < 1.5 cm^2, severe AVA < 1.0 cm^2. Furthermore, cases are separated in groups, $I_{VR} < 0.25$ (○), $0.25 < I_{VR} < 0.75$ (×) and $I_{VR} > 0.75$ (△). Note that the reported AVA is the geometric projected AVA, and not the effective orifice area (by echocardiography) as reported in the guidelines (Nishimura et al. 2014).

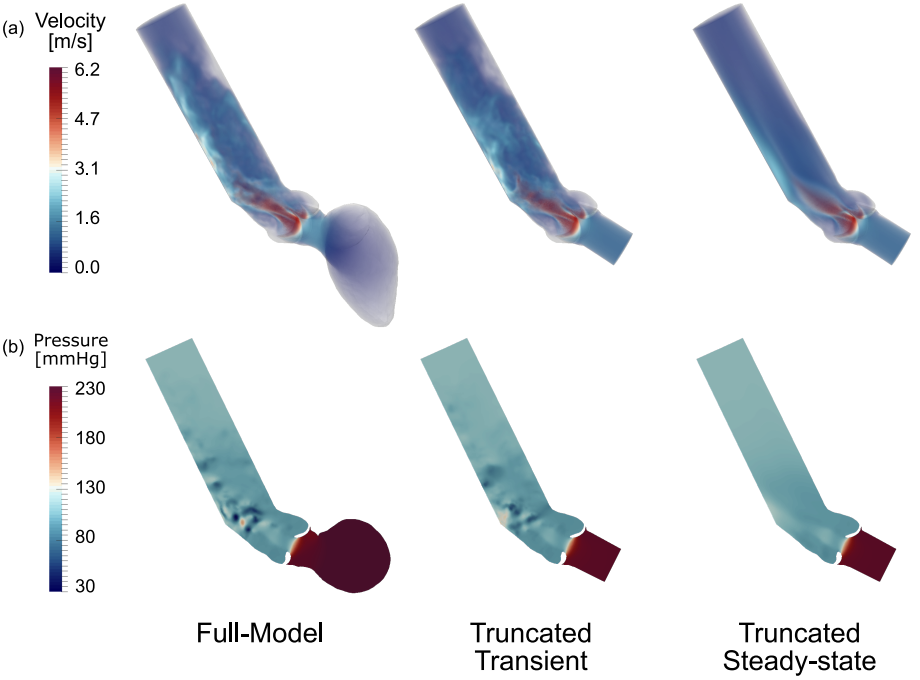

Figure 2.7 Volume render of velocity magnitude (a) and pressure contours (b) for each of the CFD models.

the the effective pressure drop between the LV and AA is about 9 mmHg for the healthy case and approximately 110 mmHg for the stenotic case.

Figure 2.6 visualizes the relationship between v_{max} and the proposed valve resistance index. When assessing AS severity by v_{max}, 12 cases would be considered healthy, one case as having a mild stenosis, and three as having a moderate stenosis. Two cases would be classified as having a severe stenosis. Cases 15 and 16 would be classified as having no or a mild stenosis. However, both exhibit large valve resistance indices of 0.84 and 0.86 respectively, of similar magnitude as the clearly stenotic cases 13 and 17. Furthermore, it is observed that case 18 actually has the largest valve resistance index, but would have been classified as moderate with v_{max} as criteria. Healthy valves exhibit valve resistance indices close to or below zero. Furthermore, an inverse linear relationship between the geometric AVA and valve resistance index may be observed; when AVA decreases, the valve resistance index increases. (Figure 2.6).

Figure 2.7a and Figure 2.7b qualitatively demonstrate the differences between each of the CFD models. Unsteady flow phenomena distal to the AV are observed. Flow patterns for the transient models are similar, but local discrepancies in the velocity field can be noticed. Unsteady flow patterns propagate far into the AA for this particular stenotic case.

Qualitatively the shape of the jet and the pressure contours are similar proximal to and in the immediate vicinity of the valve for the steady-state and transient models (Figure 2.7). However, flow structures distal to the valve are less well-matched. This is expected because the jet has had no time to develop fully in space for the transient models. Despite the loss of fidelity in the flow field, the steady-state model captures the overall pressure drop adequately. Pressures proximal to the AV, in the vena contracta and distal to the AV are approximately the same for all models.

Differences in ΔP_V of 0.3 ± 1.33 and 0.9 ± 1.63 are found between the transients models, and truncated steady and full model respectively (Figure 2.8a and b). A bias of 0.7 ± 1.07 mmHg is observed between both truncated models (Figure 2.8c). The simplified Bernoulli and full 4D CFD model are in poor agreement: a bias of 11.3 ± 6.6 mmHg (Figure 2.9b). At low-flow the simplified Bernoulli equation provides a poor estimate of the peak-systolic effective pressure-drop. Bernoulli estimates demonstrate a bias of 6.6 ± 3.27 mmHg compared to the full model. In general, discrepancies from the full model predominantly occur at low pressure pressure drops (Figure 2.8 and Figure 2.9). E.g., the relative difference between ΔP_V^{CLV} and ΔP_V^{TT} for case 6 is 140%. In contrast, a relative difference of only 2% is found for case 17.

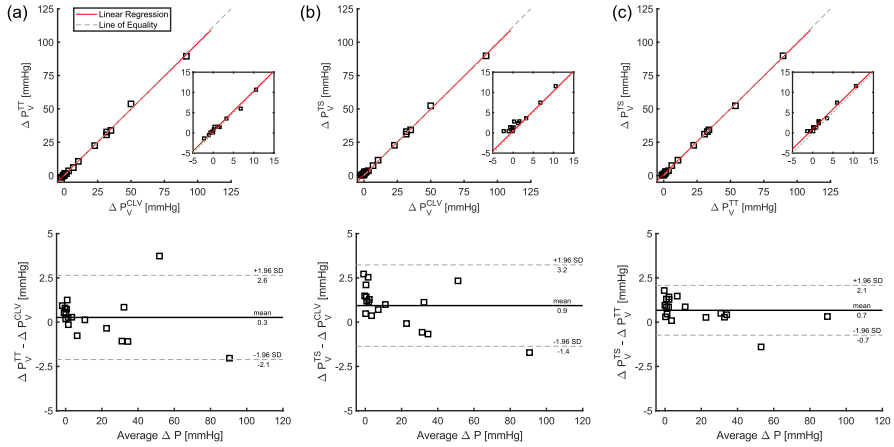

Figure 2.8 Comparison between CFD models and their respective ΔP_V. Top row: scatter plot with linear regression results and line of equality. Bottom row: Bland-Altman of the difference. (a) Transient truncated model vs. full model ($R^2 = 0.998$); (b) Truncated steady-state vs. full model ($R^2 = 0.998$); (c) Truncated steady-State vs. truncated transient model ($R^2 = 0.999$).

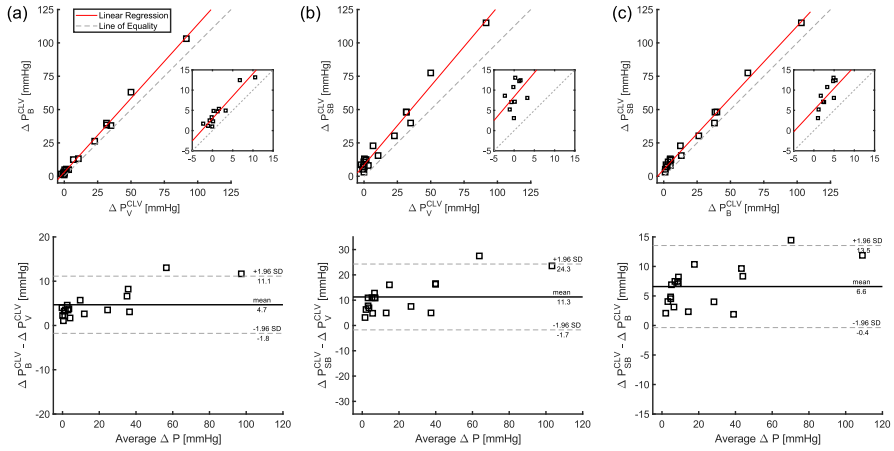

Figure 2.9 Comparison between the Bernoulli estimates and pressure drops computed with the full CFD model. (a) Bernoulli estimate vs. full model ($R^2 = 0.995$); (b) Simplifed Bernoulli ($4v^2$) estimate vs. full model ($R^2 = 0.973$); (c) Simplified Bernoulli estimate vs. Bernoulli estimate ($R^2 = 0.991$).

2.4 DISCUSSION

This chapter presents a medical image-based CFD framework to simulate flow across a patient-specific AV. A valve resistance index is defined and compared to measures

typically used in the clinic to demonstrate the frameworks potential value. Additionally, the effect of model simplifications on pressure-drop computations is presented.

2.4.1 SAMPLE CHARACTERISTICS

Computed geometric AVA's (Table 2.2) suggest that the current sample contains 11 healthy or mildly stenosed cases, six moderate cases, and one severe case (Nishimura et al. 2014). When considering v_{max} as severity index, it is found that 12 cases can be classified as healthy, one as mild, three as moderate, and two as having a severely stenotic valve. Unfortunately, no echocardiography or cardiac catheterization data was available to clinically classify the patients. Nevertheless, computed velocities, pressure-drops and AVA correspond well to values reported in literature (Chambers 2016; Baumgartner et al. 1999). For example, cardiac catheterization and echocardiography measurements in AS patients by Yang et al. (2015) show systolic pressure drops between the LV and AA up to 129 mmHg for patients with (echocardiography derived) AVA's of 0.4 cm^2. Furthermore, the same study reports echocardiography based peak-systolic v_{max} measurements of 2.3–5.2 m/s. The reported upper limits for ΔP_E and v_{max} in this study are 103 mmHg and 5.4 m/s, and thus respect the limits typically reported in literature.

2.4.2 VALVE RESISTANCE INDEX

The valve resistance index is a measure of how much pressure is lost due to the presence of the AV. This index can be interpreted as a percentage, e.g., an index of 0.60 means that 60% of pressure loss can be attributed to the AV. Figure 2.6 demonstrates that healthy valves (cases 1–9) have valve resistance indices of around zero, i.e., any pressure lost around the AV is fully recovered in the AA. For some cases, recovered pressure even exceeds pressure in the LVOT (cases 1–3). This can be explained by the fact that the cross-sectional area of the AA is typically two to three times larger than the cross-sectional area of the LVOT (see Table 2.2). Due to the larger cross-sectional area, velocity in the AA will be lower, and more kinetic energy is converted back into static pressure. Hence, pressure may recover beyond that of the LVOT, leading to a negative valve resistance index. Therefore, a healthy valve, in its open position, exerts no additional load on the left ventricle at peak systole. For severely stenotic valves, the valve dominates the effective pressure drop (cases 17 and 18), i.e., approximately 90% of the effective pressure drop is attributed to the AV. This is in line with numerical results presented by Traeger et al. (2015). Although not the main aim of their work, their illustrations suggest that a valve with an area of 0.9 cm^2 (Gorlin derived) may exhibit a valve resistance index of approximately 0.9 at flow rates of 200 and 400 ml/s.

Figure 2.6 clearly demonstrates the inability of v_{max} to identify a stenosis consistently. Due to low-flow, cases 15 and 16 demonstrate a v_{max} that would be considered normal, or mildly stenotic in clinical practice. However, the valve resistance index for these cases reveals that — similar to other stenotic valves — the effective pressure drop is dominated by the AV. A disproportional amount of the pressure loss is due to the presence of the valve. Such a conclusion can not be drawn from v_{max} (Figure 2.6) and ΔP_E measurements alone. Hence, for cases where AVA and v_{max} conflict, the valve resistance index may provide relevant information on stenosis severity.

2.4.3 COMPARISON CFD MODELS

Qualitatively, no major differences are observed between the transient models (Figure 2.7). Similar (turbulent) structures are formed distal to the AV where the jet breaks down, and pressure is recovered. Steady-state simulations demonstrate averaged velocity and pressure distributions, and do not capture local flow disturbances in detail. Nevertheless, steady-state simulations capture the global pressure drop across the AV within reasonable limits. Both truncated models provide acceptable estimates for the pressure drop across the AV. At low pressure drops (<10 mmHg) the truncated models overestimate the pressure drop considerably in the relative sense. An artificial plug-flow assumption at the inflow boundary may not be appropriate for the low-gradient cases. Indeed, velocity profiles in the LVOT are not plug-like (Garcia et al. 2011). Work by Bruening and colleagues shows that significant overestimation of the pressure drop can occur when assuming a plug-flow velocity profile opposed to a patient-specific flow profile from 4D velocity-encoded MRI (Bruening et al. 2018). However, differences between the full and truncated transient model are small in this study, and the added accuracy of the full model may therefore not outweigh the additional computational cost.

The simplified Bernoulli equation — normally derived from echocardiography measurements — overestimates the pressure drop substantially. Overestimation of the pressure drop is a well known problem with the Simplified Bernoulli equation. Both numerical (Casas et al. 2015; Donati et al. 2017) and patient studies (Baumgartner et al. 1999) have demonstrated this overestimation. It should be noted that v_{max} is directly obtained from the simulated velocity field. Clinically, measurements are done with echocardiography, and additional sources of errors are likely, such as: poor spatial resolution, misalignment of the probe, or probe settings (Lui et al. 2005).

Table 2.2 Pressure drop estimates for each case and all models, ordered by valve resistance index

Case	HR bpm	A_{LVOT} cm^2	A_{AV} cm^2	A_{AA} cm^2	Q_{max} ml/s	v_{max} m/s	ΔP_E^{CLV} mmHg	ΔP_V^{CLV} mmHg	ΔP_V^{TT} mmHg	ΔP_V^{TS} mmHg	ΔP_B^{CLV} mmHg	ΔP_{SB}^{CLV} mmHg	∇P_{LVOT}^{CLV} mmHg /mm	I_{VR}† -2mm	I_{VR}	I_{VR}‡ +2mm
1	73	4.8	3.9	10.1	489	1.47	5.7	-2.3	-1.4	0.4	1.7	8.6	-0.20	-0.33	-0.40	-0.47
2	56	5.5	4.3	14.7	433	1.14	3.4	-1.1	-0.6	0.4	1.2	5.2	-0.11	-0.25	-0.32	-0.39
3	66	4.6	3.3	9.5	397	1.33	4.6	-0.7	0.1	1.4	2.5	7.1	-0.15	-0.09	-0.15	-0.22
4	58	3.4	2.4	7.2	330	1.64	8.4	-0.2	0.4	1.2	3.3	10.8	-0.28	0.04	-0.02	-0.09
5	87	3.1	2.3	7.4	178	0.88	2.5	-0.1	0.1	0.4	1.0	3.1	-0.07	0.03	-0.02	-0.08
6	63	4.3	2.7	6.7	321	1.33	5.4	0.2	0.9	1.3	2.3	7.1	-0.18	0.09	0.03	-0.04
7	66	4.1	2.8	7.8	451	1.81	8.8	0.3	1.5	2.8	4.9	13.1	-0.25	0.09	0.03	-0.03
8	61	4.3	2.7	9.5	415	1.75	9.1	1.3	1.5	2.4	4.8	12.2	-0.32	0.21	0.14	0.07
9	66	4.5	3.2	10.2	488	1.76	9.0	1.6	1.4	2.9	5.4	12.4	-0.29	0.24	0.18	0.11
10	63	5.1	3.0	11.1	635	2.39	18.0	6.8	6.0	7.5	12.5	22.8	-0.70	0.45	0.37	0.30
11	67	4.5	2.3	12.1	296	1.42	6.8	3.3	3.5	3.6	5.0	8.1	-0.19	0.53	0.48	0.42
12	66	3.9	1.3	8.5	416	3.47	41.7	31.8	32.6	32.9	38.4	48.1	-0.63	0.79	0.76	0.73
13	74	3.8	1.2	9.3	510	4.40	65.2	50.0	53.7	52.3	63.0	77.5	-0.46	0.78	0.77	0.75
14	80	3.6	1.3	9.5	417	3.47	40.2	31.6	30.6	31.1	39.8	48.2	-0.40	0.81	0.79	0.77
15	82	5.8	1.6	11.9	302	1.97	12.6	10.6	10.7	11.5	13.2	15.5	-0.26	0.88	0.84	0.79
16	98	4.0	1.1	8.3	286	2.75	26.6	22.8	22.4	22.7	26.3	30.3	-0.26	0.88	0.86	0.84
17	57	4.7	1.0	10.9	511	5.36	102.5	91.5	89.5	89.8	103.2	115.1	-0.77	0.91	0.89	0.88
18	74	5.6	0.9	8.1	251	3.16	36.4	34.9	33.9	34.3	38.0	39.9	-0.19	0.97	0.96	0.95

† Valve resistance index when P_{LVOT} was computed 2 mm upstream of truncation plane
‡ Valve resistance index when P_{LVOT} was computed 2 mm downstream of truncation plane

2.4.4 LIMITATIONS IMAGING AND GEOMETRY

Segmentation with the SCDM is only possible for tri-cuspid AV's. Substantial segmentation errors are expected for bicuspid valves. Weese et al. (2017) showed that segmentation works in presence of calcifications. However, strong calcifications are likely to influence segmentation accuracy and blood flow. Hence, a thorough evaluation of segmentation accuracy is required. For example, it may be necessary to map patient-specific calcifications onto the SCDM.

Segmentation is performed on electrocardiography triggered CT images at 10% intervals of the R-R curve. It is assumed that the temporal resolution is sufficient to capture the (fully) open state of the AV. Poor temporal resolution may also cause over- or underestimation of flow-rate. mitral regurgitation is not quantified, and patient flow-rates are likely overestimated. For example, patients with severe mitral valve regurgitation may see a regurgitant fraction of more than 50% (Zoghbi et al. 2017).

2.4.5 LIMITATIONS CFD

No valvular fluid-solid interaction is considered in this study due to the numerical challenges and lack of patient-specific material properties. It is expected that only local intraventricular and aortic flow fields are influenced. It is not expected that peak-systolic pressure drops and v_{max} are affected. Work by Astorino et al. (2012) supports this choice. Their work suggests that modeling the valve in the fixed open position yields an acceptable approximation for flow at peak systole, opposed to simulating the fully coupled fluid-solid interaction.

The multi-cycle simulations that were performed on case 11 lacked the patient-specific mitral valve. As such, end-diastolic flow patterns may not be physiologically correct. For example, it has been shown that mitral valve opening dynamics and shape substantially influence end-diastolic vortex formation (Vasudevan et al. 2019). Whether the single-cycle approach is still acceptable in the presence of the segmented mitral valve has not been investigated.

2.5 CONCLUSION

An image-based CFD workflow of the AV and heart anatomy is presented. This workflow allows for the computation of a valve resistance index, that quantifies the contribution of the AV to the effective pressure drop from the LV to the AA. It is demonstrated that

this index has the potential to complement existing measures, such as, v_{max} and the geometric AVA for patients that demonstrate discordant grading. Furthermore, it is shown that simplified CFD models provide a reasonable estimate of the aortic valve pressure drop at a given flow rate. However, at low-flow conditions simplifications to boundary conditions may not be justified, and more physiologically accurate inflow boundary conditions should be considered.

ACKNOWLEDGEMENTS

This work was supported in part by the European Research Council Grant (Grant number: 689617) and by the PLGrid Infrastructure. The authors would like to thank V. Morgenthaler for his valuable technical input.

BIBLIOGRAPHY

Antiga, L. et al. (2008). "An image-based modeling framework for patient-specific computational hemodynamics". In: *Medical & Biological Engineering & Computing* 46.11, pp. 1097–1112.

Astorino, M. et al. (2012). "A robust and efficient valve model based on resistive immersed surfaces". In: *International Journal for Numerical Methods in Biomedical Engineering* 28.9, pp. 937–959.

Barber, D. C. and D. R. Hose (2005). "Automatic segmentation of medical images using image registration: diagnostic and simulation applications". In: *Journal of Medical Engineering & Technology* 29.2, pp. 53–63.

Baumgartner, H. et al. (1999). ""overestimation" of catheter gradients by doppler ultrasound in patients with aortic stenosis: a predictable manifestation of pressure recovery." In: *Journal of the American College of Cardiology* 33 (6), pp. 1655–1661.

Baumgartner, H. et al. (2016). "Recommendations on the echocardiographic assessment of aortic valve stenosis: a focused update from the european association of cardiovascular imaging and the american society of echocardiography". In: *European Heart Journal - Cardiovascular Imaging* 18.3, pp. 254–275.

Bruening, J. et al. (2018). "Impact of patient-specific LVOT inflow profiles on aortic valve prosthesis and ascending aorta hemodynamics". In: *Journal of Computational Science* 24, pp. 91–100.

Casas, B. et al. (2015). "4d flow MRI-based pressure loss estimation in stenotic flows: evaluation using numerical simulations". In: *Magnetic Resonance in Medicine* 75.4, pp. 1808–1821.

Chambers, J. B. (2016). "The assessment of aortic stenosis: echocardiography and beyond." In: *British journal of hospital medicine* 77 (3), pp. 141–146.

Chun, E. J. et al. (2008). "Aortic stenosis: evaluation with multidetector CT angiography and MR imaging". In: *Korean Journal of Radiology* 9.5, p. 439.

Donati, F. et al. (2017). "Beyond bernoulli: improving the accuracy and precision of noninvasive estimation of peak pressure drops". In: *Circulation: Cardiovascular Imaging* 10.1.

Ecabert, O. et al. (2008). "Automatic model-based segmentation of the heart in CT images". In: *IEEE Transactions on Medical Imaging* 27.9, pp. 1189–1201.

Ecabert, O. et al. (2011). "Segmentation of the heart and great vessels in CT images using a model-based adaptation framework". In: *Medical Image Analysis* 15.6, pp. 863–876.

Eleid, M. F. et al. (2013). "Flow-gradient patterns in severe aortic stenosis with preserved ejection fraction". In: *Circulation* 128.16, pp. 1781–1789.

Eveborn, G. W. et al. (2012). "The evolving epidemiology of valvular aortic stenosis. the tromsø study". In: *Heart* 99.6, pp. 396–400.

Garcia, J. et al. (2011). "Comparison between cardiovascular magnetic resonance and transthoracic doppler echocardiography for the estimation of effective orifice area in aortic stenosis". In: *Journal of Cardiovascular Magnetic Resonance* 13.1, p. 25.

Grbic, S. et al. (2012). "Complete valvular heart apparatus model from 4d cardiac CT". in: *Medical Image Analysis* 16.5, pp. 1003–1014.

Hughes, S. W. et al. (1996). "Application of a new discreet form of gauss' theorem for measuring volume." In: *Physics in medicine and biology* 41 (9), pp. 1809–1821.

Ionasec, R. I. et al. (2010). "Patient-specific modeling and quantification of the aortic and mitral valves from 4-d cardiac CT and TEE". in: *IEEE Transactions on Medical Imaging* 29.9, pp. 1636–1651.

Lui, E. Y. L. et al. (2005). "Human factors as a source of error in peak doppler velocity measurement". In: *Journal of Vascular Surgery* 42.5, 972.e1–972.e10.

Menter, F. R. (1994). "Two-equation eddy-viscosity turbulence models for engineering applications". In: *AIAA Journal* 32.8, pp. 1598–1605.

Nicoud, F. and F. Ducros (1999). "Subgrid-scale stress modelling based on the square of the velocity gradient tensor". In: *Flow, Turbulence and Combustion* 62.3, pp. 183–200.

Nishimura, R. A. et al. (2014). "2014 AHA/ACC guideline for the management of patients with valvular heart disease". In: *Journal of the American College of Cardiology* 63.22, e57–e185.

Nkomo, V. T. et al. (2006). "Burden of valvular heart diseases: a population-based study." In: *Lancet* 368 (9540), pp. 1005–1011.

Traeger, B. et al. (2015). "Methodological inaccuracies in clinical aortic valve severity assessment: insights from computational fluid dynamic modeling of CT-derived aortic valve anatomy". In: *Theoretical and Computational Fluid Dynamics* 30.1-2, pp. 107–128.

Vasudevan, V. et al. (2019). "Role of diastolic vortices in flow and energy dynamics during systolic ejection". In: *Journal of Biomechanics* 90, pp. 50–57.

Vogelgesang, A., G. Hasenfuss, and C. Jacobshagen (2017). "Low-flow/low-gradient aortic stenosis-still a diagnostic and therapeutic challenge". In: *Clinical Cardiology* 40.9, pp. 654–659.

Weese, J. et al. (2017). "CFD- and bernoulli-based pressure drop estimates: a comparison using patient anatomies from heart and aortic valve segmentation of CT images". In: *Medical Physics* 44.6, pp. 2281–2292.

Yang, C.-S. et al. (2015). "Discrepancies between direct catheter and echocardiography-based values in aortic stenosis". In: *Catheterization and Cardiovascular Interventions* 87.3, pp. 488–497.

Zoghbi, W. A. et al. (2017). "Recommendations for noninvasive evaluation of native valvular regurgitation". In: *Journal of the American Society of Echocardiography* 30.4, pp. 303–371.

Chapter 3

Combining statistical shape modeling, CFD, and meta-modeling to approximate the patient-specific pressure-drop across the aortic valve in real-time

This chapter is based on: **M.J.M.M. Hoeijmakers**, I. Waechter-Stehle, J. Weese, F.N. van de Vosse. Combining statistical shape modeling, CFD, and meta-modeling to approximate the patient-specific pressure-drop across the aortic valve in real-time. *International Journal for Numerical Methods in Biomedical Engineering*, 2020

ABSTRACT

Advances in medical imaging, segmentation techniques, and high performance computing have stimulated the use of complex, patient-specific, three-dimensional Computational Fluid Dynamics (CFD) simulations. Patient-specific, CFD-compatible geometries of the aortic valve are readily obtained. CFD can then be used to obtain the patient-specific pressure-flow relationship of the aortic valve. However, such CFD simulations are computationally expensive, and real-time alternatives are desired. **Aim** The aim of this work is to evaluate the performance of a meta-model with respect to high-fidelity, three-dimensional CFD simulations of the aortic valve. **Methods** Principal component analysis was used to build a statistical shape model (SSM) from a population of 74 iso-topological meshes of the aortic valve. Synthetic meshes were created with the SSM, and steady-state CFD simulations at flow-rates between 50 and 650 ml/s were performed to build a meta-model. The meta-model related the statistical shape variance, and flow-rate to the pressure-drop. **Results** Even though the first three shape modes account for only 46% of shape variance, the features relevant for the pressure-drop seem to be captured. The three-mode shape-model approximates the pressure-drop with an average error of 8.8–10.6% for aortic valves with a geometric orifice area below 150 mm^2. The proposed methodology was least accurate for aortic valve areas above 150 mm^2. Further reduction to a meta-model introduces an additional 3% error. **Conclusions** Statistical shape modeling can be used to capture shape variation of the aortic valve. Meta-models trained by SSM-based CFD simulations can provide an estimate of the pressure-flow relationship in real-time.

3.1 INTRODUCTION

ADVANCES in medical imaging and image segmentation techniques have resulted in a tremendous increase in the use of complex three-dimensional patient-specific simulations over the last two decades (Neal and Kerckhoffs 2009). The availability and applicability of complex three-dimensional computational models for clinical applications is further stimulated by high performance computing and development of more robust and efficient codes to solve the governing equations. Computational models are now widely adapted throughout the cardiovascular research community. Models are used, for example, to assess mechanical (K. Li and Sun 2016; Disseldorp et al. 2016) or hemodynamic (Min et al. 2015; Kimura et al. 2017; Morris et al. 2013; Traeger et al. 2015; Cibis et al. 2014) quantities such as stress, wall shear stress, or pressure drops.

Imaging modalities such as Computed Tomography, Magnetic Resonance Imaging, and ultrasound are used on a daily basis in the clinic. With segmentation tools, patient-specific geometries are readily obtained from the acquired imaging data. These geometries can then be used as input to computational fluid dynamics (CFD) simulations to provide detailed pressure and velocity fields in the blood vessel. These hemodynamic quantities are difficult, or sometimes impossible to assess with imaging techniques alone. Patient-specific CFD simulations have already proven their diagnostic value for coronary disease (Min et al. 2015; Morris et al. 2013). However, in the field of heart-valve disease, CFD is not yet accepted for clinical diagnostics. Instead, three-dimensional CFD simulations are primarily used to understand the fundamental principles of valve dynamics (Nobili et al. 2008), left ventricular hemodynamics (Doost et al. 2016), or for valve design (Xu et al. 2018).

It is not without reason that heart valve CFD simulations are not yet used for clinical decision making or diagnostics. Valve simulations are particularly challenging from a numerical and imaging perspective. To adequately model valve hemodynamics throughout the entire cardiac cycle, coupled fluid-structure interaction simulations are required. These simulations are difficult due to the large deformations of the valve leaflets, and consequently of the computational grid. Large grid deformations make traditional Arbitrary Euler-Lagrange less robust (convergence and mesh deformation) and efficient (re-meshing). To address these difficulties, other numerical schemes, such as immersed-boundary or adaptive cut-cell methods are generally used. These numerical methods are more efficient, at the expense of solution accuracy at the fluid-solid interface. However, even with these methods, the computational cost for such simulations is in the range of days to weeks (Bavo et al. 2017). Hence, fluid-structure interaction simulations become intractable for day-to-day clinical practice. Alternatively, simplified fixed-grid CFD

models can be used to obtain a reasonable approximation of fluid flow through, and around the aortic valve (**Chapter 2**). Indeed, the valve opens and closes very rapidly, and may not substantially influence flow patterns at peak systole. This is supported by Astorino et al. (2012), who showed that a simplified fixed grid 3-D CFD model of the aortic valve yields similar results at peak-systole as those obtained from fluid-structure interaction simulations. Even though simplified, such models may already provide valuable spatial and/or temporal hemodynamic information to clinicians. Moreover, these models are computationally cheap, more robust, and enable the development of automated simulation frameworks that are suitable for clinical practice.

Besides the numerical challenges, patient-specific three-dimensional geometrical models of the valves are difficult to obtain from imaging data. Automatic segmentation frameworks often struggle with the complex, three-dimensional, and thin nature of the leaflets. Many authors rely on semi-automatic or manual segmentation to obtain the three-dimensional geometry of the valve (Traeger et al. 2015). A small number of authors developed automated segmentation frameworks that enable (aortic) valve segmentation (Weese et al. 2017; Ecabert et al. 2011; Ionasec et al. 2010). These segmentation frameworks make use of parameterized geometries (Ionasec et al. 2010) or deformable models (Weese et al. 2017; Ecabert et al. 2011; Pouch et al. 2013) that are adapted to the patient's imaging data.

The deformable-model-based segmentation approach proposed by Weese et al. (2017) yields a structured surface mesh with consistent inter-patient topology, i.e., a triangulated surface with a consistent number of faces and vertices. Consistent inter-patient topology of the segmentation mesh enables Statistical Shape Modeling (SSM) (Heimann and Meinzer 2009; Davies et al. 2008). SSM utilizes Principal Component Analysis to extract the main directions of (geometrical) variance, interpreted as shape modes. Any patient-specific mesh can then be reconstructed by the mean mesh, and a weighted combination of a small number of shape modes. The weights can be regarded as parameters that define the geometry. This parametric description can then be used to obtain an approximate reconstruction of any mesh, within or outside of the training set. Alternatively, the SSM can be used to generate synthetic meshes that are representative of the training set.

The SSM describes the variation of shape with just a few parameters. This feature can be combined with CFD simulations to explore the relationship between shape and simulation outcome. Moreover, such a simulation framework can generate enough data to train meta-models. Meta-models typically rely on regression and/or interpolation of a set of learning points to find a relationship between model input parameters and output parameters. The continuous function describing this relationship can be an

efficient surrogate for the high fidelity, but computationally costly, simulations. Meta-models are widely used for design optimization (Forrester and Keane 2009), uncertainty quantification, and sensitivity analysis (Quicken et al. 2016). These meta-models can be constructed with various methods, such as: polynomials (Box and Draper 1987), radial basis functions (Broomhead and Lowe 1988), and Kriging (Sacks et al. 1989). Since meta-model selection is often difficult, weighted meta-model ensembles — and the automatic selection thereof — were developed (Acar 2010; Ben Salem and Tomaso 2018).

The aim of this paper is to evaluate the performance of a meta-model with respect to high-fidelity CFD simulations. To achieve this, the aortic valve was parameterized by making use of a SSM. With the resulting parametric model of the aortic valve, a large number of training samples were generated. Consequently, CFD simulations were launched, and the meta-model was trained on the SSM parameters, and the CFD results. Finally, the meta-model and CFD simulations of the reconstructed geometries are compared to the output of the CFD simulations of the segmented mesh to evaluate the quality of both the SSM and meta-model.

3.2 MATERIALS AND METHODS

3.2.1 IMAGING DATA

In this manuscript, Computed Tomography imaging datasets of 74 patients were available. From these 74 datasets, 12 were provided by three clinical centers: the Sheffield Teaching Hospital NHS Foundation Trust; the Catharina Hospital in Eindhoven; and Deutsches Herzzentrum as part of the EurValve research project. Furthermore, a retrospective data-set of 62 Computed Tomography images was available (Weese et al. 2017; Ecabert et al. 2011; Ecabert et al. 2008). Images were acquired with an in-plane spatial resolution of 0.31–0.68 mm, and slice thickness of 0.34–0.70 mm. Images were acquired with Electrocardiography gated Computed Tomography, and segmentations represent the peak-systolic state of the aortic valve.

3.2.2 AORTIC VALVE SEGMENTATION

Segmentation of the aortic valve was performed with a Shape Constrained Deformable model framework, presented in earlier work (Weese et al. 2017; Ecabert et al. 2011; Ecabert et al. 2008). In the segmentation framework, a template mesh model is iteratively adapted to an image. From the resulting segmentation mesh, a submesh ($\mathcal{M}$) was extracted for this study (Figure 3.1). The submesh $\mathcal{M}$ contains the left ventricular outflow tract, the aortic

valve, and (part of) the aortic root (Figure 3.1). $\mathcal{M}$ had a consistent number of vertices k, and consistent topology ($\mathcal{T}$), resulting in mesh correspondence between patients. Each surface mesh was defined by $k = 1808$ vertices, and 4223 triangular faces.

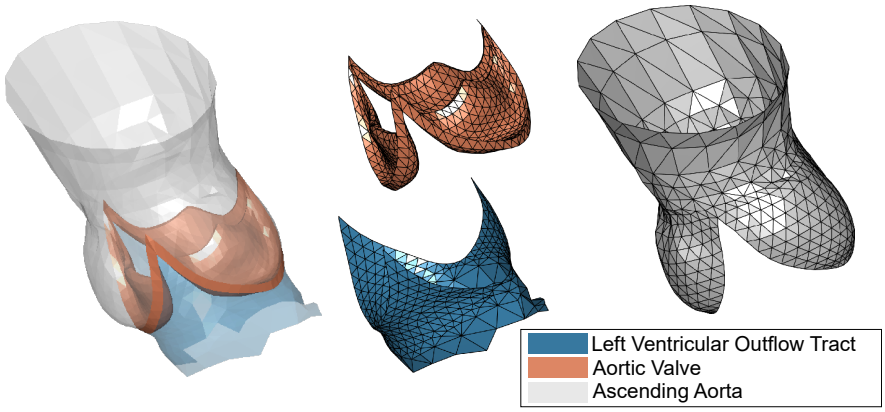

Figure 3.1 Typical example of a segmentation mesh of the aortic valve region, the output of the Shape Constrained Deformable Model framework (Ecabert et al. 2011; Weese et al. 2017). In blue: the left ventricular outflow tract. In red: the aortic valve. In gray: the aortic root.

3.2.3 STATISTICAL SHAPE MODELING

The SSM describes the training set by a mean shape and the main modes of (shape) variation. SSM's are widely described and applied in literature, and for a comprehensive overview of its applications the authors refer to a review by Heimann and Meinzer (2009) — or more recently — Biglino et al. (2016). Following segmentation, a structured surface mesh $\mathcal{M}$, representing the aortic valve, is available for each patient.

$$\mathcal{M} = \mathcal{M}(\mathbf{x}, \mathcal{T}) \tag{3.1}$$

With $\mathbf{x}$ the coordinate vector of the vertices and $\mathcal{T}$ the topology of the mesh. For the SSM, segmentation meshes were aligned by a generalized Procrustes analysis (Bookstein 1992), which optimally translated, rotated, and scaled each of the meshes by minimizing the sum of squared errors. Following alignment, the coordinates of $k = 1808$ vertices were concatenated into a single vector (column) of length $3k$ for each segmentation i:

$$\mathbf{x}_i = [x_1, y_1, z_1, x_2, y_2, z_2, ...x_k, y_k, z_k]^T \tag{3.2}$$

Averaging over N_s segmentations, the mean shape was obtained:

$$\bar{\mathbf{x}} = \frac{1}{N_s} \sum_{i=1}^{N_s} \mathbf{x}_i \tag{3.3}$$

Using $\mathbf{x}_i$ and $\bar{\mathbf{x}}$ the covariance matrix $\mathcal{S}$ with size $3k \times 3k$ was computed by:

$$\mathcal{S} = \frac{1}{N_s - 1} \sum_{i=1}^{N_s} (\mathbf{x}_i - \bar{\mathbf{x}})(\mathbf{x}_i - \bar{\mathbf{x}})^T \tag{3.4}$$

Consequently, the eigendecomposition of $\mathcal{S}$ yielded the principal modes of variation, i.e., the eigenvectors ϕ_m, and corresponding eigenvalues (λ_m). λ_m and ϕ_m were ordered from high to low explained variance. In the three-dimensional case the eigenvectors ϕ_m also have length $3k$. The eigenvectors represent the principal directions of variation, and are referred to as shape modes in the context of shape modeling. Any shape $\mathbf{x}_i$ can then be reconstructed ($\hat{\mathbf{x}}_i$) by a linear combination of N_m shape modes weighted by coefficients $\alpha_{i,m}$.

$$\hat{\mathbf{x}}_i = \bar{\mathbf{x}} + \sum_{m=1}^{N_m} \alpha_{i,m} \phi_m \qquad i \in \{1, 2, ...N_s\} \tag{3.5}$$

Note that $\hat{\mathbf{x}}_i$ in Equation 3.5 is an approximation of $\mathbf{x_i}$. The shape coefficients α_m are patient-specific, and were obtained by the dot product of the centered data and the eigenvectors:

$$\alpha_{i,m} = \phi_m^T \cdot (\mathbf{x}_i - \bar{\mathbf{x}}) \tag{3.6}$$

Where $\alpha_{i,m}$ is contained in the coefficient vector α_i:

$$\alpha_i = \{\alpha_{i,m} : m = 1, ..., N_m\} \tag{3.7}$$

In fact, Equation 3.6 is equal to minimizing the ℓ_2 norm of the difference between the reconstruction and the original:

$$\min_{\alpha_i \in \mathbb{R}^{N_m}} (||\hat{\mathbf{x}}_i(\alpha_i) - \mathbf{x}_i||_2) \tag{3.8}$$

The minimization of Equation 3.8 was manipulated with a weight vector $\mathbf{w}$ $(1 \times 3k)$ to increase the weight of regions that are physically more relevant:

$$\min_{\alpha_i \in \mathbb{R}^{N_m}} (||(\hat{\mathbf{x}}_i(\alpha_i) - \mathbf{x}_i) \cdot \mathbf{w}||_2) \tag{3.9}$$

The introduction of $\mathbf{w}$ allowed to control the weight of each vertex to the minimization problem. When computing pressure drops, the opening area of the valve is physically most relevant. Consequently, a low reconstruction error for the vertices that were part of and adjacent to the free cusp edges of the valve was desirable. $\mathbf{w}$ was empirically established, and in this study weighting the 216 vertices that were part of or adjacent to the free cusp edges (Figure 3.2) five times stronger than other vertices gave good results. Note that Equation 3.9 is the same as Equation 3.6 when $\mathbf{w} = \vec{\mathbf{1}}$. For each segmentation sample, coefficients of α were found by minimizing Equation 3.9.

Subsequently, the original vertices $\mathbf{x}$ from any segmented mesh $\mathcal{M}$ (see Equation 3.1) were replaced by $\hat{\mathbf{x}}$ to yield an approximate reconstruction $\mathcal{M}_r$ of the segmentation:

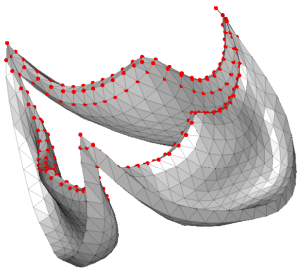

Figure 3.2 Vertices part of and adjacent to the free cusp edge are highlighted. Highlighted vertices were assigned a weighting factor of five. All other vertices were given a weight factor of 1.

$$\mathcal{M}(\mathbf{x}, \mathcal{T}) \approx \mathcal{M}_r(\hat{\mathbf{x}}, \mathcal{T}). \tag{3.10}$$

3.2.3.1 STATISTICAL SHAPE MODEL PERFORMANCE

In literature, SSM performance is typically evaluated with compactness and generalizability metrics (C. Taylor and Noble 2003). Compactness is a function of the number of modes, and defined as the sum of variances, normalized by the cumulative variance:

$$C(N_m) = \frac{\sum_{m=1}^{N_m} \lambda_m}{\sum_{m=1}^{N_t - 1} \lambda_m} \tag{3.11}$$

Where N_t is the number of samples used to train the SSM.

To test how well the model generalizes to unseen data (generalization ability), the average sum of squared errors of a leave-one-out procedure was computed:

$$G(N_m) = \frac{1}{N_t} \sum_{i=1}^{N_t} ||\mathbf{x}_i - \hat{\mathbf{x}}_i(N_m)||^2 \tag{3.12}$$

Where $\mathbf{x}_i$ is the left-out shape, and $\hat{\mathbf{x}}_i(N_m)$ the approximated shape. The approximated shape was obtained by using N_m number of shape modes from a SSM that was trained

on all samples, but excluding the sample to be approximated.

In addition, three physically relevant areas were quantified from the mesh to judge reconstruction performance, the area of the left ventricular outflow tract, aortic valve, and ascending aorta. In this manuscript, the aortic valve area refers to the geometric orifice area, and is not to be confused with the effective orifice area, the metric used in the clinic.

3.2.4 COMPUTATIONAL FLUID DYNAMICS

Sections 3.2.2 and 3.2.3 describe how the segmentation meshes $\mathcal{M}$ and the reconstructed meshes $\mathcal{M}_r$ were obtained. The volume enclosed by these surface meshes were discretized (meshed) to enable CFD simulations. To achieve this, first the outflow boundary of $\mathcal{M}$ and $\mathcal{M}_r$ were extruded by ten times the radius of the sinotubular junction. The inflow boundary normal was defined by three vertices at the valve annulus. This plane was moved proximal such that it was in the most proximal position, while still maintaining an enclosed surface. Finally, the shrink-wrapping option in ANSYS Fluent Meshing 18.2 (ANSYS Inc., Canonsburg, PA, USA) was used to automatically generate a volumetric mesh with approximately $2 \cdot 10^5$ to $3 \cdot 10^5$ polyhedral elements (Figure 3.3). Edge lengths of the polyhedrals were chosen based on a mesh-sensitivity study, and ranged between 0.15 and 2.0 mm. As part of a mesh refinement study, maximum element sizes were reduced to 1.0, and 0.5 mm respectively, which typically improved the results by less than 1%. Hence, a maximum size of 2.0 mm provided a good trade-off between accuracy and computational load.

Blood was modeled as an incompressible Newtonian fluid with a density of 1060 kg/m^3 and dynamic viscosity of 0.004 Pa·s. For the segmentation and reconstructed meshes, steady-state simulations were performed at flow rates of 200, 300, 400, 500, and 600 ml/s , and were used to approximate the pressure-drop flow relationship for each patient. At the inflow boundary a plug-velocity profile was prescribed. Pressure at the outlet was set to zero, and no-slip boundary conditions were assumed at the walls.

Areas of the left ventricular outflow tract (the inflow-boundary) were between 2.4 and 6.4 cm^2. With blood-like fluid properties, flow-rates, and geometric dimensions, inlet Reynolds numbers for the CFD simulations were estimated to be between 2400 and 12000. Hence, a Shear Stress Transport $k-\omega$ model, with 5% turbulence intensity at the inlet, was used to model turbulence (Menter 1994). The output variable of interest is the net pressure-drop across the aortic valve, and defined as the pressure at the inflow

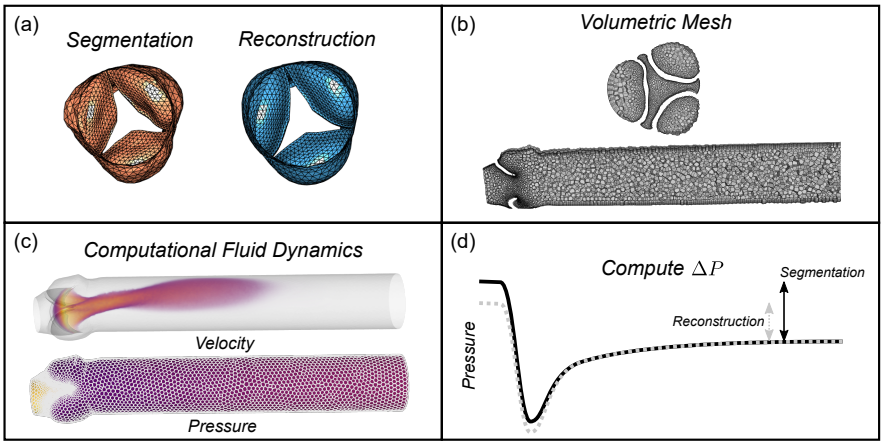

Figure 3.3 Graphical representation of the workflow from segmented and reconstructed surface meshes (a). From these surface meshes a volumetric mesh was created (b), that was used as input to the CFD simulations (c). Consequently. the recovered pressure-drop is extracted from the CFD simulations (d).

boundary minus the downstream recovered pressure (Figure 3.3d). For convenience, the downstream pressure was taken at the outflow boundary, which is a reasonable assumption when pressure-loss in the straight extended section is negligible with respect to pressure-loss due to the presence of the valve. Convergence was assumed when the pressure drop did not change anymore. Small oscillations in the solution were observed. Hence, an average pressure residual R_p was defined to monitor convergence.

$$R_p(j) = \frac{|\bar{p}_j - \bar{p}_{j-200}|}{\bar{p}_j} \leq 0.001 \tag{3.13}$$

Here $\bar{p}_j$ is the area-weighted pressure at the inlet boundary at iteration j, averaged over the last 200 iterations. $\bar{p}_{j-200}$ is then the area-weighted pressure at the inlet, averaged over the range $[i-400, i-200]$.

Out of the total of 2960 simulations that were performed (74 segmentations, 8 meshes, i.e., 7 reconstructions and 1 segmentation, and 5 flow rates), 81% exhibited maximum relative deviations of <1% with respect to the iteration-averaged mean ($\bar{p}_j$), and 99% exhibited maximum relative deviations below 5%. Only 11 (0.4%) simulations experienced relative deviations from the mean larger than 10%, but all of these yielded negligible iteration-averaged pressure-drops (<0.5 mmHg).

Table 3.1 Input parameters and their respective limits

Description	Symbol	Unit	Minimum	Maximum
Valve opening	α_1	-	$-3\sqrt{\lambda_1}$	$3\sqrt{\lambda_1}$
-	α_2	-	$-3\sqrt{\lambda_2}$	$3\sqrt{\lambda_2}$
-	α_3	-	$-3\sqrt{\lambda_3}$	$3\sqrt{\lambda_3}$
Global Mesh Scaling	s	-	0.8	1.25
Flow-rate	Q	ml/s	50	650

The governing equations were solved with ANSYS Fluent 18.2 (ANSYS Inc., Canonsburg, PA, USA), a finite volume based CFD solver. Simulations were performed on the ACC Cyfronet AGH Prometheus supercomputer (Academic Computer Centre Cyfronet, AGH University of Science and Technology, Kraków, Poland). Each CFD simulation was assigned four CPU's and took between 10 and 30 minutes to complete.

3.2.5 META-MODEL TRAINING

3.2.5.1 DESIGN OF EXPERIMENTS

Statistical shape modeling allowed us to describe geometrical changes with a limited number of parameters. These parameters were used to build a meta-model in parameter space. The parameter space was restricted to five parameters: the first three shape coefficients ($\alpha_1, \alpha_2, \alpha_3$) of the SSM trained on all available segmentations, a global scaling parameter s, and flow rate Q (Table 3.1). The three shape coefficients were used to generate synthetic meshes throughout the input space, and were constrained to lie within $[-3\sqrt{\lambda_m}, 3\sqrt{\lambda_m}]$. Feasible limits for the global mesh scaling parameter were determined from the reconstruction procedure. Flow-rates between 50 and 650 ml/s were considered. Upper and lower limits of the individual parameters are described in Table 3.1. The input-space was sampled with Latin Hypercube designs of 25, 50, 100, 200, 400, 800, and 1600 samples. Learning points were excluded from meta-model training when the aortic valve opening was less than 20 mm^2, when the pressure drop exceeded 300 mmHg, or when the simulations diverged.

3.2.5.2 META-MODEL METHODOLOGY

Selecting the most suitable meta-model, and meta-model settings is often difficult since no universal meta-model exists that performs well for all problems. Hence, several authors worked on ensemble approaches, where a weighted sum of meta-models is considered (Ben Salem and Tomaso 2018; Acar 2010). One such algorithm is the Genetic-

Aggregation meta-model, available in the commercial package ANSYS DesignXplorer (ANSYS Inc., Canonsburg, PA, USA). In this algorithm meta-model selection is automated by minimizing a penalized predictive score (Ben Salem and Tomaso 2018). In this study, the Genetic-Aggregation meta-model was trained with the available simulation data. A comprehensive overview of the advantages and shortcomings of such a ensemble-type meta-model approach is beyond the scope of this work. But to give the reader a basic understanding of the working principle, a short summary follows.

The goal of a ensemble-type meta-model is to obtain the best weighted-average of a selection of meta-models:

$$\hat{y}_{ens}(x) = \sum_{i=1}^{N_e} \beta_i \cdot \hat{y}_i(x) \tag{3.14}$$

Where $\hat{y}_{ens}$ is the prediction at x of the final meta-model, i.e., the weighted ensemble of various meta-models and their settings. $\hat{y}_i$ is the prediction at x of the ith meta-model, weighted by β_i. And N_e is the number of meta-models used. The idea is that appropriate weighting of the individual meta-models will cancel out errors in the prediction of the individual meta-model. The trick is then to find the weights that gives the best quality ensemble prediction $\hat{y}_{ens}$. However, assessing optimal quality objectively is not straightforward. In the Genetic-Aggregation algorithm, a penalized predictive score $\mathcal{L}$ is introduced (Ben Salem and Tomaso 2018). This score combines three components (Equation 3.15): (a) optimizing the internal accuracy by evaluating the mean square error on training samples/points; (b) use a 10-fold cross-validation to evaluate predictive capability on unseen samples; and (c) minimize over-fitting of the meta-model by a thin-plate spline Bending Energy Functional (Ben Salem and Tomaso 2018; Duchon 1977). The penalized predictive score is then constructed by weighting the contribution of each of these components:

$$\mathcal{L}(\hat{y}_{ens}) = \underbrace{\gamma_1 \mathcal{R}(\hat{y}_{ens})}_{\text{a}} + \underbrace{\gamma_2 \mathcal{R}_{10CV}(\hat{y}_{ens})}_{\text{b}} + \underbrace{\gamma_3 E(\hat{y}_{ens})}_{\text{c}} \tag{3.15}$$

This loss function $\mathcal{L}$ is defined for the aggregate meta-model $\hat{y}_{ens}$ on the set of training points. γ_1, γ_2, and γ_3 are constants, and kept at 1, 0.5, and 0.25 respectively. The optimal

aggregation of meta-models is then obtained by minimizing $\mathcal{L}$ under the condition that

$$\sum_{i=1}^{N_e} \beta_i = 1 \tag{3.16}$$

This problem was shown to be quadratic and has an analytic solution (Ben Salem and Tomaso 2018). In this work, we used the algorithm PPS-OS described in Ben Salem and Tomaso (2018) where 32 meta-model candidates of four types are considered: 24 Kriging, 3 polynomial regression, 2 support vector machine, and 3 moving least squares.

For a more comprehensive overview of such ensemble-type meta-models, or the Genetic-Aggregation methodology specifically, the reader is encouraged to consult the work by Viana et al. (2009), Acar (2010), or Ben Salem and Tomaso (2018).

3.2.5.3 EVALUATING APPROXIMATION ERROR

Approximate reconstruction of the segmentation mesh (Equation 3.5) inherently introduces geometrical errors which will affect the computed pressure-drop. Moreover, the meta-model is a further simplification that approximates the simulated pressure-drop. To evaluate the influence of both approximations on the pressure-drop, differences in the pressure-drop results were expressed as the root mean square error (RMSE: Equation 3.17), relative RMSE (Equation 3.18), and mean absolute percent error (MAPE: Equation 3.19):

$$\epsilon_{RMS} = \sqrt{\frac{1}{N}\sum_{i=1}^{N}(\Delta\hat{p}_i - \Delta p_i)^2} \tag{3.17}$$

$$\epsilon_{rRMS} = \sqrt{\frac{1}{N}\sum_{i=1}^{N}\left(\frac{\Delta\hat{p}_i - \Delta p_i}{\Delta p_i}\right)^2} \tag{3.18}$$

$$\epsilon_{MAP} = \frac{1}{N}\sum_{i=1}^{N}\left|\frac{\Delta\hat{p}_i - \Delta p_i}{\Delta p_i}\right| \tag{3.19}$$

Here, $\Delta\hat{p}_i$ is the approximated pressure-drop from the reconstructed mesh or meta-model, and Δp_i the pressure-drop computed from the CFD model. N represents the total number of available samples. The total number of available samples for a comparison

between the segmented model and the reconstructed model is 370 (74 segmentations times 5 flow rates).

3.3 RESULTS

3.3.1 TRAINING-SET CHARACTERISTICS

Aortic valve segmentations were split into three groups based on their projected geometric aortic valve orifice area and the recommendations from the European Association of Cardiovascular Imaging and the American Society of Echocardiography (Baumgartner et al. 2016). Threshold criteria for these groups were: severe — subgroup A: valve area below 100 mm^2; intermediate — subgroup B: valve area between 100 and 150 mm^2, and mild/healthy — subgroup C: valve area larger than 150 mm^2. Of all 74 aortic valve segmentations, 14 were in subgroup A (severe), 30 in subgroup B (intermediate), and 30 in subgroup C (mild/healthy). Figure 3.4 demonstrates how the aortic valve areas were distributed over the 74 segmentations, with a median of 143 mm^2, and mean of 166 mm^2. Cases with a valve area over 150 mm^2 were distributed over a wide range with a maximum of 440 mm^2. The smallest valve area in subgroup A was 46 mm^2.

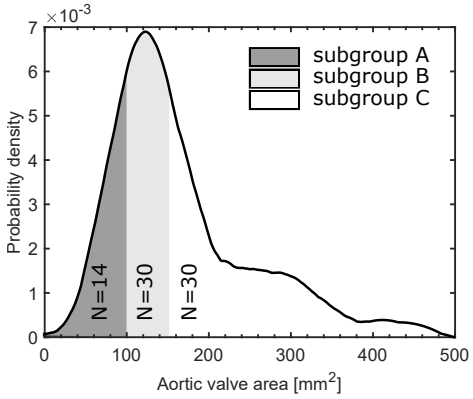

Figure 3.4 Distribution of the aortic valve area in the complete training set of all 74 segmentations. Dark gray: subgroup A — cases with a geometric valve area below 100 mm^2. Light gray: subgroup B — cases with a valve area between 100 and 150 mm^2. White: subgroup C — valve area is larger than 150 mm^2.

3.3.2 STATISTICAL AND GEOMETRICAL PERFORMANCE OF THE SHAPE MODEL

Segmentations were reconstructed with seven models, each using more shape modes for reconstruction ($N_m = \{0, 1, 2, 3, 4, 5, 20\}$). Shape coefficients for each respective model were found by Equation 3.9. The following section demonstrates how the number of shape modes affect geometrical performance of the SSM.

In Figure 3.5 the mean mesh and the first three shape modes of the aortic valve are visualized. The first shape mode accounts for most of the variance (21%) and represents the opening and closure of the aortic valve. The valve is completely open at $-3\sqrt{\lambda_1}$, and completely closed at $3\sqrt{\lambda_1}$. The mean mesh ($\bar{\mathbf{x}}$) features an aortic valve area of 170 mm^2. The first shape mode reduces the reconstruction error of the aortic valve considerably (Figure 3.6 and 3.7). The second shape mode accounts for 14% of the variance, and seems to predominantly represent the size of the sinus/annulus region. This shape mode noticeably decreases the reconstruction error for vertices in the left ventricular outflow tract (Figure 3.7). The third mode accounts for 11% of the variance, and seems to mainly affect skewness of the sinus region. Improvements are mainly observed in the region where the valve is attached to the wall. Finally, Figure 3.7 also illustrates that with 20 shape modes, the mean vertex-to-vertex reconstruction error drops to below 1 mm. Furthermore, Figure 3.6 demonstrates that the error of the left ventricular outflow tract and ascending aorta areas gradually improve between 5 and 15 shape modes. No substantial improvement for these areas is observed beyond 15 modes.

Figure 3.14 illustrates the compactness and generalizability of each model. The first three modes account for 46% of the variance. 80, 90 and 95% of the variance in the training set is captured by 11, 19 and 29 modes respectively. Generalizability of the model levels out at 15 modes, meaning that the model is unlikely to generalize to unseen data with more than 15 shape modes.

3.3.3 CFD PERFORMANCE OF THE SHAPE MODEL

To assess how many modes were required to build an accurate meta-model, 2590 CFD simulations were performed, 74 meshes times five flow rates per mesh, times seven reconstructions ($N_m = \{0, 1, 2, 3, 4, 5, 20\}$). The computed pressure-drop of each reconstruction was compared with the pressure-drop that was computed on its segmentation counterpart at five flowrates (another 370 simulations), resulting in a pressure-drop error. Pressure-drop errors are expressed in RMSE, relative RMSE, and mean absolute percent

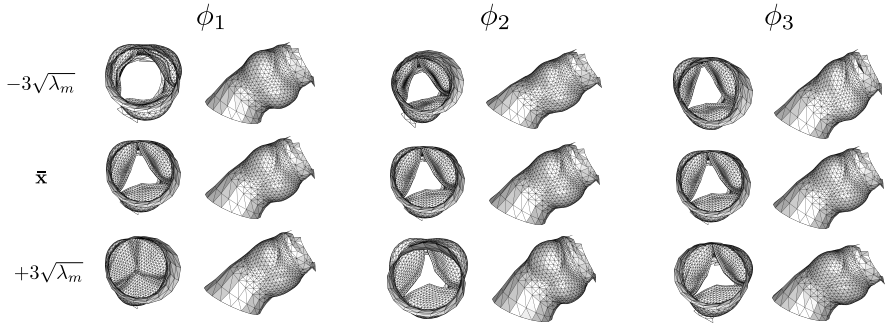

Figure 3.5 Visualization of the first three shape modes. The first shape mode represents the opening and closing of the aortic valve. The second shape mode seems to represent dilation of the base of the valve and the sinuses, the third mode seems to contain skewness/stretching in the sinuses.

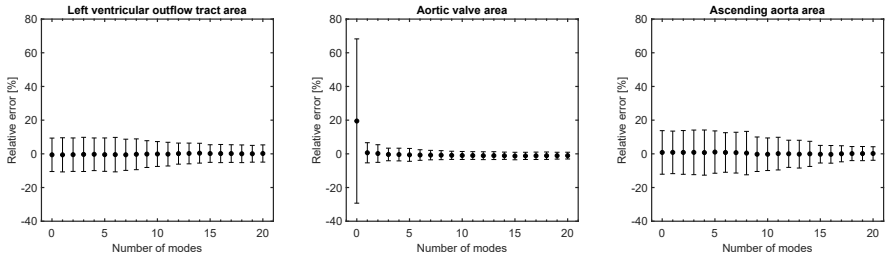

Figure 3.6 Mean absolute percent error of the LVOT, AV and AA areas as function of the number of modes. Error bars represent the mean absolute percent deviation. Steady improvements in left ventricular outflow tract area is observed between modes 7 to 11. Improvement in aortic valve area reconstruction is largest for the first mode. Improvement in ascending aorta area occurs gradually between modes 5 and 14.

errors (MAPE). (Equation 3.17–3.19).

Table 3.2 and Figure 3.8 demonstrate that the first shape mode — representing aortic valve opening/closing — substantially reduces the pressure-drop error in all subgroups. RMSE values drop from 135.5 (subgroup A), 26.0 (subgroup B), and 15.2 mmHg (subgroup C), to 36.8, 6.3, and 2.3 mmHg respectively. These reductions may also be expressed in relative metrics. Relative RMSE values drop to 24.4, 13.0, and 119.9%. Mean absolute percent error values drop to 21.4, 9.6, and 44.1%. Although, RMSE, relative RMSE, and MAPE, still decrease when including more shape modes, improvements are more gradual. With a relative RMSE of 13.6 and 10.9%, and MAPE of 10.6, and 8.8%, improvements level out at three shape modes for subgroups A and B. Furthermore, it is shown that when segmentations are reconstructed with an excesssive number of modes ($N_m = 20$) the RMSE can drop to 11.1, 2.9, and 0.6 mmHg. Relative errors of 4.8, and 4.6% can be expected. Interestingly, subgroup C exhibits an increase in relative errors with respect to the model that is reconstructed with five shape modes, indicating that more shape modes

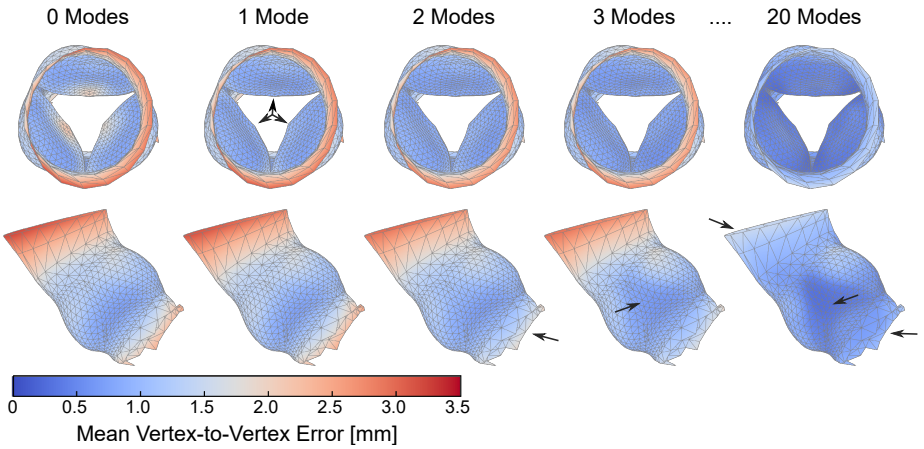

Figure 3.7 Mean vertex-to-vertex reconstruction error mapped onto the mean mesh ($\mathcal{M}(\bar{\mathbf{x}}, \mathcal{T})$). Top row: axial view, bottom row: side view. Mean vertex-to-vertex errors reduce with an increase in the number of modes. Main improvements with each added mode are highlighted with arrows. Vertices around the ascending aorta are poorly approximated with a low number of modes.

do not necessarily improve pressure-drop errors in the relative sense.

Figure 3.8 demonstrates that leave-one-out results do not deviate much from the reconstructions with the full model, RMSE, relative RMSE, and MAPE follow the same trend as those of the full-SSM.

Typical pressure-flow relationships for each subgroup and for segmentations and reconstructions ($N_m = 3$) are illustrated in Figure 3.9. Furthermore, results for all cases and subgroups can be found in Figure 3.11–3.13. These figures support the observation that reconstruction seems to yield a fair approximation of the pressure-flow relationship for subgroups A (Figure 3.11) and B (Figure 3.12). The pressure-flow relationship is poorly approximated for several cases in subgroup C (Figure 3.13 — cases: 15, 46, 47, and 51). The pressure-drop errors do not seem to improve much beyond three shape modes. Therefore, a single meta-model that takes into account the first three shape modes was generated.

3.3.4 META-MODEL PERFORMANCE

Seven meta-models were build with a Genetic-Aggregation response surface (Ben Salem and Tomaso 2018). Meta-models were trained with 25, 50, 100, 200, 400, 800 and 1600 synthetic points/samples. Quality of the meta-model depends on the number of available

Table 3.2 RMSE, relative RMSE, and mean absolute percent error by N_m and subgroup

	RMSE [mmHg]			Relative RMSE [%]			MAPE [%]		
N_m	A	B	C	A	B	C	A	B	C
0	135.5	26.0	15.2	73.4	50.8	3474.2	72.0	48.3	905.3
1	36.8	6.3	2.3	24.4	13.0	119.9	21.4	9.6	44.1
2	41.5	5.6	2.0	19.8	12.4	89.1	15.4	9.5	36.2
3	26.9	5.2	1.9	13.6	10.9	87.2	10.6	8.8	35.0
4	23.8	5.1	1.9	13.3	10.8	47.5	10.5	8.6	26.5
5	22.1	5.0	1.9	13.1	10.5	53.3	10.2	8.1	26.4
20	11.1	2.9	0.6	7.1	5.7	160.9	4.8	4.6	31.7

† Results are based on reconstructions that were performed with the SSM that was trained on all segmentations, and correspond to the black symbols in Figure 3.8.
‡ Reference pressure-drop: CFD on segmentation.

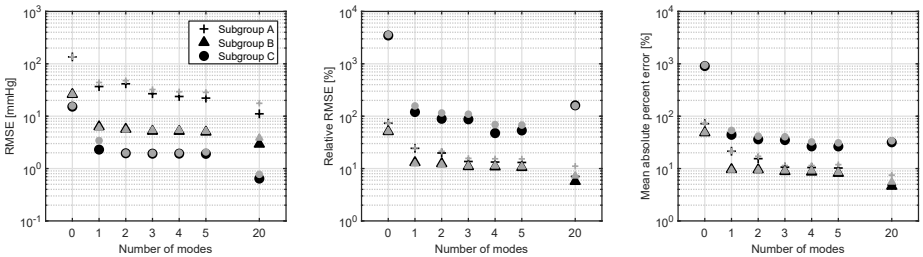

Figure 3.8 RMSE, relative RMSE, and mean absolute percent error (MAPE) of the pressure-drop for subgroups A (✚), B (▲), and C (●). Segmentation meshes were reconstructed with $N_m = \{1, 2, ...5, 20\}$. Substantial improvements are observed when including the first shape mode. Black: reconstruction performed with the SSM that is trained on all available segmentations. Gray: reconstruction based on a leave-one-out procedure: the segmented mesh is reconstructed with a SSM that is trained on all segmentations but the reconstructed segmentation.

training samples (Figure 3.10). Relative RMSE and mean absolute percent errors of the verification points do not improve beyond 600 training points, and level out at approximately 11% and 3% respectively. The RMSE decreases to a value of 1.7 mmHg.

Moreover, Figure 3.10 demonstrates that two meta-models exhibit RMSE, relative RMSE, and mean absolute percent errors of 0. That is, a perfect fit through all training points is obtained, suggesting that these models may have overfit the data. All other models show a non-zero error. In general, the meta-models with a low number of training points showed large errors on the verification points. However, errors on verification points substantially reduce when more training points (>300) were considered. This indicates that with a low number of training points, the (non-linear) behavior of the pressure-drop

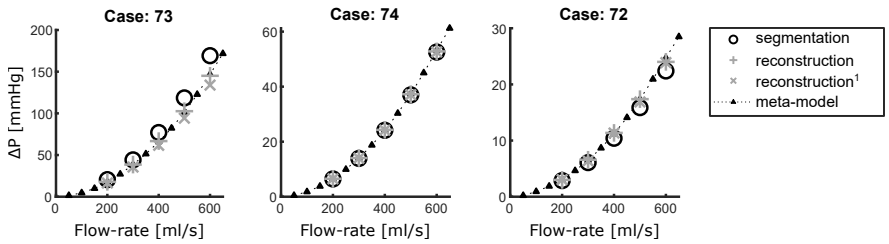

Figure 3.9 Pressure-flow relationship for three typical cases in subgroups A, B, and C (from left to right). ◯: CFD on segmentation mesh; +: CFD results for 3-mode reconstruction without leave-one-out procedure; ×: CFD results for 3-mode reconstruction with leave-one-out procedure; ▲: meta-model. Pressure-flow relationships for all cases are illustrated in Figure 3.11–3.13.

with respect to the shape coefficients is not adequately captured, i.e., the meta-model is of poor quality. Quality improves drastically beyond 300 training points, and yields an acceptable meta-model that captures behavior of the pressure-drop with respect to the shape coefficients well.

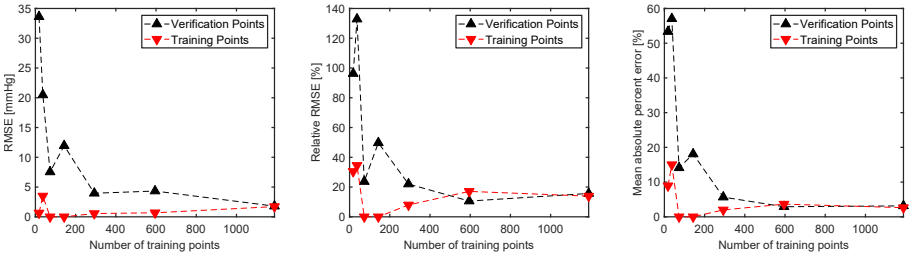

Figure 3.10 Meta-model quality as function of the number of (successfully simulated) training points. Pressure-drop errors follow from Equation 3.17-3.19 with $\Delta\hat{p}_i$ the meta-model approximation. CFD computed Pressure-drops on the reconstructed meshes were used as the reference (Δp_i). Note: reference pressure-drops were not used for training of the meta-model.

3.4 DISCUSSION

The pressure-drop across the aortic valve is a key hemodynamic metric to evaluate the severity of aortic valve stenosis. The main aim of this work was to investigate whether a meta-model can replace CFD simulations to find this pressure-drop from segmented aortic valves. To achieve this, segmentation meshes of the aortic valve were parameterized by means of statistical shape modeling. Using a SSM, segmentation meshes were reconstructed by a limited number of shape modes and their corresponding coefficients. With the SSM a set of synthetic training meshes were generated. Consequently, CFD-computed pressure-drops of the synthetic meshes were used to train a meta-model. The meta-model replaces the compute-intensive three-dimensional CFD simulations by

analytically relating three SSM shape modes, scaling, and flow rate, to the pressure-drop. This meta-model provides an estimate of the pressure-flow relationship of a segmented aortic valve in real-time.

The findings of this study illustrate that relevant geometrical variation of the aortic valve can be adequately captured by the SSM. The SSM captures the range of possible open/closed configurations of the valve. In particular, for subgroups A and B, the reconstruction and meta-model results are close to the CFD results of the segmented mesh. On average, reconstruction introduces an error in pressure-drop computations of only 10%, and further simplification to a meta-model introduces an additional 3% error on average. Even though the first three shape modes account for only 46% of the variance, the essential geometrical features — relevant for pressure-drop computations — seem to be adequately captured. One major cause of pressure-drop errors for subgroups A and B is poor approximation of the AVA (Figure 3.15). This observation supports favoring physically relevant vertices through weighting of the minimization problem (Equation 3.9). Weighting lowers the reconstruction error for the vertices part of, or adjacent to the free cusp edge, and consequently it is more likely that an accurate estimate of the aortic valve orifice area is obtained. The aortic valve is more open for subgroup C, and the effect on the pressure-drop is less pronounced. Hence, reconstruction errors in other regions will start to influence the pressure-drop as well. For example, reconstruction errors for the sinus, left ventricular outflow tract, and aorta will become more important. Nevertheless, RMSE values indicate that the error is limited, and errors of 1.9 mmHg are expected for subgroup C.

For this study, a Genetic-Aggregation meta-model (Ben Salem and Tomaso 2018) was trained that took into account just three shape modes. However, Table 3.2 suggests that with 20 modes, errors for subgroups A and B may further decrease to 4.8 and 4.6% respectively. Although not unfeasible, extensive computational costs are expected when the meta-model is trained on such a high-dimensional input space. We suggest that for such high-dimensional models additional training points are sequentially added until the meta-model is of sufficient quality.

The large number of publications in various bio-medical fields proves that statistical shape modeling is a versatile and widely accepted technique to capture anatomic variation in the population. For example, it is extensively used for organ segmentation (Yates and Untaroiu 2018; Spinczyk and Krasoń 2018; Woo et al. 2016), to extract morphological bio-markers of (diseased) organs (Suinesiaputra et al. 2018; Uetani et al. 2014; Bruse et al. 2016), or for numerous orthopedic applications (Baumbach et al. 2017; IJsseldijk et al. 2016; Z. Li et al. 2018; Nelson et al. 2017; Wang and C. Shi 2017; Fuessinger et al.

2017). Although few, several studies — mainly in the field of orthopedics — attempted to relate SSM parameterized anatomical shape variation with Finite Element Analysis (FEA). These studies used SSM and FEA to: investigate the relationship between patellofemoral shape and function (Fitzpatrick et al. 2011); force-displacement behaviour of proximal femurs (Nicolella and Bredbenner 2012); to investigate cervical spine loading (Bredbenner et al. 2014), or for real-time prediction of joint-mechanics (Gibbons et al. 2019). Literature that combines SSM with FEA/CFD simulations is more scarce in the field of cardiovascular biomechanics. To our knowledge, only Khalafvand and colleagues used a SSM in combination with CFD simulations. They utilized a SSM-driven simulation framework to systematically analyze blood flow in the left ventricle (Khalafvand et al. 2018). However, they limited their simulations to five characteristic shapes, and did not attempt to build a cheap-to-evaluate meta-model that approximates the simulation results over the entire shape space. Nevertheless, the work of Khalafvand et al., and our work demonstrate that the properties of SSM's can be exploited to yield simulation-derived, physically relevant, hemodynamic metrics.

Although the aortic valve has a complex shape and function, various authors proposed simplified parametric models (K. Li and Sun 2016; Haj-Ali et al. 2012; Loerakker et al. 2016; De Hart et al. 2003). These parametric models facilitate parametric numerical simulations. For example, to study: collagen remodeling (Loerakker et al. 2016); the effect of aortic valve geometry on peak-stress (K. Li and Sun 2016), or bi-cuspid geometry on ascending aorta hemodynamics (Vergara et al. 2011). Such parametric models are particularly powerful for obtaining fundamental understanding of the involved physics, and for determining the most relevant physical parameters. However, the relationships that are found may not hold for each patient specifically. Therefore, there seems to be a shift towards using patient-specific geometries as input for computational models (Morris et al. 2015; C. A. Taylor and Figueroa 2009). In this study, an attempt was made to parameterize the patient-specific geometries with a SSM. Fundamentally, the shape modes and shape coefficients have no physical meaning, which makes interpretation difficult. To aid interpretation, shape modes can be related to physical measures (Campbell and Petrella 2016). In this study, the first shape mode seems to be both statistically and physically the most relevant. However, this may not always be the case. Hence, future work could use sensitivity analysis to select the most physically relevant shape modes.

3.4.1 CLINICAL APPLICATIONS

Pressure-drops are indicative of aortic valve stenosis severity, and are particularly useful to determine the stenosis-induced hemodynamic burden on the patient. Hence, the methodology that was proposed may be used to augment geometrical information from

imaging systems with physiological, simulation-derived metrics that are indicative of disease severity. For routine clinical use, such decision support systems need to be robust, easy to use, and computationally cheap. The meta-model approach that is proposed would be particularly suitable for such a system.

The methodology that is proposed is also suitable for personalizing specific components of lumped-parameter models. Lumped-parameter models are popular in the cardiovascular research community to model the full-body circulation. Heart-valves in these lumped-parameter models are generally described by orifice models that relate the pressure-drop to the flow-rate (Korakianitis and Y. Shi 2006a; Korakianitis and Y. Shi 2006b). The meta-model that is proposed finds this relationship from imaging data, in real-time. Aortic valve segmentation, in combination with the meta-model, may therefore be used to further personalize these lumped-parameter models to more adequately predict the full-system hemodynamics.

Moreover, it is noted that — clinically — subgroup B is the most interesting group. The aortic valve area is between 100 and 150 mm^2, and the potential impact of the stenotic valve is not obvious. Subgroup C is clinically the least interesting, and the larger (relative) errors would not be problematic.

Finally, the authors would like to note that this is a purely numerical study, and clinical studies would be necessary to establish whether this approach yields complementary value in the clinic. Clinically, $4v^2$ is used to estimate the pressure-drop over the valve (Baumgartner et al. 2016). However, $4v^2$ represents the maximum pressure-drop, and neglects pressure-recovery, which may lead to overestimation of stenosis severity (Bahlmann et al. 2010). Hence, this study aimed to predict the recovered pressure-drop instead. Nevertheless, the same methodology could be used to predict the maximum pressure-drop, and would be useful when moving towards clinical validation of the proposed methodology. Unfortunately, patient-specific flow measurements were not available to the authors, and the methodology is patient-specific with respect to geometry only.

3.4.2 LIMITATIONS

It was shown that the methodology that is proposed could help make CFD simulations more clinically accessible. Specific components of the methodology, such as establishing the required number of shape modes, and meta-model training were validated. Other components of the methodology are less well validated. For example, (automatic) valve

segmentation currently lacks a thorough and systematic validation. An idealized tri-cuspid deformable template of the valve was used, which captured the overall feature of the valve, but details such as calcific deposits were not included. Nevertheless, Weese et al. (2017) approximated the mean segmentation error on the valve leaflets to be around 0.47mm, which is in the order of image resolution. Furthermore, the results in this study show, that accurate segmentation in the proximity of the cusp's free edges is desirable. A more thorough understanding of segmentation error may be obtained by having (clinical) experts manually create or edit "ground-truth" valve segmentations as a reference, e.g., see the work by Ecabert et al. (2011) and Pouch et al. (2013) for examples. In addition, the authors would like to note that, although accurate segmentation is necessary, the meta-model approach allows the propagation of segmentation uncertainties to uncertainties in output parameters. That is, uncertainties in valve segmentations could be related to uncertainties in shape mode coefficients. In turn, uncertainties in the shape mode coefficients could be used to obtain an estimate of the pressure-drop, augmented with its respective confidence interval.

As a consequence of the idealized template mesh, calcifications and bi-cuspid valves were not represented in the SSM. SSM worked well with Computed Tomography images, but images from 3D transesophageal echocardiograpghy lack the spatial resolution for adequate automatic segmentations, and often need manual corrections. These manual corrections would add additional variation in a SSM training set, yielding a less compact and general SSM. Moreover, the SSM requires segmentation models with consistent topology, which may not always be available.

The CFD models in this study represent a time-averaged, fully developed, (turbulent) flow. However, flow through the aortic valve is pulsatile in nature, and may not reach the fully developed turbulent state. However, it has been shown that for pressure-drops above 10 mmHg, the steady-state assumption gives a reasonable estimate for the peak-systolic pressure-drop (**Chapter 2**). Furthermore, it is noted that the proposed methodology is not limited to steady-state simulations, and simulation results of more realistic, time-dependent, and/or fluid-structure interaction simulations could be used in future studies.

3.4.3 CONCLUSION

This study evaluated the performance of a SSM-based meta-model. SSM is shown to adequately capture aortic valve shape variation. The shape coefficients of the SSM are successfully used to train a meta-model that analytically relates the shape coefficients to the pressure-flow relationship. Moreover, it is shown that the SSM-based meta-model

provides an acceptable assumption of the pressure-flow relationship, and given adequate training data, is a viable real-time alternative to 3D CFD simulations of the aortic valve.

ACKNOWLEDGEMENTS

This work was supported in part by the European Research Council (Grant number: 689617) and by the PLGrid Infrastructure. The authors would like to thank M. Ben Salem for his valuable suggestions and insights with respect to meta-modeling.

APPENDIX

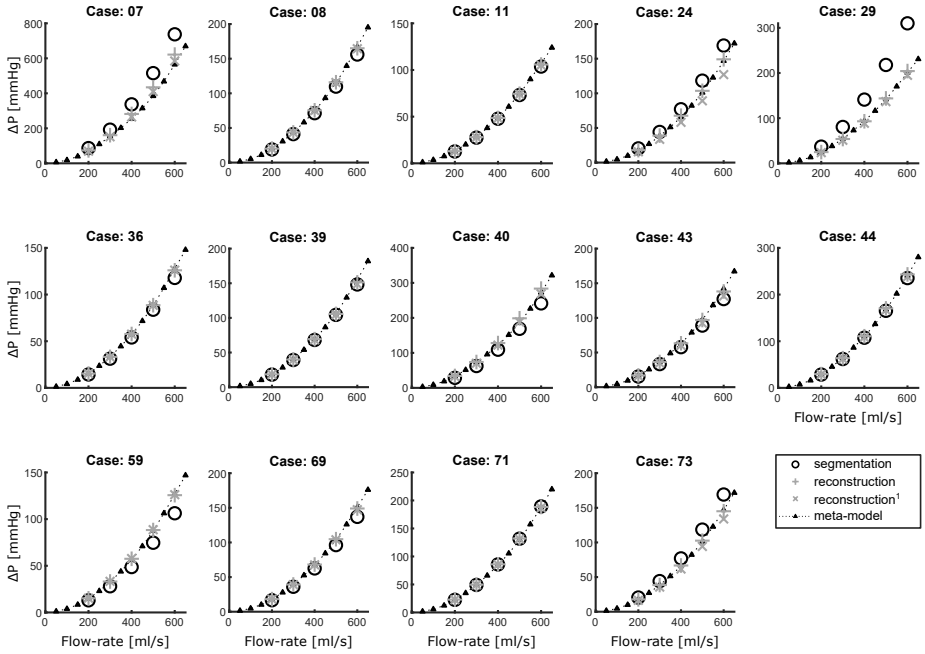

Figure 3.11 Subgroup A: cases with AVA $\leq 1.0\,\mathrm{cm}^2$. ◯: CFD segmentation mesh; $+$: CFD 3-mode reconstruction without leave-one-out procedure; $\times^1$: CFD 3-mode reconstruction with leave-one-out procedure; ▲: Meta-model

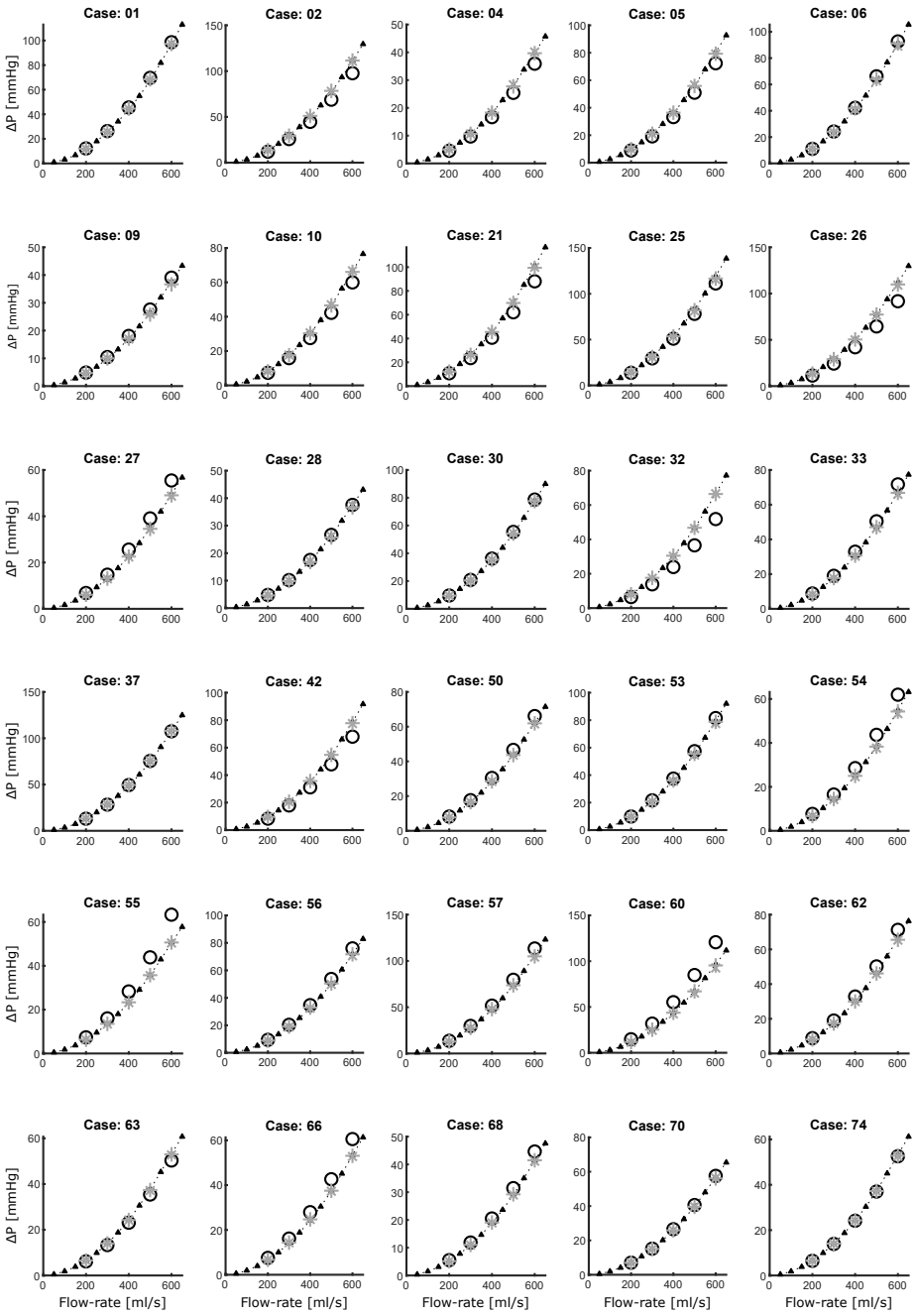

Figure 3.12 Subgroup B: cases with $1.0 < \text{AVA} \leq 1.5$ cm^2. ◯: CFD segmentation mesh; $+$: CFD 3-mode reconstruction without leave-one-out procedure; $\times$: CFD 3-mode reconstruction with leave-one-out procedure; ▲: Meta-model

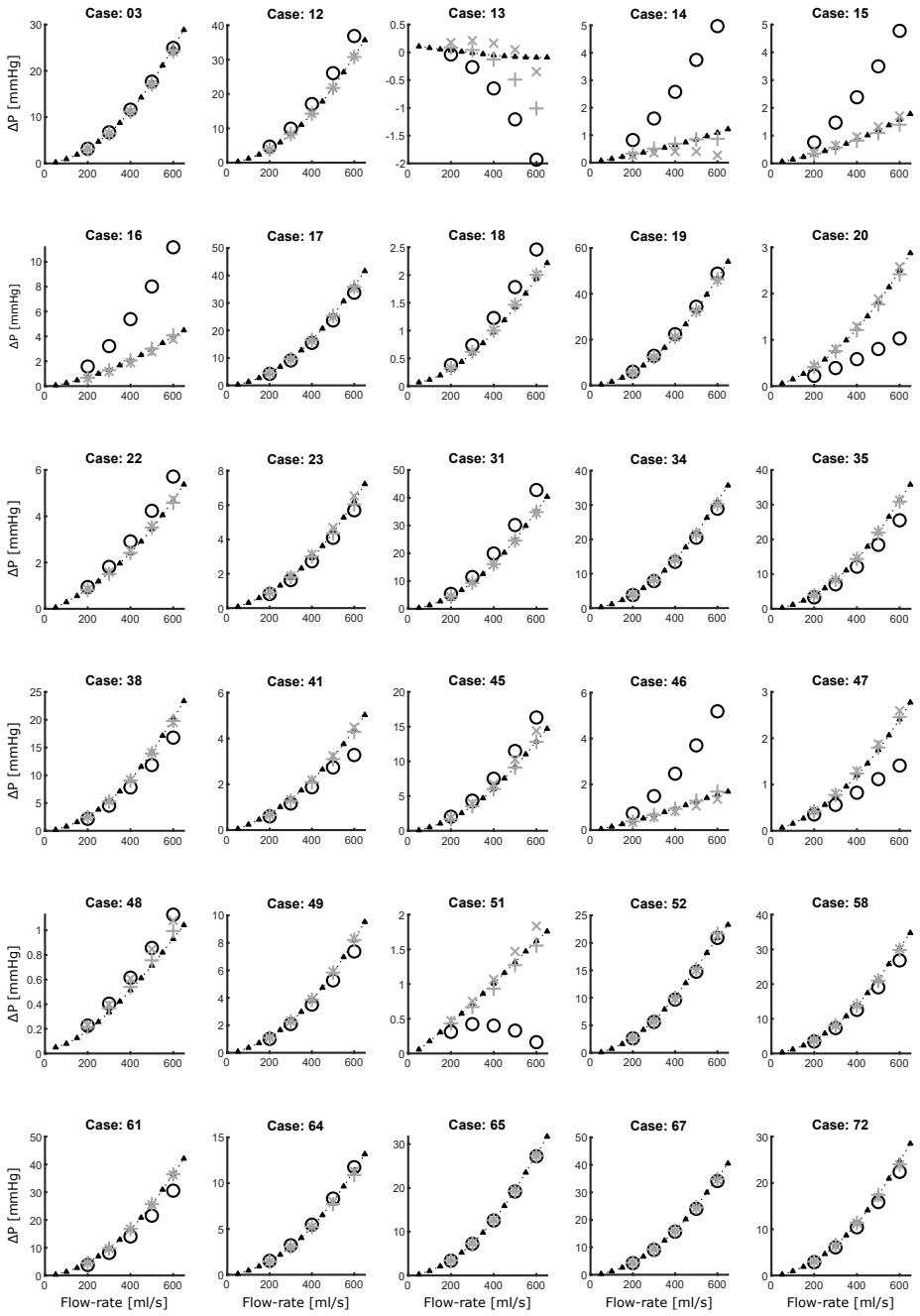

Figure 3.13 Subgroup C: cases with AVA $> 1.5\ \mathrm{cm}^2$. ◯: CFD segmentation mesh; $+$: CFD 3-mode reconstruction without leave-one-out procedure; $\times$: CFD 3-mode reconstruction with leave-one-out procedure; ▲: Meta-model

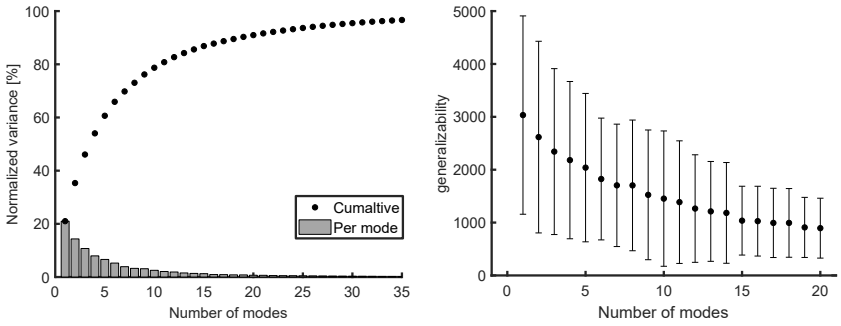

Figure 3.14 Compactness (left) and generalization ability (right) as function of the number of modes. The first three shape modes capture 46% of the variance.

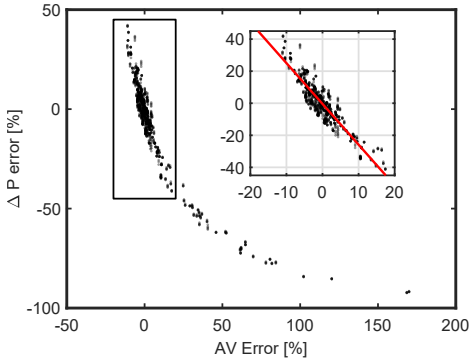

Figure 3.15 Pressure-drop error as function of the AVA reconstruction error. Subgroups A and B (AVA $\leq 150\text{mm}^2$) were considered, and CFD results of all their corresponding reconstructions ($N_m = 0, 1, \ldots, 5, 20$) are used (1540 simulations). A linear model is fitted on the aortic valve error interval $[-20, 20]$. A slope of -2.54 is found ($R^2 = 0.838$), and indicates that with every percent error in AVA reconstruction, 2.5 % error in ΔP can be expected.

BIBLIOGRAPHY

Acar, E. (2010). "Various approaches for constructing an ensemble of metamodels using local measures". In: *Structural and Multidisciplinary Optimization* 42.6, pp. 879–896.

Astorino, M. et al. (2012). "A robust and efficient valve model based on resistive immersed surfaces". In: *International Journal for Numerical Methods in Biomedical Engineering* 28.9, pp. 937–959.

Bahlmann, E. et al. (2010). "Impact of pressure recovery on echocardiographic assessment of asymptomatic aortic stenosis: a SEAS substudy". In: *JACC: Cardiovascular Imaging* 3.6, pp. 555–562.

Baumbach, S. F. et al. (2017). "Analysis of the three-dimensional anatomical variance of the distal radius using 3d shape models". In: *BMC Medical Imaging* 17.1.

Baumgartner, H. et al. (2016). "Recommendations on the echocardiographic assessment of aortic valve stenosis: a focused update from the european association of cardiovascular imaging and the american society of echocardiography". In: *European Heart Journal - Cardiovascular Imaging* 18.3, pp. 254–275.

Bavo, A. M. et al. (2017). "Patient-specific CFD models for intraventricular flow analysis from 3d ultrasound imaging: comparison of three clinical cases". In: *Journal of Biomechanics* 50, pp. 144–150.

Ben Salem, M. and L. Tomaso (2018). "Automatic selection for general surrogate models". In: *Structural and Multidisciplinary Optimization* 58.2, pp. 719–734.

Biglino, G. et al. (2016). "Computational modelling for congenital heart disease: how far are we from clinical translation?" In: *Heart* 103.2, pp. 98–103.

Bookstein, F. L. (1992). *Morphometric tools for landmark data*. Cambridge University Press.

Box, G. E. and N. R. Draper (1987). *Empirical model-building and response surfaces*. Wiley.

Bredbenner, T. L. et al. (2014). "Development and validation of a statistical shape modeling-based finite element model of the cervical spine under low-level multiple direction loading conditions". In: *Frontiers in Bioengineering and Biotechnology* 2.

Broomhead, D. and D. Lowe (1988). *Radial basis functions, multi-variable functional interpolation and adaptive networks*. Vol. RSRE-MEMO-4148. Malvern.

Bruse, J. L. et al. (2016). "A statistical shape modelling framework to extract 3d shape biomarkers from medical imaging data: assessing arch morphology of repaired coarctation of the aorta". In: *BMC Medical Imaging* 16.1.

Campbell, J. Q. and A. J. Petrella (2016). "Automated finite element modeling of the lumbar spine: using a statistical shape model to generate a virtual population of models". In: *Journal of Biomechanics* 49.13, pp. 2593–2599.

Cibis, M. et al. (2014). "Wall shear stress calculations based on 3d cine phase contrast MRI and computational fluid dynamics: a comparison study in healthy carotid arteries". In: *NMR in Biomedicine* 27.7, pp. 826–834.

Davies, R., C. Twining, and C. Taylor (2008). *Statistical models of shape: optimisation and evaluation*.

De Hart, J. et al. (2003). "A three-dimensional computational analysis of fluid-structure interaction in the aortic valve". In: *Journal of biomechanics* 36 (1), pp. 103–112.

Disseldorp, E. M. J. van et al. (2016). "Patient specific wall stress analysis and mechanical characterization of abdominal aortic aneurysms using 4d ultrasound". In: *European Journal of Vascular and Endovascular Surgery* 52.5, pp. 635–642.

Doost, S. N. et al. (2016). "Heart blood flow simulation: a perspective review". In: *BioMedical Engineering OnLine* 15.1.

Duchon, J. (1977). "Splines minimizing rotation-invariant semi-norms in sobolev spaces". In: *Constructive Theory of Functions of Several Variables*. Ed. by W. Schempp and K. Zeller. . Berlin, Heidelberg: Springer Berlin Heidelberg, pp. 85–100.

Ecabert, O. et al. (2008). "Automatic model-based segmentation of the heart in CT images". In: *IEEE Transactions on Medical Imaging* 27.9, pp. 1189–1201.

Ecabert, O. et al. (2011). "Segmentation of the heart and great vessels in CT images using a model-based adaptation framework". In: *Medical Image Analysis* 15.6, pp. 863–876.

Fitzpatrick, C. K. et al. (2011). "Development of a statistical shape model of the patellofemoral joint for investigating relationships between shape and function". In: *Journal of Biomechanics* 44.13, pp. 2446–2452.

Forrester, A. I. J. and A. J. Keane (2009). "Recent advances in surrogate-based optimization". In: *Progress in Aerospace Sciences* 45.1-3, pp. 50–79.

Fuessinger, M. A. et al. (2017). "Planning of skull reconstruction based on a statistical shape model combined with geometric morphometrics". In: *International Journal of Computer Assisted Radiology and Surgery* 13.4, pp. 519–529.

Gibbons, K. D. et al. (2019). "Development of a statistical shape-function model of the implanted knee for real-time prediction of joint mechanics". In: *Journal of Biomechanics* 88, pp. 55–63.

Haj-Ali, R. et al. (2012). "A general three-dimensional parametric geometry of the native aortic valve and root for biomechanical modeling". In: *Journal of Biomechanics* 45.14, pp. 2392–2397.

Heimann, T. and H.-P. Meinzer (2009). "Statistical shape models for 3d medical image segmentation: a review". In: *Medical Image Analysis* 13.4, pp. 543–563.

IJsseldijk, E. A. van et al. (2016). "Three dimensional measurement of minimum joint space width in the knee from stereo radiographs using statistical shape models". In: *Bone & Joint Research* 5.8, pp. 320–327.

Ionasec, R. I. et al. (2010). "Patient-specific modeling and quantification of the aortic and mitral valves from 4-d cardiac CT and TEE". in: *IEEE Transactions on Medical Imaging* 29.9, pp. 1636–1651.

Khalafvand, S. S. et al. (2018). "Assessment of human left ventricle flow using statistical shape modelling and computational fluid dynamics". In: *Journal of Biomechanics*.

Kimura, N. et al. (2017). "Patient-specific assessment of hemodynamics by computational fluid dynamics in patients with bicuspid aortopathy". In: *The Journal of Thoracic and Cardiovascular Surgery* 153.4, S52–S62.e3.

Korakianitis, T. and Y. Shi (2006a). "A concentrated parameter model for the human cardiovascular system including heart valve dynamics and atrioventricular interaction". In: *Medical Engineering & Physics* 28.7, pp. 613–628.

— (2006b). "Numerical simulation of cardiovascular dynamics with healthy and diseased heart valves". In: *Journal of Biomechanics* 39.11, pp. 1964–1982.

Li, K. and W. Sun (2016). "Simulated transcatheter aortic valve deformation: a parametric study on the impact of leaflet geometry on valve peak stress". In: *International Journal for Numerical Methods in Biomedical Engineering* 33.3, e02814.

Li, Z. et al. (2018). "Construction of a statistical cervical vertebrae geometric model for children 3–10 years old". In: *Annals of Biomedical Engineering* 46.11, pp. 1816–1829.

Loerakker, S., T. Ristori, and F. P. T. Baaijens (2016). "A computational analysis of cell-mediated compaction and collagen remodeling in tissue-engineered heart valves". In: *Journal of the Mechanical Behavior of Biomedical Materials* 58, pp. 173–187.

Menter, F. R. (1994). "Two-equation eddy-viscosity turbulence models for engineering applications". In: *AIAA Journal* 32.8, pp. 1598–1605.

Min, J. K. et al. (2015). "Noninvasive fractional flow reserve derived from coronary CT angiography". In: *JACC: Cardiovascular Imaging* 8.10, pp. 1209–1222.

Morris, P. D. et al. (2013). "Virtual fractional flow reserve from coronary angiography: modeling the significance of coronary lesions". In: *JACC: Cardiovascular Interventions* 6.2, pp. 149–157.

Morris, P. D. et al. (2015). "Computational fluid dynamics modelling in cardiovascular medicine". In: *Heart* 102.1, pp. 18–28.

Neal, M. L. and R. Kerckhoffs (2009). "Current progress in patient-specific modeling". In: *Briefings in Bioinformatics* 11.1, pp. 111–126.

Nelson, A. E. et al. (2017). "Cross-sectional associations between variations in ankle shape by statistical shape modeling, injury history, and race: the johnston county osteoarthritis project". In: *Journal of Foot and Ankle Research* 10.1.

Nicolella, D. P. and T. L. Bredbenner (2012). "Development of a parametric finite element model of the proximal femur using statistical shape and density modelling". In: *Computer Methods in Biomechanics and Biomedical Engineering* 15.2, pp. 101–110.

Nobili, M. et al. (2008). "Numerical simulation of the dynamics of a bileaflet prosthetic heart valve using a fluid–structure interaction approach". In: *Journal of Biomechanics* 41.11, pp. 2539–2550.

Pouch, A. M. et al. (2013). "Automated segmentation and geometrical modeling of the tricuspid aortic valve in 3d echocardiographic images." In: *Medical image computing and computer-assisted intervention : MICCAI ... International Conference on Medical Image Computing and Computer-Assisted Intervention* 16 (Pt 1), pp. 485–492.

Quicken, S. et al. (2016). "Application of an adaptive polynomial chaos expansion on computationally expensive three-dimensional cardiovascular models for uncertainty quantification and sensitivity analysis". In: *Journal of Biomechanical Engineering* 138.12, p. 121010.

Sacks, J. et al. (1989). "Design and analysis of computer experiments". In: *Statistical Science* 4.4, pp. 409–423.

Spinczyk, D. and A. Krasoń (2018). "Automatic liver segmentation in computed tomography using general-purpose shape modeling methods". In: *BioMedical Engineering OnLine* 17.1.

Suinesiaputra, A. et al. (2018). "Statistical shape modeling of the left ventricle: myocardial infarct classification challenge". In: *Journal of Biomedical and Health Informatics* 22.2, pp. 503–515.

Taylor, C. A. and C. A. Figueroa (2009). "Patient-specific modeling of cardiovascular mechanics". In: *Annual Review of Biomedical Engineering* 11.1, pp. 109–134.

Taylor, C. and J. A. Noble, eds. (2003). *Information processing in medical imaging*. Springer Berlin Heidelberg.

Traeger, B. et al. (2015). "Methodological inaccuracies in clinical aortic valve severity assessment: insights from computational fluid dynamic modeling of CT-derived aortic valve anatomy". In: *Theoretical and Computational Fluid Dynamics* 30.1-2, pp. 107–128.

Uetani, M. et al. (2014). "Statistical shape model of the liver and its application to computer-aided diagnosis of liver cirrhosis". In: *Electrical Engineering in Japan* 190.4, pp. 37–45.

Vergara, C. et al. (2011). "Influence of bicuspid valve geometry on ascending aortic fluid dynamics: a parametric study". In: *Artificial Organs* 36.4, pp. 368–378.

Viana, F. A. C., R. T. Haftka, and V. Steffen (2009). "Multiple surrogates: how cross-validation errors can help us to obtain the best predictor". In: *Structural and Multidisciplinary Optimization* 39.4, pp. 439–457.

Wang, J. and C. Shi (2017). "Automatic construction of statistical shape models using deformable simplex meshes with vector field convolution energy". In: *BioMedical Engineering OnLine* 16.1.

Weese, J. et al. (2017). "CFD- and bernoulli-based pressure drop estimates: a comparison using patient anatomies from heart and aortic valve segmentation of CT images". In: *Medical Physics* 44.6, pp. 2281–2292.

Woo, J. et al. (2016). "A spatio-temporal atlas and statistical model of the tongue during speech from cine-MRI". in: *Computer Methods in Biomechanics and Biomedical Engineering: Imaging & Visualization* 6.5, pp. 520–531.

Xu, F. et al. (2018). "A framework for designing patient-specific bioprosthetic heart valves using immersogeometric fluid-structure interaction analysis". In: *International Journal for Numerical Methods in Biomedical Engineering* 34.4, e2938.

Yates, K. M. and C. D. Untaroiu (2018). "Finite element modeling of the human kidney for probabilistic occupant models: statistical shape analysis and mesh morphing". In: *Journal of Biomechanics* 74, pp. 50–56.

Chapter 4

Sensitivity analysis and uncertainty quantification for transvalvular pressure-drop computations

This chapter is based on: **M.J.M.M. Hoeijmakers**, W. Huberts, M.C.M. Rutten, J. Weese, F.N. van de Vosse. Sensitivity analysis and uncertainty quantification for transvalvular pressure-drop computations. *Submitted*

ABSTRACT

Background Patient-specific image-based computational fluid dynamics (CFD) is widely adopted in the cardiovascular research community to study hemodynamics, and will become increasingly important when moving to personalized medicine. However, these computational models rely on uncertain input data. The flow domain of interest is typically reconstructed (segmented) from magnetic resonance, computed tomography (CT), or echocardiography images. Segmentation of the flow domain is, however, not exact, and some geometric uncertainty in the order of image resolution (0.5–1.0 mm) can be expected. This uncertainty propagates through the computational model, yielding uncertainty in the output parameter of interest. **Aim** In this work we aimed to quantify how geometric uncertainty of the aortic valve may influence the uncertainty in transvalvular pressure-drop computations. **Methods** Electrocardiogram-gated CT images of 74 aortic valves were segmented with a shape-constrained deformable model at peak systole. Statistical shape modeling was used to obtain an approximate parameterization (5 shape modes) of the original segmentations. This parameterization was used to train a meta-model that related the first five shape mode coefficients and flowrate to the transvalvular pressure-drop. Consequently, shape uncertainty in the order of 0.5 and 1.0 mm was emulated by manipulating the patient-specific shape mode coefficients. A global variance-based sensitivity analysis was performed for each of the 74 cases to quantify output uncertainty and to determine relative importance of each of the shape modes. **Results** The first shape mode captured the opening/closing behavior of the valve. Consequently, uncertainty in the first shape mode coefficient accounted for more than 90% of the output variance. However, sensitivity to shape uncertainty is patient-specific as well, and the relative importance of the fourth shape mode coefficient tends to increase with increases in valvular area. **Conclusion** These results show that transvalvular pressure-drop computations by CFD strongly depend on geometry. Uncertainty in the order of voxel size may lead to substantial uncertainty in CFD computed transvalvular pressure-drops. We therefore recommend that the influence of geometric uncertainty is quantified for applications that use image-based CFD models.

4.1 INTRODUCTION

Imaging modalities such as Computed Tomography (CT), Magnetic Resonance Imaging (MRI), and ultrasound are used on a daily basis in the clinic. These imaging modalities are traditionally used to extract diagnostic information directly, e.g., jet-velocity or aortic valve area for patients with suspected aortic valve stenosis (Falk et al. 2017; Baumgartner et al. 2016; Feuchtner et al. 2006). In addition to deriving diagnostic metrics directly, these images may be used to inform image-based computational models, an approach that has become increasingly popular over recent years. With segmentation tools, the complex three-dimensional (3D) patient-specific geometries are readily obtained from these images. Such patient-specific geometries have been extensively used as input to computational fluid dynamics (CFD) models, and can provide detailed pressure and velocity fields in the blood vessel. Applications of image-based CFD models include, amongst others: the estimation of the transvalvular pressure-drop (Hoeijmakers et al. 2020; Traeger et al. 2015); estimation of the significance of coronary lesions (Min et al. 2015; P. D. Morris et al. 2013); quantification of wall shear stresses in carotid arteries (Cibis et al. 2014); hemodynamic evaluation of arteriovenous dialysis grafts (Quicken et al. 2019); or estimating energy losses in intracranial aneurysms (Sen et al. 2014). However, segmentation of the patient-specific geometry is not exact, and uncertainty in the segmented shape is inevitable. Previous CFD studies have demonstrated that uncertainty in shape may substantially affect the outcome of any subsequent modeling (Cherobin et al. 2018; Sankaran et al. 2016; Sen et al. 2014). Segmentation quality is largely determined by image quality, but may also be a consequence of the segmentation method itself. The general procedure to evaluate the performance of a (semi) automatic segmentation method is to compare it to a *ground-truth* segmentation; i.e., a segmentation that is performed or corrected manually by a (clinical) expert. Though these uncertainties in shape will propagate to the output of the CFD model and can have an enormous impact on model-based decisions, output uncertainties are rarely considered, let alone quantified.

Previous studies have demonstrated that differences between automatic and manual segmentation depend on image quality and the geometry of interest. For instance, Ecabert et al. (2011) demonstrated that segmentation from CT images of the heart and surrounding vessels with a shape-constrained deformable model may introduce errors of 0.50–0.82 mm for the heart chambers, and 0.60–1.32 mm for part of the great vessels when compared to manual segmentations. With a similar approach for aortic valve tract segmentation from MRI images, Queirós et al. (2019) observed average errors of 0.54 ± 0.08 mm. The thin and flexible nature of heart valve leaflets arguably makes segmentation of these constructs more difficult. Nevertheless, various authors have proposed algorithms for segmenting heart valves from CT or echocardiography images.

Pouch et al. (2013) used a deformable model to semi-automatically segment the aortic valve from 3D transesophageal echocardiography data, and reported mean and 95^{th} percentile errors of 0.5 ± 0.1 mm and 1.0 ± 0.2 mm compared to manual segmentations. Similarly, Ionasec et al. (2010) performed a validation study of a valve segmentation tool on a data set consisting of 1516 4-D transesophageal and 690 cardiac 4-D CT images. Segmentation errors of 1.54 ± 1.17 and 1.36 ± 0.93 mm were reported for the aortic and mitral valves when using transesophageal electrocardiograms and CT images respectively. Using machine learning, Liang et al. (2016) reported mean discrepancies of 0.69 ± 0.13 mm between automatic and manual aortic valve segmentation from CT images. These contributions demonstrate that segmentation errors are typically in the order of image resolution, i.e., roughly between 0.5 and 1.0 mm with the current *state-of-the-art* hard- and software. Although seemingly small, this inherent geometric uncertainty may substantially affect any subsequent modeling of the detailed flow field.

A small number of studies have demonstrated that uncertainty in shape may substantially affect model output. Sen and colleagues compared three segmentation methods with ground-truth segmentations of 45 intracranial aneurysms, and found that, on average, CFD-computed energy losses and wall shear stresses differed by $23.2\pm8.7\%$ and $24\pm8.5\%$ respectively (Sen et al. 2014). Likewise, studies that aimed to assess coronary stenosis severity identified that geometric uncertainty (lumen diameter) may contribute substantially to uncertainty in hemodynamic simulations (Sankaran et al. 2015; Sankaran et al. 2016; Sturdy et al. 2019; Venugopal et al. 2018). In addition, the work by Sankaran et al. (2015) recognized the value of coronary lumen uncertainty, highlighting regions in the coronary tree where simulation output was sensitive to lumen uncertainty. These studies demonstrate that shape uncertainty may be a major source of error in image-based patient-specific computational models, and should be included in order to strengthen confidence in computational modeling.

In **Chapter 2** we developed a computational framework to compute the transvalvular pressure-drop from CT images by making use of CFD. In addition, we combined statistical shape modeling, meta-modeling, and CFD in order to obtain a cheap-to-evaluate meta-model, which related changes in shape to changes in the transvalvular pressure-drop vs. flow relationship (**Chapter 3**). It was shown, that with a limited number of shape modes, physically relevant geometric variation in the population was captured. However, uncertainties in valvular shape, and consequently in simulation output, were not considered. In this study, we build upon the work of **Chapter 3**, and quantified uncertainty of the transvalvular pressure-drop vs. flow relation to uncertainty in valvular shape. Uncertainty in valvular shape was imposed by assuming uncertainty in the shape mode coefficients. In addition, we performed a variance-based sensitivity analysis to

apportion the output uncertainty to uncertainties in the input (Saltelli et al. 2007).

This chapter is outlined as follows: first a brief introduction to variance-based sensitivity analysis and uncertainty quantification is presented. Second, the available data, statistical shape model, simulation framework, and meta-model are discussed. Third, specific details on how sensitivity analysis and uncertainty quantification was applied is presented. The results of the sensitivity analysis and uncertainty quantification are summarized in the results section. Finally, the discussion puts the findings in an academic and clinical perspective.

4.2 MATERIALS AND METHODS

When reducing output uncertainty of a computational model, sensitivity analysis and uncertainty quantification can be used to assess which parameters contribute most to output uncertainty, and are thus most rewarding to measure or estimate accurately (Saltelli et al. 2007). More specifically, a computational model with p stochastic input factors $\mathbf{Z} = [Z_1, Z_2, ..., Z_p]$ can be represented by an arbitrary function f, which yields an uncertain output Y, i.e.:

$$Y = f(\mathbf{Z}). \tag{4.1}$$

Typically uncertainty in the input parameters $\mathbf{Z}$ are non-negligible, and can considerably affect the uncertainty in model output Y (Eck et al. 2015). Here, a single output variable is considered, but in a similar way, a multivariable output $\mathbf{Y}$ can be analyzed. Sensitivity analysis and uncertainty quantification can be used to quantify the effect of input uncertainties on model output. For instance, by using the variance in Y as a measure for output uncertainty (Saltelli et al. 2007). Global variance-based sensitivity analysis can separate direct contributions of each individual uncertain input Z_i from interactions between different model inputs, e.g., interactions between Z_i and Z_{-i}, where Z_{-i} represents all parameters except Z_i. In variance based sensitivity analysis, the contribution of the uncertain parameters $\mathbf{Z}$ to the variance of Y can be expressed as the main (S_i) and total ($S_{T,i}$) Soboĺ sensitivity indices (Soboĺ 2001):

$$S_i = \frac{\mathbb{V}[\mathbb{E}[Y|Z_i]]}{\mathbb{V}[Y]}, \tag{4.2}$$

$$S_{T,i} = 1 - \frac{\mathbb{V}[\mathbb{E}[Y|Z_{-i}]]}{\mathbb{V}[Y]}, \tag{4.3}$$

where $\mathbb{V}[\cdot]$ and $\mathbb{E}[\cdot]$ are operators for the variance, and expected value respectively. The main indices S_i are measures for the expected reduction in variance when Z_i would be known without uncertainty. Besides the main effects, the total sensitivity index $S_{T,i}$ includes interaction as well, and reflects the contribution of all terms which include Z_i. A low total sensitivity index indicates that this parameter may be fixed within its uncertainty domain. Sensitivity indices may be computed by methods such as Monte Carlo or adaptive sparse generalized Polynomial Chaos Expansion (agPCE) (Blatman and Sudret 2010b; Blatman and Sudret 2010a).

Uncertainties in boundary conditions and shape can have a substantial influence on the output uncertainty of a three-dimensional computational model (Equation 4.1), e.g., due to segmentation errors. In traditional "forward-engineering" CAD models, shape variations are easily introduced by changing the shape-defining parameters, such as angles, diameters, ratios, or thickness (Quicken et al. 2016). However, 3D patient-specific computational models are generally of complex shape, difficult to parameterize, and the influence of shape variation is therefore mostly neglected. Instead of using physically meaningful parameters, this work used statistical shape modeling to parameterize the shape of the valve (**Chapter 3**). The statistical shape modes provided a parameterization of the geometry, and facilitated the training of a meta-model (Figure 4.1a). The meta-model was trained on the output of CFD simulations, and related variations in shape to variations in simulation output. Consequently, this cheap-to-evaluate meta-model was used in a sensitivity analysis and uncertainty quantification framework (Figure 4.1b) for two purposes: 1) to evaluate the importance of shape variation on a population level, and 2) to evaluate the importance of shape variation on the level of an individual patient, and how shape uncertainty affects model output uncertainty for that patient. Sensitivity analysis and uncertainty quantification was applied to aortic valve pressure-drop vs. flow relations, computed with a CFD model. The following sections elaborate on the individual components presented in Figure 4.1.

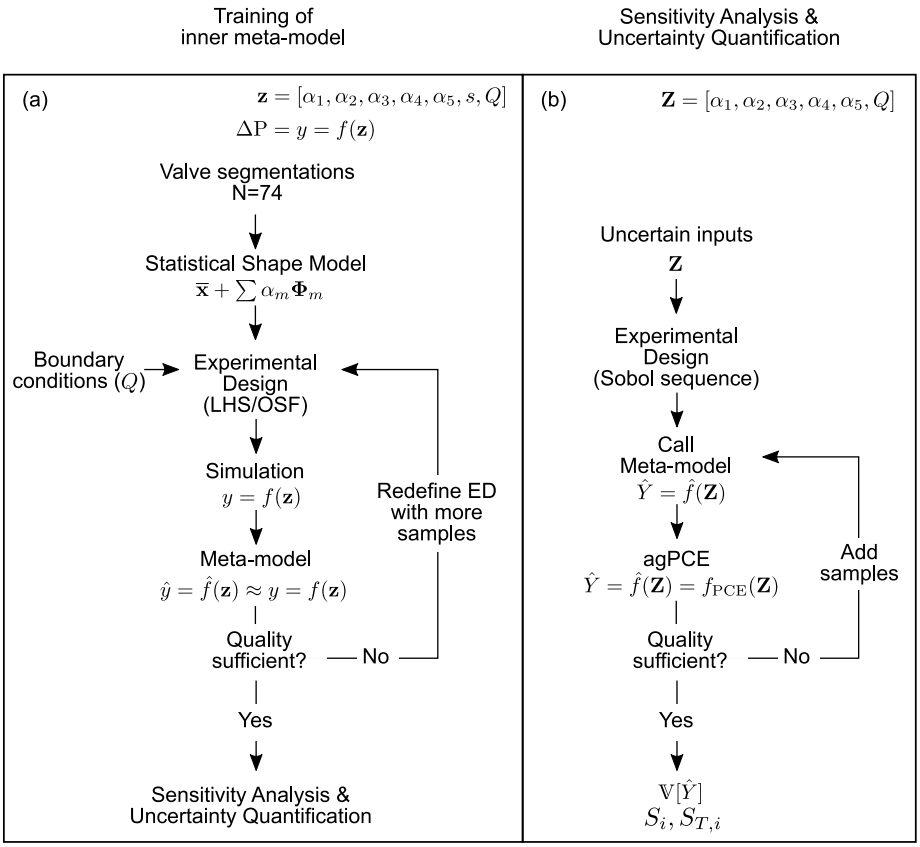

Figure 4.1 Schematic of the procedure for meta-model training (a). An inner meta-model is trained with simulation data, and yields a surrogate function $\hat{f}(z)$ that relates the simulation input (without uncertainties) $\mathbf{z}$ to simulation output y. Note that the meta-model function $\hat{f}(\mathbf{z})$ is an approximation of the original function $f(\mathbf{z})$. (b) the cheap-to-evaluate surrogate function $\hat{f}(\mathbf{z})$ can be used for sensitivity analysis and uncertainty quantification to determine how uncertain inputs $\mathbf{Z}$ propagate to output uncertainty.

4.2.1 INNER META-MODEL TRAINING

4.2.1.1 DATA ACQUISITION AND VALVE SEGMENTATION

Computed Tomography imaging datasets of 74 patients were available, and corresponded to the dataset that was used in **Chapter 3**. Images were acquired with an in-plane spatial resolution of 0.31–0.68 mm, and slice thickness of 0.34–0.70 mm. Images were acquired with Electrocardiography gated CT, and segmentations represented the peak-systolic state of the aortic valve. Consequently, aortic valve segmentation was performed with a Shape Constrained Deformable model framework, see e.g., previous work by

Ecabert et al. (2008), Ecabert et al. (2011), or Weese et al. (2017). In the segmentation framework, a template mesh model was iteratively adapted to an image. From the resulting segmentation mesh, a submesh ($\mathcal{M}$) was extracted that consisted of the left ventricular outflow tract, aortic valve, sinuses, and part of the ascending aorta (Figure 4.2). The submesh $\mathcal{M}$ consisted of $k = 1808$ vertices and 4223 triangular faces, and had a consistent topology ($\mathcal{T}$). This resulted in mesh correspondence between patients. Hence, any surface mesh $\mathcal{M}$ was completely described by the coordinate vector $\mathbf{x}$:

$$\begin{gathered} \mathcal{M} = \mathcal{M}(\mathbf{x}, \mathcal{T}) \\ \text{with:} \\ \mathbf{x} = [x_1, y_1, z_1, x_2, y_2, z_2, ..., x_k, y_k, z_k]^T. \end{gathered} \tag{4.4}$$

4.2.1.2 STATISTICAL SHAPE MODEL

Segmented aortic valves were aligned by a generalized Procrustes analysis (Bookstein 1992), which optimally translated, rotated, and scaled each of the meshes by minimizing the sum of squared errors between the mean and the target mesh. Consequently, statistical shape modeling was used to extract the main directions of shape variance from the 74 segmented aortic valves by performing an eigen-decomposition of the co-variance matrix (principal component analysis), see also **Chapter 3**. The eigenvectors of the co-variance matrix, typically referred to as shape modes, describe the main directions of shape variance. The eigenvalues λ of this eigen-decomposition describe the amount of shape variance that was captured with the corresponding eigenvector.

Using the statistical shape model, any shape in the training set $\mathbf{x}_p$ was then approximated by the mean shape of the training set ($\bar{\mathbf{x}}$) plus a linear combination of a small number of shape modes ($\mathbf{\Phi}_m$), which were weighted by $\alpha_{p,m}$. That is:

$$\mathbf{x}_p \approx \hat{\mathbf{x}}_p = \bar{\mathbf{x}} + \sum_{m=1}^{N_m} \alpha_{p,m} \mathbf{\Phi}_m \qquad p \in \{1, 2, ...N_s\}, \tag{4.5}$$

with N_s the number of shapes that were available in the training set, and N_m the number of shape modes used for the approximation. The optimal set of weights (α_p) for each patient's aortic valve was found by minimizing the difference between the original

segmentation $\mathbf{x}_p$ and the approximation $\hat{\mathbf{x}}_p$:

$$\min_{\alpha_p \in \mathbb{R}^{N_m}} (||(\hat{\mathbf{x}}_p(\alpha_p) - \mathbf{x}_p) \cdot \mathbf{w}||_2). \tag{4.6}$$

The introduction of $\mathbf{w}$ allowed to control the weight of each vertex to the minimization problem, and was chosen such that the 216 vertices that were part of, or adjacent to the free cusp edges weighted five times stronger than all other vertices. This weighting factor was empirically established, and helped to reduce the approximation error of vertices that were part of, or close to the free cusp edges. For a more elaborate explanation the authors would like to refer to the work in **Chapter 3**.

The shape coefficients $\alpha_{p,m}$ can be regarded as a patient-specific parameterization of the aortic valve and surrounding structures, and values for the 74 original valve segmentations were found by Equation 4.6. Besides approximating the surface meshes in the training set, Equation 4.5 was used to generate a population of "virtual" aortic valve geometries that were within three times the square root of the eigenvalue ($[-3\sqrt{\lambda_m}, 3\sqrt{\lambda_m}]$) of its respective shape mode, also see **Chapter 3** or Heimann and Meinzer (2009). Figure 4.2 illustrates the shape variation that was contained in the first five shape modes, and showed that the first shape mode ($\mathbf{\Phi}_1$), weighted by α_1, controlled the opening and closing behavior of the aortic valve. The second shape mode ($\mathbf{\Phi}_2$) stretches the aortic valve construct in axial direction. The third shape mode ($\mathbf{\Phi}_3$) seemed to skew/shear the valve orthogonal to the centerline. The fourth shape mode ($\mathbf{\Phi}_4$) mainly changed the diameter of the sinotubular junction. Finally, the fifth shape mode ($\mathbf{\Phi}_5$) mainly affected the size of the sinuses, and the angle between the left ventricular outflow tract and ascending aorta. Shape variation was extracted by principal component analysis, and as such, the shape modes were ordered from high to low explained shape variance, i.e., ordered with respect to statistical relevance. The first five shape modes captured 61% of the shape variance. However, statistical relevant shape variation may not correspond to physically meaningful shape variation. Hence, a computational fluid dynamics workflow was developed that allowed the computation of the transvalvular pressure-drop, given the boundary conditions (e.g., flow-rate) and valvular shape (any valve realization of Equation 4.5).

4.2.1.3 SIMULATION WORKFLOW

An automated CFD workflow was developed for computing the transvalvular pressure-drop at specified flowrates. To facilitate CFD modeling, the outflow boundary was

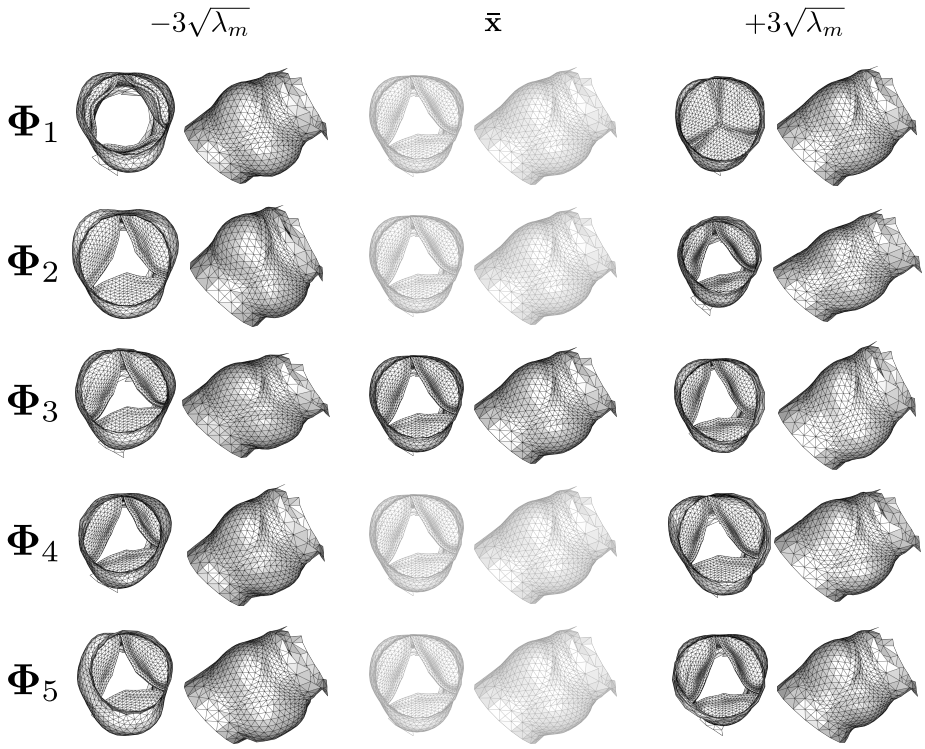

Figure 4.2 Visualization of the first five shape modes. Note that the mean mesh is the same for each realization. $\mathbf{\Phi}_1$ captures variations in the open/closed state of the aortic valve. $\mathbf{\Phi}_2$ elongates the entire valve and its surrounding structures. $\mathbf{\Phi}_3$ seems to skew the geometry orthogonal to the centerline. $\mathbf{\Phi}_4$ mainly affects the diameter of the sinotubular junction. $\mathbf{\Phi}_5$ affects sinus size, and angle between left ventricular outflow tract and the ascending aorta.

extended by 10 diameters. Additionally, the volume enclosed by the surface mesh (Figure 4.2) was discretized by approximately $2 \cdot 10^5 - 3 \cdot 10^5$ polyhedral elements (ANSYS Fluent R18.2, ANSYS Inc., Canonsburg, PA, USA). Edge lengths of the polyhedrals were chosen based on a mesh-sensitivity study, and ranged between 0.15 and 2.0 mm. Blood was modeled as an incompressible Newtonian fluid with a density of 1060 kg/m^3 and dynamic viscosity of 4 mPa·s. At the inflow-boundary (left ventricular outflow tract), a plug-velocity profile was prescribed that corresponded to steady-state volumetric flow-rates between 50 and 650 ml/s. Pressure at the ascending aorta was set to zero, and no-slip boundary conditions were assumed at the walls. Reynolds numbers at the inflow boundary depended on flowrate/shape combination, but were estimated to be between 600 and 13000, hence a Shear Stress Transport $k - \omega$ model (5% turbulent intensity at the inflow boundary) was used to model turbulence (Menter 1994). The governing equations were solved with ANSYS Fluent R18.2 (ANSYS Inc., Canonsburg, PA, USA) by

making use of the Semi-Implicit Method for Pressure Linked Equations. The (recovered) transvalvular pressure-drop was extracted from the simulation results.

4.2.1.4 INNER META-MODEL

A meta-model was trained on the simulation input parameters $\mathbf{z} = [\alpha_1, \alpha_2, \alpha_3, \alpha_4, \alpha_5, s, Q]$ (without uncertainty) and the corresponding output parameter y (the transvalvular pressure-drop). Selecting the most suitable meta-model, and meta-model settings is often difficult since no universal meta-model exists that performs well for all problems. However, it has been shown that ensemble approaches, where a weighted sum of meta-models is considered, can yield a good approximation (Ben Salem and Tomaso 2018; Acar 2010). That is, the goal of an ensemble-type meta-model is to obtain the best weighted-average of a selection of meta-models:

$$\hat{y}_{ens}(\mathbf{z}) = \sum_{i=1}^{N_e} \beta_i \cdot \hat{y}_i(\mathbf{z}), \tag{4.7}$$

where $\hat{y}_{ens}$ is the prediction at $\mathbf{z}$ of the final meta-model, i.e., the weighted ensemble of various meta-models and their settings. To find the optimal combination of meta-models a penalized predictive score was proposed by Ben Salem and Tomaso (2018). This score combined three components (Equation 4.8): (a) optimizing the internal accuracy by evaluating the mean square error on training samples/points ($\mathcal{R}$); (b) use a 10-fold cross-validation to evaluate predictive capability on unseen samples ($\mathcal{R}_{10CV}$) ; and (c) minimize over-fitting of the meta-model by a thin-plate spline Bending Energy Functional (E) (Ben Salem and Tomaso 2018; Duchon 1977). The penalized predictive score was then constructed by weighting the contribution of each of these components:

$$\mathcal{L}(\hat{y}_{ens}) = \underbrace{\gamma_1 \mathcal{R}(\hat{y}_{ens})}_{\text{a}} + \underbrace{\gamma_2 \mathcal{R}_{10CV}(\hat{y}_{ens})}_{\text{b}} + \underbrace{\gamma_3 E(\hat{y}_{ens})}_{\text{c}}. \tag{4.8}$$

In this work the Genetic-Aggregation meta-model of Ben Salem and Tomaso (2018) was used to relate the shape mode coefficients (α_1, α_2,α_3 ,α_4, α_5), a global scaling parameter (s), and the volumetric flow rate (Q) to the CFD-computed transvalvular pressure-drop.

The quality of the meta-model (Equation 4.7) should converge when the number of

training points increases. Hence, the 7-dimensional (5 shape parameters, scaling, and flowrate) input space was uniformly sampled with Latin Hypercube designs (maximin) (M. D. Morris and Mitchell 1995) of 25, 50, 100, 200, 400, 800, 1600, and 3200 samples. Samples were excluded when the transvalvular pressure-drop exceeded 300 mmHg, when the aortic valve was completely closed, or when simulations diverged. On average 26% of the simulation samples were excluded based on these criteria. The input-space for the shape parameters were limited to lie within $[-3\sqrt{\lambda_m}, 3\sqrt{\lambda_m}]$. The scaling parameter was limited to values between 0.8 and 1.25, and volumetric flow-rate between 50 and 650 ml/s. Consequently, the Genetic-Aggregation meta-model was trained on the resulting simulation data. In the remainder of this manuscript, this meta-model will be refered to as the *inner* meta-model (Figure 4.1a).

QUALITY OF THE INNER META-MODEL

Quality of this inner meta-model was evaluated by the root mean square error, relative root mean square error, and the mean absolute percent error. Figure 4.3 demonstrates that errors for the verification samples, which where excluded from training, reduced considerably with an increase in the available training samples. Additionally, Figure 4.3b and c suggest that beyond 1000 samples the quality of the meta-model levels off. The meta-model trained with the most training samples yielded the best quality, and was used as the inner meta-model which facilitated sensitivity analysis and uncertainty quantification (Figure 4.1b).

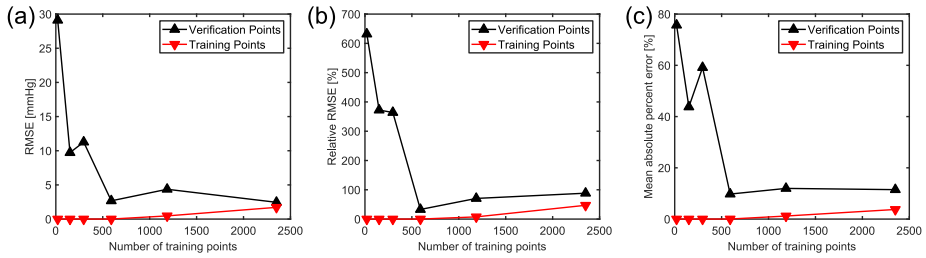

Figure 4.3 Inner meta-model quality as function of the number of successfully simulated training samples. An increase in available training samples improves the root mean square error (RMSE), relative root mean square error (rRMSE) and the mean absolute percent error (MAPE) between the meta-model and verification points which were not used for training the meta-model

4.2.2 SENSITIVITY ANALYSIS AND UNCERTAINTY QUANTIFICATION

Changes in boundary conditions and shape affect the CFD-computed transvalvular pressure drop. In order to quantify the sensitivity of the transvalvular pressure-drop to

changes in shape, main and total sensitivity indices (see Equation 4.2 and Equation 4.3) were obtained by the agPCE method (Quicken et al. 2016; Blatman and Sudret 2010b). The method uses polynomial chaos expansion in order to obtain an explicit formulation of f (Equation 4.1), and expands the stochastic model output Y into a series of orthogonal polynomials (Quicken et al. 2016). The generalized polynomial chaos expansion is defined as:

$$Y = f(\mathbf{Z}) \approx f_{\text{gPCE}}(\mathbf{Z}) = \sum_{j=1}^{N_p} c_j \Psi_j(\mathbf{Z}). \tag{4.9}$$

Where $\Psi_j(\mathbf{Z})$ represents the polynomials and c_j represents the expansion coefficients. An adaptive algorithm (agPCE) was used to include only the polynomials that significantly increased meta-model quality (Quicken et al. 2016). This kept meta-model quality high, while keeping the required training set small. Sensitivity indices were analytically derived from this expansion (Sudret 2008; Quicken et al. 2016). Quality of this "outer" meta-model was evaluated with a leave-one-out cross-validation coefficient ($\mathbb{Q}^2$). $\mathbb{Q}^2$ ranges between 0 (lowest quality) and 1 (highest quality), and it has been shown that with increasing $\mathbb{Q}^2$ sensitivity indices convergence (Quicken et al. 2016). For this study, Legendre polynomials — which are most suitable for uniform distributions — up to order 3 were considered.

POPULATION-BASED SENSITIVITY

A global variance-based sensitivity analysis was performed in order to determine the sensitivity of the transvalvular pressure-drop to changes in shape mode coefficients and flow rate. The lower and upper limits of each of the the shape mode coefficients were restricted to $-2\sqrt{\lambda_m}$ and $2\sqrt{\lambda_m}$ respectively. This range covered a wide range of feasible shapes in the population, whilst avoiding the corners of the input domain where meta-model results were likely poor. Uncertainties in flow-rate were based on the work by Namasivayam et al. (2020), who measured the average systolic flow rate in 1131 patients with severe or moderate aortic stenosis, and found mean systolic flow rates of 243 ± 42 ml/s. It was assumed that systolic flow approximately follows a sine squared profile, hence mean-systolic values were multiplied by two to obtain peak systolic flow. This resulted in a peak-systolic lower limit of 382 ml/s and upper limit of 590 ml/s in flow uncertainty. The distribution of the input uncertainties were unknown, hence a uniform distribution was assumed for all input parameters, which can be considered a conservative estimate of the uncertainty distribution.

Table 4.1 Patient-based parameter uncertainties for sensitivity analysis and uncertainty quantification

Parameter	Symbol	$\frac{\partial \epsilon_{max}}{\partial \alpha_m}$ $[mm/\alpha]^{\dagger}$	$\frac{\partial \overline{\epsilon}}{\partial \alpha_m}$ $[mm/\alpha]^{\ddagger}$	Minimum	Maximum	Assumed change in α_m
Shape mode	α_1	85	17	$\alpha_{p,1} - 0.018 \cdot 6\sqrt{\lambda_1}$	$\alpha_{p,1} + 0.018 \cdot 6\sqrt{\lambda_1}$	3.6% of $6\sqrt{\lambda_1}$
Shape mode	α_2	76	21	$\alpha_{p,2} - 0.025 \cdot 6\sqrt{\lambda_2}$	$\alpha_{p,2} + 0.025 \cdot 6\sqrt{\lambda_2}$	5.0% of $6\sqrt{\lambda_2}$
Shape mode	α_3	58	22	$\alpha_{p,3} - 0.039 \cdot 6\sqrt{\lambda_3}$	$\alpha_{p,3} + 0.039 \cdot 6\sqrt{\lambda_3}$	7.8% of $6\sqrt{\lambda_3}$
Shape mode	α_4	79	21	$\alpha_{p,4} - 0.035 \cdot 6\sqrt{\lambda_4}$	$\alpha_{p,4} + 0.035 \cdot 6\sqrt{\lambda_4}$	7.0% of $6\sqrt{\lambda_4}$
Shape mode	α_5	84	21	$\alpha_{p,5} - 0.035 \cdot 6\sqrt{\lambda_5}$	$\alpha_{p,5} + 0.035 \cdot 6\sqrt{\lambda_5}$	7.0% of $6\sqrt{\lambda_5}$

Note that with these parameters any shape variation is defined with respect to the patient-specific shape $\hat{\mathbf{x}}_p$ found by Equation 4.5, and these values of uncertainty were calibrated to emulate a maximum (ϵ_{max}) shape variation of 0.5 mm. $\epsilon_{max} = 1.0$ mm was obtained by multiplying these values by 2.

† Partial derivative indicating the maximum displacement that is observed with a unit-change in that particular shape mode coefficient. The region where vertex displacement is maximum is illustrated — per shape mode — in Figure 4.4.

‡ Partial derivative indicating the mean displacement of all vertices in the mesh with a change in that particular shape mode coefficient

PATIENT-BASED SENSITIVITY ANALYSIS AND UNCERTAINTY QUANTIFICATION

In addition to a global variance-based population sensitivity analysis, an additional sensitivity analysis was performed for each patient separately. Recall that each individual segmentation was approximated by Equation 4.5 ($N_m = 5$). With variations in these shape-mode coefficients, uncertainty in shape can be emulated. That is, the original segmentations were not exact, and some uncertainty with respect to the actual *in-vivo* geometry is expected.

Previous studies that used deformable model-based segmentation frameworks have demonstrated that segmentation errors are in the order of voxel size (Ecabert et al. 2011; Pouch et al. 2013). Hence, it is assumed that local uncertainty in shape is between 0.5 and 1.0 mm. This shape uncertainty may be imposed by introducing variations in the shape mode coefficients. That is, any change in α_m leads to (localized) changes in vertex positions in a particular direction (Figure 4.4). The maximum ($\partial \epsilon_{max}/\partial \alpha_m$) and mean ($\partial \overline{\epsilon}/\partial \alpha_m$) rate of change with respect to α_m was obtained from the mean mesh and shape modes numerically (using Equation 4.5), and depends on the specific shape mode, see Table 4.1 and Figure 4.4. Uncertainty in shape mode coefficients were calibrated to impose a maximum (ϵ_{max}) vertex-to-vertex displacement of 0.5 and 1.0 mm, which were considered in separate analyses. Figure 4.4 specifies shape uncertainty per shape mode when imposing an uncertainty of 0.5 mm. This resulted in patient-specific uncertainty ranges, and is in Table 4.1 expressed as a percentage of the total feasible range ($6\sqrt{\lambda_m}$). Only shape changes were of interest, and volumetric flow-rate was fixed and uncertainty in the scaling parameter was neglected. The uncertainties in Table 4.1 were applied to

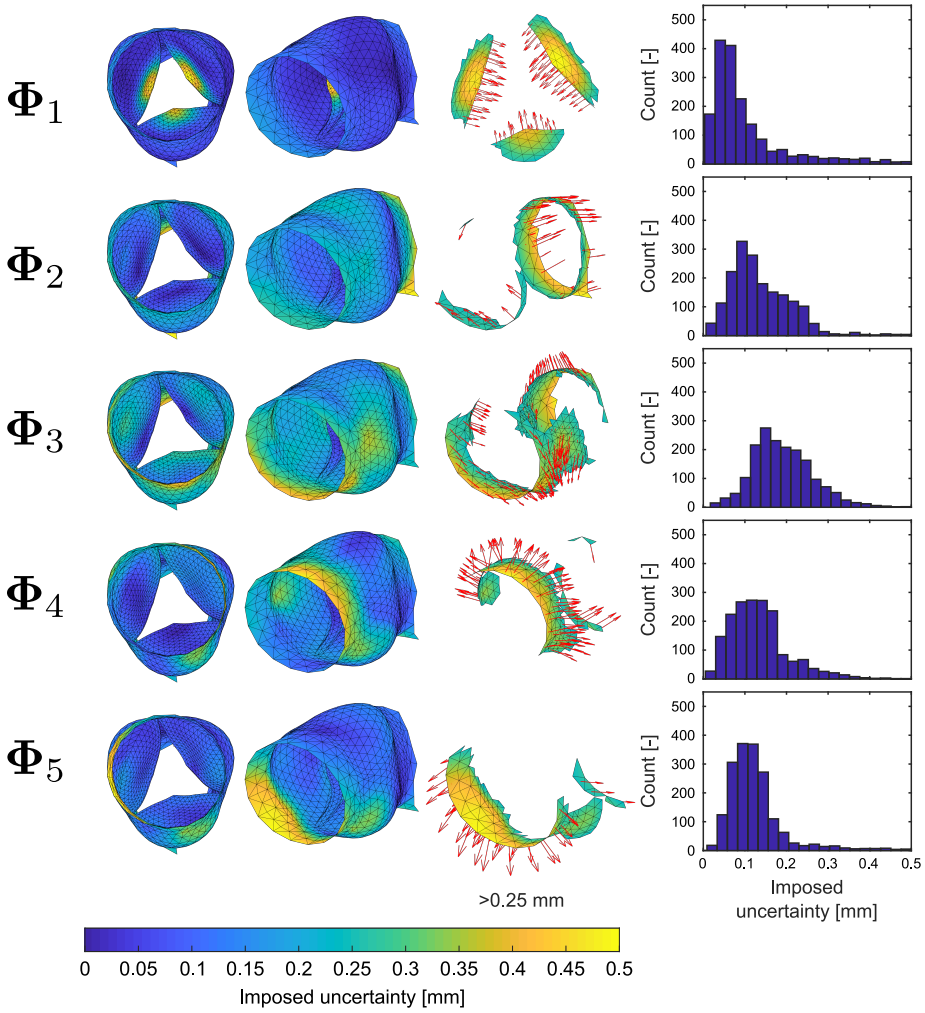

Figure 4.4 Resulting uncertainty in vertex-to-vertex position (mapped onto $\bar{\mathbf{x}}$) by introducing a 0.5 mm uncertainty by considering uncertainty in the shape mode coefficients (Table 4.1). Each shape mode introduces variation in a specific part of the surface model (first and second column) and in a particular direction (third column). The histogram illustrates how uncertainty in vertex position was distributed over all 1808 vertices for each shape mode.

each patient, and using the agPCE algorithm, the patient-specific sensitivity indices were computed. Exploratory Monte-Carlo simulations (all cases, 0.5 mm uncertainty, flowrate 400 ml/s, 500,000 samples per case) demonstrated that the distribution was different for each case, where stenotic cases generally showed more skewed output distributions.

Hence, boxplots were used to visualize uncertainty in the transvalvular pressure-drop vs. flow relation. Boxplots (min, max, 25, 50, and 75th percentiles) were constructed by making use of the samples (typically around 40) that were used to build the agPCE meta-model of highest $\mathbb{Q}^2$. Due to the low-discrepancy Soboĺ sequence sampling of the uncertain input space around each patient, it was assumed that boxplots of the agPCE samples were representative of the expected output distribution.

4.3 RESULTS

Table 4.2 Main and total sensitivity indices of the global population-based sensitivity analysis

Parameter	Symbol	S_i †	S_i Range‡	$S_{T,i}$ †	$S_{T,i}$ Range‡
Shape mode	α_1	**0.930**	**[0.900 – 0.937]**	**0.953**	**[0.900 – 0.955]**
Shape mode	α_2	0.010	[0.009 – 0.012]	0.016	[0.010 – 0.018]
Shape mode	α_3	0.011	[0.003 – 0.011]	0.018	[0.003 – 0.020]
Shape mode	α_4	0.000	[0.000 – 0.004]	0.001	[0.001 – 0.004]
Shape mode	α_5	0.010	[0.008 – 0.017]	0.018	[0.012 – 0.020]
Flow-rate	Q	0.016	[0.015 – 0.067]	0.018	[0.018 – 0.067]

† Sensitivity index obtained from the outer meta-model (agPCE) with highest $\mathbb{Q}^2$ ($\mathbb{Q}^2 = 0.9998$).
‡ Range of sensitivity indices considering all generated meta-models irrespective of $\mathbb{Q}^2$

Main and total sensitivity indices S_i and $S_{T,i}$ of the population-based sensitivity analysis are depicted in Table 4.2. The outer agPCE meta-model with highest quality reached a $\mathbb{Q}^2$ of 0.9998, which can be considered excellent quality. Results of this high-quality outer meta-model are summarized in Table 4.2, and suggest that the transvalvular pressure-drop is most sensitive to changes in the first shape mode (open/closure of the aortic valve). 93% of the output variance was explained by variations in this input parameter ($S_i = 0.930$, $S_{T,i} = 0.953$). Contribution of shape modes $\mathbf{\Phi}_2$ ($S_i = 0.010$, $S_{T,i} = 0.016$), $\mathbf{\Phi}_3$ ($S_i = 0.011$, $S_{T,i} = 0.018$), and $\mathbf{\Phi}_5$ ($S_i = 0.10$, $S_{T,i} = 0.018$) to the output variance was limited to around 1 – 2%. Although shape mode $\mathbf{\Phi}_4$ was ranked higher statistically compared to $\mathbf{\Phi}_5$, variation in α_4 did not contribute to the output variance ($S_i = 0.000$, $S_{T,i} = 0.001$). Hence, shape variation in the direction of shape mode $\mathbf{\Phi}_4$ seemed unimportant from a population perspective. Flow-rate is another contributing factor, but only accounted for 1.6% of the total output variance ($S_i = 0.016$, $S_{T,i} = 0.018$). Total sensitivity indices $S_{T,i}$ suggest that limited interaction was present between shape modes and/or flow-rate. Additionally, the total sensitivity index of α_4 remained approximately zero.

The global population-based sensitivity analysis suggests that α_4 does not contribute to

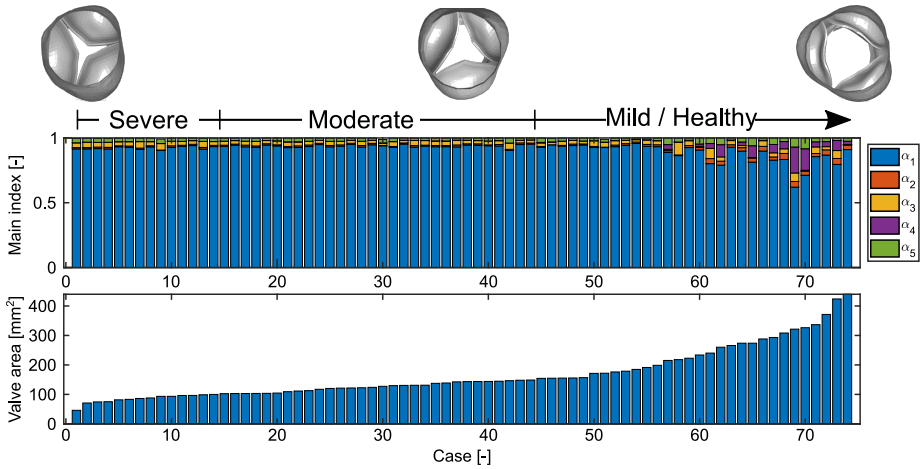

Figure 4.5 Sensitivity indices per case, given the uncertainty in the shape mode coefficients of Table 4.1. Results are sorted from small to large geometric valve area (bottom graph). With an increase in valvular area, variation in other shape modes start to have a substantial effect on the transvalvular pressure-drop. Classification according to the basic grading criteria of Baumgartner et al. (2016). Severe: valve area < 100 mm^2; moderate: valve area 100–150 mm^2; mild/healthy: valve area >150 mm^2.

the output variance, and may thus be fixed. This is partially supported by the results of the patient-based sensitivity analysis. Patient-based sensitivity indices (in order of increasing aortic valve area) are illustrated in Figure 4.5. Uncertainty in the first shape mode coefficient α_1 accounted for more than 90% of the the output variance for severely and moderately stenotic heart valves (Figure 4.5). Additionally, Figure 4.5 suggests that the remaining output variance for these two subgroups was mostly explained by uncertainty in α_3 and α_5. Similar to the observations of the population-based sensitivity analysis, uncertainty in α_4 seemed to play a minor role for severely and moderately stenotic valves. Interestingly, main sensitivity indices seem to strongly depend on valvular area. That is, importance of α_1 decreased, whereas importance of α_4 tended to increase for more open valves, and actually even exceeded that of α_3 and α_5 (e.g., see main indices of cases 69: $S_{\alpha_4} = 0.2$ and 70: $S_{\alpha_4} = 0.17$).

Besides the main and total sensitivity indices, samples that were used to construct the agPCE model were used to construct boxplots around the meta-model results. These boxplots provide and estimate for uncertainty in the transvalvular pressure-drop vs. flow relation for each case. In Figure 4.6 the transvalvular pressure-drop vs. flow curves of a typical stenotic, moderate, and mild/healthy case are enhanced with these boxplots, given an imposed uncertainty of 0.5 and 1.0 mm (Table 4.1). Figure 4.6 exposes that the uncertainty in output was considerable when uncertainties of 0.5 and 1.0 mm were imposed. For example, for Case 7 (severe aortic valve stenosis; valve area 86 mm^2), the

inner meta-model gives a transvalvular pressure-drop of 69 mmHg at 400 ml/s. However, interquartile ranges (Q3–Q1) were 74–63 (median: 68, min-max: 55–84) mmHg and 82–58 (median: 68, min-max: 44–105) mmHg for imposed uncertainties of 0.5 and 1.0 mm respectively. Case 38 (moderately stenotic), the inner meta-model yields a transvalvular pressure-drop of 25 mmHg with interquartile ranges of 26–23 (median: 25, min-max: 21–29) mmHg and 28–21 (median: 24, 17–34) mmHg, for imposed uncertainties of 0.5 and 1.0 mm respectively. Finally, for Case 73 (healthy), uncertainty seems to deteriorate in a relative sense. That is, the inner-meta model yielded a transvalvular pressure-drop of 0.6 mmHg with interquartile ranges of 0.6–0.5 mmHg (median: 0.6, min-max: 0.4–0.7), and 0.7–0.4 (median: 0.5, min-max 0.2–0.9) mmHg for imposed uncertainties of 0.5 and 1.0 mm respectfully. Transvalvular pressure-drop vs. flow relations and uncertainties for all cases can be found in Figure 4.7 – 4.9 of the appendix. These results clearly demonstrate that with small deviations in geometry, e.g., in the direction of the first shape mode, the uncertainty in the output of the model can become substantial.

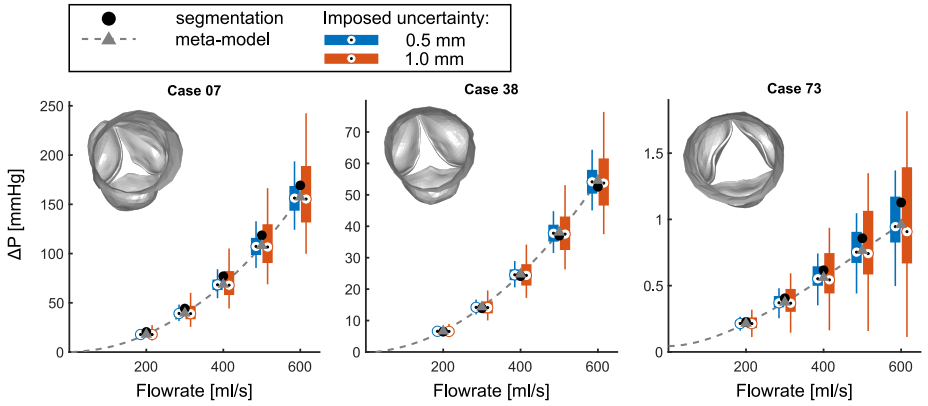

Figure 4.6 Transvalvular pressure-drop vs. flow curves for a typical severely stenotic (left), moderately stenotic (middle), and mildly stenotic/healthly (right) aortic valve. Filled circles represent the CFD results on the original segmentation mesh $\mathcal{M}(\mathbf{x}_p, \mathcal{T})$. Results of the inner meta-model (dashed line with triangles) are augmented with boxplots. Boxplots of imposed uncertainties of 0.5 mm (blue) and 1.0 mm (red) are depicted.

4.4 DISCUSSION

The aim of this study was to quantify how sensitive transvalvular pressure-drop computations were to uncertainty in valvular shape. Two sensitivity analyses were done. First, a global variance-based population-level sensitivity analysis was performed, and the main and total sensitivity indices were extracted. This revealed that uncertainty in the weighting of $\mathbf{\Phi}_1$ was most important, accounting for 93% of the expected variance. The main indices of α_2, α_3, and α_5 were low, suggesting limited importance of uncertainty in the

direction of shape modes $\mathbf{\Phi}_2$, $\mathbf{\Phi}_3$, and $\mathbf{\Phi}_5$. Similarly, the contribution of volumetric flow rate Q to output uncertainty was low and may be fixed in the range that was considered. We would like to note that Q may however become important again when uncertainty in valvular shape is substantially reduced. In addition, the total sensitivity indices of α_4 suggest that geometric changes in the direction of shape mode $\mathbf{\Phi}_4$ were unimportant.

Secondly, uncertainties in patient-specific valvular shape were imposed by considering uncertainty in shape mode coefficients. In this approach, we introduced an uncertainty in shape mode coefficients that corresponds to likely segmentation errors of up to 0.5 and 1.0 mm. With this we were able to emulate geometric uncertainties, and study how this propagated through to patient-specific pressure-drop vs. flow relationship. The results of this sensitivity analysis partly corroborate the population-based sensitivity analysis. However, main sensitivity indices from the patient-based sensitivity analysis demonstrate that the importance of shape variation is in fact patient-specific. More specifically, for severely stenotic and moderately stenotic cases, sensitivity indices roughly correspond to the indices found with the population-based analysis, i.e., uncertainty in α_1 seems most important ($S_{\alpha_1} > 0.9$). However, Figure 4.5 also shows that geometric uncertainty in the direction of the other shape modes tended to become more important with an increase in valvular area. The results from the population-based sensitivity may therefore not be representative for the entire spectrum of valve configurations.

Shape mode $\mathbf{\Phi}_1$ captures valve opening and closing, and naturally would have the most substantial effect on the computed transvalvular pressure-drop. That is, a change in the weighting of $\mathbf{\Phi}_1$ leads to a change in valvular area, and as a consequence the predicted transvalvular pressure-drop changes. Additionally, it was shown that errors in the direction of $\mathbf{\Phi}_1$ which are in the order of voxel size can lead to substantial uncertainty in the transvalvular pressure-drop. This suggest that accurate segmentation of the free cusp edge of the aortic valve could substantially reduce uncertainty in the computed transvalvular pressure-drop vs. flow relationship.

The direction of $\mathbf{\Phi}_4$ and $\mathbf{\Phi}_5$ seem to correspond with changes in ascending aorta diameter. The observation that the (recovered) transvalvular pressure-drop becomes more sensitive to changes in $\mathbf{\Phi}_4$ and $\mathbf{\Phi}_5$ with an increase in valvular area may be explained by pressure-recovery. That is, when blood is accelerated into the narrow orifice, pressure decreases. Consequently, downstream from the aortic valve flow decelerates again, and pressure is (partly) recovered (Laskey and Kussmaul 1994; Voelker et al. 1992; Bahlmann et al. 2010; Yoganathan et al. 1988). When the cross sectional area of the ascending aorta is large, more kinetic energy will be converted back to pressure. When the aortic valve is fully open (e.g., when healthy) the net transvalvular pressure-drop is small. As a consequence,

the relative importance of uncertainties in ascending aorta diameter ($\mathbf{\Phi}_4$ and $\mathbf{\Phi}_5$) will increase compared to moderately or severely stenotic cases. Nevertheless, uncertainty in α_1 is still most important, and accounts for at least 60% of output variance (e.g., see Case 69). Additionally, it is observed that for severely and moderately stenotic valves S_{α_3} and S_{α_5} generally exceed S_{α_2}. These observations indicate that geometrical variation that is statistically relevant, may not necessarily be relevant from a fluid mechanics perspective. This is supported by the work of Wu et al. (2017), who used statistical shape modeling to introduce global deformation modes to emulate airfoil geometric uncertainty. It was shown that deformation (shape) modes of lower statistical relevance can in fact be more important for transonic aerodynamic lift and drag coefficients than modes of higher statistical relevance.

Available literature shows that statistical shape modeling is a technique that has been applied for numerous applications. Some examples in the bio-medical field include, organ segmentation (Yates and Untaroiu 2018; Spinczyk and Krasoń 2018; Woo et al. 2016) and extraction of morphology from medical images (Suinesiaputra et al. 2018; Uetani et al. 2014; Bruse et al. 2016). Only a limited number of studies have tried to combine statistical shape modeling with computational models, and are mainly found for orthopedic applications. For example, statistical shape models have been used for real-time prediction of knee joint mechanics (Gibbons et al. 2019), predicting femur bone strength (Nicolella and Bredbenner 2012), or creating parametric models to model cervical spine loading (Bredbenner et al. 2014). The study by Bredbenner et al. (2014) introduced uncertainty in geometry considering cervical spines that were $\pm 1\sigma$ from the mean shape, and showed that shape variation influenced the computed axial, flexion-extension, and lateral displacements. However, sensitivity indices were not explicitly computed, and only variations from the mean shape were considered. The work by Khalafvand et al. (2018) studied the influence of shape variation on intraventricular flow variables, such as wall shear stress, vortex formation time, and the time integral of energy dissipation, but did not compute sensitivity indices of the simulation output parameters. In this study we have demonstrated that besides the accepted applications, statistical shape modeling in combination with computational modeling can also be used to determine physically relevant shape variation. Moreover, we have shown that this approach may be used to estimate how shape uncertainty affects uncertainty in the output of the computational model.

Image-based CFD models often include complex anatomical shapes. Some examples of computational models of complex shapes include: the aortic tree (Reymond et al. 2012) coronary tree (P. D. Morris et al. 2013), or lungs (Backer et al. 2010). Similar to valve geometries, these shapes are difficult to parameterize, and as such investigating how

shape uncertainty affects the results is challenging. Sankaran et al. (2015) resolved this by splitting the coronary tree into sections, and exploring the solution in a family of probable geometries with an assumed uncertainty in radius of 0.3 mm. Similar to our approach, Sankaran et al. (2015) used a a surrogate (meta) model based on machine learning to replace the compute-intensive blood flow simulations. This demonstrates that meta-models, which learn the relation between physics and shape, will be crucial for uncertainty quantification.

4.4.1 LIMITATIONS

The Shape Constrained Deformable Model framework is yet to be validated for aortic valve segmentations, and imposed uncertainties were therefore hypothetical. Nevertheless, uncertainties of 0.5 and 1.0 mm seem plausible based on existing literature (Ecabert et al. 2011; Queirós et al. 2019; Pouch et al. 2013; Ionasec et al. 2010; Liang et al. 2016). The shape modes inherently depend on the data-set. As a consequence, precise control over local shape variation was not possible with the method that was proposed. These limitations would however not change our conclusion that uncertainty in geometry and simulation output needs to be considered, and preferably quantified for image-based computational models.

The *inner* meta-model relates variations in shape modes (weighted by the shape coefficients) and flow rate to the transvalvular pressure-drop. A small number of shape modes was used, and yielded an approximation of the original segmentation. Likewise, the *inner* meta-model, relating shape coefficients to the transvalvular pressure-drop, is an approximation of the transvalvular pressure vs. flow relationship as well. Figure 4.7–4.9 demonstrate that for most cases the meta-model adequately approximates this relationship. However, for some cases in Subgroup C (healthy), this method seems to break down. That is, training of the inner meta-model seemed insufficient, or the five shape modes did not seem to adequately capture the features that were relevant for the transvalvular pressure-drop vs. flow relationship.

The agPCE method is a variance-based sensitivity method. This assumes that variance can fully capture the uncertainty in the output parameter. However, this may be inappropriate when the output distribution is skewed or multi-modal (Pianosi et al. 2016). Hence, the sensitivity indices (Figure 4.5) may not be appropriate for all cases. An exploratory Monte-Carlo simulation with the uncertainty ranges in Table 4.1 demonstrated that for healthy cases the distribution in transvalvular pressure-drop followed a normal distribution, and variance is an appropriate statistical measure. However, for moderately stenotic cases, the distribution became lightly left-skewed. Furthermore, it was observed that

left-skewness (tendency towards a lower transvalvular pressure-drop) increased with an increase in stenosis severity. Hence, variance-based methods for sensitivity analysis may not be ideal in all circumstances. Density based methods which characterize the output distribution by the cumulative density function, may in those cases be more appropriate, and should be considered in future work (Pianosi and Wagener 2015).

In line with **Chapter 3**, the transvalvular pressure-drop at peak systole was approximated by the CFD simulations, and expressed as an uncertain scalar parameter Y. *In-vivo* however, the transvalvular pressure-drop would strongly vary throughout the cardiac cycle due to flow pulsatility. Hence, the current approach could be expanded to include uncertainty in the transvalvular pressure-drop over time. This would require computationally more demanding pulsatile simulations. Moreover, Y would need to be expanded to an uncertain vector $\mathbf{Y}$ that captures temporal variation.

4.4.2 CONCLUSION

We have developed a method for sensitivity analysis and uncertainty quantification for transvalvular pressure-drop vs. flow relationships. This method assumes that physically relevant shape variation can be adequately captured with a statistical shape model. Consequently, a meta-model that is trained on a limited number of these shape modes can be used to quantify how geometric uncertainty affects the transvalvular pressure-drop computations. With this method we have demonstrated that geometric uncertainties in the order of voxel size may in fact strongly influence transvalvular pressure-drop predictions by image-based CFD. Hence, we recommend that the influence of geometric uncertainty is quantified for applications that rely on image-based CFD models.

APPENDIX

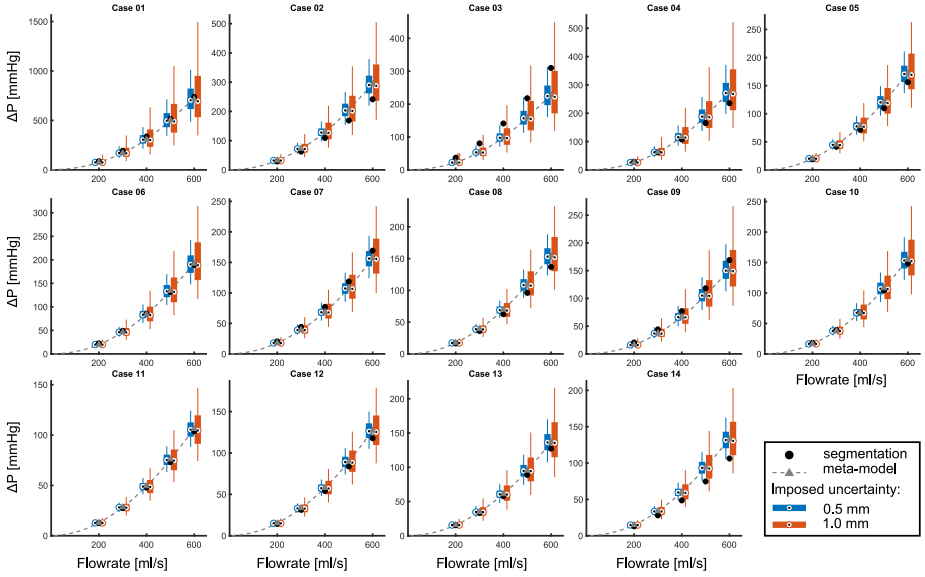

Figure 4.7 Volumetric flow-rate vs. transvalvular pressure-drop curves for subgroup A: valve opening area < 100 mm^2. Filled circles represent the CFD results on the original segmentation mesh $\mathcal{M}(\mathbf{x}_p, \mathcal{T})$. Results of the inner meta-model (dashed line with triangles) are augmented with boxplots. Boxplots of imposed uncertainties of 0.5 mm (blue) and 1.0 mm (red) are depicted.

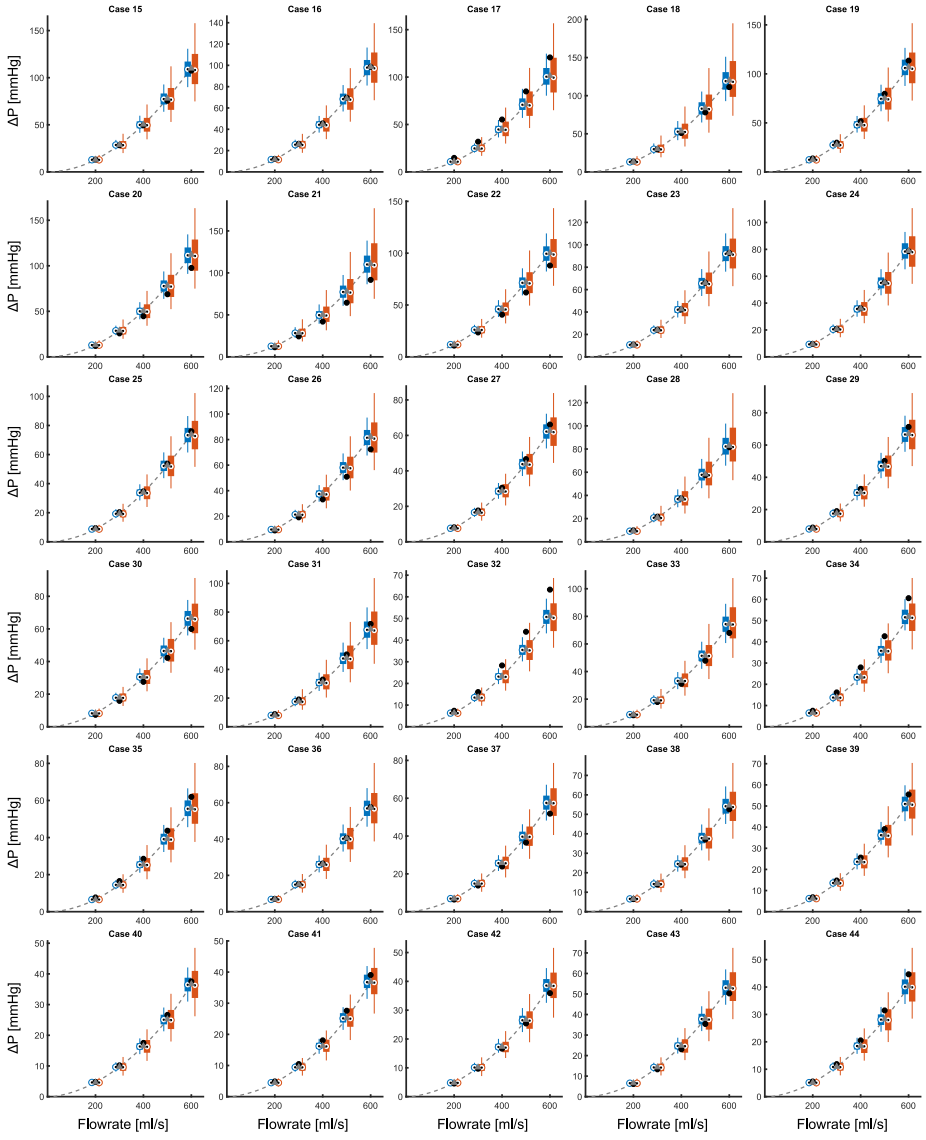

Figure 4.8 Volumetric flow-rate vs. transvalvular pressure-drop curves for subgroup B: valve opening area 100–150 mm^2. Results of the inner meta-model (dashed line with triangles) are augmented with boxplots. Boxplots of imposed uncertainties of 0.5 mm (blue) and 1.0 mm (red) are depicted.

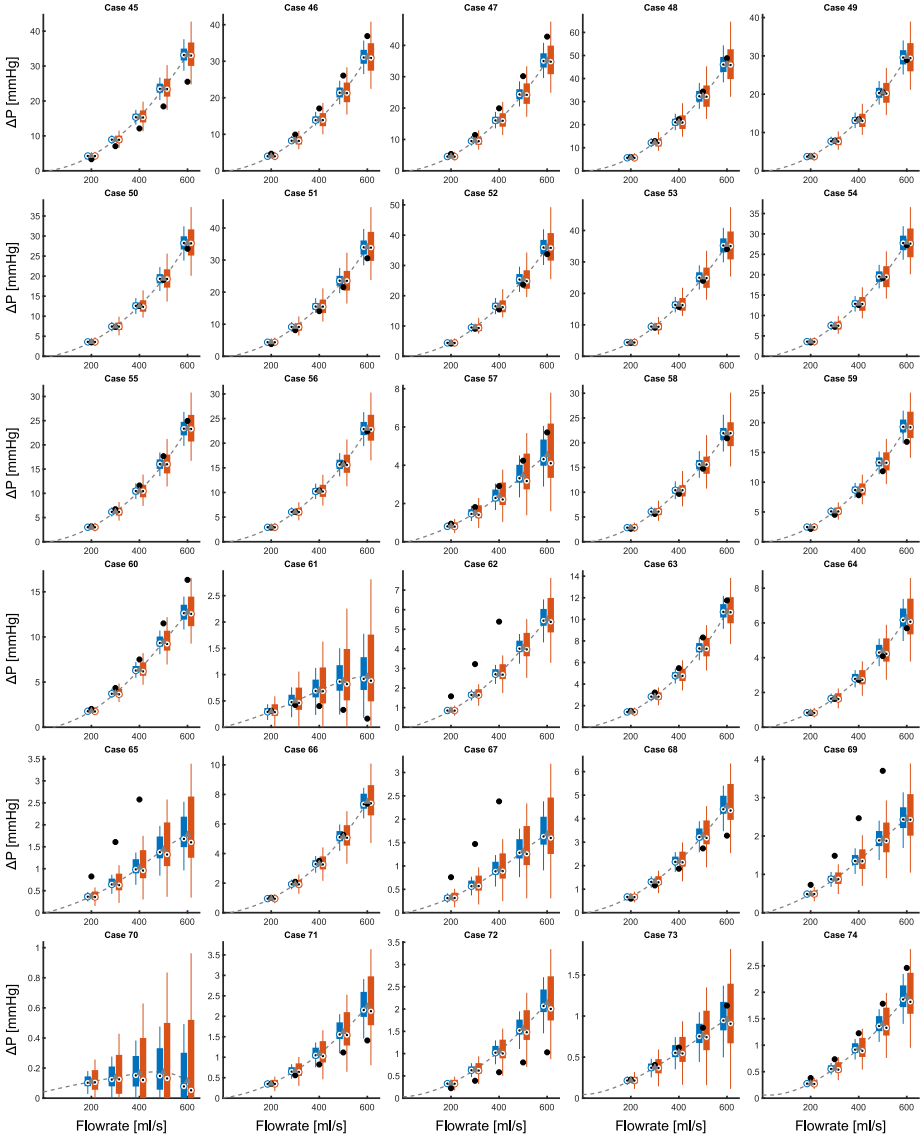

Figure 4.9 Volumetric flow-rate vs. transvalvular pressure-drop curves for subgroup C: valve opening area >150 mm^2. Results of the inner meta-model (dashed line with triangles) are augmented with boxplots. Boxplots of imposed uncertainties of 0.5 mm (blue) and 1.0 mm (red) are depicted.

BIBLIOGRAPHY

Acar, E. (2010). "Various approaches for constructing an ensemble of metamodels using local measures". In: *Structural and Multidisciplinary Optimization* 42.6, pp. 879–896.

Backer, J. W. D. et al. (2010). "Validation of computational fluid dynamics in CT-based airway models with SPECT/CT". in: *Radiology* 257.3, pp. 854–862.

Bahlmann, E. et al. (2010). "Impact of pressure recovery on echocardiographic assessment of asymptomatic aortic stenosis: a SEAS substudy". In: *JACC: Cardiovascular Imaging* 3.6, pp. 555–562.

Baumgartner, H. et al. (2016). "Recommendations on the echocardiographic assessment of aortic valve stenosis: a focused update from the european association of cardiovascular imaging and the american society of echocardiography". In: *European Heart Journal - Cardiovascular Imaging* 18.3, pp. 254–275.

Ben Salem, M. and L. Tomaso (2018). "Automatic selection for general surrogate models". In: *Structural and Multidisciplinary Optimization* 58.2, pp. 719–734.

Blatman, G. and B. Sudret (2010a). "Efficient computation of global sensitivity indices using sparse polynomial chaos expansions". In: *Reliability Engineering & System Safety* 95.11, pp. 1216–1229.

Blatman, G. and B. Sudret (2010b). "An adaptive algorithm to build up sparse polynomial chaos expansions for stochastic finite element analysis". In: *Probabilistic Engineering Mechanics* 25.2, pp. 183–197.

Bookstein, F. L. (1992). *Morphometric tools for landmark data*. Cambridge University Press.

Bredbenner, T. L. et al. (2014). "Development and validation of a statistical shape modeling-based finite element model of the cervical spine under low-level multiple direction loading conditions". In: *Frontiers in Bioengineering and Biotechnology* 2.

Bruse, J. L. et al. (2016). "A statistical shape modelling framework to extract 3d shape biomarkers from medical imaging data: assessing arch morphology of repaired coarctation of the aorta". In: *BMC Medical Imaging* 16.1.

Cherobin, G. B. et al. (2018). "Sensitivity of nasal airflow variables computed via computational fluid dynamics to the computed tomography segmentation threshold". en. In: *PLOS ONE* 13.11, e0207178.

Cibis, M. et al. (2014). "Wall shear stress calculations based on 3d cine phase contrast MRI and computational fluid dynamics: a comparison study in healthy carotid arteries". In: *NMR in Biomedicine* 27.7, pp. 826–834.

Duchon, J. (1977). "Splines minimizing rotation-invariant semi-norms in sobolev spaces". In: *Constructive Theory of Functions of Several Variables*. Ed. by W. Schempp and K. Zeller. . Berlin, Heidelberg: Springer Berlin Heidelberg, pp. 85–100.

Ecabert, O. et al. (2008). "Automatic model-based segmentation of the heart in CT images". In: *IEEE Transactions on Medical Imaging* 27.9, pp. 1189–1201.

Ecabert, O. et al. (2011). "Segmentation of the heart and great vessels in CT images using a model-based adaptation framework". In: *Medical Image Analysis* 15.6, pp. 863–876.

Eck, V. G. et al. (2015). "A guide to uncertainty quantification and sensitivity analysis for cardiovascular applications". In: *International Journal for Numerical Methods in Biomedical Engineering* 32.8, e02755.

Falk, V. et al. (2017). "2017 ESC/EACTS guidelines for the management of valvular heart disease". In: *European Journal of Cardio-Thoracic Surgery* 52.4, pp. 616–664.

Feuchtner, G. M. et al. (2006). "Multislice computed tomography for detection of patients with aortic valve stenosis and quantification of severity". In: *Journal of the American College of Cardiology* 47.7, pp. 1410–1417.

Gibbons, K. D. et al. (2019). "Development of a statistical shape-function model of the implanted knee for real-time prediction of joint mechanics". In: *Journal of Biomechanics* 88, pp. 55–63.

Heimann, T. and H.-P. Meinzer (2009). "Statistical shape models for 3d medical image segmentation: a review". In: *Medical Image Analysis* 13.4, pp. 543–563.

Hoeijmakers, M. J. M. M. et al. (2020). "Combining statistical shape modeling, CFD , and meta-modeling to approximate the patient-specific pressure-drop across the aortic valve in real-time". In: *International Journal for Numerical Methods in Biomedical Engineering*.

Ionasec, R. I. et al. (2010). "Patient-specific modeling and quantification of the aortic and mitral valves from 4-d cardiac CT and TEE". in: *IEEE Transactions on Medical Imaging* 29.9, pp. 1636–1651.

Khalafvand, S. S. et al. (2018). "Assessment of human left ventricle flow using statistical shape modelling and computational fluid dynamics". In: *Journal of Biomechanics*.

Laskey, W. K. and W. G. Kussmaul (1994). "Pressure recovery in aortic valve stenosis". In: *Circulation* 89.1, pp. 116–121.

Liang, L. et al. (2016). "Machine learning-based 3-d geometry reconstruction and modeling of aortic valve deformation using 3-d computed tomography images". In: *International Journal for Numerical Methods in Biomedical Engineering* 33.5, e2827.

Menter, F. R. (1994). "Two-equation eddy-viscosity turbulence models for engineering applications". In: *AIAA Journal* 32.8, pp. 1598–1605.

Min, J. K. et al. (2015). "Noninvasive fractional flow reserve derived from coronary CT angiography". In: *JACC: Cardiovascular Imaging* 8.10, pp. 1209–1222.

Morris, M. D. and T. J. Mitchell (1995). "Exploratory designs for computational experiments". In: *Journal of Statistical Planning and Inference* 43.3, pp. 381–402.

Morris, P. D. et al. (2013). "Virtual fractional flow reserve from coronary angiography: modeling the significance of coronary lesions". In: *JACC: Cardiovascular Interventions* 6.2, pp. 149–157.

Namasivayam, M. et al. (2020). "Transvalvular flow rate determines prognostic value of aortic valve area in aortic stenosis". In: *Journal of the American College of Cardiology* 75.15, pp. 1758–1769.

Nicolella, D. P. and T. L. Bredbenner (2012). "Development of a parametric finite element model of the proximal femur using statistical shape and density modelling". In: *Computer Methods in Biomechanics and Biomedical Engineering* 15.2, pp. 101–110.

Pianosi, F. and T. Wagener (2015). "A simple and efficient method for global sensitivity analysis based on cumulative distribution functions". In: *Environmental Modelling & Software* 67, pp. 1–11.

Pianosi, F. et al. (2016). "Sensitivity analysis of environmental models: a systematic review with practical workflow". In: *Environmental Modelling & Software* 79, pp. 214–232.

Pouch, A. M. et al. (2013). "Automated segmentation and geometrical modeling of the tricuspid aortic valve in 3d echocardiographic images." In: *Medical image computing and computer-assisted intervention : MICCAI ... International Conference on Medical Image Computing and Computer-Assisted Intervention* 16 (Pt 1), pp. 485–492.

Queirós, S. et al. (2019). "Semi-automatic aortic valve tract segmentation in 3D cardiac magnetic resonance images using shape-based B-spline explicit active surfaces". In: *Medical Imaging 2019: Image Processing*. Vol. 10949. International Society for Optics and Photonics, p. 1094918.

Quicken, S. et al. (2016). "Application of an adaptive polynomial chaos expansion on computationally expensive three-dimensional cardiovascular models for uncertainty quantification and sensitivity analysis". In: *Journal of Biomechanical Engineering* 138.12, p. 121010.

Quicken, S. et al. (2019). "Computational study on the haemodynamic and mechanical performance of electrospun polyurethane dialysis grafts". In: *Biomechanics and Modeling in Mechanobiology* 19.2, pp. 713–722.

Reymond, P. et al. (2012). "Patient-specific mean pressure drop in the systemic arterial tree, a comparison between 1-d and 3-d models". In: *Journal of Biomechanics* 45.15, pp. 2499–2505.

Saltelli, A. et al. (2007). *Global sensitivity analysis. the primer*. John Wiley & Sons, Ltd.

Sankaran, S., L. Grady, and C. A. Taylor (2015). "Fast Computation of Hemodynamic Sensitivity to Lumen Segmentation Uncertainty". In: *IEEE Transactions on Medical Imaging* 34.12, pp. 2562–2571.

Sankaran, S. et al. (2016). "Uncertainty quantification in coronary blood flow simulations: impact of geometry, boundary conditions and blood viscosity". In: *Journal of Biomechanics* 49.12, pp. 2540–2547.

Sen, Y. et al. (2014). "Image segmentation methods for intracranial aneurysm haemodynamic research". In: *Journal of Biomechanics* 47.5, pp. 1014–1019.

Soboĺ, I. M. (2001). "Global sensitivity indices for nonlinear mathematical models and their monte carlo estimates". In: *Mathematics and Computers in Simulation* 55.1-3, pp. 271–280.

Spinczyk, D. and A. Krasoń (2018). "Automatic liver segmentation in computed tomography using general-purpose shape modeling methods". In: *BioMedical Engineering OnLine* 17.1.

Sturdy, J. et al. (2019). "Uncertainty quantification of computational coronary stenosis assessment and model based mitigation of image resolution limitations". In: *Journal of Computational Science* 31, pp. 137–150.

Sudret, B. (2008). "Global sensitivity analysis using polynomial chaos expansions". In: *Reliability Engineering & System Safety* 93.7, pp. 964–979.

Suinesiaputra, A. et al. (2018). "Statistical shape modeling of the left ventricle: myocardial infarct classification challenge". In: *Journal of Biomedical and Health Informatics* 22.2, pp. 503–515.

Traeger, B. et al. (2015). "Methodological inaccuracies in clinical aortic valve severity assessment: insights from computational fluid dynamic modeling of CT-derived aortic valve anatomy". In: *Theoretical and Computational Fluid Dynamics* 30.1-2, pp. 107–128.

Uetani, M. et al. (2014). "Statistical shape model of the liver and its application to computer-aided diagnosis of liver cirrhosis". In: *Electrical Engineering in Japan* 190.4, pp. 37–45.

Venugopal, P. et al. (2018). "Sensitivity of FFR-CT to manual segmentation". In: *Medical Imaging 2018: Biomedical Applications in Molecular, Structural, and Functional Imaging*. Ed. by B. Gimi and A. Krol. SPIE.

Voelker, W. et al. (1992). "Pressure recovery in aortic stenosis: an in vitro study in a pulsatile flow model". In: *Journal of the American College of Cardiology* 20.7, pp. 1585–1593.

Weese, J. et al. (2017). "CFD- and bernoulli-based pressure drop estimates: a comparison using patient anatomies from heart and aortic valve segmentation of CT images". In: *Medical Physics* 44.6, pp. 2281–2292.

Woo, J. et al. (2016). "A spatio-temporal atlas and statistical model of the tongue during speech from cine-MRI". in: *Computer Methods in Biomechanics and Biomedical Engineering: Imaging & Visualization* 6.5, pp. 520–531.

Wu, X., W. Zhang, and S. Song (2017). "Uncertainty quantification and sensitivity analysis of transonic aerodynamics with geometric uncertainty". In: *International Journal of Aerospace Engineering* 2017, pp. 1–16.

Yates, K. M. and C. D. Untaroiu (2018). "Finite element modeling of the human kidney for probabilistic occupant models: statistical shape analysis and mesh morphing". In: *Journal of Biomechanics* 74, pp. 50–56.

Yoganathan, A. P. et al. (1988). "Review of hydrodynamic principles for the cardiologist: applications to the study of blood flow and jets by imaging techniques." In: *Journal of the American College of Cardiology* 12 (5), pp. 1344–1353.

Chapter 5

Scale-resolving simulations of steady and pulsatile flow through healthy and stenotic heart valves

This chapter is based on: **M.J.M.M. Hoeijmakers**, V. Morgenthaler, M.C.M. Rutten, F.N. van de Vosse. Scale-resolving numerical simulation of steady and pulsatile flow through healthy and stenotic heart valves. *Submitted*

ABSTRACT

Background Aortic valve stenosis is a common valvular disease that leads to disturbed blood flow in the thoracic aortic artery. *In-vivo* and *in-vitro* studies have demonstrated that blood flow downstream of the diseased aortic valve intermittently exhibits random fluctuations in the velocity field which are associated with turbulence. The wide range of time and length scales involved in such flows warrants the use of computationally demanding scale-resolving numerical models such as Direct Numerical or Large Edddy Simulations. **Aim** The aim of this work was to numerically compute the turbulent flow downstream of healthy and stenotic heart valves, in both steady as pulsatile flow conditions. **Methods** Large Eddy Simulations and Reynolds-Averaged Navier-Stokes were used to compute the flow field at Reynolds numbers of 2700 and 5400. Aortic valves with an opening area of 70 mm^2 and 175 mm^2, and their projected orifice-plate type counterparts were considered. Projections were considered since they are easily obtained and parameterized. Both steady-state and pulsatile simulations were performed. Power spectra of velocity fluctuations and downstream turbulent kinetic energy were quantified. **Results** Projected geometries exhibited an increased pressure-drop (>90%), and an increased centerline turbulent kinetic energy (>150%). Centerline turbulent kinetic energy was an order of magnitude higher in severely stenotic heart valves compared to healthy valevs. Turbulent kinetic energy peaked at 1 and 2 diameters downstream of of stenotic and healthy valves respectively. Reynolds-Averaged Navier-Stokes models adequately captured the pressure-drop over the valve, but underestimated turbulent kinetic energy. Pulsatile flow stabilized flow in the acceleration phase, whereas deceleration triggered (healthy valve) or amplified (stenotic valve) turbulence. **Conclusion** Simplification of the aortic valve by projecting the orifice area leads to an overestimation of the pressure-drop and turbulence production, and should be avoided. Reynolds-Averaged Navier-Stokes simulations may be used to predict the pressure-drop over the valve, but if detailed information of the flow field is required, scale resolving models are recommended.

5.1 INTRODUCTION

Aortic valve stenosis (AVS) is a common valvular disease that occurs in approximately 4% of the population above the age of 70 years (Nkomo et al. 2006). AVS is characterized by a narrowing of the aortic valve systolic opening area. Consequently, this narrowing leads to a significant increase in the pressure-drop between the left ventricle and the ascending aorta. This pressure-drop significantly determines the load on the left ventricle, and as such has been shown to have predictive clinical value. Clinically, the pressure-drop is estimated from the maximum velocity of blood through the valve in combination with a simplified form of the Bernoulli equation (Vahanian et al. 2012; Baumgartner et al. 2016). However, this method may not be representative for the actual pressure drop since it does not take into account pressure recovery, flow unsteadiness, or turbulent losses (Niederberger et al. 1996; Baumgartner et al. 1999; Bahlmann et al. 2010).

Early in-vivo (Stein and Sabbah 1976; Walburn et al. 1983; Nygaard et al. 1994; Ha et al. 2018b; Yamaguchi et al. 1983) and in-vitro (Bluestein and Einav 1995; Yoganathan et al. 1979; Clark 1976) studies have demonstrated that significant oscillations in blood velocity can be expected downstream of healthy and diseased heart valves. Furthermore, it was demonstrated that patients with stenotic heart valves may exhibit higher levels of turbulence compared to healthy individuals. Some studies have suggested that disturbed blood flow is associated to hemolysis (Sallam and Hwang 1984; Kameneva et al. 2004) and to thrombus formation (Stein and Sabbah 1974; Dangas et al. 2016).

Quantification of turbulence is challenging. In the 20th century, invasive patient studies established the presence of turbulent flow downstream of the aortic valve by hot-film anemometers. These, hot-film anemometers were for example fitted on catheters (Stein and Sabbah 1976; Walburn et al. 1983), or used in combination with specific vessel-mounts (Nygaard et al. 1992; Nygaard et al. 1994). In recent years, non-invasive methods such as phase-contrast Magnetic Resonance Imaging (pc-MRI) have become available. pc-MRI captures the full velocity field in space and time, and despite its limited resolution can be used to directly quantify turbulence. For example, pc-MRI can be used to quantify viscous and turbulent losses in both flow phantoms (Binter et al. 2015; Ha et al. 2018a), and patients (Ha et al. 2016; Ha et al. 2018b). Alternatively, medical imaging data can be used to derive the patient-specific geometry of the valve/aorta that can then be used in Computational Fluid Dynamics (CFD) simulations. With the increase in computational power and improvements in numerical schemes, the latter has become a powerful tool. Image-based CFD models are now widely used to study unsteady flow phenomena (including turbulence) of aortic coarctations (Andersson et al. 2017; Arzani et al. 2011; Goubergrits et al. 2013; Lantz et al. 2013), and aortic valve stenosis (Hoeijmakers et al.

2019; Gilmanov et al. 2019; Wendell et al. 2013; Luraghi et al. 2019).

Flow downstream of a (stenotic) heart valve is characterized by intermittent (low Reynolds) turbulence (Bluestein and Einav 1995). That is, turbulent structures are generated in systole, but quickly decay in diastole due to viscosity, and the lack of flow (energy source). Turbulent flows are characterized by a wide range of spatial and temporal scales in the velocity field, which makes Direct Numerical Simulation (DNS) particularly demanding from a computational point of view. Instead, in the field of engineering the flow field is computed with Reynolds Averaged Navier-Stokes (RANS) equations, or through scale-resolving models such as Large Eddy Simulation (LES). The RANS approach assumes that the flow can be decomposed into a mean part and a fluctuating part. Through closure models and a "turbulent viscosity", the mean turbulent flow is then characterized. Popular models in industry include the $k - \epsilon$ (Launder and Spalding 1974) and Shear-Stress Transport $k - \omega$ models (Menter 1994). As suggested by Yoganathan et al. (2005), these RANS models may not be suitable for the transitional and intermittent nature of turbulence encountered in cardiovascular flows. Although RANS simulations have been used for pulsatile flow, agreement with experimental data can be very poor for separated flows (Varghese and Frankel 2003). Instead, computationally demanding scale-resolving simulations — such as LES — that resolve atleast (part) of the length/time scales may be more suitable for these types of flows.

The aim of this work was to characterize the turbulent flow downstream of healthy and stenotic aortic valves by LES simulations. More specifically, the turbulent fluctuations are analyzed in steady and pulsatile flow conditions. The effect of mesh size on the computed fluctuations is systematically investigated for the steady-state LES simulations. Furthermore, the difference between flow through a valvular shape and an orifice-type opening is presented. Finally, the LES computed pressure-drop is compared to the pressure-drop computed by RANS simulations to assess whether RANS is a viable alternative.

5.2 METHODS

5.2.1 AORTIC VALVE GEOMETRY

The shape of the aortic valve leaflets was obtained from a segmentation framework, extensively described in previous work (Weese et al. 2017; Ecabert et al. 2011). The generated surface models of the aortic valve included part of the left ventricular outflow tract, ascending aorta, and sinus. These parts were removed or modified such that the

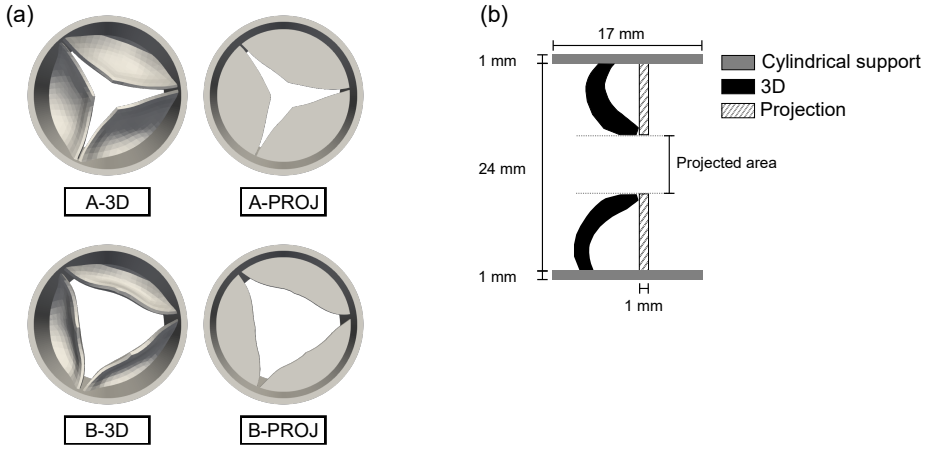

Figure 5.1 (a) axial view of all considered CAD models. Full three dimensional shape of the leaflets (A-3D and B-3D) and their projected counter parts (A-PROJ and B-PROJ) were used. (b) the geometric area is projected onto a single plane, resulting in a orifice-plate type construct (A-PROJ and B-PROJ).

construct fitted in a circular support with an internal diameter of 24 mm, a length of 17 mm and thickness of 1 mm. Moreover, additional Computer Aided Design (CAD) models were derived from the valvular shapes by projecting the geometric opening area along the valve axis on a plane of 1 mm thickness (Figure 5.1). This was done to imitate clinical practice in which the aortic valve opening area may be extracted by planimetry of echocardiography (Okura et al. 1997) or CT (Shah et al. 2009) images.

Valves A and B were selected based on their opening area. Valve A had an opening area of 70 mm^2, corresponding to a stenotic heart valve. Valve B had a geometric orifice area of 175mm^2, and represented a healthy/mildy stenotic heart valve.

5.2.2 NUMERICS

To facilitate CFD modeling, the CAD model of Figure 5.1 was extended at the upstream side by a tube with an inner diameter of 26 mm, and length of 1.7 diameters. Additionally, a downstream section with a length of 20 diameters was added. Note that the inner diameter of the up- and downstream sections was 2 mm larger than the valvular section, and corresponded to the dimensions of the physical model that was 3D printed for validation of the computed pressure-drop (**Chapter 6**).

Table 5.1 Approximate cell sizes and number of cells in the computational domain

		Cell Size [mm]			Cell count	
Type	Name	Upstream	0D-5D	5D-20D	0D-5D†	Total
3D	A-3D-M1	2.00	2.00	2.00	$8.6 \cdot 10^3$	$1.5 \cdot 10^6$
	A-3D-M2	2.00	1.00	2.00	$6.9 \cdot 10^4$	$1.6 \cdot 10^6$
	A-3D-M3	2.00	0.50	2.00	$5.5 \cdot 10^5$	$2.5 \cdot 10^6$
	A-3D-M4	2.00	0.25	2.00	$4.4 \cdot 10^6$	$6.4 \cdot 10^6$
	B-3D-M3	2.00	0.50	2.00	$5.5 \cdot 10^5$	$2.5 \cdot 10^6$
	B-3D-M4	2.00	0.25	2.00	$4.4 \cdot 10^6$	$6.7 \cdot 10^6$
Projected	A-PROJ-M1	2.00	2.00	2.00	$8.6 \cdot 10^3$	$0.8 \cdot 10^6$
	A-PROJ-M2	2.00	1.00	2.00	$6.9 \cdot 10^4$	$0.9 \cdot 10^6$
	A-PROJ-M3	2.00	0.50	2.00	$5.5 \cdot 10^5$	$1.5 \cdot 10^6$
	A-PROJ-M4	2.00	0.25	2.00	$4.4 \cdot 10^6$	$5.7 \cdot 10^6$

† Estimated by dividing the volume of 0D-5D by the volume of a single hexahedral cell.

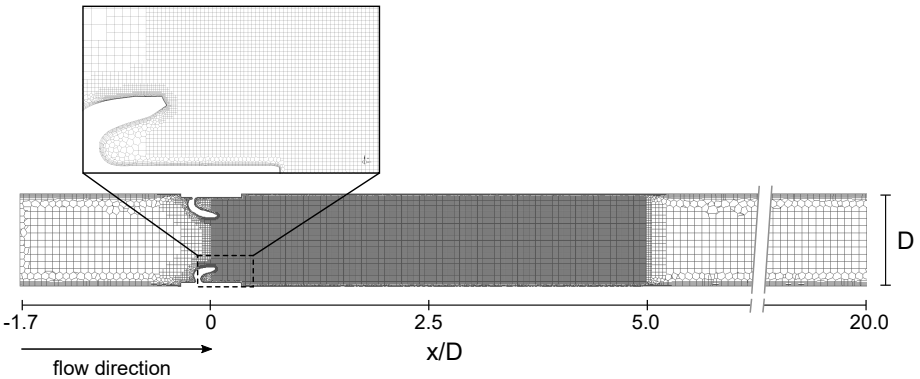

Figure 5.2 Cross sectional view of the discretized fluid domain of B-3D-M4. Different element sizes were considered in the region of interest (0D-5D).

5.2.2.1 MESH GENERATION

Volumetric discretization of the fluid volume was performed with ANSYS Fluent Meshing R19.2 (ANSYS Inc, Canonsburg, Pennsylvania, United States). Volumetric meshes consisted of regular hexahedral elements in the core, which transitioned to polyhedral elements close to the boundary (poly-hexcore). Features such as the expected point of seperation were reconstructed with extremely small cell sizes of 0.05 mm (Figure 5.2).

Moreover, cell sizes of 0.25 mm were introduced in all other areas that were in proximity of the valve construct (see Figure 5.1). Upstream of the valve and between 5 and 20 diameters downstream of the valve, coarse cells were used (2x2x2 mm). Volumetric meshes were refined in the area deemed relevant for jet development and breakdown, that is, between 0D and 5D downstream of the valve. In this section, four levels of refinement were considered to establish mesh sensitivity: cells of 2x2x2 mm, 1x1x1 mm, 0.5x0.5x0.5 mm, and 0.25x0.25x0.25 mm (Table 5.1).

5.2.2.2 GOVERNING EQUATIONS

Fluid flow of a viscous and incompressible fluid (constant density) are governed by the Navier-Stokes equations (in Einstein notation):

$$\frac{\partial u_i}{\partial t} + \frac{\partial}{\partial x_j}(u_i u_j) = -\frac{1}{\rho}\frac{\partial p}{\partial x_i} + \frac{\partial}{\partial x_j}\Big[\nu\Big(\frac{\partial u_i}{\partial x_j} + \frac{\partial u_j}{\partial x_i}\Big)\Big] \qquad (5.1)$$

$$\frac{\partial u_i}{\partial x_i} = 0$$

With u_i the velocity, p the pressure, and ν the kinematic viscosity of the fluid. In general, three approaches to modeling turbulent flows exist. 1) Resolve all length and time-scales of the turbulent flow by making use of the Navier-Stokes equations (Equation 5.1) directly, known as DNS. 2) Resolve the time-averaged flow field, and use a model to approximate the contribution of turbulence, known as Reynolds Averaged Navier Stokes (RANS). Or 3) separate the length scales in the turbulent flow by resolving the largest scales, and modeling the small sub-grid scales, known as LES. The following paragraphs briefly describe the RANS and LES approaches.

REYNOLDS AVERAGED NAVIER STOKES

In RANS models, Reynolds decomposition is used to separate the velocity components of Equation 5.1 into the time-average ($\overline{\ }$) and fluctuating parts ($'$):

$$u_i = \overline{u}_i + u_i', \quad p = \overline{p} + p' \qquad (5.2)$$

When substituting Equation 5.2 into Equation 5.1 the partial differential equations that govern the mean (incompressible) turbulent flow can be obtained (Alfonsi 2009):

$$\overline{u}_j \frac{\partial \overline{u}_i}{\partial x_j} = -\frac{1}{\rho}\frac{\partial \overline{p}}{\partial x_i} + \frac{\partial}{\partial x_j}\Big[\nu\Big(\frac{\partial \overline{u}_i}{\partial x_j} + \frac{\partial \overline{u}_j}{\partial x_i}\Big)\Big] - \underbrace{\frac{\partial \tau_{ij}}{\partial x_j}}_{\substack{\text{Reynolds} \\ \text{stress tensor}}} \tag{5.3}$$

$$\frac{\partial \overline{u}_i}{\partial x_i} = 0$$

Note that the time-derivative now disappeared from Equation 5.3. The Reynolds stress tensor in Equation 5.3 includes the effects of turbulent motions on the mean stress, but is in fact unknown. That is, it actually introduces six additional independent unknowns. However, it can be approximated by the Boussinesq approximation (Hinze 1975):

$$\tau_{ij} = \overline{u_i' u_j'} \approx \frac{2}{3} k \delta_{ij} - \nu_t\Big(\frac{\partial \overline{u}_i}{\partial x_j} + \frac{\partial \overline{u}_j}{\partial x_i}\Big) \tag{5.4}$$

With δ_{ij} the Kronecker delta, k the turbulent kinetic energy, and ν_t the turbulent stresses that need to be modeled. For modeling ν_t the Shear Stress Transport $k-\omega$ model was used in this study. This models the contribution of turbulence by introducing two additional transport equations, one for the transport of turbulent kinetic energy k, and one for transport of the specific dissipation rate ω (Menter 1994).

LARGE EDDY SIMULATION

The LES method spatially filters only the small-scale turbulent structures, and thus resolves the larger (anistropic) structures. Structures below the spatial filter (typically grid size) still need to be modeled, and are known as subgrid-scale (SGS) models. Spatially filtered flow variables are denoted by $\tilde{}$. The (spatially) filtered momentum and continuity equations (Equation 5.1) then read:

$$\frac{\partial \tilde{u}_i}{\partial t} + \frac{\partial}{\partial x_j}(\tilde{u}_i \tilde{u}_j) = -\frac{1}{\rho}\frac{\partial \tilde{p}}{\partial x_i} + \frac{\partial}{\partial x_j}\Big[\nu\Big(\frac{\partial \tilde{u}_i}{\partial x_j} + \frac{\partial \tilde{u}_j}{\partial x_i}\Big)\Big] - \frac{\partial \tau_{ij}}{\partial x_j} \tag{5.5}$$

$$\frac{\partial \tilde{u}_i}{\partial x_i} = 0$$

Note that — in contrast to the RANS formulation — the time-derivative is now non-zero,

and is included in the solution process. Similar to the RANS equation, the Boussinesq hypothesis is used, but now only for the subgrid scales:

$$\tau_{ij} = \frac{1}{3}\tau_{kk}\delta_{ij} - \nu_t\Big(\frac{\partial \tilde{u}_i}{\partial x_j} + \frac{\partial \tilde{u}_j}{\partial x_i}\Big) \tag{5.6}$$

Similarly to Equation 5.4, a turbulent viscosity ν_t is introduced, and was in this study accounted for by the dynamic Smagorinsky model (Lilly 1992).

5.2.2.3 SOLUTION PROCEDURE

Steady flow conditions were simulated with both the RANS approach (Equation 5.3) as the LES approach (Equation 5.5). Pulsatile flow conditions exclusively used the LES formulation .

STEADY FLOW

Inflow-diameter-based Reynolds numbers of 2700 and 5400 were considered, and corresponded to a flow of 3.5 and 7.0 Lmin^{-1} of a fluid with water-like properties. Density of the fluid was set at 998 kgm^{-3}, and viscosity was set at $1.05 \cdot 10^{-3}$ Pa·s (water at 18° Celsius). Reynolds numbers corresponded to typical mean and peak-systolic *in-vivo* flow conditions in rest. A fully developed turbulent flow was assumed at the inflow boundary. This profile followed a $1/7^{\text{th}}$ power-law (Equation 5.7), representative for the time-averaged fully developed turbulent velocity profile (Chant 2005).

$$\begin{aligned} u(r) &= U_{max}\big(1 - \frac{r}{R}\big)^{1/n} \\ &\text{with :} \\ U_{max} &= \frac{1}{2}\frac{Q}{A_0}\frac{(n+1)(2n+1)}{n^2} \end{aligned} \tag{5.7}$$

Where Q is the volumetric flow rate, A_0 the area of the circular vessel, and $n = 7$. Furthermore, a constant zero pressure outlet boundary condition, and no-slip walls were used. With these boundary conditions the RANS solution with the Shear Stress Transport $k - \omega$ turbulence model was obtained. Besides the RANS simulations, additional LES simulations were performed that resolved a large part of the turbulent fluctuations.

The RANS solution was used as an initial guess of the time-averaged flow field, and helped speed up convergence of the LES model which used the same boundary conditions. Once in LES-mode, time advancement was performed by the non-iterative fractional step method (Armfield and Street 1999). Time-advancement was performed with a constant time-step of $1 \cdot 10^{-4}$ s. A total of 6 seconds of steady flow was simulated (60000 time-steps). The first two seconds (approximately one flow-through time) were excluded from analysis. Consequently, the remaining 4 seconds (40000 time-steps) were used to analyze the statistics of the steady flow. A time-step of $1 \cdot 10^{-4}$ s, peak centerline velocity of approximately 3 ms^{-1}, and grid size of $0.25 \cdot 10^{-3}$ m ensured that the Courant number stayed below one throughout the domain. Note that this is an estimate based on A-PROJ-M4, and given the lower jet-velocity in all other cases, should thus be a conservative estimate.

PULSATILE FLOW

To simulate pulsatile flow conditions, a sine squared-based boundary condition was adopted which closely matched a Fourier series representative of aortic blood-flow that was presented by Olufsen et al. (2000). That is, the volumetric flow rate Q depended on time:

$$Q(t) = \begin{cases} Q_0 \; sin^2\big(t\frac{\pi}{2T_{acc}}\big) & t < T_{acc} \\ Q_0 \; sin^2\big((t + T_{dec} - T_{acc})\frac{\pi}{2T_{dec}}\big) & T_{acc} \leq t \leq T_{systole} \\ 0 & t > T_{systole} \end{cases} \tag{5.8}$$

Here, T_{acc} and T_{dec} represent the period of the acceleration and deceleration slopes respectively. With $T_{acc} = 0.12T_{cycle}$ and $T_{dec} = 0.22T_{cycle}$, systole becomes a fraction of the full cardiac cycle: $T_{systole} = 0.34T_{cycle}$. Q_0 represents the flow-rate at peak-systole, and was set at 7.0 Lmin^{-1}. For all pulsatile simulations $T_{cycle} = 3.33$ s, resulting in a Womersley parameter of approximately 14. With these water-like fluid properties, the cycle time is considerably longer than *in-vivo*, but ensured that the physiological ratio between transient inertial forces and viscous forces was maintained. Similar to steady flow simulations, the velocity profile at the inflow boundary was prescribed as a $1/7^{\text{th}}$ power law (Equation 5.7), and time-advancement was performed with a constant time-step of $1 \cdot 10^{-4}$ s by the non-iterative fractional step method. Data of the first cycle was discarded from all analyses.

5.2.3 POST-PROCESSING

Multiple monitor points were defined along the centerline at 0.2D intervals (0D-5D), and 0.5D intervals (5D-20D). At these locations along the centerline, the instantaneous velocity components $\mathbf{u}(\mathbf{x}, t)$ were sampled during the solution process. Using Reynolds decomposition, the fluctuating part $\mathbf{u}'(\mathbf{x}, t)$ was separated from the time-average $\overline{\mathbf{u}}(\mathbf{x})$. For continuous records the time-average of $\mathbf{u}(\mathbf{x}, t)$ over a period of time T is defined as:

$$\overline{\mathbf{u}}(\mathbf{x}) = \frac{1}{T} \int_{t_0}^{t_0+T} \mathbf{u}(\mathbf{x}, t) dt \tag{5.9}$$

Or for discrete periodic time-series with N samples and a constant time-step:

$$\overline{\mathbf{u}}(\mathbf{x}) = \frac{1}{N} \sum_{i=1}^{N} \mathbf{u}(\mathbf{x})_i \tag{5.10}$$

The deviations from the mean velocity $\mathbf{u}'(\mathbf{x}, t)$ are then defined as:

$$\mathbf{u}'(\mathbf{x}, t) = \mathbf{u}(\mathbf{x}, t) - \overline{\mathbf{u}}(\mathbf{x}) \tag{5.11}$$

For the steady-state flow conditions that were simulated with LES, computing $\overline{\mathbf{u}}(\mathbf{x})$ and $\mathbf{u}'(\mathbf{x}, t)$ was straightforward, and time-averaged velocities were computed over the interval $t = [2, 6]$ seconds.

When applying the same procedure for the pulsatile simulations, $\overline{\mathbf{u}}(\mathbf{x})$ would contain the large-scale fluctuations that are due to the pulsatility of the flow. Hence, to distinguish between actual turbulent fluctuations and large-scale motions, an ensemble average (Mittal et al. 2003; Scotti and Piomelli 2001; Varghese et al. 2007b) was taken over N cycles with period T. That is:

$$\overline{\mathbf{u}}_{ens}(\mathbf{x},t) = \frac{1}{N}\sum_{n=0}^{N-1}\mathbf{u}(\mathbf{x},t+nT) \tag{5.12}$$

In periodic time-series, the ensemble average of $\overline{\mathbf{u}}_{ens}(\mathbf{x},t)$ would then reflect the mean velocity at a specific location, at a specific phase of the cardiac cycle, thus accounting for the large-scale pulsating motion of the fluid. Consequently, for pulsatile simulations $\mathbf{u}'(\mathbf{x},t)$ was obtained by replacing $\overline{\mathbf{u}}(\mathbf{x})$ with $\overline{\mathbf{u}}_{ens}(\mathbf{x},t)$. Data of the first cycle was discarded, and 30 cycles were used to construct $\overline{\mathbf{u}}_{ens}(\mathbf{x},t)$.

Power spectral density of the fluctuating velocity magnitude $|\mathbf{u}'|$ was estimated by Welch's method (Welch 1967) (steady-state: eight segments, 50% overlap, pulsatile: 30 segments, 50% overlap) at five points along the centerline, and is similar to the approach employed by Bergersen et al. (2018) and Varghese et al. (2007b). Furthermore, the turbulent kinetic energy k was computed from the fluctuating velocity components $u'(\mathbf{x},t)$, $v'(\mathbf{x},t)$, and $w'(\mathbf{x},t)$ by:

$$k = \frac{1}{2}\left(\overline{(u')^2} + \overline{(v')^2} + \overline{(w')^2}\right) \tag{5.13}$$

Finally, planes orthogonal to the centerline at $x/D = [0.0, 0.2, 0.4, 1.0, 2.0]$ were used to visualize instantaneous, time-averaged and the fluctuating part (root mean square) of $\mathbf{u}(\mathbf{x},t)$.

5.3 RESULTS

STEADY FLOW

Steady flow conditions were simulated with the RANS and LES approach. The first two seconds (20000 timesteps) of the steady flow LES results were excluded from the analysis. Figure 5.3 suggests that excluding the first two seconds was sufficient to avoid a potential simulation start-up effect, fluctuations seem to be random between 2 and 6 seconds of steady flow time. Furthermore, Figure 5.3 shows that the magnitude of velocity fluctuations was much larger for valve A than for valve B (both projected and 3D). Moreover, Figure 5.3 suggests that fluctuations strongly depend on axial position, and were smaller in magnitude for the 3D valves than for their projected counterparts.

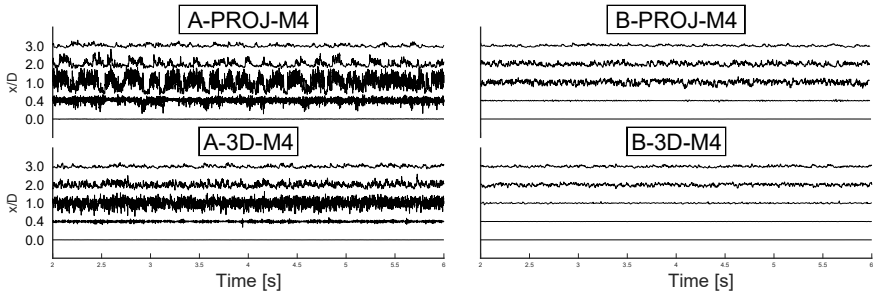

Figure 5.3 Fluctuations in velocity magnitude for projected and 3D configurations of valve A and B over 4 seconds at steady flow conditions. Tracings contain 40000 samples at five specific points along the centerline.

PULSATILE FLOW

Normalized centerline velocity magnitudes of valve A and B in pulsatile flow conditions are illustrated in Figure 5.4 and 5.5. Significant fluctuations in centerline velocity magnitude of Valve A (stenotic) were initiated at $x/D \geq 0.6$, and were maintained up to approximately $x/D = 1.8$. At $x/D = 4.0$ fluctuations have decreased substantially. Fluctuations in Valve A were initiated in early systole, and persist throughout a large part of the systolic phase. Tracings of the ensemble average show that the overall input waveform (see $x/D = 0.0$) was maintained between $x/D = 0.0$ and $x/D = 2.0$, but slightly flattens further downstream.

Similar behavior was observed in valve B (Figure 5.5). However, in contrast to valve A, fluctuations were generally observed further downstream $x/D \geq 1.0$. Additionally, fluctuations were not present in the acceleration phase, but were triggered immediately after peak systole ($t > 0.12T_{cycle}$), i.e., where flow decelerates.

5.3.1 POWER SPECTRA VELOCITY MAGNITUDE

STEADY FLOW

Power spectra of the velocity fluctuations show how the power of the fluctuations is distributed over the involved frequencies. Low frequencies and high power are associated to larger eddies passing the observation point, whereas higher frequencies of low power are associated with smaller eddies. For LES simulations, power spectra therefore strongly depend on mesh density. That is, a finer mesh resolves a larger part of the energy spectrum, and a smaller part needs to be modeled. Figure 5.6 depicts the power spectral density, and demonstrates that the density of the mesh downstream of the valve clearly affected the power spectra. For both the projected and 3D configuration, the smaller elements captured fluctuations over a larger frequency range. Furthermore, Figure 5.6

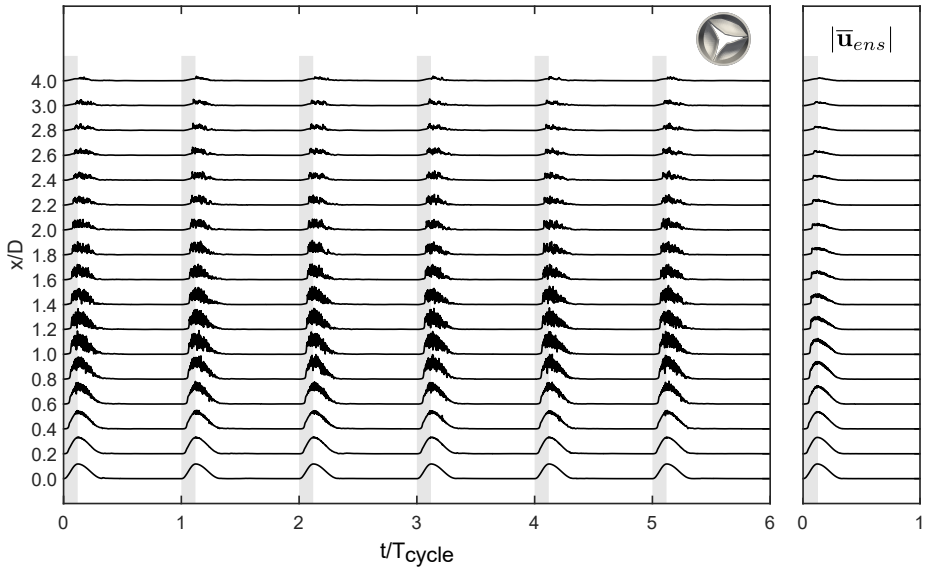

Figure 5.4 Left: numerically computed time history of the normalized velocity magnitude of 5 out of 30 cycles for A-3D-M4 in pulsatile flow conditions. Right: ensemble average of velocity magnitude over 30 cycles. Superimposed gray patch indicates the acceleration phase of systole.

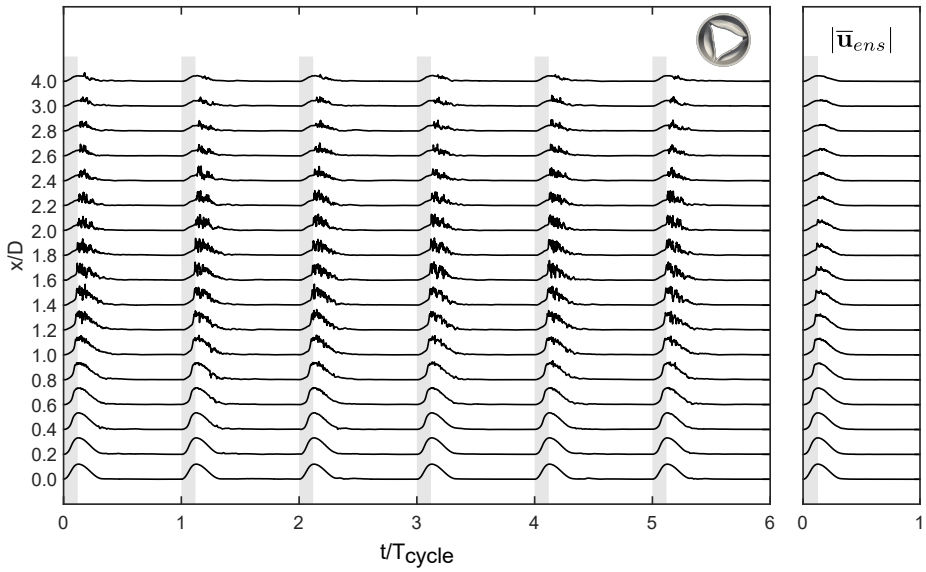

Figure 5.5 Left: numerically computed time history of the normalized velocity magnitude of 5 out of 30 cycles for B-3D-M4 in pulsatile flow conditions. Right: ensemble average of velocity magnitude over 30 cycles. Superimposed gray patch indicates the acceleration phase of systole.

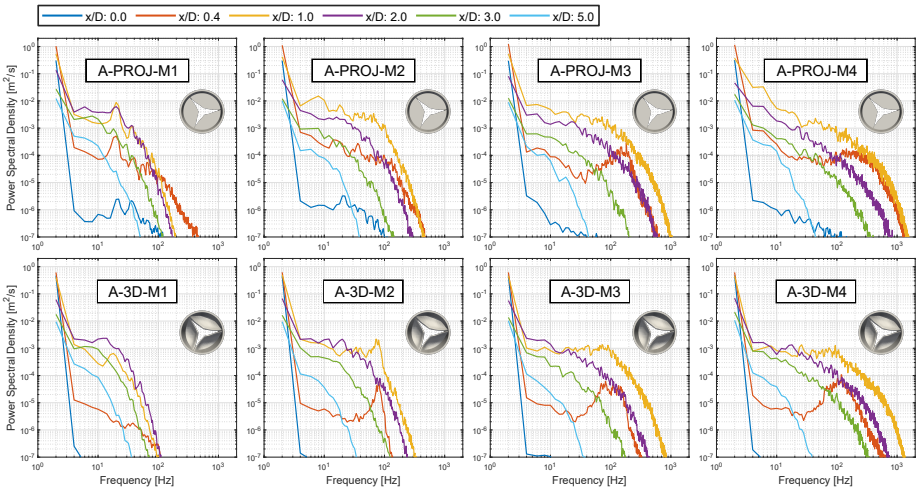

Figure 5.6 Power spectral density for different mesh densities and at 0.0, 0.4, 1.0, 2.0, 3.0 and 5.0 diameters downstream of the valve at steady flow conditions (7 Lmin^{-1}; $Re = 5400$). Top row: projection of valve A; bottom column: 3D configuration of valve A.

illustrates that for both valves the power of high frequency velocity oscillations on the centerline was strongest at approximately $x/D = 1.0$. Additionally, Figure 5.3 and Figure 5.6 suggest that the power of fluctuations was lower in the 3D configuration at $x/D = 0.4$. Power spectra between 10 and 100 Hz of the projection (A-PROJ-M4) and 3D configuration (A-3D-M4) at locations $x/D = [1.0, 2.0, 3.0, 5.0]$ were comparable. The power spectrum for the projected case (A-PROJ-M4) seems to deviate mainly in the lower frequency range (<30 Hz). These low-frequency fluctuations for A-PROJ-M4 are also clearly visible at $x/D = 1.0$ in the velocity time-series (Figure 5.3).

Furthermore, Figure 5.6 demonstrates that at the valve opening ($x/D = 0.0$), and at $x/D = 5.0$ high frequency oscillations in velocity magnitude were not present. This indicates that at these locations turbulence was not yet triggered ($x/D = 0.0$), or has decayed substantially ($x/D = 5.0$).

Figure 5.7 illustrates the effect of the inflow Reynolds number on the power spectra. With an increase in steady-state flowrate, (and thus Reynolds number), the power of the fluctuations increased substantially. For example, at $x/D = 2.0$ the power of fluctuations of valve A at 100 Hz was 10 times higher at a Reynolds number of 5400 compared to 2700. Although fluctuations were of lower frequency and magnitude in B-3D-M4, a similar 10-fold increase in power at $x/D = 2.0$ was observed at higher Reynolds numbers.

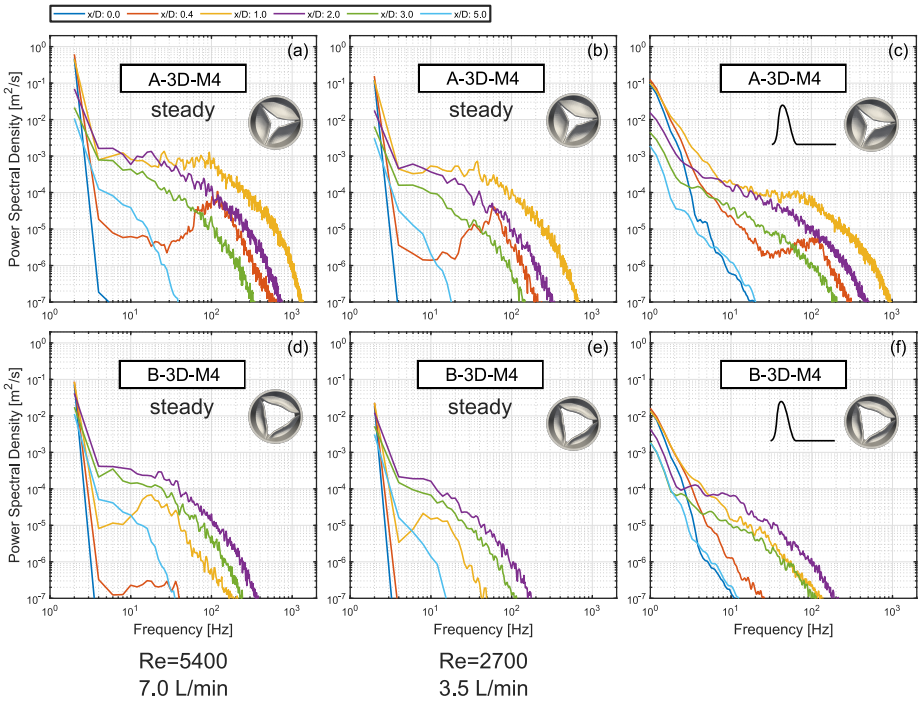

Figure 5.7 Power spectra for valve A (top row) and valve B (bottom row) in steady-flow (left column: Re=5400; middle column: Re=2700) and pulsatile flow conditions (right column). A shift towards higher frequencies, and stronger fluctuations was observed when 1) the valve was more stenotic, and 2) the inflow Reynolds number was larger.

PULSATILE FLOW

Power spectra of valve A and B in pulsatile flow conditions can be found in Figure 5.7. Maximum power and highest frequencies were found at $x/D = 1.0$ and $x/D = 2.0$ for valves A and B respectively. This is in line with observations in steady flow conditions, e.g., see Figure 5.6 and Figure 5.7. Pulsatile flow was characterized by a mean flow rate of 3.5 $Lmin^{-1}$ (Re=2700), and peak flow-rate of 7.0 $Lmin^{-1}$ (Re=5400). Power spectra of steady and pulsatile flow conditions suggests that steady-flow at mean flow rates (3.5 $Lmin^{-1}$) was more representative for pulatile flow than steady flow at peak-systolic flowrates (7.0 $Lmin^{-1}$).

5.3.2 TURBULENT KINETIC ENERGY

STEADY FLOW

Figure 5.8 illustrates the resolved part (with LES) of the turbulent kinetic energy along the centerline, and gives information on the kinetic energy associated with turbulent eddies. In line with the observations in Figure 5.6, a finer mesh resolves a larger part of the turbulent fluctuations. Indeed, Figure 5.8 demonstrates that a coarse mesh under-resolves the turbulent kinetic energy, and a finer meshes seems more appropriate since they allow the model to resolve a larger part of the turbulent kinetic energy. The most coarse mesh (M1) only resolved around $1/3^{\text{th}}$ of the turbulent kinetic energy that was resolved with meshes M2-M4. With these more dense grids a much larger part of the turbulent kinetic energy was resolved. For M2-4, peak centerline turbulent kinetic energy was reached around $x/D = 1.0$, the same for both the projected and 3D valve. Judging from Figure 5.8, refining beyond mesh M4 would give marginal improvements in the estimation of turbulent kinetic energy. Furthermore, it was observed that generation of turbulent kinetic energy in the projected cases was approximately two times larger. Additionally, the level of stenosis plays a substantial role, and peak turbulent kinetic energy was ten times higher for a stenotic valve (A-3D-M4: 0.211 m^2s^{-2}) than for a healthy valve (B-3D-M4: 0.022 m^2s^{-2}). Also note that for healthy valves (B-3D-M4) the peak in turbulent kinetic energy was shifted further downstream to $x/D = 2.0$.

Opposed to the LES simulations, the RANS simulations do not directly resolve the turbulent fluctuations. Instead, production and transport of k was entirely modeled through the Shear-Stress Transport model. Table 5.3 demonstrates that this approach may underestimate the production of turbulent kinetic energy along the centerline. Although not included in the current results, it was observed that the RANS simulations generally over-predict the downstream distance of maximum turbulent kinetic energy.

PULSATILE FLOW

Turbulent kinetic energy k for the pulsatile flow condition was computed by making use of the ensemble average $\overline{\mathbf{u}}_{ens}(\mathbf{x}, t)$ (Equation 5.12). Turbulent kinetic energy distribution along the centerline at eight time instances are visualized in Figure 5.9. In the stenotic valve (Valve A), turbulent kinetic energy builds up in the acceleration phase of systole (t_2), and reached a maximum between t_3 and t_4, i.e., just after systole. At $t \geq t_4$ turbulent kinetic energy rapidly reduceed to negligible levels at the end of systole (t_7). The healthy valve (Valve B) does not exhibit elevated levels of turbulent kinetic energy until peak systole t_3. However, in the deceleration phase, turbulent kinetic energy was drastically amplified, and reached a maximum at approximately t_5 and — similar to valve A —

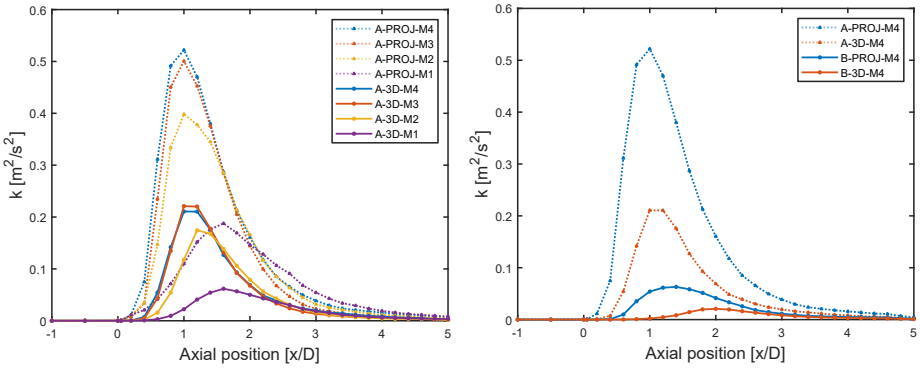

Figure 5.8 Turbulent kinetic energy at Re=5400 (7 Lmin^{-1}) for each mesh density, projected and 3D configurations and valves A and B. The coarsest mesh under-resolved the turbulent fluctuations, and turbulent kinetic energy was substantially underestimated. Peak turbulent kinetic energy was approximately 10 times higher for the stenotic valve A when compared to valve B.

quickly diminishes late systole ($t_6 - t_7$).

Valve A exhibits a peak in centerline turbulent kinetic energy at approximately $x/D = 1.2$. In valve B, peak turbulent kinetic energy is shifted further downstream, and is observed at $x/D = 2.0$. This is in line with the steady-state results, where the same observation is made (Figure 5.8). Compared to the steady-state simulations, maximum turbulent kinetic energy levels were of the same order of magnitude for the pulsatile simulations, but were only maintained for a short time span. It should be noted that with $k_{max} = 0.304$ and $k_{max} = 0.036$ maximum turbulent kinetic energy was somewhat higher during pulsatile flow (Table 5.2). However, k was derived from a limited number of cycles, e.g., with 30 cycles the ensemble average, and all derived metrics, may not have completely converged from a statistical point of view.

5.3.3 CENTERLINE VELOCITY AND PRESSURE

Time-averaged centerline maximum velocity magnitude and pressure-drop results of each simulated case are summarized in Table 5.3 (steady flow) and Table 5.2 (pulsatile flow).

STEADY FLOW

Maximum centerline velocities for A-3D were 2.0 and 1.0 m/s for flow rates of 7.0 and 3.5 Lmin^{-1} respectively. At 7.0 Lmin^{-1} valve A exhibited a pressure-drop of 12.3 mmHg, and at 3.5 Lmin^{-1} a pressure-drop of 3.1 mmHg. A-3D-M4 yielded a maximum centerline

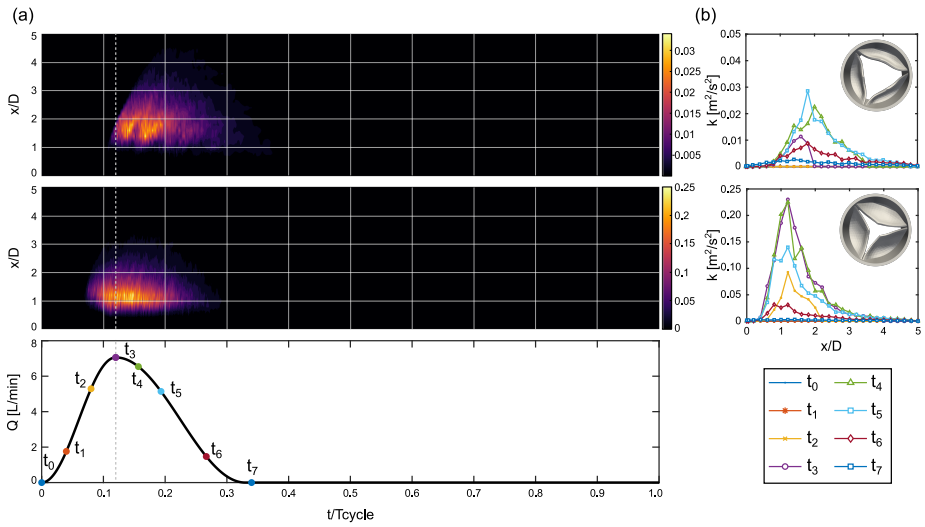

Figure 5.9 Turbulent kinetic energy at specific time instances in systole. Valve A: turbulent kinetic energy builds up in the acceleration phase (t_2), and is maximal at peak systole, and was sustained over the time interval $t_3 - t_4$, k decays between t_5 and t_6, and was completely diminished by the end of systole (t_7). Valve B: turbulent kinetic energy was zero in the entire acceleration phase, but was elevated at peak systole (t_3), and further amplified in the deceleration phase ($t_3 - t_5$). Turbulent kinetic energy rapidly decays in late systole ($t_6 - t_7$). Levels of k were an order of magnitude lower in valve B.

velocity that was 4% higher than A-3D-M1, the coarsest mesh. Pressure-drop results were consistent for mesh sizes A-3D-M[1-4]. RANS simulations yielded maximum centerline velocity magnitudes and pressure-drops that were in line with LES results of both A-3D as B-3D.

Projected cases exhibited a significantly higher centerline velocity than 3D cases. For example, A-PROJ-M4 exhibited a peak centerline velocity of 2.69 m/s, approximately 35% higher than A-3D-M4. The increased jet velocity in A-PROJ-M4 translates to a 90% increase in the pressure-drop (23.4 vs. 12.3 mmHg). Similarly, B-PROJ-M4 exhibited a pressure drop that is 92% higher (1.2 vs. 2.3 mmHg). Differences in maximum centerline velocity magnitude and pressure-drop between LES simulations and RANS simulations were negligible.

PULSATILE FLOW

Table 5.2 summarizes velocity and pressure-drop results for the pulsatile flow condition. Maximum centerline velocity magnitude at peak systole computed from $\overline{\mathbf{u}}_{ens}(\mathbf{x}, t)_{max}$ are 2.07 and 0.72 m/s for Valve A and B respectively. Velocities compared well to the steady flow conditions at 7.0 Lmin^{-1}. Furthermore, ΔP over both valves, at peak systole,

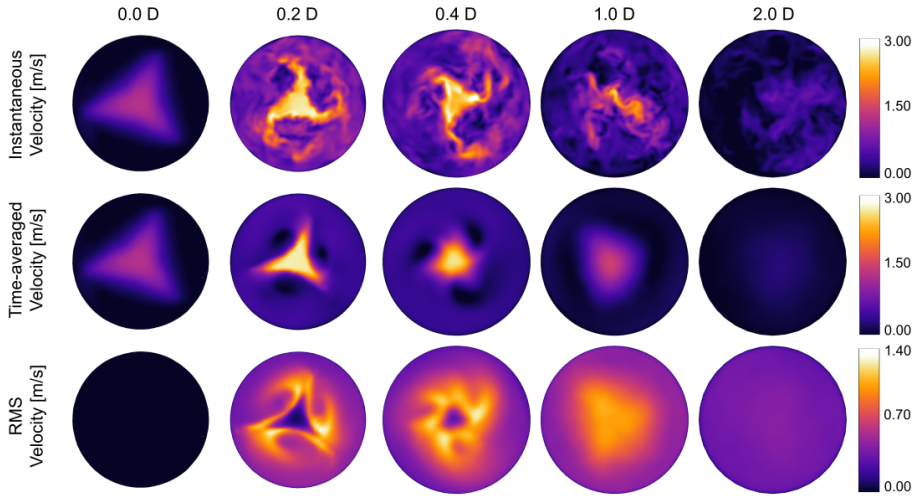

Figure 5.10 Contours along the centerline of instantaneous (top row - T=6s), time-averaged (middle row) and root mean square (bottom row) of the velocity magnitude (A-PROJ-M4).

corresponded to ΔP results of the steady-state simulations at 7.0 $Lmin^{-1}$. The combined effect of acceleration and the stenosis — represented by ΔP_{max} — shows that the effect of acceleration on ΔP was marginal in Valve A (13.2 vs. 12.4 mmHg). The effect of fluid acceleration was more clear in Valve B. The maximum pressure-drop in systole was 4.3 mmHg, whereas the pressure-drop at peak systole was only 1.2 mmHg, indicating that unsteadiness was more important. For Valves A and B, the mean pressure-drop over systole — which contained both acceleration/deceleration effects as the effect of stenosis — was around $1/3^{th}$ the pressure-drop that was observed at peak systole.

5.3.4 CROSS SECTIONAL VELOCITY DISTRIBUTION

STEADY FLOW

In Figure 5.10 and 5.11 the instantaneous, mean and root mean square of the velocity magnitude of A-PROJ-M4 and A-3D-M4 at specific cross-sections are visualized. A clear jet-like structure is observed for both cases up to 0.4D downstream of the valve. The high-velocity core slowly dissipates, and at $x/D = 1.0$ and $x/D = 2.0$ is not visible anymore. Large RMS values throughout the cross section indicate that jet breakdown was initiated.

The instantaneous contours of A-PROJ-M4 suggest that the jet was rotating clockwise

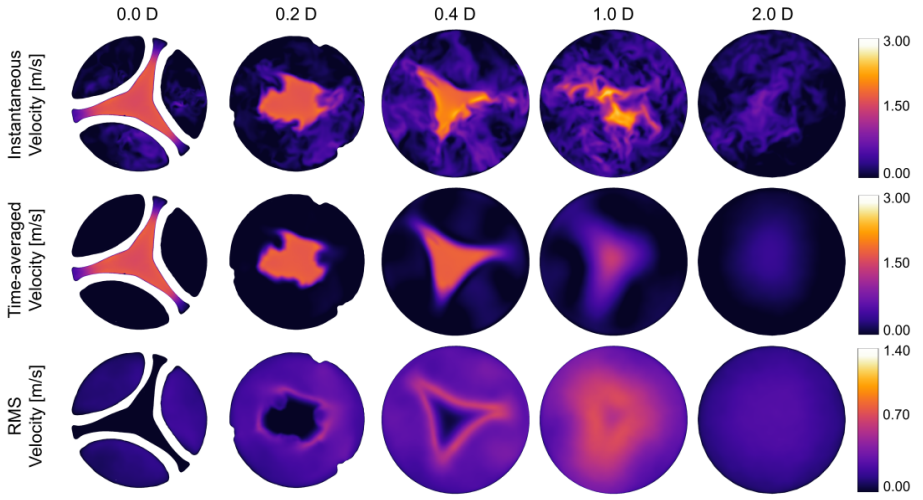

Figure 5.11 Contours along the centerline of instantaneous (top row - T=6s), time-averaged (middle row) and root mean square (bottom row) of the velocity magnitude (A-3D-M4).

at that time instance. However, the time-averaged contours at 0.2D do not show this rotation, suggesting that this was averaged out over time, and may be caused by a counter-clockwise, and clockwise alternation of the jet. This appears to influence the centerline velocity downstream, i.e., low-frequency behavior is observed in the tracings of Figure 5.3 at x/D=1.0 and x/D=2.0.

Instantaneous and time-averaged contours of A-3D-M4 illustrate that there was a transition from a triangular shaped jet, to a triangular shaped jet that was rotated 180 degrees around the centerline. This apparent 180 degrees rotation may be a result of radial momentum provoked by the presence of the leaflets, essentially carrying flow to the opposite side of the vessel. As expected, RMS values show that velocity fluctuations were particularly strong at the edge of the (stable) core-region of the jet. Similar to A-PROJ-M4, jet breakdown of A-3D-M4 occurs approximately 1.0D downstream of the valve. Furthermore, RMS values around the core of the jet at 0.4D demonstrate that instabilities of the turbulence-triggering shear layer seem to be captured with the finest grid level.

Results for B-3D-M4 are not shown, but showed similar patterns, with the exception that velocities and RMS of velocity fluctuations were lower, and jet breakdown occurs further downstream, e.g., see evolution of centerline k in Figure 5.8.

Table 5.2 Simulation results for pulsatile simulations

	Flow Type	Sim. Type	Q_{mean} [Lmin^{-1}]	Q_{max} [Lmin^{-1}]	Re [-]	$\|\overline{\mathbf{u}}_{ens}\|_{max}$ [ms^{-1}]	ΔP_{mean} [†] [mmHg]	ΔP_{peak} [‡] [mmHg]	ΔP^{*}_{max} [mmHg]	k_{max} [m^{2}s^{-2}]
A-3D-M3	pulsatile	LES	3.5	7.0	2700	2.07	4.5	12.4	13.2	0.304
B-3D-M3	pulsatile	LES	3.5	7.0	2700	0.72	0.4	1.2	4.3	0.036

† Mean pressure-drop over systole
‡ Pressure-drop at peak-systole. i.e. no acceleration or deceleration
* Maximum observed pressure-drop in acceleration phase. I.e. Acceleration effects are included in the pressure-drop.

5.4 DISCUSSION

The main aim of this study was to numerically compute and characterize the turbulent flow downstream of four aortic-valve-like geometries in steady and pulsatile flow conditions. This was done in order to establish the validity of steady-flow assumptions in cardiovascular modeling. Fluctuations in the steady turbulent flow and pulsatile intermittent turbulent flow were characterized by means of power-spectra at specific locations along the centerline. Additionally, the distribution of turbulent kinetic energy along the centerline was presented. It was demonstrated that substantial differences in power spectra, pressure-drop, and turbulent kinetic energy can be expected when simplifying the complex valvular shape to orifice-plate type geometries. Additionally, from the power spectra it was observed that turbulent fluctuations were particularly strong for stenotic valves. Turbulent kinetic energy along the centerline is substantially higher for the stenotic configuration (valve A) compared to the healthy configuration (valve B). An order-of-magnitude difference is observed when an inflow Reynolds number of 5400 is used.

In pulsatile flow conditions, deceleration initiates or amplifies fluctuations and turbulent kinetic energy. Acceleration has a stabilizing effect. Nevertheless, substantial fluctuations were observed downstream of the stenotic valve during flow acceleration. In the healthy valve, fluctuations were only triggered upon onset of the deceleration phase.

5.4.1 NUMERICS

Blood flow in the cardiovascular system is mostly low-Reynolds number laminar pulsating flow. However, a stenosis of the blood vessel may cause flow separation, recirculation, and together with the pulsating nature of blood flow may cause intermittent transition to turbulence in large vessels. For example, it has been observed that (transitional) turbulent

Table 5.3 Simulation results for all steady-state simulations

Name	Flow Type	Simulation Type	Q [Lmin^{-1}]	Re [-]	$\|\overline{\mathbf{u}}\|_{\max}$ [ms^{-1}]	$\Delta P^{\dagger}$ [mmHg]	$k_{\max}{}^{\ddagger}$ [m^{2}s^{-2}]
A-3D-M1	steady-state	LES	7.0	5400	1.92	12.3	0.062
A-3D-M2	steady-state	LES	7.0	5400	1.98	12.3	0.174
A-3D-M3	steady-state	LES	7.0	5400	1.98	12.3	0.221
A-3D-M4	steady-state	LES	7.0	5400	2.00	12.3	0.211
A-3D-M3	steady-state	LES	3.5	2700	1.00	3.1	0.055
A-3D-M4	steady-state	LES	3.5	2700	1.00	3.1	0.058
B-3D-M3	steady-state	LES	7.0	5400	0.73	1.2	0.022
B-3D-M3	steady-state	LES	3.5	2700	0.37	0.3	0.006
B-3D-M4	steady-state	LES	7.0	5400	0.72	1.2	0.021
B-3D-M4	steady-state	LES	3.5	2700	0.37	0.3	0.006
A-3D-M1	steady-state	RANS SST $k-\omega$	7.0	5400	1.91	12.4	0.180
A-3D-M2	steady-state	RANS SST $k-\omega$	7.0	5400	1.96	12.4	0.170
A-3D-M3	steady-state	RANS SST $k-\omega$	7.0	5400	1.96	12.3	0.161
A-3D-M4	steady-state	RANS SST $k-\omega$	7.0	5400	1.98	12.4	0.156
B-3D-M4	steady-state	RANS SST $k-\omega$	7.0	5400	0.72	1.2	0.012
A-3D-M1	steady-state	RANS SST $k-\omega$	3.5	2700	0.96	3.1	0.044
A-3D-M2	steady-state	RANS SST $k-\omega$	3.5	2700	0.99	3.1	0.042
A-3D-M3	steady-state	RANS SST $k-\omega$	3.5	2700	0.99	3.1	0.039
A-3D-M4	steady-state	RANS SST $k-\omega$	3.5	2700	0.99	3.2	0.040
B-3D-M4	steady-state	RANS SST $k-\omega$	3.5	2700	0.37	0.3	0.003
A-PROJ-M1	steady-state	LES	7.0	5400	2.69	22.7	0.188
A-PROJ-M2	steady-state	LES	7.0	5400	2.71	23.2	0.398
A-PROJ-M3	steady-state	LES	7.0	5400	2.74	24.8	0.501
A-PROJ-M4	steady-state	LES	7.0	5400	2.69	23.4	0.522
B-PROJ-M4	steady-state	LES	7.0	5400	0.94	2.3	0.063
A-PROJ-M1	steady-state	RANS SST $k-\omega$	7.0	5400	2.72	22.7	0.197
A-PROJ-M2	steady-state	RANS SST $k-\omega$	7.0	5400	2.72	22.8	0.317
A-PROJ-M3	steady-state	RANS SST $k-\omega$	7.0	5400	2.74	23.6	0.346
A-PROJ-M4	steady-state	RANS SST $k-\omega$	7.0	5400	2.72	23.3	0.421

† Represents the time-averaged pressure-drop over 4 seconds.
‡ Maximum turbulent kinetic energy along the centerline. k is computed by Equation 5.13.

flow may occur downstream of both healthy as stenotic heart valves (Nygaard et al. 1994; Stein and Sabbah 1976). Several attempts were made to model such flows through DNS. For example, Varghese and colleagues performed both steady-state (Varghese et al. 2007a) and pulsatile (Varghese et al. 2007b) simulations in an idealized axi-symmetric and eccentric 75% stenosed vessels at inlet Reynolds numbers of 1000. It was observed that the jet transitioned to full turbulence at about x/D=5 downstream of the stenosis. In a similar numerical study, Khair et al. observed a peak in turbulent kinetic energy two channel heights downstream of a 75% stenosis (Khair et al. 2015) at a Reynolds number of 2000.

Similar observations were made in this study. A peak in turbulent kinetic energy at x/D=2.0 was found for valve B. However, with more severe constrictions (valve A), jet break-down occurred closer to the valve, typically around x/D=1.0. This indicates that jet formation for healthy valves is present, but that such a jet is typically more stable than for stenotic valves, and yields turbulent fluctuations of substantially lower intensity.

5.4.2 STEADY VS. PULSATILE FLOW

From experimental and numerical studies it is known that pulsatility of cardiovascular flows has a suppressing effect on turbulence production (Varghese et al. 2007a; Sherwin and Blackburn 2005; Bluestein and Einav 1995). That is, turbulent fluctuations are stabilized in the accelerating phase of the cycle. Consequently, at peak-systole, the adverse pressure-gradient destabilizes the flow, and turbulence is triggered. Subsequently, in diastole flow loses momentum, and the flow field will relaminarize. This process is further stimulated during the acceleration phase of the next cardiac cycle. Similar behavior is observed in the presented numerical simulations. Even though the inflow Reynolds number is expected to be in the turbulent regime, valve A does not exhibit random fluctuations in a large part of the acceleration phase, but instabilities in the flow field were only observed late in the acceleration phase. Fluctuations were further amplified upon onset of deceleration. This is in line with DNS simulations by Varghese et al. (2007b), who observed similar behavior in a pulsating flow through a 75% stenosis at (inlet-based) peak Reynolds numbers of 1000. Although their lower Reynolds number meant that these fluctuations were observed further downstream, i.e., at $x/D \geq$4 and $x/D \leq$8.

These numerical results are also in line with *in-vivo* and *in-vitro* studies. Stein and Sabbah (1976) showed that for diseased valves turbulent fluctuations close to the valve and in the ascending aorta were present throughout ejection. For healthy cases, downstream turbulence dissipated more quickly. Additionally, Walburn et al. (1983) showed that close to healthy aortic valves turbulent fluctuations may occur, that stabilize in early

systole. Bluestein and Einav (1995) was able to replicate this effect in an *in-vitro* study as well, and showed that the root mean square of velocity fluctuations, measured 30 mm (approximately 1 diameter) downstream, substantially reduced during acceleration, but was elevated again in the decelerating phase. Root mean square values between 0.4 and 1.5 m/s were found for a 90% stenosis, and 0.25-1.5 m/s for a 65% stenosis, which seems to correspond to the RMS values found in our steady-state simulations.

Figure 5.7 reveals that the frequency and power of velocity fluctuations of pulsatile flow seems to correspond better to steady flow with mean systolic flow rate, opposed to peak systolic flow rate. Additionally, Figure 5.9 corroborates earlier observations by Bluestein and Einav (1995) and Yamaguchi et al. (1983), who observed that turbulence peaked during the deceleration phase. This study clearly demonstrated that peak turbulence in stenotic heart valves occured just after peak systole, whereas in healthy valves peak systolic velocity fluctuations were relatively low, and were triggered in late systole. Similar to the steady flow conditions, k may be an order of magnitude higher in stenotic heart valves compared to healthy valves.

5.4.3 PROJECTION VS. 3D CONFIGURATION

It is well established that valvular shape substantially affects the instantaneous pressure-drop over the aortic valve. For example, Gilon et al. (2002) found that dome-shaped valves exhibit a substantially higher coefficient of contraction compared to flattened valves with the same anatomic orifice area. Differences of up to 40% in pressure-drop were observed. Furthermore, *in-vitro* work by Garcia and colleagues showed that a contraction coefficient of 0.6 can be expected for circular flat-plate orifices, and approximately 1 for funnel-type orifices (Garcia et al. 2004; Garcia and Kadem 2006). This is in line with the findings in the current study. Indeed, the pressure-drop computed for the 3D valvular shapes is much lower than for the projected cases due to the contraction coefficient being closer to unity. Furthermore, the results of this study suggests that a straightforward projection would lead to a severe overestimation of expected turbulent kinetic energy. Contour plots of the RMS (Figure 5.10 and 5.11) suggest that velocity fluctuations in the shear layer are considerably higher for the projected case. Due to the lower jet velocity of the 3D configuration, jet velocity (and thus jet Reynolds number) is lower, and consequently fluctuations in the shear layer are substantially lower as well. Hence, careful consideration is needed when designing *in-vitro* validation studies that aim to replicate *in-vivo* flow conditions. For example, Ha et al. (2018a) used simple 3D printed circular orifice models in an *in-vitro* setup, and assessed the generation of turbulent kinetic energy in the shear-layer through pc-MRI. Due to the effect of valvular shape on turbulence production, extrapolation of those results to the *in-vivo* situation should be done with caution.

5.4.4 TURBULENCE MODELING

Modeling turbulent flows is typically done with RANS, LES, or DNS. However consensus on the best approach seems to be absent. For example, results from a inter-laboratory study by the Food and Drug Administration demonstrated that 26 out of 28 participants used RANS models when asked to solve the turbulent flow (Reynolds numbers between 3500 and 6500) in a device that contains a nozzle and sudden expansion (Stewart et al. 2012). Flow through such a device shows some similarities to flow through the aortic valve. Furthermore, results of Stewart et al. (2012) show a wide spread in agreement between experiments and RANS simulations, specifically for Reynolds numbers below 3500. Better agreement between experimental observations and numerical results were found at higher Reynolds numbers (6500). Demonstrating that even though CFD modeling is widely used, tackling turbulent flows is still challenging. Our results, and the results by Stewart et al. (2012) show that RANS models should be used carefully, and comparison with high quality scale-resolving simulations is desirable, in particular for flows that are in the transitional regime. Nevertheless, when interested in the transvalvular pressure-drop, RANS simulations seem to yield adequate results when compared to the, computationally much more expensive, scale-resolving methods.

Several other studies have suggested the use of compute-intensive scale-resolving methods such as LES (Bergersen et al. 2018; Janiga 2014) or even DNS (Abad et al. 2020). But these studies have demonstrated that even with these more accurate models, prediction of jet-breakdown is not guaranteed for low Reynolds numbers. For example, Bergersen et al. (2018) observed that by refining the mesh, jet breakdown unexpectedly shifted further downstream. Similarly, DNS simulations of Abad et al. (2020) demonstrated similar behavior for throat Reynolds numbers of 5000, more-accurate higher order spectral elements (polynomial order 7) predicted jet-transition to be further downstream than experimental observations. This demonstrates that even with scale-resolving methods, correct prediction of flow physics is not guaranteed, and results should be scrutinized.

5.4.5 TRANSVALVULAR PRESSURE-DROP

The transvalvular pressure-drop and mean transvalvular pressure-drop are well established indicators of aortic valve stenosis severity. Typical peak pressure-drop values measured in patients with aortic stenosis range between 40-65 mmHg for moderate aortic stenosis. Severe aortic stenosis is classified by a peak pressure-drop larger than 65 mmHg (Bohbot et al. 2017; Falk et al. 2017; Nishimura et al. 2014; Baumgartner et al. 2016), and can sometimes even exceed 100 mmHg for some extreme cases (Yang et al. 2015).

The simulated pressure-drops in this study are substantially lower. And one could argue that the simulated flow conditions are therefor not in the physiological range for aortic valve stenosis. However, to facilitate comparisons with *in-vitro* measurements, water-like fluid properties were chosen (**Chapter 6**). Consequently, boundary conditions were adjusted to make sure that the Reynolds number in the simulation matched with the Reynolds number expected for physiological flow conditions, i.e., a physiological cardiac output of 23 Lmin^{-1}, density of 1060 kg/m^2, and viscosity of 0.0035 Pa·s. Hence, the magnitude of the velocity is lower than the *in-vivo* situation, which in turn results in a lower pressure-drop. For flows where dynamic effects are dominant, the pressure is typically scaled with ρU^2. Hence, the simulated pressure-drop can be scaled back to the expected *in-vivo* scale by: $\Delta P_p = \Delta P_m \frac{\rho_p U_p^2}{\rho_m U_m^2} \approx 12 \Delta P_m$. Where the subscripts p represents the physiological density and characteristic velocity, and subscript m indicates the density and characteristic velocity of the simulations.

When taking this pressure-scaling into account, the pressure losses correspond to those that are typically observed in patients with mild or severely stenotic heart valves. Clearly, valve A is at the extreme side of the clinical spectrum with a re-scaled pressure-drop of $12 \cdot 12.4 \approx 150$ mmHg. Similarly, valve B can be considered healthy or mildly stenosed with a re-scaled pressure-drop of $12 \cdot 1.2 \approx 14$ mmHg.

5.4.6 LIMITATIONS

The main limitation in the current study is the absence of the opening- and closing function of the aortic valve during the pulsatile flow condition. Additionally, it was assumed that the aortic valve opening area remains consistent irrespective of flow rate. However, results from dobutamine stress studies in aortic stenosis patients have demonstrated that valve opening area is a function of flow-rate, and may show strong intra-patient variability (Johnson et al. 2018; Takeda et al. 2001; Blais et al. 2006). Additionally, variations in the aortic root were not considered in the present work. The shape of the aorta and aortic root may have considerable effects on the generation of Reynolds shear stresses (Barannyk and Oshkai 2015; Zhu et al. 2018).

In addition, any non-Newtonian effects (e.g., shear-thinning) were neglected. It is well known that blood behaves as a non-Newtonian fluid (Long et al. 2005). It has been shown that non-Newtonian effects may affect the flow field for abdominal aneurysms (Deplano et al. 2014), or may prolong flow stabilization in stenosed vessels (Walker et al. 2013). Although non-Newtonian behavior may affect the flow field locally, it was shown that the transvalvular pressure-drop remains insensitive to non-Newtonian behavior (Vita

et al. 2015).

5.4.7 CONCLUSION

This study numerically computed and characterized turbulent flow downstream of four rigid aortic valve-like geometries. Simplification of the aortic valve geometry to an orifice plate-type geometry by projection results in a significant overestimation of velocity fluctuations, and pressure-drop, and should be avoided. Additionally, it was demonstrated that both stenotic and healthy aortic valves exhibit significant fluctuations downstream of the valve, both in steady as pulsatile flow conditions. In pulsatile flow conditions, fluctuations are either triggered (healthy valve), or amplified (stenotic valve) in the deceleration phase. During flow acceleration and in the diastolic phase fluctuations were mostly absent. Turbulent kinetic energy can be an order of magnitude higher in severely stenotic valves, in both steady as pulsatile flow conditions. Finally, RANS simulations yield similar peak-systolic transvalvular pressure-drops as LES simulations, and may thus be a computationally efficient alternative to predict the peak-systolic transvalvular pressure-drop.

ACKNOWLEDGEMENTS

The authors would like to thank J. Weese and I. Waechter-Stehle of Philips Research in Hamburg for providing the necessary data to generate the geometries of the aortic valve.

BIBLIOGRAPHY

Abad, N. S. et al. (2020). "Simulation strategies for the food and drug administration nozzle using nek5000". In: *AIP Advances* 10.2, p. 025033.

Alfonsi, G. (2009). "Reynolds-averaged navier–stokes equations for turbulence modeling". In: *Applied Mechanics Reviews* 62.4.

Andersson, M. et al. (2017). "Multidirectional WSS disturbances in stenotic turbulent flows: a pre- and post-intervention study in an aortic coarctation". In: *Journal of Biomechanics* 51, pp. 8–16.

Armfield, S. and R. Street (1999). "The fractional-step method for the navier–stokes equations on staggered grids: the accuracy of three variations". In: *Journal of Computational Physics* 153.2, pp. 660–665.

Arzani, A. et al. (2011). "In vivo validation of numerical prediction for turbulence intensity in an aortic coarctation". In: *Annals of Biomedical Engineering* 40.4, pp. 860–870.

Bahlmann, E. et al. (2010). "Impact of pressure recovery on echocardiographic assessment of asymptomatic aortic stenosis: a SEAS substudy". In: *JACC: Cardiovascular Imaging* 3.6, pp. 555–562.

Barannyk, O. and P. Oshkai (2015). "The influence of the aortic root geometry on flow characteristics of a prosthetic heart valve". In: *Journal of Biomechanical Engineering* 137.5.

Baumgartner, H. et al. (1999). ""overestimation" of catheter gradients by doppler ultrasound in patients with aortic stenosis: a predictable manifestation of pressure recovery." In: *Journal of the American College of Cardiology* 33 (6), pp. 1655–1661.

Baumgartner, H. et al. (2016). "Recommendations on the echocardiographic assessment of aortic valve stenosis: a focused update from the european association of cardiovascular imaging and the american society of echocardiography". In: *European Heart Journal - Cardiovascular Imaging* 18.3, pp. 254–275.

Bergersen, A. W., M. Mortensen, and K. Valen-Sendstad (2018). "The FDA nozzle benchmark: "in theory there is no difference between theory and practice, but in practice there is"". In: *International Journal for Numerical Methods in Biomedical Engineering* 35.1, e3150.

Binter, C. et al. (2015). "On the accuracy of viscous and turbulent loss quantification in stenotic aortic flow using phase-contrast MRI". in: *Magnetic Resonance in Medicine* 76.1, pp. 191–196.

Blais, C. et al. (2006). "Projected valve area at normal flow rate improves the assessment of stenosis severity in patients with low-flow, low-gradient aortic stenosis". In: *Circulation* 113.5, pp. 711–721.

Bluestein, D. and S. Einav (1995). "The effect of varying degrees of stenosis on the characteristics of turbulent pulsatile flow through heart valves". In: *Journal of Biomechanics* 28.8, pp. 915–924.

Bohbot, Y. et al. (2017). "Impact of mean transaortic pressure gradient on long-term outcome in patients with severe aortic stenosis and preserved left ventricular ejection fraction". In: *Journal of the American Heart Association* 6.6, e005850.

Chant, L. J. D. (2005). "The venerable 1/7th power law turbulent velocity profile: a classical nonlinear boundary value problem solution and its relationship to stochastic processes". In: *Applied Mathematics and Computation* 161.2, pp. 463–474.

Clark, C. (1976). "Turbulent velocity measurements in a model of aortic stenosis". In: *Journal of Biomechanics* 9.11, pp. 677–687.

Dangas, G. D. et al. (2016). "Prosthetic heart valve thrombosis". In: *Journal of the American College of Cardiology* 68.24, pp. 2670–2689.

Deplano, V. et al. (2014). "Flow of a blood analogue fluid in a compliant abdominal aortic aneurysm model: experimental modelling". In: *Journal of Biomechanics* 47.6, pp. 1262–1269.

Ecabert, O. et al. (2011). "Segmentation of the heart and great vessels in CT images using a model-based adaptation framework". In: *Medical Image Analysis* 15.6, pp. 863–876.

Falk, V. et al. (2017). "2017 ESC/EACTS guidelines for the management of valvular heart disease". In: *European Journal of Cardio-Thoracic Surgery* 52.4, pp. 616–664.

Garcia, D. and L. Kadem (2006). "What do you mean by aortic valve area: geometric orifice area, effective orifice area, or gorlin area?" In: *The Journal of heart valve disease* 15 (5), pp. 601–608.

Garcia, D. et al. (2004). "Estimation of aortic valve effective orifice area by doppler echocardiography: effects of valve inflow shape and flow rate". In: *Journal of the American Society of Echocardiography* 17.7, pp. 756–765.

Gilmanov, A. et al. (2019). "Image-guided fluid-structure interaction simulation of transvalvular hemodynamics: quantifying the effects of varying aortic valve leaflet thickness". In: *Fluids* 4.3, p. 119.

Gilon, D. et al. (2002). "Effect of three-dimensional valve shape on the hemodynamics of aortic stenosis". In: *Journal of the American College of Cardiology* 40.8, pp. 1479–1486.

Goubergrits, L. et al. (2013). "The impact of MRI-based inflow for the hemodynamic evaluation of aortic coarctation". In: *Annals of Biomedical Engineering* 41.12, pp. 2575–2587.

Ha, H. et al. (2018a). "Validation of pressure drop assessment using 4d flow MRI-based turbulence production in various shapes of aortic stenoses". In: *Magnetic Resonance in Medicine* 81.2, pp. 893–906.

Ha, H. et al. (2016). "Turbulent kinetic energy measurement using phase contrast MRI for estimating the post-stenotic pressure drop: in vitro validation and clinical application". In: *PLOS ONE* 11.3. Ed. by J. C. del Alamo, e0151540.

Ha, H. et al. (2018b). "Age-related vascular changes affect turbulence in aortic blood flow". In: *Frontiers in Physiology* 9.

Hinze, J. O. (1975). *Turbulence*. McGraw-Hill.

Hoeijmakers, M. J. M. M. et al. (2019). "Estimation of valvular resistance of segmented aortic valves using computational fluid dynamics". In: *Journal of Biomechanics*.

Janiga, G. (2014). "Large eddy simulation of the FDA benchmark nozzle for a reynolds number of 6500". In: *Computers in Biology and Medicine* 47, pp. 113–119.

Johnson, N. P. et al. (2018). "Pressure gradient vs. flow relationships to characterize the physiology of a severely stenotic aortic valve before and after transcatheter valve implantation". In: *European Heart Journal*.

Kameneva, M. V. et al. (2004). "Effects of turbulent stresses upon mechanical hemolysis: experimental and computational analysis". In: *ASAIO Journal* 50.5, pp. 418–423.

Khair, A., B.-C. Wang, and D. C. S. Kuhn (2015). "Study of laminar–turbulent flow transition under pulsatile conditions in a constricted channel". In: *International Journal of Computational Fluid Dynamics* 29.9-10, pp. 447–463.

Lantz, J. et al. (2013). "Numerical and experimental assessment of turbulent kinetic energy in an aortic coarctation". In: *Journal of Biomechanics* 46.11, pp. 1851–1858.

Launder, B. E. and D. B. Spalding (1974). "The numerical computation of turbulent flows". In: *Computer Methods in Applied Mechanics and Engineering* 3.2, pp. 269–289.

Lilly, D. K. (1992). "A proposed modification of the germano subgrid-scale closure method". In: *Physics of Fluids A: Fluid Dynamics* 4.3, pp. 633–635.

Long, J. A. et al. (2005). "Viscoelasticity of pediatric blood and its implications for the testing of a pulsatile pediatric blood pump". In: *ASAIO Journal* 51.5, pp. 563–566.

Luraghi, G. et al. (2019). "On the modeling of patient-specific transcatheter aortic valve replacement: a fluid-structure interaction approach". In: *Cardiovascular Engineering and Technology* 10.3, pp. 437–455.

Menter, F. R. (1994). "Two-equation eddy-viscosity turbulence models for engineering applications". In: *AIAA Journal* 32.8, pp. 1598–1605.

Mittal, R., S. P. Simmons, and F. Najjar (2003). "Numerical study of pulsatile flow in a constricted channel". In: *Journal of Fluid Mechanics* 485, pp. 337–378.

Niederberger, J. et al. (1996). "Importance of pressure recovery for the assessment of aortic stenosis by doppler ultrasound. role of aortic size, aortic valve area, and direction of the stenotic jet in vitro." In: *Circulation* 94 (8), pp. 1934–1940.

Nishimura, R. A. et al. (2014). "2014 AHA/ACC guideline for the management of patients with valvular heart disease". In: *Journal of the American College of Cardiology* 63.22, e57–e185.

Nkomo, V. T. et al. (2006). "Burden of valvular heart diseases: a population-based study." In: *Lancet* 368 (9540), pp. 1005–1011.

Nygaard, H. et al. (1992). "Quantitation of the turbulent stress distribution downstream of normal, diseased and artificial aortic valves in humans". In: *European Journal of Cardio-Thoracic Surgery* 6.11, pp. 609–617.

Nygaard, H. et al. (1994). "Turbulent stresses downstream of three mechanical aortic valve prostheses in human beings." In: *The Journal of thoracic and cardiovascular surgery* 107 (2), pp. 438–446.

Okura, H. et al. (1997). "Planimetry and transthoracic two-dimensional echocardiography in noninvasive assessment of aortic valve area in patients with valvular aortic stenosis". In: *Journal of the American College of Cardiology* 30.3, pp. 753–759.

Olufsen, M. S. et al. (2000). "Numerical simulation and experimental validation of blood flow in arteries with structured-tree outflow conditions". In: *Annals of Biomedical Engineering* 28.11, pp. 1281–1299.

Sallam, A. M. and N. H. C. Hwang (1984). "Human red blood cell hemolysis in a turbulent shear flow: contribution of reynolds shear stresses". In: *Biorheology* 21.6, pp. 783–797.

Scotti, A. and U. Piomelli (2001). "Numerical simulation of pulsating turbulent channel flow". In: *Physics of Fluids* 13.5, pp. 1367–1384.

Shah, R. G. et al. (2009). "Aortic valve area: meta-analysis of diagnostic performance of multi-detector computed tomography for aortic valve area measurements as compared to transthoracic echocardiography". In: *The International Journal of Cardiovascular Imaging* 25.6, pp. 601–609.

Sherwin, S. J. and H. M. Blackburn (2005). "Three-dimensional instabilities and transition of steady and pulsatile axisymmetric stenotic flows". In: *Journal of Fluid Mechanics* 533.

Stein, P. D. and H. N. Sabbah (1976). "Turbulent blood flow in the ascending aorta of humans with normal and diseased aortic valves". In: *Circulation Research* 39.1, pp. 58–65.

Stein, P. D. and H. N. Sabbah (1974). "Measured turbulence and its effect on thrombus formation". In: *Circulation Research* 35.4, pp. 608–614.

Stewart, S. F. C. et al. (2012). "Assessment of CFD performance in simulations of an idealized medical device: results of FDA's first computational interlaboratory study". In: *Cardiovascular Engineering and Technology* 3.2, pp. 139–160.

Takeda, S., H. Rimington, and J. Chambers (2001). "Prediction of symptom-onset in aortic stenosis: a comparison of pressure drop/flow slope and haemodynamic measures at rest". In: *International Journal of Cardiology* 81.2-3,

pp. 131–137.

Vahanian, A. et al. (2012). "Guidelines on the management of valvular heart disease (version 2012): the joint task force on the management of valvular heart disease of the european society of cardiology (ESC) and the european association for cardio-thoracic surgery (EACTS)". in: *European Heart Journal* 33.19, pp. 2451–2496.

Varghese, S. S. and S. H. Frankel (2003). "Numerical modeling of pulsatile turbulent flow in stenotic vessels". In: *Journal of Biomechanical Engineering* 125.4, pp. 445–460.

Varghese, S. S., S. H. Frankel, and P. F. Fischer (2007a). "Direct numerical simulation of stenotic flows. part 1. steady flow". In: *Journal of Fluid Mechanics* 582, pp. 253–280.

— (2007b). "Direct numerical simulation of stenotic flows. part 2. pulsatile flow". In: *Journal of Fluid Mechanics* 582, pp. 281–318.

Vita, F. D., M. D. de Tullio, and R. Verzicco (2015). "Numerical simulation of the non-newtonian blood flow through a mechanical aortic valve". In: *Theoretical and Computational Fluid Dynamics* 30.1-2, pp. 129–138.

Walburn, F. J., H. N. Sabbah, and P. D. Stein (1983). "An experimental evaluation of the use of an ensemble average for the calculation of turbulence in pulsatile flow". In: *Annals of Biomedical Engineering* 11.5, pp. 385–399.

Walker, A. M., C. R. Johnston, and D. E. Rival (2013). "On the characterization of a non-newtonian blood analog and its response to pulsatile flow downstream of a simplified stenosis". In: *Annals of Biomedical Engineering* 42.1, pp. 97–109.

Weese, J. et al. (2017). "CFD- and bernoulli-based pressure drop estimates: a comparison using patient anatomies from heart and aortic valve segmentation of CT images". In: *Medical Physics* 44.6, pp. 2281–2292.

Welch, P. (1967). "The use of fast fourier transform for the estimation of power spectra: a method based on time averaging over short, modified periodograms". In: *IEEE Transactions on Audio and Electroacoustics* 15.2, pp. 70–73.

Wendell, D. C. et al. (2013). "Including aortic valve morphology in computational fluid dynamics simulations: initial findings and application to aortic coarctation". In: *Medical Engineering & Physics* 35.6, pp. 723–735.

Yamaguchi, T. et al. (1983). "Measurement of turbulence intensity in the center of the canine ascending aorta with a hot-film anemometer". In: *Journal of Biomechanical Engineering* 105.2, pp. 177–187.

Yang, C.-S. et al. (2015). "Discrepancies between direct catheter and echocardiography-based values in aortic stenosis". In: *Catheterization and Cardiovascular Interventions* 87.3, pp. 488–497.

Yoganathan, A. P., K. B. Chandran, and F. Sotiropoulos (2005). "Flow in prosthetic heart valves: state-of-the-art and future directions". In: *Annals of Biomedical Engineering* 33.12, pp. 1689–1694.

Yoganathan, A. P., W. H. Corcoran, and E. C. Harrison (1979). "In vitro velocity measurements in the vicinity of aortic prostheses". In: *Journal of Biomechanics* 12.2, pp. 135–152.

Zhu, C., J.-H. Seo, and R. Mittal (2018). "Computational modelling and analysis of haemodynamics in a simple model of aortic stenosis". In: *Journal of Fluid Mechanics* 851, pp. 23–49.

Chapter 6

Experimental validation of the simulated transvalvular pressure-drop in steady and pulsatile flow conditions

This chapter is based on: **M.J.M.M. Hoeijmakers**, M.C.M. Rutten, F.N. van de Vosse. Experimental validation of the simulated transvalvular pressure-drop of healthy and stenosed heart valves in steady and pulsatile flow conditions. *In preparation*

ABSTRACT

Background The transvalvular pressure-drop is a key indicator for aortic valve stenosis severity, and as such of clinical interest. Accurate assessment of the transvalvular pressure-drop requires catheterization, an invasive procedure. Doppler echocardiography allows for non-invasive assessment, but accurate assessment of the irreversible pressure-drop is challenging. However, recent developments in medical imaging, segmentation techniques, and Computational Fluid Dynamics (CFD), provide an alternative for non-invasive assessment of the transvalvular pressure-drop. But flow through the aortic valve is complex, and modeling strategies need to be validated with experimental data. Hence, the aim of this work was to validate the CFD computed transvalvular pressure-drop with *in-vitro* experimental data. **Methods** Four 3D valves with opening areas of 70, 122, 175, and 230 mm^2, and their projected counterparts were printed with a 3D printer. A gear-pump driven flow-circuit was designed and used for steady and pulsatile flow generation. Two pressure transducers, placed at 1.7 diameters upstream of the valve and 20 diameters downstream of the valve, were used to evaluate the (recovered) transvalvular pressure-drop in steady and pulsatile flow conditions. Reynolds numbers of 2700 and 5400 were considered. Eight CFD models were developed that corresponded to the *in-vitro* models. Steady flow conditions were simulated with the Shear Stress Transport $k-\omega$ model, and pulsatile flow conditions with Large Eddy Simulation. **Results** Projection of valve area lead to an overestimation of ΔP between 28 and 82%, and depended on valve area magnitude. For stenotic valves (70 mm^2) good agreement between computed and experimentally obtained maximum and peak-systolic transvalvular pressure-drops was found. The maximum transvalvular pressure-drop occurred before peak-systole. CFD models tended to underestimate steady and peak-systolic ΔP, but adequately captured the pressure-drop waveform in pulsatile flow conditions. **Conclusion** In stenotic aortic valves, the pressure-drop was dominated by the narrowing of the valve. However, with increasing valve area, the pressure loss due to the valve became lower, while unsteadiness became more important, and should be included to obtain a good estimate of the pressure-drop. CFD models tended to underestimate steady and peak-systolic ΔP, regardless of model choice, but adequately captured the pressure-drop waveform in pulsatile flow conditions.

6.1 INTRODUCTION

Aortic valve stenosis is characterized by a narrowing of the aortic valve opening area in systole. As a result, the transvalvular pressure drop and load on the left ventricle is increased. The increased load on the heart induces a hypertrophic response, thickening the heart muscle which may eventually lead to heart failure, limiting the day-to-day activities of a patient. Clinically, the transvalvular pressure-drop is used to assess the severity of aortic valve stenosis and to guide treatment strategies (Baumgartner et al. 2016).

In the past, the transvalvular pressure-drop was obtained by cardiac catheterization (Nishimura and Carabello 2012). However, in current clinical practice the transvalvular pressure-drop is estimated by Doppler echocardiography, which allows for cheap non-invasive assessment of the pressure-drop (Nishimura and Tajik 1994). With Doppler echocardiography the velocity of blood through the valve is measured. Consequently, this velocity is used in combination with the simplified Bernoulli equation, and an estimate of the transvalvular pressure-drop is obtained ($\Delta P = 4v^2$, with v the measured velocity) (Hatle et al. 1980). The simplified Bernoulli method assumes that when flow accelerates into the orifice, energy conversion from potential to kinetic energy in the constriction is irreversible. However, numerous studies have shown that pressure-recovery downstream of the stenotic valve can be considerable, leading to Doppler echocardiography overestimating the severity of mild to moderate stenoses (Niederberger et al. 1996; Voelker et al. 1992; Bahlmann et al. 2010; Laskey and Kussmaul 1994). Hence, non-invasive alternatives that complement the Bernoulli equation in order to better reflect stenosis severity are desirable.

As one extension to the Bernoulli equation it has been proposed to take into account the post-stenotic pressure-recovery. For example, Garcia et al. (2000) proposed to extend the simplified Bernoulli equation by taking into account the effective orifice area of the stenosis and the cross sectional area of the ascending aorta (both approximated by echocardiography). This was shown to better reflect the severity of aortic valve stenosis. Similary, Ha et al. (2018) showed that phase-contrast resonance imaging (pc-MRI) can be used to non-invasively estimate the pressure-drop by evaluating turbulence production, good agreement with the extended Bernoulli equation of Garcia et al. (2000) was obtained. Alternatively, image-based three-dimensional computational fluid dynamics (CFD) can be used to approximate the patient-specific flow field. From these models an approximation of the patient-specific transvalvular pressure-drop can consequently be obtained (**Chapter 2** and **Chapter 3**).

Medical imaging techniques such as MRI and computed-tomography, enable detailed three-dimensional digital reconstructions of (specific) parts of the cardiovascular system. That is, medical images have been used to generate high quality and detailed surface models of — among others — the left ventricle, mitral valve and the aortic valve (Ionasec et al. 2010; Ecabert et al. 2008; Grbic et al. 2012). Consequently, such models can be used to simulate blood flow with CFD. Given a set of appropriate boundary conditions, CFD provides approximate solutions to the governing Navier-Stokes equations, yielding detailed information of the expected flow field. CFD models have been used to obtain an estimate of patient-specific flow patterns and transvalvular pressure-drops (Weese et al. 2017; Hoeijmakers et al. 2019; Hoeijmakers et al. 2020; Bruening et al. 2018). Although CFD is widely used for research purposes in the field of cardiovascular research, it is still an intricate tool where model simplifications are often a necessity to keep computational cost reasonable. Some typical simplifications include: 1) assuming fully developed turbulence; 2) neglecting flow pulsatility; 3) neglecting non-Newtonian behavior; and 4) neglecting vessel compliance. Hence, modeling work should ideally be closely integrated with and guided by *in-vitro* and *in-vivo* experimental validation to determine the most appropriate modeling approach.

Anatomical structures are often of complex shape, and it is challenging to create an accurate physical model of the patient-specific geometry for *in-vitro* validation studies. However, with developments in 3D printing — an additive manufacturing technique — generation of physical models has become much more accessible. For example, 3D printing has been used to generate patient-specific molds or models of coronaries, carotids, aortic and cerebral aneurysms, and aortic valves (Brunette et al. 2004; P. Cao et al. 2015; Sulaiman et al. 2008; Yagi et al. 2013; Ferrari et al. 2019; Zelis et al. 2020). In addition, these models can be used to study patient-specific hemodynamics, e.g., by Particle Image Velocimetry (PIV) (Yagi et al. 2013) or by pressure measurements (Zelis et al. 2020).

In previous chapters we have used CFD models in order to approximate the patient-specific transvalvular pressure-drop in steady (**Chapter 3**) or pulsatile flow conditions (**Chapters 2** and **5**). These chapters exclusively used numerical models to predict the pressure-drop. In this chapter we aim to validate the numerical models with *in-vitro* measurements. To achieve this, 3D printing was used to create physical models of the aortic valve, which were then inserted into an *in-vitro* setup that allowed pressure-drop measurements.

6.2 METHODS

6.2.1 AORTIC VALVE GEOMETRIES

The shape of the aortic valve leaflets was obtained from the statistical shape model that was used in **Chapters 3** and **4**. The statistical shape model was generated by making use of 74 aortic valve segmentations, which were obtained by the segmentation framework that is extensively described in previous work (Weese et al. 2017; Ecabert et al. 2011). Four aortic valves at different stages of opening were created with the statistical shape model (**Chapters 3** and **4**). The generated surface models of the aortic valve also included part of the left ventricular outflow tract, ascending aorta, and aortic sinuses. These parts were removed or modified such that the construct fitted in a circular support with an internal diameter of 24 mm, a length of 17 mm and thickness of 1 mm. Moreover, four models of the same valve, at different stages of opening, were created by taking a planar projection of the geometric opening area along the valve axis (Figure 5.1). Projected orifice areas were: 70 mm^2 (Valve A); 122 mm^2 (Valve B); 175 mm^2 (Valve C); and 230 mm^2 (Valve D), and represent several degrees of stenosis.

6.2.2 3D PRINTING

An Objet Connex 350 (Stratasys, Eden Prairie, USA) professional 3D printer was used to print all four (rigid) geometries out of VeroWhite, a photo-polymer. Minimum layer thickness was 16 μm, but actual printing accuracy was approximately 100 μm. To verify 3D printing accuracy, a Scanco Medical 100 μCT scanner (Brüttisellen, Switzerland) was used to generate a digital image with a resolution of 17 μm of the printed models. The resulting 3D images were segmented with 3D Slicer (Kikinis et al. 2013) with a fixed gray scale threshold. Segmentations were converted into a high-resolution stereo-lithography file.

6.2.3 EXPERIMENTAL SETUP

A flow circuit to measure the transvalvular pressure-drop was designed, and driven by a Liquiflo 37F gear-pump (Liquiflo, Garwood, United States) with a theoretical displacement of 0.023 L/Rev (Figure 6.2). Flow-rate was determined by gear-pump rotation speed, which was controlled by a servo-motor (Parker-Hannifin, Oldenzaal, The Netherlands).

Upstream and downstream of the valve housing, two rigid, transparent tubes with an inner diameter of 26 mm and a length of 520 mm (20 diameters) were connected

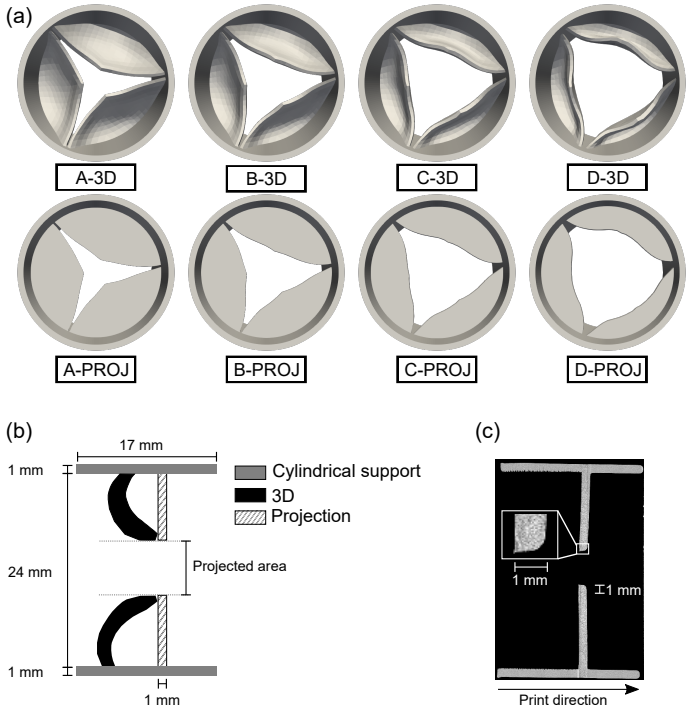

Figure 6.1 (a) Axial view of each of the CAD models that were experimentally tested. (b) graphical illustration on how the projected geometries were obtained. (c) Result of the μCT scan, note the unintentional rounding of the sharp edges due to the 3D printing process.

to generate a straight flow channel, intended to obtain fully developed entry flow at the throat of the valve. 20 diameters upstream of the valve, a settling chamber (50% water, 50% air) was included: the air compartment in this chamber effectively acted as a physical low-pass filter, and filtered out gear-pump induced vibrations. In pulsatile flow conditions this chamber was completely filled with water to avoid compliance in the system. To monitor flowrate an ultrasonic flow rate sensor (ME13PXN Inline, Transonic Systems Inc, Ithaca, NY, USA) was placed upstream of the settling chamber. Furthermore, a Windkessel afterload module with a variable resistance was installed 20 diameters downstream of the valve, and was consequently connected to the reservoir. Two pressure transducers (P10EZ-1; Beckton Dickinson Medical, Sint-Niklaas, Belgium) with a range of -50–350 mmHg were installed 1.7 diameters upstream, and 20 diameters downstream from the valve. Data were acquired at 200 Hz with dedicated LabVIEW (National Instruments, Austin, USA) hard- and software of the pump.

Steady flow-rates between 1.0 and 11.0 $Lmin^{-1}$ (43 and 478 rev/min respectively) at 1.0

Lmin^{-1} intervals were considered. Pulsatile flow conditions were obtained by imposing a time-varying rotation speed. The flow waveform followed a sine squared-based waveform (also see **Chapter 5**) that closely matched a Fourier series representative of aortic blood-flow (Olufsen et al. 2000). That is:

$$Q(t) = \begin{cases} Q_0 \; sin^2\big(t\frac{\pi}{2T_{acc}}\big) & t < T_{acc} \\ Q_0 \; sin^2\big((t + T_{dec} - T_{acc})\frac{\pi}{2T_{dec}}\big) & T_{acc} \leq t \leq T_{systole} \\ 0 & t > T_{systole} \end{cases} \tag{6.1}$$

Here, T_{acc} and T_{dec} represent the period of the acceleration and deceleration slopes respectively. With $T_{acc} = 0.12T_{cycle}$ and $T_{dec} = 0.22T_{cycle}$, systole becomes a fraction of the full cardiac cycle: $T_{systole} = 0.34T_{cycle}$. Note that with this choice of parameters the deceleration phase is approximately twice as long as the acceleration phase. Q_0 represents peak-systolic flow-rate, and was set at 7.0 Lmin^{-1}, in line with the simulations of (**Chapter 5**). For all pulsatile simulations $T_{cycle} = 3.33$ s, resulting in a Womersley parameter of approximately 14. The lower viscosity of water results in a cycle time that is considerably longer than *in-vivo*, but ensured that the physiological ratio between transient inertial forces and viscous forces was maintained.

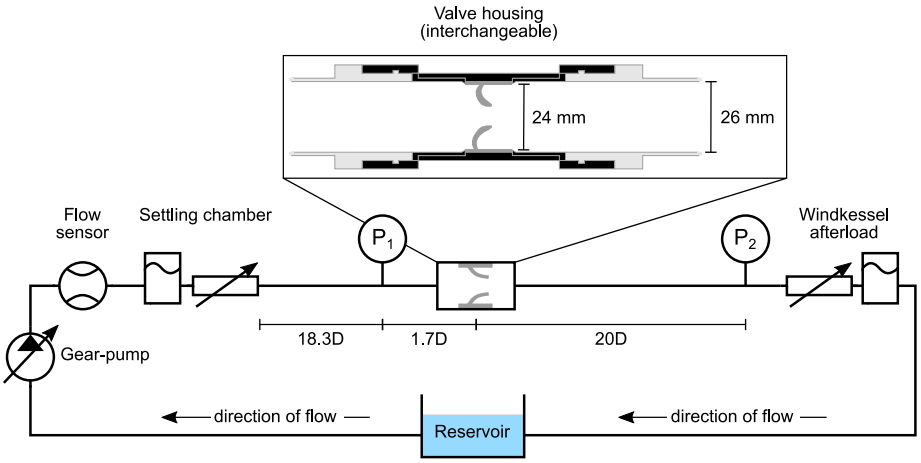

Figure 6.2 Schematic of the experimental setup. The gear-pump extracted water from the reservoir, and was used as a fixed (steady flow) or variable displacement (pulsatile flow) pump. A flow-sensor was included upstream of the settling chamber. The settling chamber consisted of a fluid filled chamber, and a variable resistance. Pressure transducers were included 1.7D upstream and 20D downstream of the valve housing. An afterload module was used to adjust the RC time of the system in pulsatile flow conditions.

6.2.3.1 DATA ACQUISITION AND PROCESSING

Measurements in steady flow conditions were performed for 120 seconds, of which only the last 30 seconds were used for further data analysis. Steady flow pressure data were filtered with a first-order low-pass Butterworth filter with a cut-off frequency of 0.5 Hz. Filtered data were used to compute the time-averaged pressure difference between transducers P_1 and P_2 (Figure 6.2) over the last 30 seconds.

Unlike the steady-flow data, pulsatile data did not require additional filtering. Data of 120 cardiac cycles (equivalent to 400 seconds) were collected and analyzed. Measured flow data were used to identify the start of systole in each cycle. Consequently, the peak systolic, maximum, and mean systolic pressure-drop between P_1 and P_2 was computed.

6.2.4 COMPUTATIONAL METHODS

The section between both pressure transducers (Figure 6.2) was reproduced in a CAD model (also see **Chapter 5**). Volumetric discretization of the fluid volume was performed with ANSYS Fluent Meshing R19.2 (ANSYS Inc, Canonsburg, Pennsylvania, United States). Volumetric meshes consisted predominantly out of regular hexahedral elements in the core, which transitioned to polyhedral elements close to the boundary (poly-hexcore). Features such as the expected point of separation were discretized with extremely small cell sizes, down to 0.05 mm. Moreover, cell sizes of 0.25 mm were introduced in all other areas that were in proximity of the valve construct (see Figure 6.1). Upstream of the valve and between 5 and 20 diameters downstream of the valve coarse cells were used (2x2x2 mm). Volumetric meshes were refined in the area deemed relevant for jet development and breakdown, that is, between 0D and 5D downstream of the valve. In this section, hexahedral elements sized 0.25x0.25x0.25 mm. The total number of elements was between 6 and 7 million.

Inflow-diameter-based Reynolds numbers of 2700 and 5400 were considered, and corresponded to a flow of 3.5 and 7.0 $Lmin^{-1}$. Density of the fluid was set at $998\ kg{\cdot}m^{-3}$, and viscosity was set at $1.05 \cdot 10^{-3}$ Pa·s, the approximate viscosity of water at 18° Celsius. A $1/7^{th}$ power-law velocity profile, corresponding to that of a fully developed turbulent flow (Chant 2005), was prescribed at the inflow boundary. That is:

$$u(r) = U_{max}\left(1 - \frac{r}{R}\right)^{1/n} \tag{6.2}$$

with:

$$U_{max} = \frac{1}{2}\frac{Q}{A}\frac{(n+1)(2n+1)}{n^2}$$

and:

$$n = 7$$

A constant zero-pressure boundary condition on the outflow boundary, and no-slip walls were used. The solution in steady-state flow conditions was obtained with the Reynolds Averaged Navier Stokes Shear-Stress-Transport $k-\omega$ model. The solution of pulsatile conditions was obtained by Large Eddy Simulations, using a constant time-step of $1{\cdot}10^{-4}$ seconds and the non-iterative fractional step method (Armfield and Street 1999). The time-step was kept constant between geometries, and ensured that the Courant number was below 1. Five pulsatile cycles were simulated, and the mean systolic pressure-drop (ΔP_{mean}), the max systolic pressure-drop (ΔP_{max}), and the peak-systolic pressure-drop (ΔP_{peak}) were evaluated.

6.3 RESULTS

Figure 6.1c demonstrates that the μCT scan of the 3D printed model deviates from the original CAD model. The 3D printing process did not seem to capture sharp edges very well, e.g., the 90 degree angles in the projections, and seemed to strongly depend on printing direction. A fillet with a radius of approximately 0.5 mm was observed at the downstream edge.

Experimentally measured ΔP_{peak} was consistently larger in the projected cases: with respect to the 3D configuration increases of 76% (Valve A), 53% (Valve B), 82% (Valve C), and 28% (Valve C) were observed (Table 6.1). Similar differences between the 3D and projected configuration were found in steady flow conditions: at 7.0 and 3.5 $Lmin^{-1}$ an increase in ΔP of 82–87% (Valve A), and 75–91% (Valve B) were observed in the projected cases (with respect to the 3D configuration). In valves C and D at 3.5 $Lmin^{-1}$ $\Delta P \approx 0$, and pressure seems to have fully recovered. CFD simulations demonstrated similar relative differences in ΔP between the 3D and projected configurations. Steady flow simulations suggested that ΔP is between 66–113% larger for projected geometries.

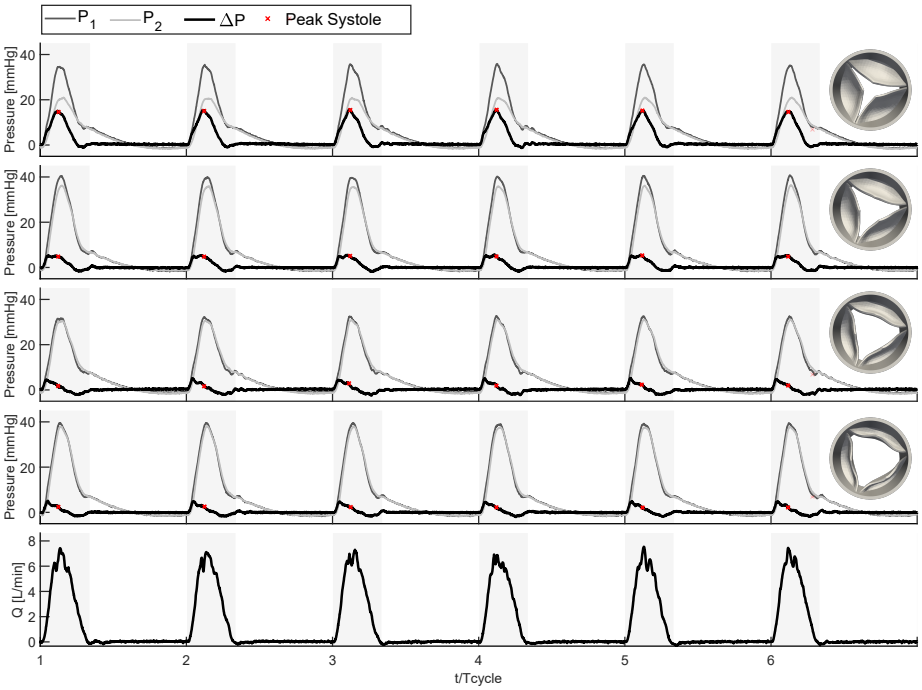

Figure 6.3 Typical example of measured pressures by sensor P_1 and P_2. The pressure-drop was defined as: $\Delta P = P_1 - P_2$. Last graph depicts measured flow rate. x indicates time of peak systolic flow rate.

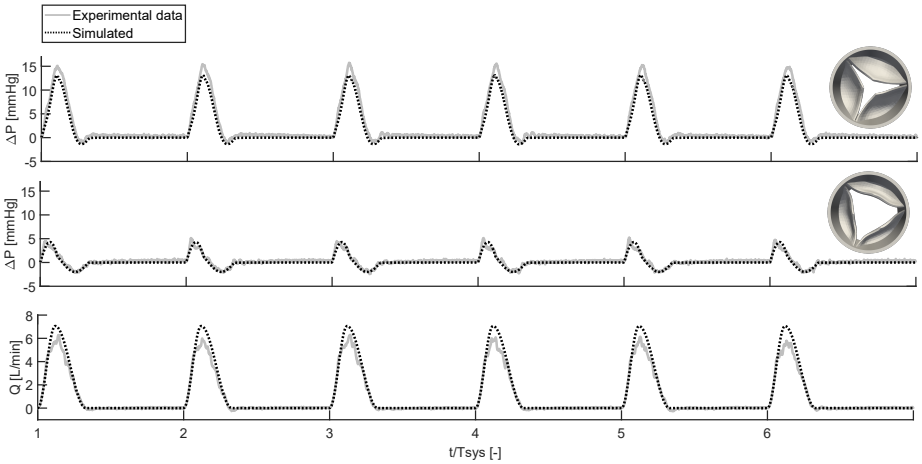

Figure 6.4 Experimentally measured ΔP vs. simulated ΔP. Top, valve A; bottom: valve C. Overall agreement between simulation results and experimental data is good. In valve A, the peak-systolic pressure-drop is underestimated.

ΔP_{max} is affected by the flow unsteadiness and the presence of the valve, and was reached before peak systolic flow. Figure 6.5 demonstrates that $\Delta P_{max} \sim \Delta P_{peak}$ for valves A and B: relative differences of 1% (Valve-A-3D), 2% (Valve-A-PROJ), 12% (Valve-B-3D), and 4% (Valve-B-PROJ) were observed. However, for more open valves (Valves C and D), the influence of the stenosis reduced, and ΔP_{max} was mainly associated with the acceleration of the fluid. Hence, for valves C and D, $\Delta P_{max} \nsim \Delta P_{peak}$: relative differences of 138% (Valve-C-3D), 32% (Valve-C-PROJ), 120% (Valve-D-3D), and 70% (Valve-D-PROJ) were observed.

With $\Delta P_{mean} = 6.0$ mmHg, the mean systolic pressure-drop of Valve A was the largest of all valves, and corresponded to $0.4\Delta P_{peak}$. The ratio between ΔP_{mean} and ΔP_{peak} decreased when the valve was more open, and may reach values as low as $0.3\Delta P_{peak}$. Steady-state experiments showed that ΔP_{peak} in pulsatile flow conditions agree well with steady flow conditions at 7.0 $Lmin^{-1}$ (corresponds to peak-systolic flow). Steady flow conditions at 3.5 $Lmin^{-1}$ (corresponding to mean flow rate in systole) yielded ΔP values that generally under predict ΔP_{mean}.

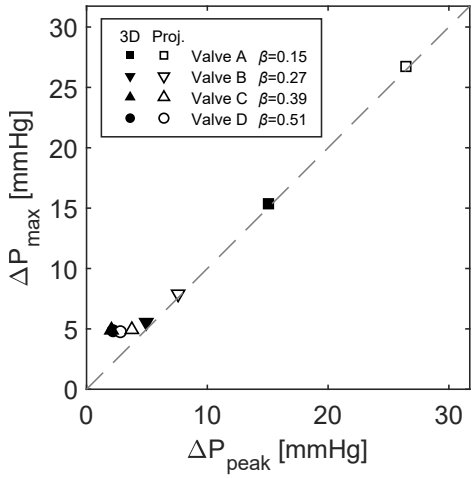

Figure 6.5 ΔP_{max} vs. ΔP_{peak}. For the most stenotic valves A and B the pressure-drop at peak systole reflects the maximum pressure drop in systole. For valves C and D, the peak systolic pressure-drop is not representative for the maximum pressure-drop in systole, i.e., unsteadiness dominates the pressure-drop. Significant differences in pressure-drop are observed between the full 3D configuration (filled markers) and its projected counterpart (open markers).

Figure 6.3 demonstrates that cycle-to-cycle variation in pressure waveforms was generally small. This is corroborated by relatively small standard deviations in Table 6.1. Additionally, Figure 6.4 demonstrates that the simulated pressure and flow wave forms agree reasonably well. In line with the results in Table 6.1, it becomes clear from Figure 6.4 that

ΔP_{peak} was underestimated by the CFD simulations. Additionally, Figure 6.4 suggests that the experimentally measured ΔP_{max} of Valve C occured slightly earlier in systole compared to the CFD simulation.

Figure 6.6 shows that in steady flow conditions CFD-computed ΔP may substantially underestimate experimental ΔP. Good agreement between ΔP_{exp} and ΔP_{CFD} was observed for Valve A-PROJ at all flow-rates. However, agreement at low-ΔP was generally poor for all other valves and their projected counterparts. CFD simulations seemed to predominantly underestimate the experimentally measured pressure-drop at low ΔP.

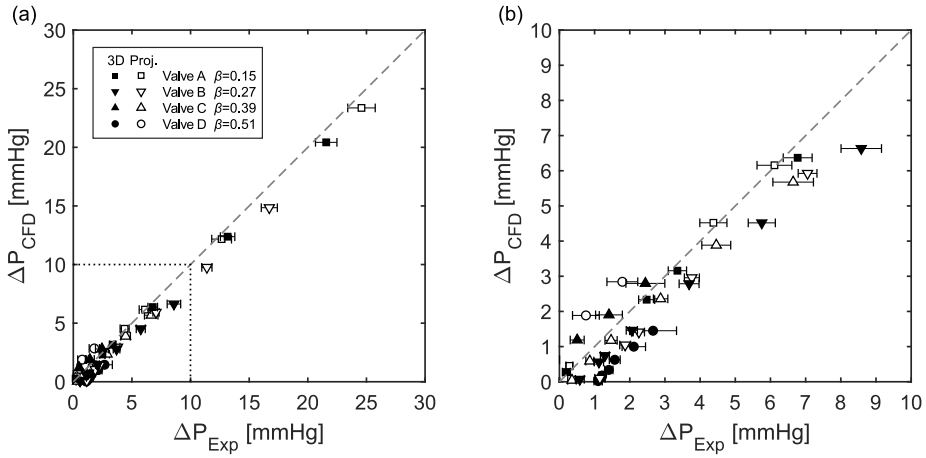

Figure 6.6 (a): ΔP_{exp} vs. ΔP_{CFD} in steady flow conditions. (b) zoomed to dotted section of (a). Error bars represent one standard deviation in the experimentally measured pressure-drop (unfiltered difference between P_1 and P_2).

Table 6.1 Experimental and numerical results of the transvalvular pressure-drop

				Experimental								Numerical				
				Pulsatile flow†						*Steady flow*‡		*Pulsatile flow*#			*Steady flow**	
	Orifice Area	β ratio								*3.5 Lmin*$^{-1}$	*7.0 Lmin*$^{-1}$				*3.5 Lmin*$^{-1}$	*7.0 Lmin*$^{-1}$
				ΔP_{mean}		ΔP_{max}		ΔP_{peak}		ΔP	ΔP	ΔP_{mean}	ΔP_{max}	ΔP_{peak}	ΔP	ΔP
Units	mm^2	A_1 / A_2		mmHg		mmHg		mmHg		mmHg	mmHg	mmHg	mmHg	mmHg	mmHg	mmHg
Valve A	70	0.15	3D	6.0	(0.03)	15.4	(0.34)	15.1	(0.37)	3.4 (0.3)	13.2 (0.6)	4.5	13.1	12.4	3.2	12.4
			Projection	10.8	(0.05)	26.7	(0.36)	26.4	(0.41)	6.1 (0.5)	24.6 (1.2)				6.2	23.4
Valve B	122	0.27	3D	1.9	(0.03)	5.5	(0.16)	4.9	(0.22)	1.3 (0.1)	3.7 (0.3)	1.0	5.0	2.8	0.7	2.8
			Projection	2.9	(0.03)	7.9	(0.17)	7.6	(0.22)	2.3 (0.2)	7.1 (0.3)				1.4	5.9
Valve C	175	0.39	3D	0.6	(0.03)	4.9	(0.27)	2.1	(0.26)	-0.5 (0.1)	0.5 (0.2)	0.4	4.3	1.2	0.3	1.2
			Projection	1.4	(0.04)	4.9	(0.18)	3.8	(0.27)	0.9 (0.1)	2.9 (0.2)				0.6	2.4
Valve D	230	0.51	3D	0.8	(0.03)	4.8	(0.16)	2.2	(0.21)	1.2 (0.1)	1.6 (0.2)	0.2	4.0	0.7	0.2	0.6
			Projection	1.0	(0.03)	4.8	(0.17)	2.8	(0.21)	-1.2 (0.1)	-0.4 (0.2)				0.3	1.1

† Averaged over 100 cycles. Value between parentheses represents the standard deviation
‡ Reflects the steady-flow time-averaged ΔP over an interval of 30 seconds. Value between parentheses indicates the (unfiltered) standard deviation from the time-average.
# Based on LES simulations
* Based on RANS simulations

6.4 DISCUSSION

The availability of robust commercial codes and developments in high performance computing have made CFD models popular in the cardiovascular research community. However, model results should be corroborated with *in-vitro* and *in-vivo* validation studies when possible. In this controlled study, we have shown that generally, CFD models and experimental results demonstrate the same trends. That is, both CFD and experimental measurements showed that a projected geometry may significantly overestimate ΔP. In addition, we demonstrate that the evolution of ΔP in pulsatile flow conditions is captured reasonably well. However, it was also demonstrated that agreement between the computational results and experiments is not guaranteed. For all geometrical combinations, the CFD model tends to underestimate ΔP in steady flow conditions, and underestimate ΔP at peak systole in pulsatile flow conditions. In severely stenotic valves (Valve A) ΔP is dominated by the presence of the stenosis. However, with an increase in valve opening flow unsteadiness becomes increasingly important.

The observation that the three-dimensional shape (projected vs. 3D) significantly influences ΔP can be explained by a reduction in the ratio between the effective and anatomical orifice area, in literature referred to as the contraction coefficient ($C_c = A_{jet}/A_{anatomical}$). The contraction coefficient is a measure for how much the streamlines contract downstream of an orifice and is the point where velocity reaches a maximum. *In-vivo* (Migliore et al. 2017) and *in-vitro* (Gilon et al. 2002) work has shown that valvular shape can have a substantial effect on the contraction coefficient, e.g., $C_c = 0.85 - 0.9$ and $C_c = 0.71 - 0.76$ were reported for dome and flat shaped valves respectively.

Pressure waveforms (Figure 6.3) demonstrate that ΔP reversal ($P_2 > P_1$) occurs in late systole. Pressure-drop reversal occurs later in systole for severely stenotic valves (Valve A), indicating that energy loss due to the presence of the valve is considerable throughout most of systole. In less stenotic valves (Valve C–D), $P_2 > P_1$ for a larger part of the cycle, and is observed once flow deceleration is initiated. This is in line with findings in animal studies, where normalized time to ΔP reversal was 93 $\pm$13% and 69 $\pm$ 36% for mongrel dogs with aortic valve stenosis and healthy controls respectively (Bermejo et al. 2002). In addition, *in-vivo* measurements by Firstenberg et al. (2000) demonstrated that including flow unsteadiness in the Bernoulli equation yielded better estimates of the the maximum pressure-drop across normal mitral valves. This suggests that flow unsteadiness may be more important for moderately stenosed or healthy valves. This is further supported by our numerical and experimental observations of ΔP_{peak}. ΔP_{peak} agrees well with ΔP_{max} for Valves A and B. However, when the transvalvular peak systolic pressure-drop (ΔP_{peak}) is negligible, ΔP_{max} becomes higher than ΔP_{peak}, and occurs at the time instant

of maximum acceleration.

Results in Figure 6.4, Figure 6.6, and Table 6.1 suggest that ΔP in steady flow conditions and at peak systole is underestimated by CFD. Underestimation of ΔP in CFD simulations is common. For example, an *in-vitro* validation study by Quaini et al. (2011) reported an underestimation of ΔP in rectangular (35 mm^2) and circular orifices (40 mm^2) that were used to model mitral valve regurgitation. CFD generally underestimated ΔP by 5–16%. In pulsatile flow conditions, data of a follow up study showed that CFD underestimated ΔP at peak flow by approximately 20% (Wang et al. 2017). In a similar study on mitral regurgation, Sonntag et al. (2014) demonstrated good agreement between jet velocity measurements by Particle Image Velocity and CFD in circular (38.5 mm^2), rectangular (60 mm^2), and star-shaped (63 mm^2) orifices with a thickness of 5 mm. CFD consistently underestimated jet velocity up to approximately 10% in steady flow conditions, differences in ΔP were unfortunately not reported. Differences between experimental measurements and CFD computed pressure-drops were larger in this study, and could either be due to model assumptions and/or experimental inaccuracies. Both are briefly discussed in the following sections.

6.4.1 ASSUMPTION OF FULLY DEVELOPED FLOW

Flow through a stenotic valve is similar to flow through a nozzle or orifice. In industry, the pressure difference caused by such a constriction is exploited to measure flow-rate, and is well documented in the ISO-5167 standard (ISO5167 2003). In orifice-type flow-meters the measured pressure differential is empirically related to the flowrate by the discharge coefficient, and accurate flow measurements require the flow to be fully developed (Reader-Harris 2015). For example, it has been demonstrated that when the upstream velocity profile had a deficit on the centerline, ΔP across the orifice exceeds that of fully developed flow (Morrow et al. 1991; Morrison et al. 1992). Morris and colleagues demonstrated that in extremely skewed velocity profiles the coefficient of discharge can change by 20% (Morrison et al. 1992). Since the discharge coefficient is inversely proportional to the square root of ΔP ($C_d \propto \frac{1}{\sqrt{\Delta P}}$), the observations by Morrison et al. (1992) would suggest that ΔP can vary substantially with underdeveloped flow profiles. Although these observations were made in fully turbulent flow ($Re = 80000$), it is likely that at lower Re, under developed flow-profiles can affect the transvalvular pressure-drop as well. Hence, the assumption of a, symmetric, fully developed turbulent flow (described by the $1/7^{\text{th}}$ power law) that was made in the simulations may not be representative for the — potentially underdeveloped — velocity profile in the experimental setup. Hence, it is recommended that future studies make an effort to quantify the upstream velocity profile to verify that 20 diameters of smooth upstream tubing is enough to ensure fully

developed flow. For example, by making use of flow visualization techniques such as PIV, Tomo-PIV (3D) or Laser Doppler Velocimetry.

6.4.2 EXPERIMENTAL INACCURACIES

Pressure sensors have a finite accuracy in combination with bridge amplifiers. Two individual pressure transducers were placed in the experimental setup, and error sources for both may be different. For example, errors due to linearity and hysteresis are ± 0.1 mmHg over 0 to 10 mmHg. Moreover, pressure transducers have a sensitivity of approximately 5 μV/V/mmHg ($\pm 1\%$). At low pressure-drops these inherent characteristics of measuring devices may have dominated the results. It should be noted that water was used as a working fluid for practical reasons, and low flow-rates were used to maintain physiological Re numbers. As a consequence, at low-flow-rates and for open valves, very low steady-state/peak-systolic pressure-drops (< 1 mmHg) were observed, and were difficult to accurately measure. Experimental errors may be reduced by using water-glycerol mixtures (Yazdi et al. 2018), which would require larger flowrates to maintain the Reynolds number, and lead to larger pressure-drops. Alternatively, pressure transducers that are suitable for a smaller range may be used to obtain more reliable results at low transvalvular pressure-drops. However, it remains unclear to what extent this affected the accuracy of the results.

6.4.3 LIMITATIONS

Flow characteristics of upstream flow were not quantified, and it is suggested that future work attempts to quantify upstream conditions in order to verify the numerical assumption of fully developed (turbulent) flow. Aortic valve stiffness is important in valvular behavior but was neglected in this study. Furthermore, the sinus region was not included, but may be of importance, e.g., it has been shown that coronary flow may suppress vortex development behind the leaflets of the valve (K. Cao and Sucosky 2016).

6.4.4 CONCLUSION

In this study we validated a 3D CFD model of aortic-valve like geometries and their projected counterparts. Projected orifices yielded pressure-drops that were substantially larger than their 3D counterparts. Additionally, we have shown that the 3D CFD simulations were able to reproduce ΔP waveforms to an acceptable level in pulsatile flow conditions. However, peak-systolic ΔP and ΔP in steady flow conditions measured in our experiments were underestimated by CFD.

BIBLIOGRAPHY

Armfield, S. and R. Street (1999). "The fractional-step method for the navier–stokes equations on staggered grids: the accuracy of three variations". In: *Journal of Computational Physics* 153.2, pp. 660–665.

Bahlmann, E. et al. (2010). "Impact of pressure recovery on echocardiographic assessment of asymptomatic aortic stenosis: a SEAS substudy". In: *JACC: Cardiovascular Imaging* 3.6, pp. 555–562.

Baumgartner, H. et al. (2016). "Recommendations on the echocardiographic assessment of aortic valve stenosis: a focused update from the european association of cardiovascular imaging and the american society of echocardiography". In: *European Heart Journal - Cardiovascular Imaging* 18.3, pp. 254–275.

Bermejo, J. et al. (2002). "In-vivo analysis of the instantaneous transvalvular pressure difference-flow relationship in aortic valve stenosis: implications of unsteady fluid-dynamics for the clinical assessment of disease severity." In: *The Journal of heart valve disease* 11 (4), pp. 557–566.

Bruening, J. et al. (2018). "Impact of patient-specific LVOT inflow profiles on aortic valve prosthesis and ascending aorta hemodynamics". In: *Journal of Computational Science* 24, pp. 91–100.

Brunette, J., R. Mongrain, and J. C. Tardif (2004). "A realistic coronary artery phantom for particle image velocimetry". In: *Journal of Visualization* 7.3, pp. 241–248.

Cao, K. and P. Sucosky (2016). "Aortic valve leaflet wall shear stress characterization revisited: impact of coronary flow". In: *Computer Methods in Biomechanics and Biomedical Engineering* 20.5, pp. 468–470.

Cao, P. et al. (2015). "Feasibility of the fabrication of the silicone carotid model by 'multi-piece-mold-injection' method". In: *Journal of Medical and Bioengineering* 4.4, pp. 302–306.

Chant, L. J. D. (2005). "The venerable 1/7th power law turbulent velocity profile: a classical nonlinear boundary value problem solution and its relationship to stochastic processes". In: *Applied Mathematics and Computation* 161.2, pp. 463–474.

Ecabert, O. et al. (2008). "Automatic model-based segmentation of the heart in CT images". In: *IEEE Transactions on Medical Imaging* 27.9, pp. 1189–1201.

Ecabert, O. et al. (2011). "Segmentation of the heart and great vessels in CT images using a model-based adaptation framework". In: *Medical Image Analysis* 15.6, pp. 863–876.

Ferrari, E. et al. (2019). "Suitability of 3d-printed root models for the development of transcatheter aortic root repair technologies". In: *ASAIO Journal* 65.8, pp. 874–881.

Firstenberg, M. S. et al. (2000). "Noninvasive estimation of transmitral pressure drop across the normal mitral valve in humans: importance of convective and inertial forces during left ventricular filling". In: *Journal of the American College of Cardiology* 36.6, pp. 1942–1949.

Garcia, D. et al. (2000). "Assessment of aortic valve stenosis severity". In: *Circulation* 101.7, pp. 765–771.

Gilon, D. et al. (2002). "Effect of three-dimensional valve shape on the hemodynamics of aortic stenosis". In: *Journal of the American College of Cardiology* 40.8, pp. 1479–1486.

Grbic, S. et al. (2012). "Complete valvular heart apparatus model from 4d cardiac CT". in: *Medical Image Analysis* 16.5, pp. 1003–1014.

Ha, H. et al. (2018). "Validation of pressure drop assessment using 4d flow MRI-based turbulence production in various shapes of aortic stenoses". In: *Magnetic Resonance in Medicine* 81.2, pp. 893–906.

Hatle, L., B. A. Angelsen, and A. Tromsdal (1980). "Non-invasive assessment of aortic stenosis by doppler ultrasound." In: *Heart* 43.3, pp. 284–292.

Hoeijmakers, M. J. M. M. et al. (2019). "Estimation of valvular resistance of segmented aortic valves using computational fluid dynamics". In: *Journal of Biomechanics*.

Hoeijmakers, M. J. M. M. et al. (2020). "Combining statistical shape modeling, CFD , and meta-modeling to approximate the patient-specific pressure-drop across the aortic valve in real-time". In: *International Journal for Numerical Methods in Biomedical Engineering*.

Ionasec, R. I. et al. (2010). "Patient-specific modeling and quantification of the aortic and mitral valves from 4-d cardiac CT and TEE". in: *IEEE Transactions on Medical Imaging* 29.9, pp. 1636–1651.

ISO5167 (2003). *Measurement of fluid flow by means of pressure differential devices inserted in circular cross-section conduits running full*. Standard. Geneva, CH: International Organization for Standardization.

Kikinis, R., S. D. Pieper, and K. G. Vosburgh (2013). "3d slicer: a platform for subject-specific image analysis, visualization, and clinical support". In: *Intraoperative Imaging and Image-Guided Therapy*. Springer New York, pp. 277–289.

Laskey, W. K. and W. G. Kussmaul (1994). "Pressure recovery in aortic valve stenosis". In: *Circulation* 89.1, pp. 116–121.

Migliore, R. A. et al. (2017). "Estimation of contraction coefficient of gorlin equation for assessment of aortic valve area in aortic stenosis". In: *World Journal of Cardiovascular Diseases* 07.04, pp. 119–130.

Morrison, G. L., R. E. DeOtte, and E. J. Beam (1992). "Installation effects upon orifice flowmeters". In: *Flow Measurement and Instrumentation* 3.2, pp. 89–93.

Morrow, T. B., J. T. Park, and R. J. McKee (1991). "Determination of installation effects for a 100 mm orifice meter using a sliding vane technique". In: *Flow Measurement and Instrumentation* 2.1, pp. 14–20.

Niederberger, J. et al. (1996). "Importance of pressure recovery for the assessment of aortic stenosis by doppler ultrasound. role of aortic size, aortic valve area, and direction of the stenotic jet in vitro." In: *Circulation* 94 (8), pp. 1934–1940.

Nishimura, R. A. and B. A. Carabello (2012). "Hemodynamics in the cardiac catheterization laboratory of the 21st century". In: *Circulation* 125.17, pp. 2138–2150.

Nishimura, R. A. and A. J. Tajik (1994). "Quantitative hemodynamics by doppler echocardiography: a noninvasive alternative to cardiac catheterization". In: *Progress in Cardiovascular Diseases* 36.4, pp. 309–342.

Olufsen, M. S. et al. (2000). "Numerical simulation and experimental validation of blood flow in arteries with structured-tree outflow conditions". In: *Annals of Biomedical Engineering* 28.11, pp. 1281–1299.

Quaini, A. et al. (2011). "A three-dimensional computational fluid dynamics model of regurgitant mitral valve flow: validation against in vitro standards and 3d color doppler methods". In: *Cardiovascular Engineering and Technology* 2.2, pp. 77–89.

Reader-Harris, M. (2015). *Orifice plates and venturi tubes*. Springer International Publishing.

Sonntag, S. J. et al. (2014). "Combined computational and experimental approach to improve the assessment of mitral regurgitation by echocardiography". In: *Annals of Biomedical Engineering* 42.5, pp. 971–985.

Sulaiman, A. et al. (2008). "In vitro non-rigid life-size model of aortic arch aneurysm for endovascular prosthesis assessment". In: *European Journal of Cardio-Thoracic Surgery* 33.1, pp. 53–57.

Voelker, W. et al. (1992). "Pressure recovery in aortic stenosis: an in vitro study in a pulsatile flow model". In: *Journal of the American College of Cardiology* 20.7, pp. 1585–1593.

Wang, Y. et al. (2017). "3d experimental and computational analysis of eccentric mitral regurgitant jets in a mock imaging heart chamber". In: *Cardiovascular Engineering and Technology* 8.4, pp. 419–438.

Weese, J. et al. (2017). "CFD- and bernoulli-based pressure drop estimates: a comparison using patient anatomies from heart and aortic valve segmentation of CT images". In: *Medical Physics* 44.6, pp. 2281–2292.

Yagi, T. et al. (2013). "Experimental insights into flow impingement in cerebral aneurysm by stereoscopic particle image velocimetry: transition from a laminar regime". In: *Journal of The Royal Society Interface* 10.82, p. 20121031.

Yazdi, S. G. et al. (2018). "A review of arterial phantom fabrication methods for flow measurement using PIV techniques". In: *Annals of Biomedical Engineering* 46.11, pp. 1697–1721.

Zelis, J. M. et al. (2020). "3d-printed stenotic aortic valve model to simulate physiology before, during, and after transcatheter aortic valve implantation". In: *International Journal of Cardiology* 313, pp. 32–34.

Chapter 7

General discussion

7.1 OVERVIEW OF MAIN FINDINGS

In this thesis, CFD models were used to analyze blood flow through healthy and stenotic heart valves. Valvular shapes were obtained from CT images, and enabled patient-specific CFD simulations. These CFD simulations allow for the computation of transvalvular pressure-drop vs. flow relationships (**Chapters 2** and **3**), new indices of stenosis severity (**Chapter 2**), or extensive analysis of specific characteristics of the flow field (**Chapter 5**). When sufficient valvular shapes are available, statistical shape modeling and CFD models may be used to train efficient surrogates (meta-models) of the computationally expensive model (**Chapter 3**). In addition, techniques from the field of sensitivity analysis and uncertainty quantification were used in order to estimate the sensitivity of results to potential segmentation errors (**Chapter 4**). In **Chapter 5**, high-fidelity CFD models were used to quantify the intermittent turbulent behavior of flow downstream of healthy and stenotic aortic valves. Ultimately, the computational models were validated against *in-vitro* measurements (**Chapter 6**). The main findings of this thesis are:

- Image-based CFD models have the potential to provide relevant diagnostic information that may complement existing clinical measures (**Chapter 2**).

- Steady-state simulations are adequate to estimate the peak-systolic transvalvular pressure-drop (**Chapters 2**, **5** and **6**).

- Statistical shape modeling can be effective in extracting physiologically relevant shape variation (**Chapter 3**).

- Statistical shape modeling and CFD models can be used to reduce compute-intensive computational models to real-time by using meta-models (**Chapter 3**).

- Uncertainty in valvular shape may substantially affect the predicted transvalvular pressure-drop vs. flow relationship (**Chapter 4**).

- Intermittent turbulence exists in both healthy and stenotic valves. Turbulent kinetic energy can be up to an order of magnitude higher in stenotic valves (**Chapter 5**).

- Experimental validation showed that pressure-drop evolution over the cardiac cycle can be modeled by CFD. Peak-systolic pressure-drops may however be underestimated by CFD models (**Chapter 6**).

In the following sections the implications of these findings are discussed. In addition, limitations and recommendations for future work and clinical practice are provided.

7.2 IMAGE-BASED COMPUTATIONAL MODELS

Aortic valve stenosis is characterized by a long asymptomatic latent period, but upon onset of symptoms prognosis is poor (Ross and Braunwald 1968). The threshold for severe aortic valve disease is currently set at a jet-velocity of >4 m·s^{-1}, and a valve area of <1.0 cm^2, which comes from observations in prospective studies that two-year survival in asymptomatic patients with excessive jet velocities is poor (Otto et al. 1997; Lancellotti et al. 2018). However, these clinical indicators of aortic valve stenosis are population based (Otto et al. 1997; Falk et al. 2017), and may not be representative for the hemodynamic state of the individual. This is reflected in discrepancies in the grading of aortic valve stenosis at low flows — known as *low-flow/low-gradient* aortic valve stenosis — which is present in approximately 10% of all aortic valve stenosis patients (Kulik 2006). In this subgroup of patients, stenosis severity is uncertain and the benefit of valve replacement is not obvious (Clavel et al. 2016).

To aid diagnosis and disease management, patient-specific image-based computational models — such as those in **Chapter 2** — may be of complementary value. In **Chapter 2**, an image-based computational framework was developed, which was used to compute an index that reflects the energy loss due to the presence of the stenosis. Although this model inevitably contains significant simplifications, it was shown that velocity measurements alone do not properly reflect stenosis severity. The image-based model in **Chapter 2** assumes that the valve is imaged in the most open position, and reflects maximum opening at the time of imaging. As such, the valve resistance index of **Chapter 2** relies heavily on adequate imaging of the valve. This is supported by the observations in **Chapter 4**, where we have shown that uncertainties in the exact valvular shape may propagate through the CFD model, yielding an uncertain estimate of the transvalvular pressure-drop. Moreover, since no valvular motion is modeled, the model of **Chapter 2** would in fact not be able to distinguish between *true* and *pseudosevere* aortic valve stenosis. To differentiate between *true* and *pseudosevere*, the model of **Chapter 2** would need to be extended with a fluid-structure interaction model. With such an extension, valve opening and closing can be modeled. Consequently, dobutamine stress testing — a clinical method to distinguish between *true* and *pseudosevere* aortic valve stenosis — could be simulated. A requirement for this approach would be non-invasive extraction of material properties. Material properties affect valve dynamics (Gilmanov et al. 2019), and can potentially be inferred from 4D CT (Hamdan et al. 2012). In addition, calcific distribution in the valve

apparatus may influence valve dynamics as well, and may need to be included in order to obtain realistic valve behavior (Bosi et al. 2018; Luraghi et al. 2019a).

Inclusion of fluid-structure interaction or high-fidelity, time-dependent simulations — such as the simulations that were presented in **Chapter 5** — may be more appropriate. However, such simulations generally lead to excessive computational times that require in the order of days or weeks to complete (Bavo et al. 2016; Luraghi et al. 2019b). For such demanding simulations using meta-models (**Chapter 3**) — a "model of a model" — may be an attractive solution.

7.3 IN PURSUIT OF FAST AND ACCURATE PATIENT-SPECIFIC MODELS: IS META-MODELING THE SOLUTION?

Computational models are commonly used in the cardiovascular research community, and will become increasingly important for fundamental understanding of the development and progression of cardiovascular diseases. In addition, such models have the potential to yield clinically relevant, diagnostic information, which has been demonstrated by the industry's success-story of HeartFlow™, a company that offers solutions for virtual diagnosis of coronary disease based on blood simulations and CT data (Kawaji et al. 2016; Morris et al. 2017; Min et al. 2015). Such patient-specific computational models are in general very time-consuming, and require extensive pre- and post-processing by an expert. Both these issues inhibit integration of image-based patient-specific computational models into the clinical workflow. Techniques from the field of machine learning may help provide a solution for this. For example, statistical shape modeling (**Chapter 3**) makes use of principal component analysis, a dimensionality reduction technique, which extracts the main directions of shape variation (Heimann and Meinzer 2009; Biglino et al. 2016). In **Chapter 3**, we showed that this method can effectively describe changes in shape by just a few (statistically relevant) parameters. Consequently, a large number of simulations may generate enough data to train a meta-model, i.e., a *model of a model*, that covers the entire input-space. This meta-model can "learn" the relationship between shape variation, and simulation output, and can for any patient, including "unseen" patients, provide a decent prediction of the simulation results. This approach becomes increasingly attractive when computational cost of a single simulation increases, and would therefore also be convenient when more complex models are required, e.g., time-dependent models (**Chapter 5**), or those that aim to model fluid-structure interaction.

Furthermore, meta-models facilitate sensitivity analysis and uncertainty quantification (Quicken et al. 2016). With the shift from population-based medicine to personalized-

medicine, predicting the uncertainty of model output will become increasingly important (Eck et al. 2015). In **Chapter 4**, meta-models were used in order to predict the sensitivity of the transvalvular pressure-drop to potential segmentation errors. More importantly, it was shown that the uncertainty in model input may lead to substantial uncertainties in model output. Quantification of these uncertainties, and identification of parameters contributing to uncertainty, will be key in the road towards clinical acceptance of computational models.

7.4 VALIDATION OF NUMERICAL MODELS

The computational models presented in **Chapters 2**, **3**, and **5** represent only a small part of the complete cardiovascular system. In **Chapter 6**, the computational models of **Chapters 2** and **3** were further simplified, and validated by experimental measurements. Validation studies are required to establish credibility of any computational model, and is gaining increasingly more attention in the field of cardiovascular modeling. For example, in 2018, the American Society of Mechanical Engineering released a new Verification & Validation standard for computational modeling of medical devices (V&V40 2018; Morrison et al. 2019). The main idea of this medical device standard is that credibility requirements of a computational model should be consistent with the risk associated with model use. That is, if the model influence on a decision is high, and the consequence of a decision may lead to adverse events (e.g., surgical intervention), the credibility of the model should also be high. For medical device development, such risks can be mitigated by providing extensive *in-vitro* test data. However, in the case of clinical decision support tools, *in-vitro* test data to improve model credibility will not be available on a routine and patient-specific basis, and would need to be tested rigorously beforehand. Hence, extensive *in-vitro* and *in-vivo* data will be required to establish evidence of model credibility. Some methods to establish CFD model credibility include: PC-MRI for measuring turbulence production (Arzani et al. 2011); invasive *in-vivo* transvalvular pressure-drop measurements by cardiac catheterization during aortic valve replacement procedures (Luraghi et al. 2019a); *in-vitro* Doppler and pressure measurements in flow phantoms (Wang et al. 2017); and particle image velocimetry (*in-vitro*) to verify the computed intraventricular flow patterns (Khalafvand et al. 2018).

These examples show that validation of computational models is usually a task that requires significant effort. In fact, for most complex systems true validation experiments are often infeasible or impractical. Therefore, most validation studies are split into small more manageable blocks (unit-problems), e.g., by making use of validation tiers (Figure 7.1a) (American Institute of Aeronautics and Astronautics, Inc. 1998; Oberkampf

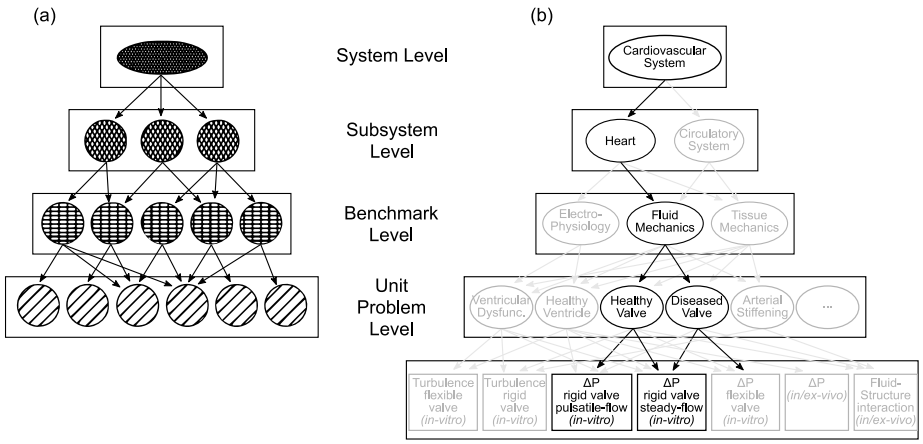

Figure 7.1 (a) Validation tiers as proposed by the American Institute of Aeronautics and Astronautics (Oberkampf and Trucano 2002). (b) Validation tiers applied to (parts of) a model of the cardiovascular system, with the path to the unit-problems that were addressed in this thesis highlighted in black. In gray: some examples of potential unit-problems to improve model credibility.

and Trucano 2002). Such a tiered strategy allows for validation at multiple degrees of complexity, such as geometric complexity or physics coupling. In Figure 7.1b, these conceptual validation tiers are applied to the computational model that is considered in this thesis. In **Chapter 6**, the computed transvalvular pressure-drop was validated by *in-vitro* measurements. However, Figure 7.1 demonstrates that additional experiments may need to be designed to further improve the credibility of the model. For example, turbulence production in steady and pulsatile flow conditions was quantified by computational models (**Chapter 5**), but was not validated with *in-vitro* measurements. Furthermore, valves were assumed to be rigid, but would in reality be flexible. Each of such adaptations to the computational model would impose stricter or different requirements on the experimental studies as well. For instance, validation of turbulence production would require measuring local velocity fluctuations by, for example, hot-wire anemometers. Similarly experimental validation of a computational model that incorporates valve flexibility would need to properly tune afterload impedance, or include coronary flow (Cao and Sucosky 2016), in order to obtain realistic valve motion. It should be noted that experimental validation does not assume that the experimental measurements are more accurate than the computational results. Instead experimental measurements should be seen as the most faithful reflection of reality for the purpose of validation (Oberkampf and Trucano 2002).

7.5 LIMITATIONS & RECOMMENDATIONS FOR FUTURE WORK

Fluid-structure interactions were neglected in all computational models that were presented in this thesis, and can be considered as a major limitation of this thesis. In fact, aortic valves rapidly open and close, and mechanical properties of the valve may change with age (Geemen et al. 2016). Furthermore, the presence of calcifications may affect the dynamics of the aortic valve (Halevi et al. 2016). Obtaining reasonable patient-specific material properties will pose a significant challenge for future work, but will be essential in order to build suitable patient-specific computational models of the (diseased) aortic valve. Additionally, the segmentation framework that was employed in **Chapters 2** and **3** was not validated, and validation should be done in order to establish segmentation accuracy. We suggest that "ground-truth" segmentations are constructed in order to evaluate the accuracy of the Shape Constrained Deformable Model Framework for aortic valves (Ecabert et al. 2011; Weese et al. 2017). Consequently, results of such a validation study can be used to provide better estimates of model output uncertainty (**Chapter 4**).

Chapters 2 and **3** assume that turbulence is fully developed at peak-systole. However, **Chapter 5** demonstrated that flow through the aortic valve may not reach the fully developed state. Although in **Chapters 2** and **5** it was shown that the transvalvular pressure-drop is nevertheless adequately captured, RANS models may not provide a representative realization of time-averaged systolic flow patterns. Hence, scale-resolving models should be preferred when interested in more detailed flow features, such as wall shear stresses. In addition, it is recommended that future work attempts to quantify turbulence production and flow fields downstream of stenotic and healthy heart valves by *in-vitro* experimentation. For example, by making use of hot-wire anemometry, particle image velocimetry, or Doppler ultrasound, ideally in combination with a working fluid that demonstrates blood-like non-Newtonian behavior.

7.6 FUTURE OUTLOOK ON COMPUTATIONAL MODELING IN CARDIOLOGY

The computational models presented in **Chapters 2** and **3** provide image-based patient-specific clinically relevant information. Although not considered in this thesis, computational models may also provide information on the predicted (post-surgery) hemodynamic state of the patient, for instance with lumped parameter (Meiburg et al. 2020) or finite element models (Luraghi et al. 2019b). These examples from literature only consider short-term effects. However, in the case of aortic valve stenosis, predicting cardiac remodeling would be crucial in order to predict long-term disease progression. Similarly,

this may be achieved through lumped parameter (Rondanina and Bovendeerd 2019) or by finite element models (Kroon et al. 2008; Genet et al. 2015). Integration of each of these computational models into the clinical workflow poses substantial challenges, but may eventually lead to a "Digital Twin" of a patient (Corral-Acero et al. 2020). For such "Digital Twins" both mechanistic (e.g., CFD, lumped parameter models, finite element models) and statistical models (e.g., statistical shape modeling) will play a vital role. Synergy between mechanistic and statistical models may assist in interpreting structure-function relationships or in risk prediction. For instance, supervised principal component analysis of cardiac motion predicted survival in patients with pulmonary hypertension, independent of conventional risk factors. (Dawes et al. 2017). Additionally, statistical models are able to relate specific features to disease progression, whereas mechanistic models may assist in understanding the physical meaning of such features, further increasing the credibility of the model (Corral-Acero et al. 2020).

7.7 CONCLUDING REMARKS

In this thesis, a patient-specific computational workflow was developed that enabled the modeling and analysis of blood flow through healthy and stenotic aortic valves. We showed that these models may be used to extract clinically relevant metrics, such as the valve resistance index and pressure-drop. High fidelity simulations showed that flow downstream of healthy and stenotic valves is complex, and characterized by intermittent turbulence. Precise modeling of this complex flow may however not be necessary to adequately approximate the transvalvular pressure-drop. The combined use of statistical shape models, CFD models, and meta-models may significantly reduce computational time, while facilitating uncertainty quantification at the same time. Both of these features could promote the acceptance of computational models in clinical practice.

BIBLIOGRAPHY

American Institute of Aeronautics and Astronautics, Inc. (1998). *Guide: guide for the verification and validation of computational fluid dynamics simulations (AIAA g-077-1998(2002))*.

Arzani, A. et al. (2011). "In vivo validation of numerical prediction for turbulence intensity in an aortic coarctation". In: *Annals of Biomedical Engineering* 40.4, pp. 860–870.

Bavo, A. M. et al. (2016). "Fluid-structure interaction simulation of prosthetic aortic valves: comparison between immersed boundary and arbitrary lagrangian-eulerian techniques for the mesh representation". In: *PLOS ONE* 11.4. Ed. by I. Borazjani, e0154517.

Biglino, G. et al. (2016). "Computational modelling for congenital heart disease: how far are we from clinical translation?" In: *Heart* 103.2, pp. 98–103.

Bosi, G. M. et al. (2018). "Population-specific material properties of the implantation site for transcatheter aortic valve replacement finite element simulations". In: *Journal of Biomechanics* 71, pp. 236–244.

Cao, K. and P. Sucosky (2016). "Aortic valve leaflet wall shear stress characterization revisited: impact of coronary flow". In: *Computer Methods in Biomechanics and Biomedical Engineering* 20.5, pp. 468–470.

Clavel, M.-A., J. Magne, and P. Pibarot (2016). "Low-gradient aortic stenosis". In: *European Heart Journal* 37.34, pp. 2645–2657.

Corral-Acero, J. et al. (2020). "The 'digital twin' to enable the vision of precision cardiology". In: *European Heart Journal*.

Dawes, T. J. W. et al. (2017). "Machine learning of three-dimensional right ventricular motion enables outcome prediction in pulmonary hypertension: a cardiac MR imaging study". In: *Radiology* 283.2, pp. 381–390.

Ecabert, O. et al. (2011). "Segmentation of the heart and great vessels in CT images using a model-based adaptation framework". In: *Medical Image Analysis* 15.6, pp. 863–876.

Eck, V. G. et al. (2015). "A guide to uncertainty quantification and sensitivity analysis for cardiovascular applications". In: *International Journal for Numerical Methods in Biomedical Engineering* 32.8, e02755.

Falk, V. et al. (2017). "2017 ESC/EACTS guidelines for the management of valvular heart disease". In: *European Journal of Cardio-Thoracic Surgery* 52.4, pp. 616–664.

Geemen, D. van et al. (2016). "Age-dependent changes in geometry, tissue composition and mechanical properties of fetal to adult cryopreserved human heart valves". In: *PLOS ONE* 11.2. Ed. by A. J. Engler, e0149020.

Genet, M. et al. (2015). "Modeling pathologies of diastolic and systolic heart failure". In: *Annals of Biomedical Engineering* 44.1, pp. 112–127.

Gilmanov, A. et al. (2019). "Image-guided fluid-structure interaction simulation of transvalvular hemodynamics: quantifying the effects of varying aortic valve leaflet thickness". In: *Fluids* 4.3, p. 119.

Halevi, R. et al. (2016). "Fluid–structure interaction modeling of calcific aortic valve disease using patient-specific three-dimensional calcification scans". In: *Medical & Biological Engineering & Computing* 54.11, pp. 1683–1694.

Hamdan, A. et al. (2012). "Deformation dynamics and mechanical properties of the aortic annulus by 4-dimensional computed tomography". In: *Journal of the American College of Cardiology* 59.2, pp. 119–127.

Heimann, T. and H.-P. Meinzer (2009). "Statistical shape models for 3d medical image segmentation: a review". In: *Medical Image Analysis* 13.4, pp. 543–563.

Kawaji, T. et al. (2016). "Feasibility and diagnostic performance of fractional flow reserve measurement derived from coronary computed tomography angiography in real clinical practice". In: *The International Journal of*

Cardiovascular Imaging 33.2, pp. 271–281.

Khalafvand, S. S. et al. (2018). "Assessment of human left ventricle flow using statistical shape modelling and computational fluid dynamics". In: *Journal of Biomechanics*.

Kroon, W. et al. (2008). "Computational modeling of volumetric soft tissue growth: application to the cardiac left ventricle". In: *Biomechanics and Modeling in Mechanobiology* 8.4, pp. 301–309.

Kulik, A. (2006). "Long-term outcomes after valve replacement for low-gradient aortic stenosis: impact of prosthesis-patient mismatch". In: *Circulation* 114.1_suppl, pp. I–553–I–558.

Lancellotti, P. et al. (2018). "Outcomes of patients with asymptomatic aortic stenosis followed up in heart valve clinics". In: *JAMA Cardiology* 3.11, p. 1060.

Luraghi, G. et al. (2019a). "Does clinical data quality affect fluid-structure interaction simulations of patient-specific stenotic aortic valve models?" In: *Journal of Biomechanics* 94, pp. 202–210.

Luraghi, G. et al. (2019b). "On the modeling of patient-specific transcatheter aortic valve replacement: a fluid-structure interaction approach". In: *Cardiovascular Engineering and Technology* 10.3, pp. 437–455.

Meiburg, R. et al. (2020). "Uncertainty in model-based treatment decision support: applied to aortic valve stenosis". In: *International Journal for Numerical Methods in Biomedical Engineering*.

Min, J. K. et al. (2015). "Noninvasive fractional flow reserve derived from coronary CT angiography". In: *JACC: Cardiovascular Imaging* 8.10, pp. 1209–1222.

Morris, P. D. et al. (2017). "Fast virtual fractional flow reserve based upon steady-state computational fluid dynamics analysis". In: *JACC: Basic to Translational Science* 2.4, pp. 434–446.

Morrison, T. M. et al. (2019). "Assessing computational model credibility using a risk-based framework". In: *ASAIO Journal* 65.4, pp. 349–360.

Oberkampf, W. L. and T. G. Trucano (2002). "Verification and validation in computational fluid dynamics". In: *Progress in Aerospace Sciences* 38.3, pp. 209–272.

Otto, C. M. et al. (1997). "Prospective study of asymptomatic valvular aortic stenosis". In: *Circulation* 95.9, pp. 2262–2270.

Quicken, S. et al. (2016). "Application of an adaptive polynomial chaos expansion on computationally expensive three-dimensional cardiovascular models for uncertainty quantification and sensitivity analysis". In: *Journal of Biomechanical Engineering* 138.12, p. 121010.

Rondanina, E. and P. H. M. Bovendeerd (2019). "Evaluation of stimulus-effect relations in left ventricular growth using a simple multiscale model". In: *Biomechanics and Modeling in Mechanobiology* 19.1, pp. 263–273.

Ross, J. and E. Braunwald (1968). "Aortic stenosis". In: *Circulation* 38.1s5.

V&V40 (2018). *V&v 40 verification and validation in computational modeling of medical devices*. Standard. New York, USA: ASME.

Wang, Y. et al. (2017). "3d experimental and computational analysis of eccentric mitral regurgitant jets in a mock imaging heart chamber". In: *Cardiovascular Engineering and Technology* 8.4, pp. 419–438.

Weese, J. et al. (2017). "CFD- and bernoulli-based pressure drop estimates: a comparison using patient anatomies from heart and aortic valve segmentation of CT images". In: *Medical Physics* 44.6, pp. 2281–2292.

SUMMARY

Aortic stenosis is characterized by a narrowing of the aortic valve opening area, and is predominantly caused by calcification of the leaflets. Calcific deposits cause the valve to be more stiff, impeding the opening and closing function of the valve. The partial opening of the valve imposes a large resistance to blood flow in systole, accompanied by a large (irreversible) transvalvular pressure-drop, which subsequently causes excessive loads on the left ventricle and the heart. The transvalvular pressure-drop is an important clinical indicator of stenosis severity. Non-invasive estimation of this pressure-drop is however challenging. Combining medical imaging data, such as those from Computed Tomography and Magnetic Resonance Imaging, with three-dimensional Computational Fluid Dynamics (CFD) may help to address this issue. Recent advances in medical imaging, segmentation techniques, and CFD allow such models to be developed. The development and improvement of such image based computational models is the focus of this thesis.

In **Chapter 2**, a proof-of-concept CFD simulation framework is presented that estimates the patient-specific transvalvular pressure-drop from segmented aortic valves. This framework is applied to obtain image-based CFD results for 18 patients. From these results, we propose a valve resistance index which serves as an easy-to-interpret metric for the relative importance of the stenosis.

The computational models of **Chapter 2** are computationally expensive, and not feasible for day-to-day clinical practice. In **Chapter 3** we therefore propose to use a statistical shape model to capture physically relevant shape variation. With this approach we were able to capture the valvular shape with a limited number of parameters, and facilitated the simulation of a large number of virtual patients. This simulation data was subsequently used to build a cheap-to-evaluate (surrogate) meta-model. It was shown that this meta-model was of sufficient quality, and allowed for real-time evaluation of the transvalvular pressure-drop vs. flow relation of 74 patients with varying degrees of aortic valve stenosis. In **Chapter 4** we expanded on this work by taking into account shape uncertainty. It was demonstrated that CFD-computed transvalvular pressure-drops strongly depend on geometry. Perturbations in valvular shape that are in the order of 0.5 to 1.0 mm introduced substantial uncertainty in model output.

Flow downstream of stenotic valves is characterized by intermittent turbulence. In **Chap-**

ters 2, **3**, and **4**, turbulence was modeled through the Reynolds Averaged Navier-Stokes equations, which computes the fully developed, time-averaged flow field. In **Chapter 5** this assumption is tested by making use of computationally expensive, and scale resolving simulations. With this, we gained a deeper understanding of the intermittent nature of flow downstream of healthy and stenotic heart valves. For healthy valves, turbulence is triggered in late systole upon onset of the deceleration phase, and quickly dissipates in diastole. For stenotic valves, turbulent flow is present throughout most of systole, and can be an order of magnitude stronger than for healthy valves. Despite this strong intermittency that characterizes aortic valve blood flow, the Reynolds-Averaged Navier-Stokes equations seem to be acceptable for capturing transvalvular pressure-drops.

Experimental validation is crucial in order to strengthen confidence in computational modeling. In the last chapter, we experimentally validate the computational model of **Chapter 6**. We designed a gear-pump driven flow-circuit to experimentally measure the (recovered) transvalvular pressure-drop in steady and pulsatile flow conditions. Heart valves were 3D printed with a high-resolution 3D printer, and covered the full spectrum of possible valve configurations, from completely open to severely stenotic. Reasonable agreement between experimental results and the computational model was found. However, the computational model tended to underestimate peak-systolic and steady-state transvalvular pressure-drops.

With this thesis we have shown that image-based computational models may provide clinically relevant and complementary diagnostic information. However, we recognize that, at this moment, such models may not be suitable for day-to-day clinical practice due to the excessive computational burden. We attempted to address this by systematically investigating and validating model assumptions, and by introducing a meta-model that can function as a surrogate for the computationally expensive simulations.

SAMENVATTING

Aortaklepstenose wordt gekenmerkt door een vernauwing van het openingsvlak van de aortaklep en wordt voornamelijk veroorzaakt door verkalking van de klepbladen. Door deze verkalking worden de klepbladen stijver, wat het functioneren van de aortaklep belemmerd. De aortaklep gaat hierdoor in systole niet meer volledig open, wat leidt tot een (onherstelbare) drukval tussen het linker ventrikel en de aortaboog. Deze drukval resulteert in extra belasting van de hartspier en wordt in de kliniek gebruikt om de ernst van een aortaklepstenose te bepalen. In de klinische praktijk is het niet-invasief bepalen van deze drukval echter een uitdaging. Het gebruik van beeldvormende technieken zoals computertomography (CT) en magnetic resonance imaging (MRI) kunnen hiervoor uitkomst bieden. Met behulp van deze beelden kunnen computermodellen ontwikkeld worden die de bloedstroom door de aortaklep simuleren, en zodoende gebruikt kunnen worden voor het niet-invasief bepalen van de ernst van de aortaklepstenose. De ontwikkeling en verbetering van dergelijke computermodellen staat centraal in dit proefschrift.

In **Hoofdstuk 2** wordt er aandacht besteed aan het ontwikkelen van een *proof-of-concept* computermodel voor het bepalen van de drukval aan de hand van CT beelden. Dit *proof-of-concept* vormt een raamwerk voor het verdere proefschrift en wordt in **Hoofdstuk 2** gebruikt om de bloedstroming van 18 patiënten te simuleren. Vervolgens gebruiken we de resultaten om een eenvoudig te interpreteren index op te stellen die aangeeft hoeveel drukverlies wordt veroorzaakt door de aortaklep, en zodoende een maat is voor de ernst van de stenose.

De computermodellen die worden besproken in **Hoofdstuk 2** vereisen bijzonder veel rekenkracht en tijd. In **Hoofdstuk 3** proberen we via een statistisch vormmodel voor deze tekortkoming een oplossing te vinden. Dit vormmodel beschrijft de vorm van de klep met slechts enkele parameters en maakt het mogelijk om een virtuele patiëntenpopulatie te simuleren. Deze simulatiedata kan vervolgens gebruikt worden om met een meta-model de relatie tussen de vorm van de aortaklep en de drukval over de aortaklep te bepalen. We laten zien dat dit meta-model weinig verschilt van de daadwerkelijke simulatiedata. Bovendien is dit meta-model, in tegenstelling tot de daadwerkelijke bloedstroomsimulatie, zeer efficiënt, vereist het weinig rekenkracht, en is daardoor geschikter voor implementatie in de klinische praktijk. De efficiëntie van dit meta-model maakt het bovendien geschikt voor gevoeligheidsanalyse en het kwantificeren

van model-onzekerheid (**Hoofdstuk 4**). Met deze analyses laten we zien dat de drukval buitengewoon gevoelig kan zijn voor kleine (0.5-1.0 mm) variaties in de vorm van de aortaklep.

Bloedstroming distaal van een aortaklep wordt gekarakteriseerd door periodiek optredende turbulentie. Computermodellen voor het nauwkeurig simuleren van dergelijke stromingen zijn bijzonder complex. In **Hoofdstuk 2**, **3**, en **4** werd deze stroming gesimuleerd door gebruik te maken van de Reynolds-Gemiddelde Navier-Stokes vergelijkingen, die een volledig ontwikkeld en tijds-gemiddeld stromingsveld aannemen. In **Hoofdstuk 5** wordt deze aanname getoetst met behulp van simulaties die het pulserende en turbulente karakter van de bloedstroming nauwkeuriger benaderen. Met deze bloedstroomsimulaties krijgen we een beter beeld van de periodiek optredende turbulentie bij gezonde en stenotische aortakleppen. Voor gezonde kleppen wordt turbulentie slechts aangewakkerd ná piek-systole. Terwijl bij een aortaklepstenose turbulentie al optreed vóór piek-systole. De Reynolds-Gemiddelde Navier-Stokes vergelijkingen kunnen deze eigenschappen niet nauwkeurig modelleren, maar zijn desalniettemin bruikbaar als men enkel geïnteresseerd is in de drukval over de aortaklep.

Bij het modelleren van bloedstroming is het cruciaal om te bepalen in hoeverre simulatiedata overeenkomt met de fysische werkelijkheid. In **Hoofdstuk 6** worden de resultaten van het computermodel uit **Hoofdstuk 5** vergeleken met data van experimentele metingen. Met een 3D printer zijn fysieke modellen van de aortaklep nagemaakt en vervolgens in een experimentele opstelling geplaatst. De (herstelde) drukval over aortakleppen in uiteenlopende klepstanden werd bepaald tijdens constante en pulserende stroming. We vonden een redelijke overeenkomst tussen het computermodel en de experimentele metingen. Over het algemeen onderschat het computermodel echter de drukval bij zowel constante als pulserende stroming.

Met dit proefschrift hebben we laten zien dat computermodellen voor het simuleren van bloedstroming mogelijk toegevoegde diagnostische waarde hebben voor de klinische praktijk. Echter erkennen we dat dergelijke tijdrovende simulaties niet geschikt zijn voor de dagelijkse klinische praktijk. Vandaar dat dit proefschrift de nadruk legt op het systematisch onderzoeken en het valideren van modelaannames, om zodoende tot een nauwkeurig maar toch zeer efficiënt surrogaat model te komen.

CURRICULUM VITAE

Martinus Jan Mathijs Martijn Hoeijmakers was born on the 15th of March 1988 in Venray, The Netherlands. He grew up in the village of Kronenberg, a rural area in the north of Limburg. Martijn completed his pre-university education at the Dendron College in Horst, from which he graduated in 2007. Martijn started his university education at Maastricht University, where he studied General Health Sciences between 2007 and 2010. In the same year he enrolled in the Master program Biology of Human Performance and Healthy at Maastricht University, which he successfully completed in 2011. During his time at Maastricht University, Martijn specialized in the analysis of kinematics and kinetics of the lower-extremity. Between 2012 and 2013 he joined Topsport Expertise & Innovatie Centrum in Sittard as a Human Movement Scientist. As an embedded scientist, he was involved in developing video-based analysis tools for pole-vaulting in collaboration with the national pole-vaulting coach. Martijn enrolled in the Master Biomedical Engineering at the Eindhoven University of Technology in 2013. Between 2013 and 2016 he was part of the Cardiovascular Biomechanics group of prof. dr. ir. Frans van de Vosse. During this time he developed an interest for fluid mechanics. For his internship and graduation project, Martijn spend over one year at the Medical Physics group of the University of Sheffield. There he started working on image-based computational models of blood flow under prof. dr. Rod Hose. Martijn obtained a Master degree in Biomedical Engineering in 2016. In the same year he started his doctorate at the Cardiovascular Biomechanics group of prof. dr. ir. Frans van de Vosse. Funded by Ansys, a company that develops and provides engineering simulation software, Martijn got the opportunity to continue his research into image-based computational models of blood flow at the Eindhoven University of Technology. He was part of the EU-funded EurValve project, in which he focused on applying simulation tools in the context of heart valve disease. Martijn presented his work at various international conferences, including: the Virtual Physiological Human Conference (2016: Amsterdam, 2018: Zaragoza, and 2020: Paris); the 8th World Congress of Biomechanics in Dublin; and the 16th International Symposium on Computer Methods in Biomechanics and Biomedical Engineering in New York. Martijn continues working at Ansys, developing, implementing, and stimulating (the use of) simulation tools for clinical applications.

LIST OF PUBLICATIONS

SCIENTIFIC JOURNALS

M.J.M.M. Hoeijmakers, V. Morgenthaler, M.C.M. Rutten, F.N. van de Vosse. Scale-resolving numerical simulation of steady and pulsatile flow through healthy and stenotic heart valves. *Submitted*.

M.J.M.M. Hoeijmakers, W. Huberts, M.C.M. Rutten, J. Weese, F.N. van de Vosse. Sensitivity analysis and uncertainty quantification for transvalvular pressure-drop computations. *Submitted*.

M.J.M.M. Hoeijmakers, I. Waechter-Stehle, J. Weese, F.N. van de Vosse. Combining statistical shape modeling, CFD, and meta-modeling to approximate the patient-specific pressure-drop across the aortic valve in real-time. *International Journal for Numerical Methods in Biomedical Engineering*, 2020.

M.J.M.M. Hoeijmakers, D.A. Silva Soto, I. Waechter-Stehle, et al. Estimation of valvular resistance of segmented aortic valves using computational fluid dynamics. *Journal of Biomechanics*, 2019.

CONFERENCE CONTRIBUTIONS

M.J.M.M. Hoeijmakers, M.C.M. Rutten, I. Waechter-Stehle, J. Weese, F.N. van de Vosse. Experimental validation of the pressure-drop over 3D printed valves: how not being sharp may lead to misinterpretation. *Virtual Physiological Human*, Paris, 2020.

M.J.M.M. Hoeijmakers, I. Waechter-Stehle, J. Weese, F.N. van de Vosse. A meta-model of the transvalvular pressure-gradient by combining statistical shape modeling and computational fluid dynamics. *Computer Methods in Biomechanics and Biomedical Engineering*, New York, 2019.

M.J.M.M. Hoeijmakers, M. Rochette, J. Weese, D.R. Hose, F.N. van de Vosse. Real-time transaortic pressure gradient computational from parameterized aortic valve geometries. *World Congress of Biomechanics*, Dublin, 2018.

M.J.M.M. Hoeijmakers, M. Rochette, M. Kasztelnik, J. Weese, D.R. Hose, F.N. van de

Vosse. Towards real-time transaortic pressure gradient computation. *Virtual Physiological Human*, Zaragoza, 2018.

D.A. Silva Soto, **M.J.M.M. Hoeijmakers**, A. Narracott, J. Weese, M. Rochette, F.N. van de Vosse, D.R. Hose. CFD-based pressure-drop estimates across the aortic valve. *Virtual Physiological Human*, Amsterdam, 2016.